Multistage Compression and Transient Flow in CO_2 Pipelines with Line Packing

A thesis submitted to University College London for the degree
of

Doctor of Philosophy

By

Nor Khonisah binti Daud

Department of Chemical Engineering

University College London

Torrington Place

London WC1E 7JE

March 2018

DEPARTMENT OF CHEMICAL ENGINEERING

I, Nor Khonisah binti Daud confirm that the work presented in this thesis is my own. Where information has been derived from other sources, I confirm that this has been indicated in the thesis.

Abstract

The main purpose of this thesis is to develop rigorous analytical and CFD models followed by their applications to real case studies in order to:

i) identify the optimum multistage compression strategies for minimising the compression and intercooler power requirements for real CO_2 feed streams containing various types and amounts of impurities associated with the various types of CO_2 capture technologies;

and

ii) investigate the buffering efficacy of realistic CO_2 transmission pipelines as a line packing strategy for smoothing out temporal fluctuations in feed loading and maintaining the desired dense-phase flow for both pure CO_2 and its various realistic mixtures representative of the most common types of capture technologies.

An analytical model based on thermodynamics principles is developed employing Plato Silverfrost FTN95 software and applied to determine the power requirements for various compression strategies and inter-stage cooling duties for typical pre-combustion (98.07 % v/v of CO_2) and oxy-fuel CO_2 mixtures of 85 and 96.7 % v/v CO_2 purity compressed from a gaseous state at 15 bar and 38 ^{o}C to the dense-phase fluid at 151 bar. Compression options examined include conventional multistage integrally geared centrifugal compressors, advanced supersonic shockwave compressors and multistage compression combined with subcritical and supercritical liquefaction and pumping. In each case, the compression power requirement is calculated numerically using a 15-point Gauss-Kronrod quadrature rule in QUADPACK library, and employing the Peng-Robinson Equation of State (PR EOS) implemented in REFPROP v.9.1 to predict the pertinent thermodynamic properties of the CO_2 and its mixtures. In the case of determining the power demand for inter-stage cooling and liquefaction, a thermodynamic model based on Carnot refrigeration cycle is applied. The study shows that a decrease in the impurity content from 15 to 1.9 % v/v in the CO_2 streams reduces the total compression power requirement by *ca.* 1.5 % to as much as 30 %, while for all cases, inter-stage cooling duty is predicted to be significantly higher than the compression power demand. It is found that multistage compression combined with subcritical liquefaction using utility streams and subsequent pumping can offer a higher efficiency than conventional integrally geared centrifugal compression for high purity (> 96.7 % v/v) CO_2 streams. In the case of a raw/dehumidified oxy-fuel mixture, that carries a relatively large amount of impurities (85 % v/v CO_2), subcritical liquefaction at 62.53 bar is shown to increase the cooling duty by as much 50 % as compared to that for pure CO_2.

The second part of this study focuses on the development and testing of a numerical CFD model employing Plato Silverfrost FTN95 software for simulating the transient fluid flow behaviour in CO_2 pipelines with line packing. The model is based on the numerical solution of the conservation equations using the Method of Characteristics, incorporating PR EOS to deal with CO_2 and its various mixtures. Following its verification, the numerical model is employed to conduct a systematic study on the impact of operational flexibility involving a temporal reduction in the upstream CO_2 feed flow rate on the transient flow behaviour in the pipe over a period of 8 hours. A particular focus of attention is determining the optimum pipeline design and operating line packing conditions required in order to maximise the delay in the transition from dense phase flow to the highly undesirable two-phase flow following the ramping down of the CO_2 feed flow rate. The investigations were conducted for both pure CO_2 and its various realistic mixtures. For the case studies examined, the results show that the efficacy of line packing can be increased by increasing the pipeline length from 50 to 150 km for the same pipe inner diameter of 437 mm. However, as the pipelines length increased to 150 km, the increase in the pipe inner diameter beyond 486 mm was found to have no further impact on the line drafting time. While, in the case of inlet feed temperature, the line drafting time increases following an increase in the inlet feed temperature of transported fluid from 283.15 K up to 303.15 K. Beyond the operating inlet feed temperature of 311.15 K, the line drafting time only marginally increased. It is also shown that the presence of impurities reduces the transition time to two-phase flow following the ramping down of the feed flow rate.

Impact statement

CO_2 compression and transportation are essential elements in CCS which are gaining importance in the current worldwide discussion of low carbon energy generation. The outcome from this study intends to give future direction for research and development in this area. The simulation results demonstrate opportunities to optimise the CCS configuration and improve the overall economics of the power plant. These findings also provide relevant data and act as a benchmark since its exemplify how various industrial compression strategies can be integrated in the CCS system for typical CO_2 streams captured from various capture technologies.

In the case of pipeline transportation, this work highlighted a control strategy that can be considered during flexible operation or short-term maintenance activities to ensure the safe operation of the high-pressure CO_2 pipeline. Temporary storage or line packing can be a useful strategy for controlling the CO_2 flow in a pipeline to minimise mass flow variations during these upset conditions. The simulation results provide a better understanding of transport phenomena during transport of CO_2 from the capture point to the storage point of a CCS process.

This study also introduces appropriate simulation tools to determine the power requirement for the compression processes and enable the transient analysis of CO_2 in transport pipelines. The development of analytical and numerical solution techniques for modelling such conditions is considered as the Holy Grail by the pipeline modellers.

Publications

Impact of stream impurities on CO_2 compression for Carbon Capture and Sequestration (CCS), N.K. Daud, S. Martinov, S. Brown and H. Mahgerefteh, ChemEngDay UK 2014, The University of Manchester, 7-8 April 2014 (Poster Presentation).

Impact of stream impurities on CO_2 compression for Carbon, Capture and Sequestration (CCS), N.K. Daud, S. Martinov, S. Brown and H. Mahgerefteh, UKCCSRC Biannual Meeting, University of Cardiff, 10-11th September 2014 (Poster Presentation).

Compression Requirements for Post-Combustion, Pre-Combustion and Oxy-Fuel CO_2 Streams in CCS, N.K. Daud, S. Martinov, S. Brown and H. Mahgerefteh, International Forum on Recent Developments of CCS Implementation, Athens Ledra Hotel, Athens, Greece, 26-27th March 2015 (Poster Presentation).

Compression Requirements for Post-Combustion, Pre-Combustion and Oxy-Fuel CO_2 Streams in CCS, N.K. Daud, S. Martinov, S. Brown and H. Mahgerefteh, ChemEngDay 2015, Sheffield, 8-9th April 2015 (Poster Presentation).

Simulation of Transient Flow in CCS Pipelines with Intermediate Storage, N.K. Daud, S. Martynov, S. Brown and H. Mahgerefteh, 2nd International Forum on Recent Developments of CCS Implementation, St. George Lycabettus Boutique Hotel, Athens, Greece, 16-17th December 2015 (Poster Presentation).

Impact of stream impurities on compressor power requirements for CO_2 pipeline transportation, S.B. Martynov, N.K. Daud, H. Mahgerefteh and R.J. Porter, International Journal of Greenhouse Gas Control, 54 (2016) 652-661.

Acknowledgements

I wish to thank the following people and organisations who have contributed so much in many ways to facilitate the completion of this thesis.

Firstly, the Almighty God, who reigns over us. Thank you for being with me through thick and thin.

To Ministry of Education Malaysia (MOE) and Universiti Malaysia Pahang (UMP) for providing me with the financial resource which enabled me to complete my work.

My supervisor, Prof. Haroun Mahgerefteh for the opportunity given to me to study in this field and your excellent supervision.

To Dr. Sergey Martynov and Zhang Wentian, for all the motivation, advice and criticism through the course of my time at UCL.

To my family and husband, Mrs. Sopiah Binti Din and Mr. Fais Hidayat Bin Ya'amah for their never-ending support and motivation.

Finally to all my colleagues, Rev, Jian, Dr. Richard, Ernie, Chi Ching, Sakiru, Kak Zai, Saad, Kak Ana, Ikin, Am and Jan. Thank you for all their encouragement and help.

Table of contents

List of figures

List of tables

List of abbreviations

CCS	Carbon Capture and Sequestration
CO_2	Carbon Dioxide
CFD	Computational Fluid Dynamics
MW	Megawatt
PR EOS	Peng-Robinson Equation of State
MOC	Method of Characteristics
REFPROP	Reference Fluid Thermodynamic and Transport Properties Database
kW	Kilowatt
ORC	Organic Rankine Cycle
COE	Cost of Electricity
TEG	Triethylene Glycol
LHS	Left Hand Side
RHS	Right Hand Side
GERG	Groupe Européen de Recherches Gazières
VLE	Vapour Liquid Equilibrium
LK	Lee-Kesler
SAFT	Statistical Associating Fluid Theory
RK	Redlich-Kwong
SRK	Soave-Redlich-Kwong
PT	Patel-Teja
AAD	Absolute Average Deviation
FDM	Finite Difference Methods
FVM	Finite Volume Methods
PDE	Partial Differential Equation
CG	Characteristic Grid
MST	Method of Specified Time Intervals
ODE	Ordinary Differential Equation
CFL	Courant-Friedrichs-Lewy
OLGA	Oil and Gas Simulator
GDTF	Gas Dynamic Test Facility
HEM	Homogeneous Equilibrium Mixture Model
CNGS-MOC	Compound Nested Grid System Method of Characteristics
PDU	Pressure, density and velocity
PHU	Pressure, enthalpy and velocity
PSU	Pressure, entropy and velocity
COSTALD	Corresponding State Liquid Density
PROFES	Probabilistic Finite Element System
IGCC	Integrated Gasification Combine Cycle
ASU	Air Separation Unit
AGR	Acid Gas Recovery
QUADPACK	A Subroutine Package for Automatic Integration
ANN	Artificial Neural Network
RES	Renewable Energy Resources
PC	Pulverised Coal

IGCC	Integrated Gasification Combine Cycle
NGCC	Natural Gas Combine Cycle
CCGT	Combine Cycle Gas Turbine
LOX	Liquid Oxygen
AGRU	Acid Gas Removal Unit
MAOP	Maximum Allowable Operating Pressure
ISO	Independent System Operator

CHAPTER 1:

INTRODUCTION

Carbon Capture and Sequestration (CCS) has been proposed as a promising technology to mitigate the impact of anthropogenic CO_2 emissions from the manufacturing industry and power generation sources, such as coal-burning power plants, on global warming (Metz et al., 2005). A fundamental part of the CCS chain is the transportation of CO_2 captured from emitters to locations of geological sequestration. Long-distance onshore and offshore transportation of large quantities of CO_2 can be efficiently achieved using pipelines transmitting CO_2 in the dense phase at pressures typically above 86 bar (McCoy and Rubin, 2008), i.e. above the fluid critical point pressure (Seevam et al., 2008, Yoo et al., 2013). Given the relatively low pressure of captured CO_2 (Pei et al., 2014), the pipeline transportation requires additional facilities for compression of the stream which can be extremely energy intensive and hence expensive.

Compression of captured CO_2 to the high pressures suitable for transportation can be accompanied by a significant temperature rise, typically above 100 ^{o}C. Such high temperatures can damage the compressor and pipeline internal coatings employed to reduce pipeline degradation. Therefore, cooling is applied during compression and before the pipeline transportation of the CO_2 stream. The cost of CO_2 compression is however significant, and may be up to 8-12 % of the electricity generated from the power plant (Moore et al., 2011). In addition, the available conventional CO_2 compression systems are prohibitively expensive due to the high overall pressure ratio (e.g. 100:1) used. The above highlight the necessity for detailed analysis in order to minimise both compressor power and capital cost requirements of the compression system. Several options have been recently analysed in the literature for compression of CO_2 for transportation in pipelines (Witkowski and Majkut, 2012). These options include those using conventional multistage centrifugal compressors, compressors combined with subcritical and supercritical liquefaction and pumping, and supersonic axial compressors. Among these options, the multistage compression combined with liquefaction and pumping has been reported to be the most efficient (Witkowski and Majkut, 2012). This option is practically attractive since the pumping of a liquid is less energy demanding than gas-phase compression, while relatively high boiling of pure CO_2 point (*ca.* 20 ^oC at 60 bar) allows using utility streams for the liquefaction process. Supersonic shock-wave compressors can be used for the compression of large amounts of fluid, having lower capital costs than traditional centrifugal compressors.

In the case of industrial-grade CO_2, the presence of any impurities is expected to diminish the net amount of CO_2 processed, and hence reduce the efficiency of the entire CCS operation. However, once the stream is purified to an acceptable level for pipeline transport and geological storage, it is important to identify the compression strategy giving rise to the lowest cost for the particular CO_2 composition. The choice of the compression strategy and costs associated with compression depend on the physical properties of the CO_2 mixture, such as fluid compressibility, density and saturation temperature and pressure. For example, when using multistage compression combined with liquefaction, the variation of the fluid boiling point with the CO_2 stream composition will have a direct impact on the liquefaction pressure and, hence, the efficiency of the compression process. At present, however, the qualitative impact of CO_2 stream impurities on the power requirements and choice of the optimum compression strategy remains unclear.

For these reasons, the development of efficient schemes for the compression and conditioning of CO_2 prior to its transportation by pipeline, and integration of these schemes within CCS, is an important practical issue, which is attracting increasing attention (Ludtke, 2004, Romeo et al., 2009, Moore et al., 2011, Witkowski and Majkut, 2012). However, the selection and development of optimal compression strategies are particularly dependent on the type of the CO_2 separation technology employed. In a typical post-combustion capture, nearly pure CO_2 stream is separated from the flue gas stream close to ambient pressure, while in pre-combustion and oxy-fuel captures, *ca.* 15-30 bar separation pressures are applied (Witkowski and Majkut, 2012, Besong et al., 2013), with ‘double flash’ or distillation cryogenic separation methods commonly proposed for the removal of non-condensables (e.g. N_2, O_2 and Ar).

Oxy-fuel is one of the capture technologies which has recently gained significant attention due to its eligibility for retrofitting and CCS-ready concepts. However, compared to the more traditional post-combustion and pre-combustion capture technologies, oxy-fuel technology produces a raw CO_2 stream with relatively high concentration of impurities that may require partial or a high level of removal and whose presence can be expected to increase the costs of CO_2 compression and pipeline transportation compared to pure CO_2. Since CO_2 compression systems are commonly designed assuming negligible amount of impurities in the CO_2 fluid, it is of practical interest to evaluate the impact of impurities in pre-combustion and oxy-fuel streams on the compression power requirements.

Therefore, this study is motivated by the need to gain a better understanding of the possibilities and limitations of the impure CO_2 compression process for oxy-fuel and pre-combustion capture applications. An investigation into the efficient transportation of CO_2 during flexible operation is the second purpose of this study. The existing commercial application of CO_2 pipelines is based on 'base-load operation', i.e. no significant temporal variations in the feed rate is envisaged (IEAGHG, 2012). In practice however, depending on the CO_2 emission source, variations in the CO_2 feed flow rate, for example during uncertain electricity supply and demand from fossil fuel power plants will be inevitable. Hence in these circumstances designing a self-regulating CO_2 pipeline transport system enabling the steady flow delivery of CO_2 to the sequestration sites becomes important.

Chalmers and Gibbins (2007) suggest that any restrictions on short-term operating patterns can be avoided by adopting operating procedures that allow for some CO_2 buffering in the pipeline transportation system. The use of a pipeline as short-term storage is an appropriate strategy to ensure the fluctuation of the flow in the pipeline system can be minimised. This strategy is defined as 'line-packing' where the pipeline pressure is varied to pack more or less CO_2 by employing the pipeline as storage vessel (Jensen et al., 2016b).

Some works have been carried out on the dynamics of CO_2 transport pipeline systems (Liljemark et al., 2011, Klinkby et al., 2011, Mechleri et al., 2016, Aghajani et al., 2017). These findings lend support and provide guidelines to investigate the flexibility in the pipeline system by employing the pipe as short-term storage. In order to investigate the efficacy of this method, the stored CO_2 is de-packed or drafted to supply the needs during periods of significant load fluctuation to maintain the flow into the pipeline and sequestration site. In pipeline terminology, increasing the inventory is called line packing, while decreasing it is called line drafting (de Nevers and Day, 1983). The time available to under-take line drafting is called the line-drafting time. In this study, the flexibility to line-draft a pipeline is assessed by determining the time available for an operator to de-pack dense phase CO_2 in the pipeline during flexible operations.

The optimum parameters selection for line packing is investigated by studying the impact of pipeline design parameters, inlet mass flow rate and inlet temperature on the available line drafting time. The selection of the range of pipeline dimensions in terms of length, diameter and wall thickness is based on the design criterion outlined in McCoy and Rubin (2008) and Aghajani et al. (2017). The efficacy of the optimised line packing is investigated by studying the impact of impurities on the line drafting time, the CO_2 mixtures captured from pre-combustion and oxy-fuel capture technologies are employed based on the compression case study. In particular, these impurities have a significant impact on the physical properties of the transported CO_2 which make it difficult to maintain the single-phase flow. The presence of impurities also affect pipeline resistance to fracture propagation, corrosion, non-metallic deterioration, the formation of clathrates and hydrates as well as changing the capacity of the pipeline itself (Seevam et al., 2008, Jensen et al., 2016b). All these effects have direct implications for both the technical and economic feasibility of designing an efficient CO_2 pipeline transport.

Therefore, the main purpose of this study is to develop mathematical models to:

i) identify the optimum multistage compression strategies for minimising compression power consumption for real CO_2 feed streams containing various types and amounts of impurities;

and

ii) investigate the buffering efficacy of realistic CO_2 transmission pipelines as a strategy for smoothing out temporal fluctuations in feed loading associated with typical emission sources.

Hence, the main objectives of this study are:

1. To develop a rigorous mathematical model for multistage compression of pure and impure CO_2 streams captured from pre-combustion and oxy-fuel capture technologies as well as to determine and compare the corresponding compression power requirements.
2. To determine the optimum multistage compression strategies in order to minimise the power requirements in the compression system.
3. To develop a transient pipeline flow model to simulate feed load ramping during flexible operation.
4. Use the transient flow model developed above to investigate the impacts of pipeline overall dimensions, inlet fluid temperature, inlet mass flow rate and CO_2 impurities on the efficacy of a pipeline as line packing.

This thesis is divided into 5 chapters:

In chapter 2, the theoretical basis for calculating the compression power and intercooling heat in a multistage compression system are presented and discussed. The general equations to calculate the compression power and thermodynamics properties are derived and explained. The implementation of these equations from the previous reported studies are also reviewed in the following section. This chapter also covers the theoretical basis in developing the pipeline flow model for dense phase CO_2 streams together with its assumptions and justifications. The mass, momentum and energy conservation equations for the fluid flow in the pipeline system are presented.

The numerical methods used for solving the conservation equations including the method of characteristics (MOC) are discussed. The mathematical models available in the open literature for simulating the transient flow in the high-pressure CO_2 pipeline system are also reviewed in this chapter.

Chapter 3 covers the description of the types of industrial compression technologies employed and the impurities present in the pre-combustion and oxy-fuel streams. This section also presents a description of the rigorous thermodynamic model developed to determine the total power consumption for multistage compression of pure and impure captured CO_2 streams. From the developed mathematical model, the optimum multistage compression schemes are determined depending on the outlet pressure from the separation unit of the captured streams and the thermodynamic properties of the CO_2 mixtures. The calculated power requirements for compression and intercooling heat for various compression schemes for particular CO_2 mixtures are compared and discussed.

In chapter 4, the influence of line packing on maintaining the near-steady flow condition for pure and impure CO_2 during flexible operation is discussed. The development of the numerical transient pipe flow model and simplified analytical model are presented, including the governing conservation equations, the boundary conditions and the solution method. Steady state flow is established in the pipeline before the transient feed loadings are mimicked by gradually closing a feed valve at the upstream of the pipe. The effect of operational flexibility on pipe is investigated accounting for impurities components. The validity of the simplified analytical model is studied against developed transient pipe flow model. A number of hypothetical but nevertheless realistic flexible loading scenarios are simulated in order to demonstrate the robustness and the efficacy of the flow model as a control design and operation tool. The impact of pipeline overall dimensions, inlet temperature, inlet mass flow rate and CO_2 impurities on the line drafting time are simulated and the results are discussed. Chapter 5 summarises the key outcomes of the study and suggestions for future research.

CHAPTER 2:

THEORETICAL MODELLING OF MULTISTAGE COMPRESSION POWER REQUIREMENT AND TRANSIENT FLUID FLOW

2.0 Introduction

In this chapter, the theoretical bases for calculating the compression power and intercooling heat exchanges in a multistage compression system are presented. The general equations to calculate the compression power and thermodynamics properties are discussed. The implementation of these equations from the previous reported studies are also reviewed. This chapter also covers the theoretical basis for modelling the transient fluid flow in the high-pressure CO_2 pipeline together with its assumptions and justifications. The mass, momentum and energy conservation equations for the fluid flow in the pipeline system are also presented. The numerical methods used for solving the conservation equations in particular the Method of Characteristics (MOC) are discussed. The mathematical models available in the open literature for simulating the transient flow in the high-pressure CO_2 pipeline system are also reviewed in this chapter as a prelude to the next chapter dealing with the pressure and flow fluctuations during load change.

2.1 Modelling of multistage compression power requirement

This section deals with the general equations to determine the total power consumption for multistage compression system equipped with intercooling equipment. Fundamentally, these equations are derived from basic thermodynamic and energy balance relations.

2.1.1 Compression model

The compression work, W_{comp} for isentropic, polytropic and isothermal processes between pressure levels, P_1 and P_2, based on ideal gas assumption are respectively given by (Cengel and Boles, 2011),

Isentropic (PV^{κ} = constant):

$$W_{comp} = \frac{\kappa}{\kappa - 1} RT_1 \left[\left(\frac{P_2}{P_1} \right)^{\frac{\kappa-1}{\kappa}} - 1 \right] \qquad 2.1$$

Polytropic (PV^n = constant):

$$W_{comp} = \frac{n}{n - 1} RT_1 \left[\left(\frac{P_2}{P_1} \right)^{\frac{n-1}{n}} - 1 \right] \qquad 2.2$$

Isothermal (PV = constant):

$$W_{comp} = RT \ln \frac{P_2}{P_1} \qquad 2.3$$

where P, V, R, T, κ and n are the pressure, volume of the fluid, universal gas constant, fluid temperature and the isentropic as well as polytropic exponents, respectively. The subscripts 1 and 2 indicate the conditions at the suction and discharge of the compressor.

The equations 2.1-2.3 are appropriate for the calculation and analysis of an ideal gas. In the case of a real gas such as CO_2, from the general energy balance relations (Cengel and Boles, 2011),

$$\begin{matrix}\text{Rate of net energy transfer in} \\ \text{by heat, work and mass, E in}\end{matrix} = \begin{matrix}\text{Rate of net energy transfer out} \\ \text{by heat, work and mass, E out}\end{matrix} \qquad 2.4$$

Noting that energy can be transferred by heat, work and mass only, the energy balance in equation 2.4 for a general steady-flow system can also be written more explicitly as (Cengel and Boles, 2011):

$$Q_{in} + W_{in} + \sum_{in} m\left(h + \frac{v^2}{2} + gz\right) = Q_{out} + W_{out} + \sum_{out} m\left(h + \frac{v^2}{2} + gz\right) \qquad 2.5$$

where *h*, *v*, *z* and *g* are the fluid enthalpy, velocity, height and gravity, respectively. Q_{in}, W_{in} and m_{in} are the heat transferred, total work and mass flow rate into the system, while Q_{out}, W_{out} and m_{out} are the heat transferred, total work and mass flow rate out of the system.

Compressors are devices used to increase the pressure of a fluid. Work is supplied to this device from an external source through a rotating shaft. Therefore, compressors involve work inputs at a rate of *W*, while heat is assumed to be transferred from the system (heat output) and at a rate of *Q*. Thus, the energy balance relation for a general steady-flow system becomes:

$$W - Q = \sum_{out} m\left(h + \frac{v^2}{2} + gz\right) - \sum_{in} m\left(h + \frac{v^2}{2} + gz\right) \qquad 2.6$$

For single-stream devices, the steady flow energy balance equation 2.6 becomes:

$$W - Q = m\left[h_2 - h_1 + \frac{v_2^2 - v_1^2}{2} + g(z_2 - z_1)\right] \qquad 2.7$$

In the case of the compressor, the fluid experiences negligible changes in its kinetic and potential energies. The velocities involved are usually too low to cause any significant change in the kinetic energy. This change is usually very small relative to the change in enthalpy, and thus it is often disregarded. Heat transfer from compressors is usually negligible $(Q \approx 0)$ since they are typically well insulated unless there is intentional cooling. The energy balance equation (equation 2.7) is thus reduced further to:

$$W_{comp} = m(h_2 - h_1) \qquad 2.8$$

where *m*, h_1 and h_2 are the mass flow rate, suction and discharge enthalpies, respectively. Thus, the compression work of a single compressor for a real gas fluid can be determined using equation 2.8.

2.1.2 Compressor efficiency

Compression system analysis is often carried out assuming a constant isentropic efficiency for compressors. The isentropic compression system is impossible in reality. However, for the simplification of the calculation, the isentropic efficiency is employed because it can be directly derived from the station design parameters, i.e. gas composition, suction temperature and pressure as well as discharge pressure. Whereas, the definition of polytropic efficiency requires the additional knowledge of the discharge temperature of the compression system. The isentropic efficiency of a compression process can be defined as:

$$\eta_{is,comp} = \frac{W_s}{W_a} = \frac{\Delta h_s}{\Delta h_a} \qquad 2.9$$

where W_s, W_a, Δh_s and Δh_a are the compression work of an isentropic process, the actual compression work, the specific enthalpy change in an isentropic process and the specific enthalpy change of the actual process, respectively. In any real process, the isentropic efficiency is smaller than unity (Austbø, 2015).

The effect of the compressor isentropic efficiency on the compression work can be presented in figure 2.1.

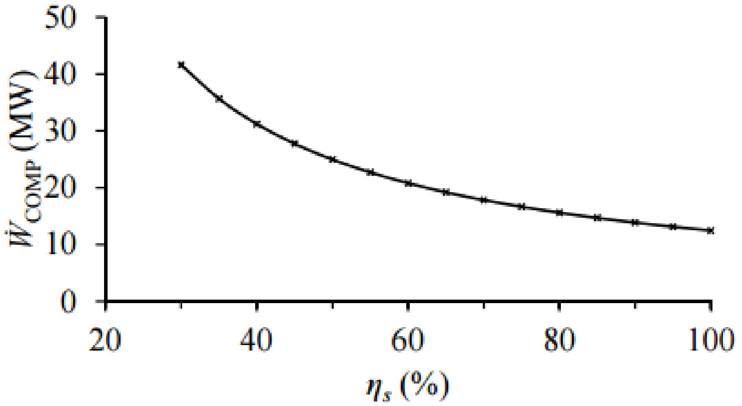

Figure 2.1: Compression power as function of compressor isentropic efficiency (Austbø, 2015).

As can be observed in figure 2.1, the compression work decreases with increasing isentropic efficiency. Also, larger absolute savings in power consumption are obtained when the efficiency is high.

In order to calculate the compression work (equation 2.8) for a real gas, the discharge enthalpy, h_2 can be determined using isentropic efficiency, $\eta_{is,comp}$ of the compressor,

$$h_2 = h_1 + \frac{h_{is,2} - h_1}{\eta_{is,comp}} \tag{2.10}$$

where $h_{is,2}$ is the discharge enthalpy for the isentropic process.

The value of $\eta_{is,comp}$ greatly depends on the design of the compressor. Well-designed compressors have isentropic efficiencies that range from 80 to 90 % (Cengel and Boles, 2011).

2.1.3 Multistage compression with intercooling

Multistage compression with intercooling is an efficient means for reducing power consumption. It is clear that cooling a gas as it is compressed is desirable since this reduces the required work input to the compressor and avoids damage to the compressor seals due to high temperatures. However, often it is not possible to have adequate cooling through the casing of compressor, and it becomes necessary to use other techniques to achieve effective cooling. One such technique is multistage compression with intercooling, where the gas is compressed in stages and cooled between each stage by passing it through a heat exchanger called an intercooler as shown in figure 2.2.

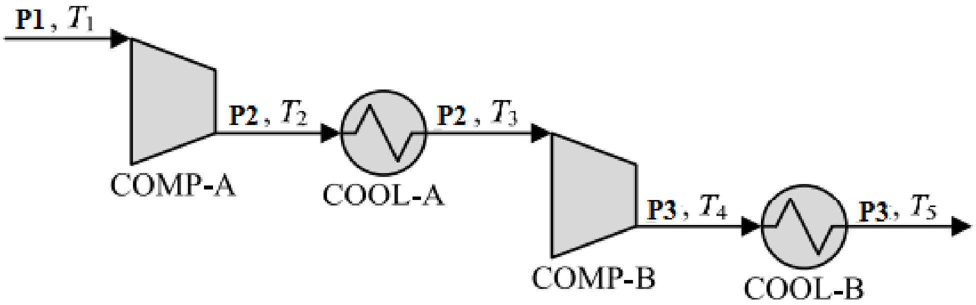

Figure 2.2: Two-stage compression with intercooling (Austbø, 2015).

Ideally, the cooling process takes place at constant pressure, and the gas is cooled to the initial temperature at each intercooler. Multistage compression with intercooling is especially attractive when a gas is to be compressed to very high pressures.

The effect of intercooling on compressor work is illustrated on *P-h* diagram in figure 2.3 for a two-stage compressor, where P_1 and P_3 are the suction pressure and discharge pressure, respectively.

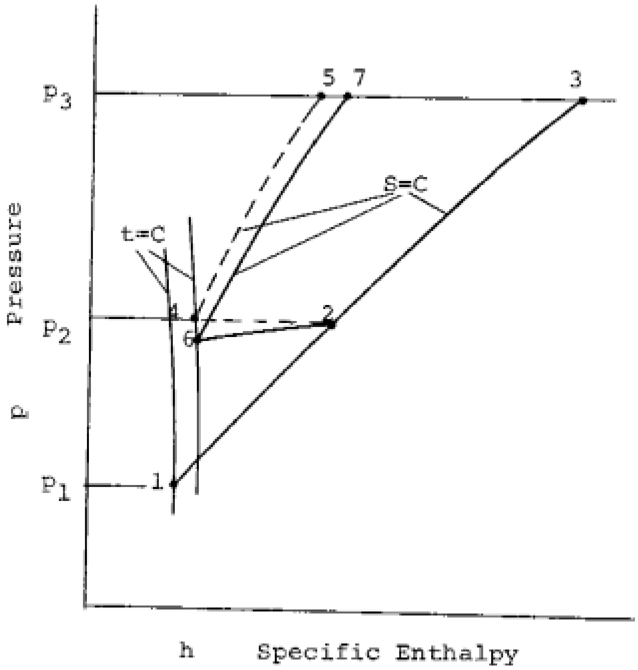

Figure 2.3: A *P-h* diagram for two-stage compressor with an intercooler (Wu et al., 1982).

The compression work, $W_{comp,1}$ of the single isentropic compressor equals the specific enthalpy difference between point 3 and point 1 multiplied by the mass flow rate, *m* of the gas and can be expressed as:

$$W_{comp,1} = m(h_3 - h_1) \qquad 2.11$$

If two-stage compression is used instead of one-stage compression, and the assumption is made that there is no pressure drop in the intercooler, the overall compressive process curve is presented by the paths 1-2-4-5 in figure 2.3. The gas is compressed in the first stage from P_1 to an intermediate pressure P_2 at point 2, cooled at constant pressure at point 4 and compressed in the second stage to the final pressure, P_3 at point 5. The area in the process curve 2-3-4-5 on the *P-h* diagram represents the work saved as a result of two-stage compression with intercooling. The size of the saved work varies with the value of the intermediate pressure and it is of practical interest to determine the conditions under which this area is maximised. The total compression work for a two-stage compressor is the sum of the work inputs for each stage of compression, as determined from:

$$W^{'}_{comp,2} = m(h_2 - h_1) + m(h_5 - h_4) \qquad 2.12$$

Since the slope of the process curve 4-5 is larger than the slope of the curve 1-3 and the pressure limits are equal, then,

$$(h_5 - h_4) < (h_3 - h_2) \qquad 2.13$$

The compression work saved by using this ideal intercooler is:

$$\Delta W^{'} = m(h_3 - h_2) - m(h_5 - h_4) \qquad 2.14$$

In fact, there is pressure drop in a non-ideal intercooler, thus, the pressure of gas at the outlet of the intercooler is P_6, less than P_4. The total compression work for the two-stage compressor, $W_{comp,2}$ then equals

$$W_{comp,2} = m(h_2 - h_1) + m(h_7 - h_6) \qquad 2.15$$

The actual compression work saved is given as:

$$\Delta W = m(h_3 - h_2) - m(h_7 - h_6) \qquad 2.16$$

ΔW is less than $\Delta W'$ because $h_4 \approx h_6$ and $h_7 > h_5$. Theoretically, the higher the heat transfer rate of the intercooler, the lower the temperature at point 6 will be and the greater the quantity of energy can be saved. But it is impossible to remove too much heat from gas to water because of the cost limitation of the intercooler (Wu et al., 1982).

2.1.4 Compression pressure ratio

The intermediate pressure value, P_2 as shown in figure 2.2, that minimises the total work is determined by introducing the compression pressure ratio terms. The compression pressure ratios, *PR* for compressors A (COMP-A) and B (COMP-B) (see figure 2.2) are defined as:

$$PR_{COMP-A} = \frac{P_2}{P_1}$$
$$PR_{COMP-B} = \frac{P_3}{P_2} \qquad 2.17$$

where P_2 and P_1 are the discharge and suction pressures of the compressor A, while P_3 and P_2 are the discharge and suction pressures of the compressor B, respectively.

An acceptable compression pressure ratio for centrifugal compressors is *ca.* 1.5 to 2 (Menon, 2005). A larger number requires more compressor power. If the number of stages of compressor is installed in series to achieve the required compression pressure ratio, then each compressor stage can be operated at a compression pressure ratio of (Menon, 2005),

$$PR = PR_t^{\frac{1}{N}} \qquad 2.18$$

where PR_t and N are the overall compression pressure ratio and the number of compressor stages in series respectively.

Figure 2.4 shows the comparison of the energy savings in the two-stage compression with different compression pressure ratio, *PR* where T_1 and T_3 are the initial gas temperature at the inlet first compressor and the gas temperature after cooling from the first intercooler (see figure 2.2) respectively.

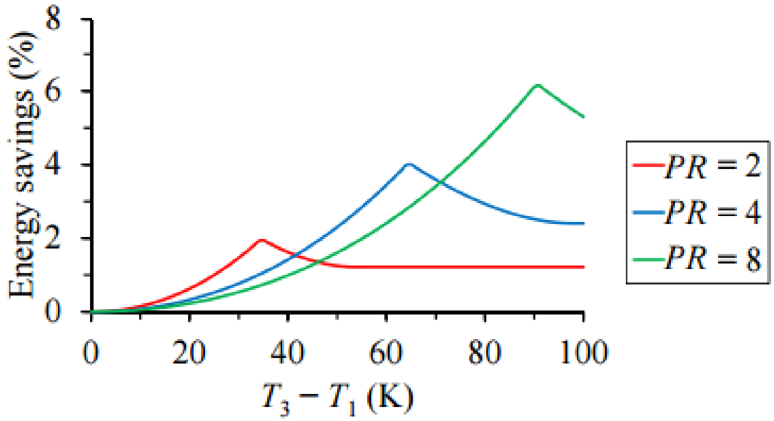

Figure 2.4: Comparison of the energy savings in two-stage compression with intercooling with different pressure ratio (Austbø, 2015).

With increasing pressure ratio, the peak in energy savings is moved to a larger value of $T_3 - T_1$. Since the overall pressure ratio is larger, so is the discharge temperatures of the compressors. The isentropic efficiency of the compressors and the pressure level do not affect the difference in total compression power related to the intermediate pressure level. The isentropic efficiency would, however, influence the magnitude of suction temperature leading to a discharge temperature equal to the intercooling temperature (Austbø, 2015).

The sum of power input to all stages of compression for a real gas is determined from:

$$W_{comp} = \sum_{i=1}^{N} m\left(h_i - h_{i-1}\right) \qquad 2.19$$

where *i* and *N* are the number of compressor stages, respectively.

As the number of stages is increased, the compression process becomes nearly isothermal at the compressor inlet temperature, and the compression work decreases.

2.1.5 Intercooling heat

In order to reduce the compression work, the specific volume of the gas should be kept as small as possible during the compression process. This may be done by maintaining the temperature of the gas as low as possible during compression. In general this heat is rejected to low temperature cooling equipment in order to reduce compression penalty. This strategy is beneficial for operation, especially in cold locations, but total capital requirement could increase due to the necessity of larger heat exchangers for gas cooling in locations with higher temperatures (Romeo et al., 2009). The total heat absorbed, Q_w by circulating the cooling water in the intercooler to cool down the compression fluid is calculated as:

$$Q_w = \sum_{i=2}^{L} \left(h_{i-1,cooler} - h_{i,cooler} \right) \qquad 2.20$$

where $h_{i,cooler}$ and $h_{i-1,cooler}$ are the enthalpies of CO_2 stream at *i* and *i-1*-th intercooling stages, respectively while, *i* and *L* are the number of intercoolers between compressor stages.

2.1.6 Properties of CO_2 mixtures with impurities

Accurate and efficient prediction of thermodynamic properties of pure CO_2 and its mixtures with non-condensable gases is key to successful modelling of multistage compression power requirement and intercooling heat. In order to achieve this, an appropriate Equation of State (EOS) is required to predict the thermodynamic properties of CO_2 and its mixtures. Peng-Robinson Equation of State (PR EOS) (Peng and Robinson, 1976) is employed in the present study for this purpose. This equation is chosen as one of the most computationally efficient for modelling of vapour-liquid behaviour of CO_2 and its mixtures with various components (Seevam et al., 2008, Zhao and Li, 2014, Duschek et al., 1990, Li and Yan, 2009, Vrabec et al., 2009, Woolley et al., 2014, Martynov et al., 2016). The PR EOS is given by Peng and Robinson (1976) can be written as:

$$P = \frac{RT}{V - b_V} - \frac{a_V \alpha}{V^2 + 2b_V V - (b_V)^2} \qquad 2.21$$

where:

$$a_V = \frac{k_1 R^2 T_c^2}{P_c^2} \qquad 2.22$$

$$b_V = \frac{k_2 R T_c}{P_c} \qquad 2.23$$

For mixtures,

$$a_v \alpha = \sum_{i=1}^{n} \sum_{j=1}^{n} y_i y_j (a_v \alpha)_{ij} \qquad 2.24$$

$$(a_V \alpha)_{ij} = (1 - K_{ij}) \sqrt{(a_V \alpha)_i (a_V \alpha)_j} \qquad 2.25$$

$$b_{v,i} = \sum_{i=1}^{n} y_i b_{v,i} \qquad 2.26$$

where P_c, T_c, V, R, α and K_{ij} are the critical pressure, critical temperature, fluid's molar volume, universal gas constant, alpha function and binary interaction parameter, respectively. k_1 and k_2 are respectively the constants specific while y_i and y_j are the component mole fractions of the fluid.

Given the fluid molecular weight, M_w with the relation to the fluid density, ρ can be written as:

$$\rho = \frac{M_w}{V} \qquad 2.27$$

Thus substituting equation 2.27 into equation 2.21, the PR EOS becomes:

$$P = \frac{\rho R' T}{1 - \rho b} - \frac{\rho^2 a \alpha}{1 + 2\rho b - b^2 \rho^2} \qquad 2.28$$

where,

$$R' = \frac{R}{M_w} \qquad 2.29$$

$$a = \frac{k_1 R^2 T_c^2}{P_c^2 M_w^2} \qquad 2.30$$

$$b = \frac{k_2 R T_c}{P_c M_w} \qquad 2.31$$

Twu et al. (1991) studied the effect of the generalised alpha function, α on the predictions obtained from a cubic equation of state. The authors assert that the ability of a cubic EOS to correlate the phase equilibria of mixtures depends not only on the mixing rule but also on the form of the generalised alpha function employed (Twu et al., 1995). The original form of the generalised alpha-function widely accepted and used in phase equilibria calculations were given by Soave (1972):

$$\alpha = \left[1 + m\left(1 - T_r^{0.5}\right)\right]^2 \qquad 2.32$$

where,

$$T_r = \frac{T}{T_c} \qquad 2.33$$

$$m = 0.480 + 1.574\omega - 0.175\omega^2 \qquad 2.34$$

Here, T_r and ω are the reduced temperature and acentric factor, respectively.

In this work, the above properties are calculated using PR EOS implemented in REFPROP package (Lemmon and Huber, 2010).

The discharge enthalpy for the isentropic process, h_2 (equation 2.10) can be calculated by employing PR EOS at given pressure and entropy $h_{is,2} = h(s_2, P_2)$, while the exit entropy, s_2 can be determined from the requirement that the entropy of the gas remains constant $(s_2 = s_1)$, i.e. $s_2 = s(P_1, T_1)$. The exit temperature of the compressor, T_2 can be determined at the given pressure and enthalpy, $T_2 = T(P_2, h_2)$.

2.2 Application of the compression model

In the following, the application of the general equations in modelling the multistage compressor and intercooler to compress to high pressurised fluid for the pipeline transportation as discussed in section 2.1 is presented and reviewed.

2.2.1 Witkowski and Majkut (2012) and Witkowski et al. (2013)

Witkowski and Majkut (2012) and Witkowski et al. (2013) have employed various compression equations to quantify the power demands for 13 different compression strategies for compression of pure CO_2 from a coal-fired power plant. These technologies consist of conventional in-line centrifugal compression, conventional multistage integrally geared centrifugal compression, advanced supersonic shockwave compression and multistage compression combined with liquefaction and pumping. The process simulator Aspen Plus has been used to predict the thermodynamic properties of the CO_2 stream at required conditions and to quantify the performance of each compression chain option accordingly.

Tables 2.1 to 2.3 summarise the compression options employed and the power requirement for each thermodynamic process. The pure CO_2 with the initial conditions of 1.515 bar inlet pressure, P_1 and 28 ^oC inlet temperature, T_1 is compressed to 153 bar discharge pressure, P_2 using different compression options studied. The inter-stage suction temperature, T_s and the compressors' efficiencies, η_p change depending on the compression technology and the number of compressor's stage employed. As the results show, the amount of power required by each compression option varies significantly with the compression technology. Option C_1, the conventional centrifugal 16-stage with four section compressors requires total power of 57787 kW with acted as a baseline case. In the case of conventional centrifugal 16-stage with six section compressor (option C_2), with most intensive cooling provides small compressor power savings above the baseline case (7.5 %). Eight stage centrifugal geared compressor with 7 intercoolers (option C_3) shows that integrally geared centrifugal compressors with intercoolers between each stage result in significant power savings above baseline case, C_1. The thermodynamic analysis indicates *ca.* 21 % reduction in compressor power compared to the conventional process. The recoverable of useful heat from the compression system offers the potential for significant heat integration with the power plant process. Here, a certain temperature level must be reached in the heat exchangers to generate useful heat by the rejection of the 7th intercooler in the eighth stage of the integrally geared compressor (options C_4, C_6 and C_8).

This disadvantage of having a higher compression temperature after the last stage by leaving the ideal process of isothermal compression can be compensated for by the advantage of heat recovery and power optimization in the plant.

Table 2.1: Comparison of compression technology options (Witkowski and Majkut, 2012).

Option	Compression technology	Process definition	Power requirements, N_s (kW)	Difference from option C_1 (%)
C_1	Conventional centrifugal 16-stage four section compressor	P_1 = 1.515 bar, P_2 = 153 bar, T_1 = 28 °C, T_s = 38 °C, η_p = 0.85-0.70	57787.4	0.00
C_2	Conventional centrifugal 16-stage six section compressor	P_1 = 1.515 bar, P_2 = 153 bar, T_1 = 28 °C, T_s = 38 °C, η_p = 0.85-0.70	53443.8	-7.50
C_3	Eight stage centrifugal geared compressor with 7 intercoolers	P_1 = 1.515 bar, P_2 = 153 bar, T_1 = 28 °C, T_s = 20 °C, η_p = 0.84-0.70	44152.5	-21.2
C_4	Eight stage centrifugal geared compressor with rejection of the 7th intercooler	P_1 = 1.515 bar, P_2 = 153 bar, T_1 = 28 °C, T_s = 20 °C, η_p = 0.84-0.70 Heat recoverable to 90 °C	48689.3 11132.2	-13.1 -35.0
C_5	Eight stage centrifugal geared compressor with 7 intercooler	P_1 = 1.515 bar, P_2 = 153 bar, T_1 = 28 °C, T_s = 20 °C, η_p = 0.84-0.56	47560.5	-15.2
C_6	Eight stage centrifugal geared compressor with rejection of the 7th intercooler	P_1 = 1.515 bar, P_2 = 153 bar, T_1 = 28 °C, T_s = 20 °C, η_p = 0.84-0.56 Heat recoverable to 90 °C	53751.0 14349.5	-4.10 -28.9
C_7	Eight stage centrifugal geared compressor with 7 intercooler	P_1 = 1.515 bar, P_2 = 153 bar, T_1 = 28 °C, T_s = 38 °C, η_p = 0.84-0.70	48555.1	-13.4
C_8	Eight stage centrifugal geared compressor with rejection of the 7th intercooler	P_1 = 1.515 bar, P_2 = 153 bar, T_1 = 28 °C, T_s = 38 °C, η_p = 0.84-0.70 Heat recoverable to 90 °C	52919.3 17664.1	5.60 -36.2

In the case of supersonic shock wave compression, this two-stage technology which has higher efficiency and pressure ratio is expected to reduce the capital cost of CO_2 compression equipment by as much as 50 %, and reduce the operating costs of the CO_2 capture and sequestration system by at least 15 % (Witkowski and Majkut, 2012). An additional benefit is that the stage discharge temperature, $T_{2/2}$ ranges from 246 to 285 ^{o}C, depending on the inlet gas cooling water temperatures produces the heat that could potentially be used to regenerate amine solutions or pre-heat the boiler feed-water.

Table 2.2: Options CS_1 and CS_2 (Witkowski and Majkut, 2012).

Option	Compression technology	Process definition	Power requirements, N_s (kW)	Heat recoverable to 90 ^{o}C (kW)
CS_1	Two stage shock wave compression	P_1 = 1.528 bar, P_2 = 153 bar, T_1 = 28 ^{o}C, T_s = 20 ^{o}C, η_p = 0.86-0.80, $T_{2/2}$ = 246.5 ^{o}C	57500.5	58520.5
CS_2	Two stage shock wave compression	P_1 = 1.528 bar, P_2 = 153 bar, T_1 = 28 ^{o}C, T_s = 38 ^{o}C, η_p = 0.86-0.80, $T_{2/2}$ = 285 ^{o}C	62016.5	65619.8

Table 2.3 shows the power requirements for the centrifugal compression followed by liquefaction and pumping (options CP_1-CP_3). The compressor pressure ratio, *PR* is applied depending on the discharge pressure, P_2 and the number of compressor stage employed. The results for the options CP_1 and CP_2 show that the power requirement can be reduced by up to 14.6 % at the compressor outlet pressure of 80 bar and by up to 20.44 % at the subcritical pressure of 60 bar. This minimum liquefaction pressure is dictated by the cooling medium temperature if water at ambient conditions is used.

In option CP_3, CO_2 is brought to liquefaction pressure of 17.45 bar through four compression sections intercooled to 38 ^{o}C with water followed by liquefaction using ammonia as working fluid at -25 or -30 ^{o}C before pumping to the final pressure. This option resulted in the greatest energy savings at *ca.* 45.8 % reduction in compression power compared to the conventional process as shown in table 2.3. However, the liquefaction of CO_2 requires large amount of refrigeration energy. Liquefaction and pumping equipment will entail additional capital expenses, but some of this will be offset by the lower cost of pumps compared to high-pressure compressors.

Table 2.3: Summary of compression and pumping power reduction (Witkowski and Majkut, 2012).

Option	Compression technology	Process definition	Power requirements, (kW)	Difference from option C_1 (%)
CP_1	Six stage integrally geared compressor with five inter-stage coolers	P_1 = 1.515 bar, P_2 = 80 bar, T_1 = 28 ^{o}C, T_s = 38 ^{o}C, η_p = 0.84-0.72, PR= 1.937	N_c = 46750	
	Pumping with supercritical liquefaction	P_1 = 80 bar, T_1 = 31 ^{o}C, η_p = 0.8	N_p = 2582.9 N_c+N_p = 49332.9	-14.6
CP_2	Six stage integrally geared compressor with five inter-stage coolers	P_1 = 1.515 bar, P_2 = 60 bar, T_1 = 28 ^{o}C, T_s = 38 ^{o}C, η_p = 0.84-0.73, PR = 1.846	N_c = 43718.2	
	Pumping with subcritical liquefaction	P_1 = 60 bar, T_1 = 20 ^{o}C, η_p = 0.8	N_p = 2257.6 N_c+N_p = 45975.8	-20.4
CP_2	Four stage integrally geared compressor with three inter-stage coolers	P_1 = 1.515 bar, P_2 = 17.59 bar, T_1 = 28 ^{o}C, T_s = 38 ^{o}C, η_p = 0.84-0.756, PR = 1.846	N_c = 28910	
	Refrigerated pumping	P_1 = 17.59 bar, P_2 = 153 bar, T_1 = -25 ^{o}C, ρ_2 = 1015.89 kg/m^3	N_p = 2392.7 N_T = N_c+N_p N_T = 31302.7	-45.8

At the moment, the impact of impurities on the CO_2 compression is not clear. However, the above studies did not explore the impact of impure components in the CO_2 streams on the compression and intercooling process. These reported studies also only account the compression work without considering the power demand in the intercooling system when calculating the total power consumption in the compression system.

2.2.2 Pei et al. (2014)

Pei et al. (2014) examined the opportunity to recover waste heat from the different compression strategies as an effort to reduce the energy consumption of these technologies by adopting the compression equations as discussed in section 2.1. The Organic Rankine Cycle (ORC) was integrated with 7-stage intercooling compression and 2-stage shockwave compression to recover waste heat produced and the results obtained are illustrated in tables 2.4 and 2.5 respectively.

Table 2.4 lists the calculated performance of the intercooling compression chain coupled with the ORC system.

Table 2.4: Performance of intercooling compression coupled with ORC (Pei et al., 2014).

Exit temperature of the heat exchanger, T_e (K)	Compressor shaft power (kW)	Power generated (kW)	Specific compression energy (kWh/t of CO_2)	$\eta_{thermal}$ (%)	η_{exy} (%)
330	49711	5777	77.7	12	44
335	49711	6465	76.5	13	49
340	49711	7113	75.4	14	54
345	49711	7724	74.3	16	59
350	49711	8299	73.3	17	63

The system performance improves with an increase in the exit temperature of the heat exchanger, T_e. The specific compression energy ranges from 73.3 to 77.7 kWh/t of CO_2. Without heat recovery, the specific compression energy was over 88 kWh/t of CO_2. Therefore, the ORC helps reduce the energy consumption of the system up to 17 %.

Table 2.5 lists the calculated performance of the 2-stage shockwave compression coupled with ORC system.

Table 2.5: Performance of 2-stage shockwave compression coupled with ORC (Pei et al., 2014).

Exit temperature of	Compressor shaft power	Power generated	Specific compression	$\eta_{thermal}$	η_{exy} (%)

the heat exchanger , T_e (K)	(kW)	(kW)	energy (kWh/t of CO_2)	(%)	
428	56891	16303	71.8	17	70
438	56891	16822	70.9	18	72
448	56891	17278	70.1	18	74
458	56891	17672	69.4	19	76
468	56891	18007	68.8	19	77

The specific compression energy is between 68.8 and 71.8 kWh/t of CO_2, which is lower than that in the case of intercooling compression (table 2.4). It is worth mentioning that, without ORC coupling, the specific compression energy requirement is 100.7 kWh/t of CO_2, higher than for intercooling compression. Coupling the ORC system resulted in compression savings of over 30 %, making shockwave compression more advantageous than the intercooling option. Thanks to the higher temperature of the pressurised CO_2, the shockwave with ORC compression chain is able to capture more waste heat and offset the compressor shaft power requirement, rendering the shockwave compression more energy efficient than the intercooling option. In other words, the waste heat provided by the shockwave compression has a higher quality than that provided by the intercooling compression.

However, this reported study only focused on the 7-stage intercooling compression and 2-stage shockwave compression, the other approaches or strategies such as conventional in-line and multistage compression integrated with pumping also should be considered in recovering waste heat as an effort in reducing the energy consumption of the compression system.

2.2.3 Romeo et al. (2009)

Romeo et al. (2009) analysed and optimised the design of a CO_2 intercooling compression system by taking advantage of the low temperature heat duty in the low pressure heaters of a steam cycle. In order to minimise the incremental Cost of Electricity (COE) associated with CO_2 compression, the introduction of a two stage intercooling layout in 4-stage of compression is proposed. In the first stage, the extracted heat could be used in the low-pressure part of the steam cycle for water pre-heating, while in the second stage, the extracted heat is dissipated in the cooling tower after reduction of CO_2 temperature and at the same time reduces the power requirements of the compressor.

Based on their results, the authors concluded that the integration of CO_2 intercooling waste energy into the steam cycle reduces *ca.* 23 % of the incremental COE associated with compression (approximately 0.8 €/MWh). In the meantime, a drop of *ca.* 9 % of the compression cost from 25.1 M€ to 22.8 M€ can be observed when 80 % of the compressor efficiency is increased to 90 %. However, reducing the number of stages from four to three with 80 % of efficiency increases *ca.* 0.19 €/MWh of the COE. This proposed integration scheme can be used to reduce the energy and efficiency penalty of CO_2 capture processes thereby reducing the CO_2 capture cost.

2.2.4 Moore et al. (2011)

Moore et al. (2011) presented a study on the development of novel compression and pumping processes for CCS applications. An internally-cooled compressor diaphragm was developed to remove the compressor heat using an optimal designed cooling jacket based on a state of the art aerodynamic flow path without introducing an additional pressure drop. An existing centrifugal compressor installed in a closed loop test facility was retrofitted with the new cooled diaphragm concept.

From the validation results utilizing 3D CFD and experimental data, an optimal design was achieved that provided good heat transfer while adding no additional pressure drop. Various tests conducted demonstrated the effectiveness of the design.

However, the above studies (Romeo et al., (2009) and Moore et al., (2011)) did not explore the energy saving potential in CO_2 compression and liquefaction process. Considering that there is abundant heat resource in coal-fired power plants, especially the exhaust heat with low temperature. The exhaust heat with lower level can be utilised to decrease the energy consumption in the process of CO_2 compression and liquefaction, which will be helpful to reduce the thermal efficiency penalty when CCS is applied in power plants.

2.2.5 Duan et al. (2013)

Duan et al. (2013) analysed and compared the energy consumptions of conventional systems and a new process for CO_2 compression and liquefaction. The conventional method involves a four-stage gas compression while the new method employs three-stage gas compression and one stage pump pressurisation. The refrigeration process driven by the lower level heat from the coal-fired power plant is integrated in the new compression and liquefaction system. The cooling needed to liquefy the CO_2 is provided by an ammonia absorption refrigerator driven by exhaust heat.

Eight different cases have been investigated to study the effects of the refrigeration temperature on the total energy consumption of CO_2 compression and liquefaction. The corresponding performance data for each system is presented in table 2.6. The first case presents the conventional multistage compression with 30 ^oC water cooling (C-C) and the remaining six cases are the single refrigeration compression with different refrigeration temperature (R-C1 to R-C6) while, the last case employs a double-effect refrigeration compression with two evaporation temperatures (DR-C).

As shown in table 2.6, the total energy consumption, W_{CO2} using conventional methods to compress and liquefy CO_2 is huge, reaching about 358.84 kJ/kg CO_2.

Table 2.6: Performance data of different CO_2 compression and liquefaction processes (Duan et al., 2013).

Parameter	C-C	R-C1	R-C2	R-C3	R-C4	R-C5	R-C6	DR-C
Refrigeration temperature, t_c (^{o}C)	30	-15	-20	-25	-30	-35	-40	-15, -30
Initial pressure from capture, $P_{initial}$ (*MPa*)	0.1	0.1	0.1	0.1	0.1	0.1	0.1	0.1
Pressure at the inlet compressor, P_l (*MPa*)	7.2127	2.2908	1.9696	1.6827	1.4278	1.2024	1.0045	1.4278
Final pressure for pipeline transport, P_{final} (*MPa*)	8.1	8.1	8.1	8.1	8.1	8.1	8.1	8.1
Final temperature of liquid, t_l (^{o}C)	30	25	25	25	25	25	25	25
CR	3	3.85	2.73	2.57	2.43	2.31	2.16	2.43
Compression work, W_c (*kJ/kg* CO_2)	357.56	222.75	208.89	190.69	175.33	160.81	143.95	175.33
Work consumption of liquid CO_2 pump, W_3 (*kJ/kg* CO_2)	-	7.61	7.79	8.07	8.23	8.32	8.43	8.23
Cooling capacity to cool down per kg of CO_2, Q_o (*kJ/kg* CO_2)	-	347.7	363.4	379.2	385.2	374.4	361.8	385.2
Total heat absorbed by the circulating cooling water to cool down per kg of CO_2, Q_W (*kJ/kg* CO_2)	495.3	1040.6	1125.3	1221.8	1300.1	1336.7	1378.1	1107.8
Pump work for the circulating cooling water, W_W (*kJ/kg* CO_2)	1.28	2.70	2.92	3.17	3.37	3.47	3.57	2.87
COP	-	0.502	0.477	0.450	0.421	0.389	0.356	0.533
Thermal energy of hot fluid consumed by NH_4, Q_{CO2} (*kJ/kg* CO_2)	-	692.8	761.9	842.6	914.9	962.4	1016.3	722.7
Temperature of hot fluid, t_e (^{o}C)	-	137.8	145	151	159	167.5	175.5	159.0
Power influence coefficient, X	-	0.0787	0.0838	0.0888	0.0939	0.0992	0.1046	0.0939
The converted work of the hot fluid, W_{CV} (*kJ/kg* CO_2)	-	54.53	63.85	74.83	85.91	95.47	106.30	67.86
Total power consumption for compression and liquefaction, W_{CO2} (*kJ/kg* CO_2)	358.84	287.58	283.44	276.75	272.84	268.07	262.25	254.29

The compressor work reaches 357.56 kJ/kg CO_2, accounting for the major portion of total energy consumption. When the new method is applied, the total energy consumption of CO_2 compression and liquefaction decreases with the decrease in the refrigeration temperature, t_c. The total energy consumption reduces by *ca.* 27 % for the case of R-C6 as compared to the conventional method, C-C. For case DR-C with a double-effect refrigeration compression, the total energy consumption is reduced up to 254.29 kJ/kg CO_2, with *ca.* 29 % decrease of energy consumption.

The advantage of lower energy consumption is reduced as the converted work of extracted steam, W_{CV} increases with the decrease in the refrigeration temperature. Figure 2.5 shows the comparison of gas compression work and total work consumption with and without recovering the cold energy of liquefied CO_2 for CO_2 compression and liquefaction in different cases.

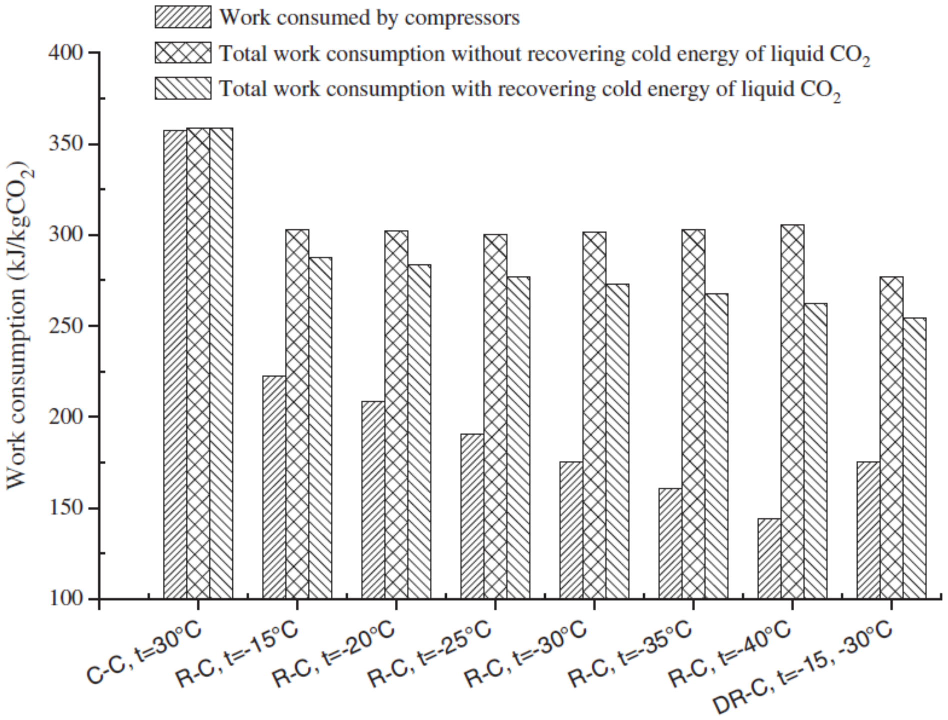

Figure 2.5: Compression work and total work consumption for different CO_2 compression scenarios (Duan et al., 2013).

Although the compression work, W_{CO2} decreases as the refrigeration temperature drops, the total work consumption without cold energy recovery of liquid CO_2 does not decrease continuously. This is because the converted work of the extracted steam accounts for an increasing proportion of the total work consumption as the cooling temperature decreases. The increased converted work neutralises the decreased compression work, and in the refrigeration temperature range from -15 ^oC to -40 ^oC, the total power consumption without recovering cold energy of liquid CO_2 decreases slightly at first and increases soon afterwards. Thus, in some cases for the fixed refrigerator performance, the refrigeration temperature should not be set too low. Evidently, there exists an optimal refrigeration temperature for minimising the total power consumption. In the case of DR-C process, CO_2 was cooled by double-effect refrigerator in the refrigeration process that provides the different levels of cold energy. Applying this process reduces the exergy loss of heat transfer and increases the cooling efficiency of the refrigerator. As can be seen from figure 2.5, the DR-C process with -15 ^oC and -30 ^oC evaporation temperatures has the lowest total power consumption out of the eight cases. Table 2.7 shows the comparison results from the Pulverised Coal (PC) plant with and without CO_2 capture process.

Table 2.7: The comparison results of different CO_2 compression methods (Duan et al., 2013).

Parameter	PC without CO_2 capture	PC+CCS CO_2 compression with the conventional method	PC+CCS CO_2 compression with new method
Gross power plant (MW)	604.3	533.16	527.78
Power plant inner loss (MW)	30.22	30.22	30.22
CO_2 capture power (MW)	-	21.28	21.28
CO_2 compression power (MW)	-	28.62	14.55
Plant electrical power consumption (MW)	30.22	80.12	66.05
Plant net output power (MW)	574.09	453.04	461.73
Power plant net thermal efficiency (%)	40.28	31.79	32.40
Efficiency loss (%)	-	8.49	7.88
CO_2 recovery ratio (%)	-	85	85
CO_2 emission (generator output) (g/kWh)	566.3	94.9	95.87
Reduced CO_2 emission (generator output) (g/kWh)	-	535.3	540.76

The CO_2 compression power requirement in case of integrating the power plant with the CCS and a conventional compression and liquefaction method was 28.62 MW, compared to 14.55 MW in case of the power plant with the CCS and the refrigerating compression combined with exhausted heat utilisation (new method). Advantageously, the drop in compression power also results in an increase in the net power output of the plant. According to the data in table 2.7, using the conventional method to compress and liquefy CO_2, results in an efficiency loss of 8.49 % as compared to PC plant without CO_2 capture when the net thermal efficiency of the power plant drops from 40.28 to 31.79 %. On the other hand, when the new compression method is employed, the efficiency loss decreases to 7.88 %, and the net thermal efficiency of the power plant will be 32.40 %, corresponding to a marginal increase of 0.61 %.

According to Duan et al. (2013), a large amount of low quality heat is demanded in the refrigerating compression combined with exhausted heat utilisation process which occupies a big proportion of the total power consumption if the heat is converted into work. However, this process is especially suitable for coal-fired power plants which have a large amount of lower level heat and need to compress and liquefy CO_2 in a large scale.

In this reported study, the new process for CO_2 compression and liquefaction employing complex refrigeration system powered by exhaust heat will need plenty of mechanical work to produce the low temperature. The liquefaction and pumping equipment also will entail additional capital expenses compared to conventional compression system.

2.2.6 Modekurti et al. (2017)

Modekurti et al. (2017) investigated the performance of both an inline and integral gear multistage compressor to compress the CO_2 stream in the gas phase to supercritical conditions by considering the variable mass flow rate during a flexible operation in the power plant. The compression systems during steady state and transient conditions modelled accounting for inter-stage coolers, flash vessel, glycol tower and the CO_2 inventory from a post-combustion CO_2 capture process.

According to the results presented by Modekurti et al. (2017), the inline compressor system consumes *ca.* 29700 kW, which is 19 % more than that for the 8-stage integral gear compressor system for compressing the CO_2 stream from 1.15 to 152.8 bar as shown in table 2.8. This difference compares well with the work of Wacker and Kisor (2012), where the authors have reported 18 % more power consumption for compressing CO_2 from 1 bara to 150 bara in an inline compressor with 2 sections, a total of 15 stages, and 3 intercoolers in comparison to an integral gear compressor with 8 stages and 6 intercoolers. However, a high amount of recoverable heat produced from the coolers in the inline compressor that can be used elsewhere, such as providing heat to the reboiler of the CO_2 capture system or for generating steam.

Table 2.8: Compressor comparison summary (Modekurti et al., 2017).

	Integral gear	Inline
Total power (kW)	24970	29700
Average polytropic efficiency (%)	84.7	84.0
Total cooling (kWth)	44900	48000
TEG reboiler duty (kWth reboiler at 121 ^oC)	790	1340
Recoverable heat (kWth above 121 ^oC)	900	23550
CO_2 recycle from the TEG stripper (%)	2.25	3.0

Concentration of CO_2 in the feed to the compression system can vary due to operational changes in the CO_2 capture system. According to Modekurti et al. (2017), all the compressor stages will approach the surge condition when the mass flow rate reduces to 45 % reduction.

However, based on the results presented in table 2.8, the total power reported for both integral gear with 8 stages and 6 intercoolers and inline compressor with 15 stages and 3 intercoolers are approximately 50 % below than the reported values from Witkowski and Majkut (2012) and Witkowski et al., (2013).

While the above studies (Witkowski and Majkut (2012), Witkowski et al., (2013), Pei et al., (2014), Romeo et al., (2009), Moore et al., (2011) and Modekurti et al., (2017)) have primarily focused on the development of suitable compression strategies for high-purity CO_2, it has also been recognised that CO_2 streams in CCS inevitably carry some amount of impurities, whose nature and concentrations depend on the emission source and capture technology applied. These impurities are expected to reduce the effective storage capacity of the reservoir and also affect the physical properties and vapour-liquid phase equilibrium of the CO_2 stream, directly impacting the design of compression equipment and the CO_2 pipeline transport.

2.2.7 Aspelund and Jordal (2007)

Aspelund and Jordal (2007) investigated and compared three different CO_2 transport chains using both pipeline and ship. The first chain (P1) consists of compression to 60 bar, liquefaction of CO_2 stream using sea water at 10 ^oC and pumping to 150 bar while the second chain (P2) involves direct compression to 150 bar. In both P1 and P2, the gas is compressed in centrifugal compressors in four stages. In case of the ship transport process (S1), the gas stream is conditioned to ship and reservoir specifications before liquefaction at *ca.* 6-7 bar at -52 ^oC. The liquid stream is then sent to an intermediate storage before being pumped to a ship-based transport, which transports the CO_2 stream to the sequestration site.

From the reported results shown in figure 2.6, process chain P1 shows approximately 10 % higher energy efficiency compared to P2 and S1. At atmospheric pressure, the energy requirement for P1 and P2 or S1 is approximately 95 and 105 kWh/tonne CO_2, respectively. Thus, P1 is the preferred solution for process plants with access to sea water with a relatively low temperature. However, P2 will have lower investment costs and is favourable for higher seawater temperatures.

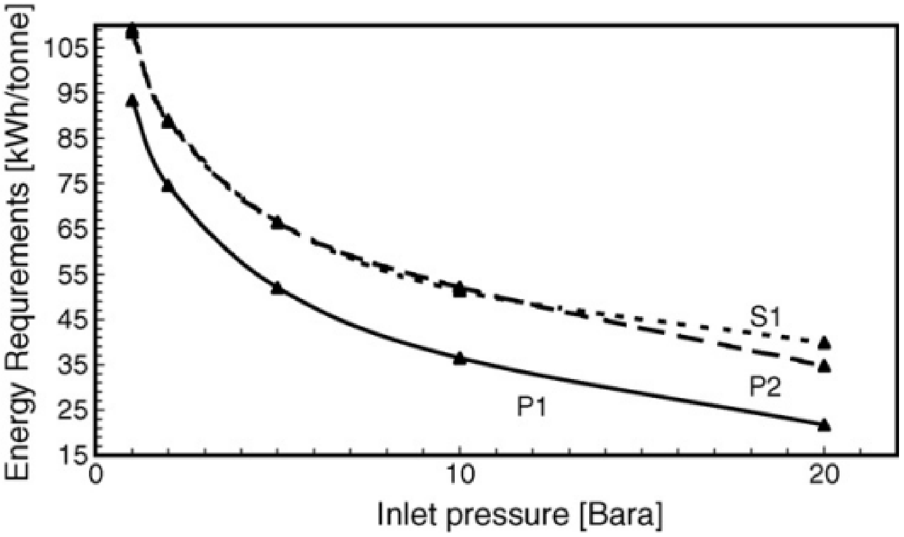

Figure 2.6: Variation of energy requirement for P1, P2 and S1 as a function of inlet pressure (Aspelund and Jordal, 2007).

The effect of volatiles by adding nitrogen to the feed is shown in figure 2.7.

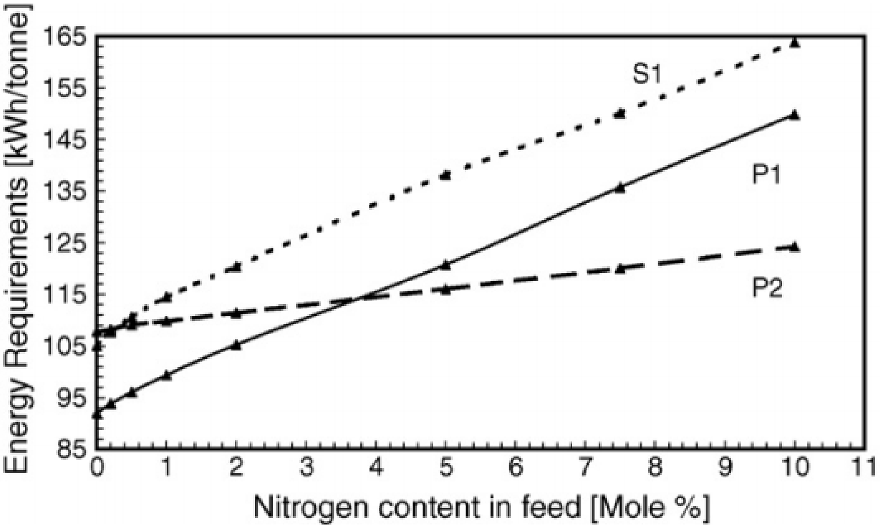

Figure 2.7: Variation of energy requirement for P1, P2 and S1 as a function of inert gas content (Aspelund and Jordal, 2007).

As expected the power requirements for the process with direct compression (P2) increases linearly with the increases of nitrogen content in the feed by approximately 2 kWh/mole nitrogen. In the case of P1 and S1 which involve the liquefaction of CO_2 and the removal of the volatiles in an inert column, a linear increase in power requirements of *ca.* 6 kWh/mole nitrogen can be observed in figure 2.7. According to the authors, the presence of large amount of volatiles in the captured CO_2 stream will increase the bubble point pressure of the mixture as well as increase the column condenser and re-boiler duty.

2.2.8 de Visser et al. (2008)

de Visser et al. (2008) investigated the range of allowable concentrations of impurities in the pre-combustion stream for safe transportation in pipelines. The issues addressed in the authors work are safety and toxicity limits, hydrate formation, corrosion, free water formation as well as compression work. Compression work calculations for a representative CCS stream from 14.5 to 150 bar have been conducted including small percentages of non-condensable gases, using two alternative compression processes which are condensation by cooling and pumping and multi-stage compression. The results show that the increase in compression work depends linearly on the concentration of the gaseous impurity and it is approximately 2.5, 3.5 and 4.5 % for a concentration of 1 % of O_2, N_2 and H_2, respectively. In addition, the results also show that both the total compression work and the impact of other components vary with the selection of compression process. All non-condensable gases require additional compression work, but the effect of hydrogen is the strongest.

2.2.9 Goos et al. (2011)

Goos et al. (2011) determined the specific energy consumption of the compression process for the different CO_2-N_2 gas mixtures. The captured CO_2 stream at 50 ^{o}C and 1 bar with the flow rate of 1000 kmol/h is compressed using an 8-stage compressor compressed to the final pressure of 110 bar. Their simulations are performed employing PRO/II software (McMullen, 2016) and the results are presented in table 2.9.

Table 2.9: Comparison of the specific compression power for different CO_2 gas mixtures compressed to 110 bar (Goos et al., 2011).

Gas mixture	Composition	Specific energy (kWh/t CO_2)	Density (kg/m^3) (Kunz et al., 2007)
1	100 mole % CO_2	86	792
2	95 mole % CO_2, 5 mole % N_2	87	681
3	90 mole % CO_2, 10 mole % N_2	88	536

4	80 mole % CO_2, 20 mole % N_2	89	343

From the results presented in table 2.9, it can be seen that by increasing the impurity in the CO_2 stream, the specific compression power requirement to drive the compressor to reach the end condition will be increased. In particular, the compression power is inversely proportional to the fluid density which progressively decreases with the existence of impurities.

2.2.10 Chaczykowski and Osiadacz (2012)

Chaczykowski and Osiadacz (2012) carried out simulations to compare the compression power for different CO_2 mixture compositions corresponding to different capture technologies under transient flow conditions. The variable CO_2 production rates are simulated, assuming the mass flow rate in the capture plant varies linearly at a rate of 0.25 kg/min between the values of 40 and 100 kg/s. The compressor suction pressure of 0.2 MPa and suction temperature of 40 ^oC is employed and results are illustrated in figure 2.8.

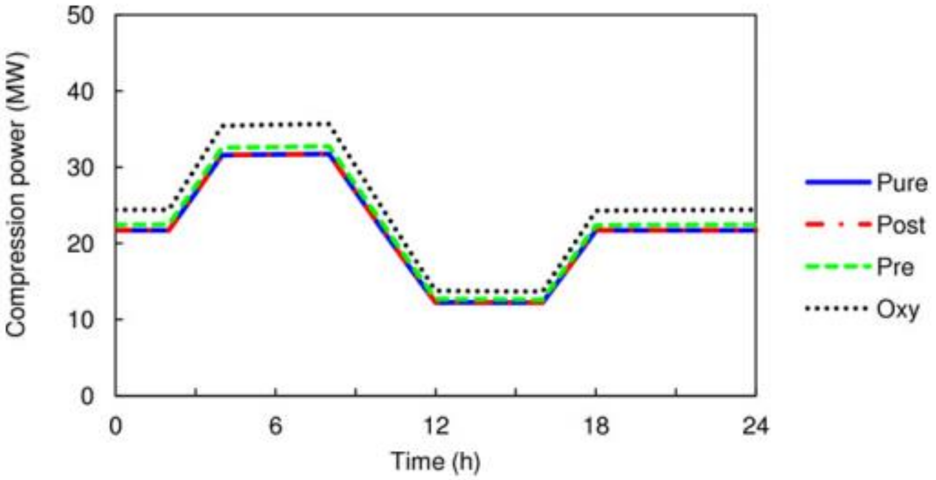

Figure 2.8: Variation of compressor station power (Chaczykowski and Osiadacz, 2012).

According to the data in figure 2.8, the compression power for the 24 hours simulation period in the case of oxy-fuel stream is 24.5 MW, compared to 21.83 MW in the case of pure CO_2 stream. For pre-combustion and post-combustion streams, the figures are 22.54 and 22 MW respectively. Therefore, the total energy demand for the transportation of oxy-fuel, pre-combustion and post-combustion mixtures in the simulation period is respectively, 12.2, 3.2 and 0.78 % higher than that of the pure CO_2 stream. Based on the figure 2.8, it may be reasonably concluded that in the case of oxy-fuel and pre-combustion technologies, the compressors and after-cooler facilities will incur higher operational costs due to the higher fuel and electric power consumption.

Based on the above studies (Aspelund and Jordal (2007), de Visser et al., (2008), Goos et al., (2011) and Chaczykowski and Osiadacz (2012)), in order to minimise the compression costs associated with the presence of impurities in the CO_2 stream, optimising the CO_2 separation and purification processes should be investigated. In the case of relatively small CO_2 emission sources, compression and transportation of low-grade CO_2 carrying more than 5 % of impurities, may be required prior to its further purification. However, to date, the compression requirements for industrial low-grade CO_2 streams have not been systematically assessed.

2.3 Concluding remarks

In this chapter the basic thermodynamic and energy balance relations for calculating the power requirement of multistage compression and cooling duty were presented. These presented equations coupled with a Cubic Equation of State representing the foundation of the multistage compression model. The thermodynamic relations for predicting the pertinent fluid properties such as the fluid enthalpy, entropy and discharge temperature were presented.

In chapter 3, the details for the calculation of compression power consumption and cooling duty are presented. Particular attention is paid to the Peng-Robinson Equation of State as a solution to determine the thermodynamic properties given its popularity due to its accuracy and robustness.

It is also clear that most of the above review employed the conventional CO_2 compression strategy which is responsible for a large portion of the enormous capital and operating cost penalties as well as sizable parasitic energy consumer. Thus, it is incompatible with the original intention of energy saving and emission reduction. Any approach or strategy resulting in a reduction in the CO_2 compression workload directly contributes to an improvement of net plant efficiency. It is the purpose of this thesis to investigate different compression strategies and identify the optimum number of stage of compression system to minimise the associated cost and energy penalties.

While the above reported studies also quantified the power requirements for industrial compression of CO_2, their practical application is, however, limited due to the underlying assumption of negligibly amounts of impurities in the CO_2 stream. In practice, the CO_2 streams in CCS will contain some impurities with range and level, mostly depending on the capture technology. The impact of a varying CO_2 stream concentration on the compression power requirement is not fully understood.

In chapter 3, the selection of an appropriate compression strategy for realistic CO_2 streams and associated compression work penalty costs is investigated.

2.4 Modelling of transient fluid flow in pipelines

The development of a transient flow model is based on the application of the governing equations of fluid dynamics. These equations are derived from the fundamental physical principles by assuming mass, momentum and energy are conserved. However, with respect to the pipeline flow, their precise formulation depends on a number of considerations such as interface topology, multi-component exchanges, dissipative fluid/wall interactions, pipeline elasticity and rigidity as well as pipeline elevation (Menon, 2005, Bratland, 2009).

In essence, interface topology accounts for various flow regimes. These, for example, may include fully dispersed two-phase, stratified, annular or churn flows. Multi-component exchanges on the other hand deal with equilibrium as opposed to non-equilibrium effects. Dissipative fluid/wall interactions represent the effects resulting from heat transfer and friction. Pipeline elasticity and rigidity refer to the degree of compliance and as to whether or not the pipeline is rigidly clamped. Pipeline elevation on the other hand accounts for unevenness in terrain and considers the effect of gravity on fluid flow in the pipeline. The degree of complexity of any mathematical model developed is closely related to its ability to adequately incorporate all the above mentioned effects in its formulation.

Consequently, a detailed model should comprise of the equations of mass, momentum and energy conservation for turbulent single/multi-phase flow, and should account for some, if not all, of the effects mentioned earlier. For these, the Navier-Stokes equations represent the most complete formulation that describes any fluid flow situation (Bratland, 2009). These equations allow for the variation of fluid property in four dimensions, i.e. the three dimensions of space, x, y, and z, and also time, t. However, the solution of the full system of these equations and the numerical discretisation necessary to accomplish this for a whole range of fluid flows is extremely difficult and requires substantial computational resources. Nevertheless, depending on the type of flow scenario that needs to be resolved, certain terms in the equations will have a negligible effect on the final solution and can be safely ignored without any serious loss of accuracy. At the same time, advantageously, these simplifications generally lead to less computationally expensive models, but on the other: the greater the simplification, the higher the likelihood of introducing modelling inaccuracies. Nonetheless, the final form of the conservation equations, derived through simplifying assumptions, may, in the more general classification, be linear, quasi-linear or non-linear, parabolic or hyperbolic, and first- or second-order.

There has been much research activity in the field of theoretical modelling of fluid flow transients. Various assumptions and simplifications have been made in order to suit a particular method of solution or application. Suwan and Anderson (1992) argued that alternative formulations, interpolations, friction force representation, or time integration, which may be appropriate for parabolic problems, will all violate the basic wave like characteristics of a hyperbolic problem. Most cases of unsteady one-dimensional flow where disturbance propagation velocities do not vary significantly are characterised by quasi-linear hyperbolic partial differential equations for continuity and momentum. On the other hand, complex phenomena such as stratified and intermittent stratified-bubble (slug) flows require a two-dimensional transient analysis for a complete treatment of the problem.

Various analytical techniques have been used to reduce the number of equations before employing the relevant numerical procedure. van Deen and Reintsema (1983) for example, introduced a technique which reduces the energy equation to a single parameter-in-mass equation without the assumption of isothermal or isentropic flow.

In fluid flow problems the dependent variables i.e. pressure, P, density, ρ, and velocity, v are functions of the independent variables i.e. time, t and distance, x in the case of one-dimensional flow. In any given flow situation, the determination by experiment or theory of the fluid properties as a function of x and t is considered to be the solution to the problem. There are two distinct fundamental ways of specifying the flow field, namely the Lagrangian and Eulerian descriptions (Sidek, 2013).

In the Lagrangian approach, the fluid is considered to comprise a large number of finite sized fluid particles which have mass, momentum, internal energy and other properties. The mathematical equations are derived for each fluid particle. A major drawback of this approach is restrictively time consuming when considering even a very small volume of fluid. Even when a gas is being considered where there are few molecules, a relatively larger time-step compared to the Eulerian approach must to be employed due to the longer mean free path of the molecules resulted in lower computational run times (Sidek, 2013).

The Eulerian approach considers how the flow properties change at a fluid element as function of time and space. The information about the flow is obtained in terms of what happens at fixed points in space as the fluid flows through those points (Sidek, 2013).

According to Richtmyer (1960), the Lagrangian approach is generally preferred for some problems in a one space variable. For problems in two or more space variables and time, the Lagrangian method encounters serious difficulties. In particular, the accuracy usually decreases significantly as time goes on, due to distortions, unless a new Lagrangian point-net is defined from time to time, which requires cumbersome and usually rather inaccurate interpolations.

In fluid dynamics measurements, the Eulerian method is the most suitable. The Eulerian formulation has almost exclusively been used in all recent studies even through in some cases according to the above discussion, the Lagrangian description would seem more appropriate (Sidek, 2013).

In the deriving the conservation equations, both descriptions are used depending on the circumstance, with the Euler concept being denoted by $\frac{\partial a}{\partial t}$ or $\frac{\partial a}{\partial x}$ and the Lagrange concept being denoted by $\frac{Da}{Dt}$ (Price, 2006). The relationship between the two is given by,

$$\frac{Da}{Dt} = \frac{\partial a}{\partial t} + v\frac{\partial a}{\partial x} \qquad 2.35$$

where a denotes pressure, density, velocity etc. of the fluid flows in the pipeline.

In the following section, the mathematical model used to simulate the transient flow in a pipeline is derived. The equations will be derived from first principles and any assumptions or simplifications will be accounted for.

2.4.1 Model assumptions

In this section, the following assumptions are employed in the development of the numerical pipeline fluid flow model:

- Steady state exists prior to the transient conditions. The fluid properties obtained from a steady state calculation act as the initial conditions required for the hyperbolic system.
- The flow is predominantly one-dimensional, that is, the rate of change of flow variables normal to the axial direction is negligible relative to those along the axial direction.
- When multiphase are present, the phases are assumed to be homogeneously mixed and in thermodynamic equilibrium at all times during the transient flow conditions.
- Each pipeline is rigidly clamped and of uniform cross sectional area.

2.4.2 Conservation of mass

Figure 2.9 shows a schematic diagram of fluid flowing through a pipe section.

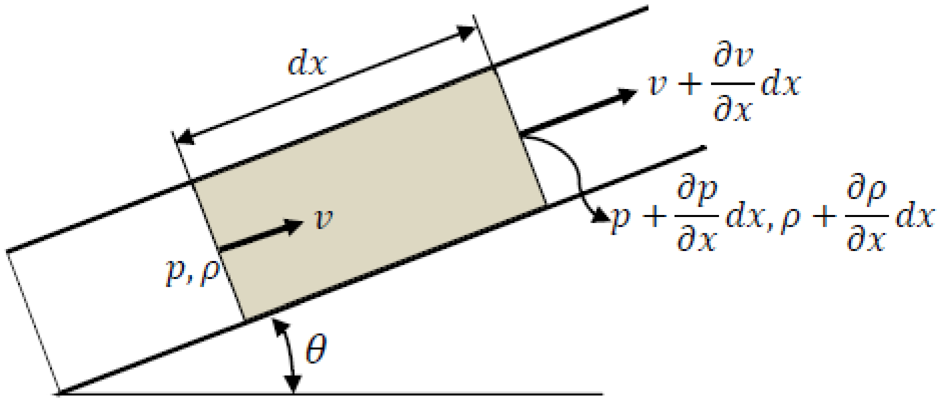

Figure 2.9: A schematic representation of flow and space variables of a representative pipeline to the vertical and horizontal planes (Bratland, 2009).

The conservation equations are derived by assuming the control volume is stationary. A flow can be assumed to be one-dimensional if the rate of change of fluid properties normal to the streamline direction is negligible compared with the rate of change along the streamline. This means that over any cross-section of the pipe all the fluid properties may be assumed to be the same.

For an element of fluid, the law of conservation of mass can generally be expressed as:

$$\begin{matrix}\text{Rate of accumulation} \\ \text{of mass in the fluid element}\end{matrix} = \text{mass flow in - mass flow out} \qquad 2.36$$

$$Adx\frac{\partial \rho}{\partial t} = a\rho v - A\left(\rho + \frac{\partial \rho}{\partial x}dx\right)\left(v + \frac{\partial v}{\partial x}dx\right) \qquad 2.37$$

where *A* and *v* are the area of the pipe and fluid velocity, respectively.

By neglecting the higher order terms in equation 2.37, this leads to:

$$\frac{\partial \rho}{\partial t} + v\frac{\partial \rho}{\partial x} + \rho\frac{\partial v}{\partial x} = 0 \qquad 2.38$$

The last two terms in equation 2.38 can be transformed as:

$$v\frac{\partial \rho}{\partial x}+\rho\frac{\partial v}{\partial x}=\frac{\partial(\rho v)}{\partial x} \qquad 2.39$$

In the case of one-dimensional flow, the mass conservation equation is represented as:

$$\frac{\partial \rho}{\partial t}+\frac{\partial(\rho v)}{\partial x}=0 \qquad 2.40$$

With the aid of suitable thermodynamic relations, the total derivative of density with respect to time and space in equation 2.40 can be reformulated and expressed in terms of fluid pressure and enthalpy/entropy. This reformulation enables the derivative terms in the conservation equations to be expressed only in terms of fluid pressure, enthalpy/entropy and velocity. The importance of this approach, especially with respect to reduction in computational run time, is elaborated latter.

For any fluid, the fluid pressure can be expressed as a function of density, ρ and entropy, s i.e., $P = f(\rho, s)$. Thus, in partial differential form, this relationship can be written as:

$$dP=\left(\frac{\partial P}{\partial \rho}\right)_s d\rho+\left(\frac{\partial P}{\partial s}\right)_\rho ds \qquad 2.41$$

where:

$$\left(\frac{\partial P}{\partial \rho}\right)_s=a^2 \qquad 2.42$$

$$\left(\frac{\partial P}{\partial s}\right)_\rho=\varphi \qquad 2.43$$

Hence by substituting equations 2.42 and 2.43 into equation 2.41, the substantial derivative of pressure with time can be expressed as:

$$\frac{dP}{dt}=a^2\frac{d\rho}{dt}+\varphi\frac{ds}{dt} \qquad 2.44$$

By rearranging equation 2.44 and making the total derivative of density as the subject gives:

$$\frac{d\rho}{dt} = \frac{1}{a^2}\left(\frac{dP}{dt} - \varphi\frac{ds}{dt}\right) \qquad 2.45$$

For any fluid, the total derivative of enthalpy is given by Walas (1985):

$$dh = Tds + \frac{1}{\rho}dP \qquad 2.46$$

Thus from equation 2.46, the total derivative for enthalpy with respect to time becomes:

$$\frac{dh}{dt} = T\frac{ds}{dt} + \frac{1}{\rho}\frac{dP}{dt} \qquad 2.47$$

Rearranging equation 2.47 gives:

$$\frac{1}{T}\left[\frac{dh}{dt} - \frac{1}{\rho}\frac{dP}{dt}\right] = \frac{ds}{dt} \qquad 2.48$$

Substituting equation 2.48 into equation 2.44 by replacing the total derivative of entropy with time results in:

$$\frac{dP}{dt} = a^2\frac{d\rho}{dt} + \frac{\varphi}{T}\left[\frac{dh}{dt} - \frac{1}{\rho}\frac{dP}{dt}\right] \qquad 2.49$$

By rearranging equation 2.49, an expression for the total derivative of density with respect to time in terms of fluid pressure and enthalpy is obtained as:

$$\frac{d\rho}{dt} = \frac{1}{a^2}\left[\frac{dP}{dt}\left(1 + \frac{\varphi}{\rho T}\right) - \frac{\varphi}{T}\frac{dh}{dt}\right] \qquad 2.50$$

Substituting equations 2.45 or 2.50 into equation 2.40 gives:

$$\frac{dP}{dt} - \varphi\frac{ds}{dt} + \rho a^2\frac{\partial v}{\partial x} = 0 \qquad 2.51$$

$$[\rho T + \varphi]\frac{dP}{dt} - \rho\varphi\frac{dh}{dt} + \rho^2 a^2 T\frac{\partial v}{\partial x} = 0 \qquad 2.52$$

Equations 2.51 and 2.52 represent the reformulated mass conservation equation for one-dimensional flow in terms of pressure-entropy and pressure-enthalpy, respectively.

2.4.3 Conservation of momentum

The momentum conservation equation is derived from the application of Newton's second law of motion. By applying this law to the control volume as shown in figure 2.9, gives (Bratland, 2009):

$$\text{Mass} \times \text{acceleration} = \text{net pressure force} + \text{friction} + \text{gravity} \qquad 2.53$$

$$A\rho dx\frac{dv}{dt} = PA - \left(P + \frac{\partial P}{\partial x}dx\right)A - \frac{f_w \rho dx}{2d}v|v|A - A\rho g dx \sin\theta \qquad 2.54$$

where $\frac{dv}{dt}$, P, f_w, v, g and θ are the acceleration, pressure, friction factor, velocity, gravity and degree of the inclination of the pipe, respectively. Equation 2.54 can reformulate to give:

$$\rho\frac{dv}{dt} = -\frac{\partial P}{\partial x} - \frac{f_w \rho}{2d}v|v| - \rho g \sin\theta \qquad 2.55$$

where,

$$\frac{dv}{dt} = \frac{\partial v}{\partial t} + \frac{\partial v}{\partial x}\frac{dx}{dt} \qquad 2.56$$

By inserting equation 2.56 into equation 2.55 gives:

$$\rho\frac{\partial v}{\partial t} + \rho v\frac{\partial v}{\partial x} = -\frac{\partial P}{\partial x} - \frac{f_w \rho}{2d}v|v| - \rho g \sin\theta \qquad 2.57$$

The left hand side of equation 2.57 describes the inertia part of Newton's equation. It has two terms, indicating that each fluid particle can accelerate both in time and space.

2.4.4 Conservation of energy

Heat flow can have a major impact on pipeline hydraulics, and accurate pipeline modelling often require the underlying model to include thermal effects. This is particularly true for compressible fluid flow, since the fluid's temperature strongly affects density. Energy conservation means that net energy coming in to the fluid has to accumulate within it and can be presented as:

$$\begin{array}{l}\text{Rate of change}\\\text{of energy inside the fluid}\end{array} = \begin{array}{l}\text{Net heat flux into}\\\text{the fluid}\end{array} + \begin{array}{l}\text{Rate of work done}\\\text{on the fluid}\end{array} \qquad 2.58$$

The term on the left hand side (LHS) of equation 2.58 can be written as (Bratland, 2009):

$$LHS = \frac{d}{dt}\left(\rho A dx E_s\right) \qquad 2.59$$

where ρAdx and E_s are the control volume's total mass and total energy per unit mass, respectively. By assuming ρAdx is a constant, equation 2.59 gives:

$$LHS = \rho A dx \frac{dE_s}{dt} \qquad 2.60$$

Equation 2.60 is reformulated to give:

$$LHS = \rho A dx \left(\frac{\partial E_s}{\partial t} + v \frac{\partial E_s}{\partial x} \right) \qquad 2.61$$

From equation 2.61, it is given by:

$$\frac{\partial(\rho E_s)}{\partial t} + \frac{\partial(\rho v E_s)}{\partial x} = \rho \frac{\partial E_s}{\partial t} + E_s \frac{\partial \rho}{\partial t} + E_s \frac{\partial(\rho v)}{\partial x} + \rho v \frac{\partial E_s}{\partial x} \qquad 2.62$$

The continuity equation 2.40 implies:

$$E_s \frac{\partial \rho}{\partial t} + E_s \frac{\partial(\rho v)}{\partial x} = 0 \qquad 2.63$$

And therefore, equation 2.62 reduces to:

$$\frac{\partial(\rho E_s)}{\partial t}+\frac{\partial(\rho v E_s)}{\partial x}=\rho\left(\frac{\partial E_s}{\partial t}+v\frac{\partial E_s}{\partial x}\right) \qquad 2.64$$

By inserting equation 2.64 into equation 2.61,

$$LHS = Adx\left(\frac{\partial(\rho E_s)}{\partial t}+\frac{\partial(\rho v E_s)}{\partial x}\right) \qquad 2.65$$

The specific energy E_s in the control volume has three parts:

$$E_s = u+\frac{v^2}{2}+gz \qquad 2.66$$

where u, $\frac{v^2}{2}$ and gz are the fluid's specific internal energy, the kinetic energy and the potential energy due to the elevation, z from a reference level, respectively.

On the right hand side (RHS) of the equation 2.58, the only heat coming from the surroundings into the pipe is the convection going through the pipe wall. The heat per unit volume of pipe, q is the net heat flux into the element.

The last term in equation 2.58, rate of work done on the element is the net rate of work done by pressure in the axial direction, x. Since forces in the positive x-direction do positive work, a growing pv means negative work is done, and so:

$$RHS = qAdx-\frac{\partial(Pv)}{\partial x}dxA \qquad 2.67$$

Combining equations 2.65, 2.66 and 2.67 gives:

$$\frac{\partial}{\partial t}\left[\rho\left(u+\frac{v^2}{2}+gz\right)\right]=-\frac{\partial}{\partial x}\left[\rho v\left(u+\frac{v^2}{2}+gz+\frac{P}{\rho}\right)\right]+q \qquad 2.68$$

Introducing the enthalpy, h, which by definition is:

$$h = u+\frac{p}{\rho} \qquad 2.69$$

Equation 2.68 is transformed into:

$$\frac{\partial}{\partial t}\left[\rho\left(u+\frac{v^2}{2}+gz\right)\right]=-\frac{\partial}{\partial x}\left[\rho v\left(h+\frac{v^2}{2}+gz\right)\right]+q \qquad 2.70$$

Expanding the brackets in equation 2.70 gives:

$$\begin{aligned}&\rho\frac{\partial u}{\partial t}+u\frac{\partial \rho}{\partial t}+\frac{\rho u}{2}\frac{\partial u}{\partial t}+\frac{u}{2}\frac{\partial(\rho u)}{\partial t}+\rho g\frac{\partial z}{\partial t}+gz\frac{\partial \rho}{\partial t}+\rho v\frac{\partial h}{dx}+\\&h\frac{\partial(\rho v)}{\partial x}+\frac{\rho v}{2}\frac{\partial v}{\partial x}+\frac{v}{2}\frac{\partial(\rho v)}{\partial x}+gz\frac{\partial(\rho v)}{\partial x}+g\rho v\frac{\partial z}{\partial x}=q\end{aligned} \qquad 2.71$$

where,

$$\frac{\partial z}{\partial x}=\sin\theta \qquad 2.72$$

Since the pipeline inclination is time invariant, hence:

$$\frac{\partial z}{\partial t}=0 \qquad 2.73$$

Substituting equations 2.72 and 2.73 into equation 2.70 and rearranging gives:

$$\frac{\partial}{\partial t}\left[\rho\left(u+\frac{v^2}{2}\right)\right]+\frac{\partial}{\partial x}\left[\rho v\left(h+\frac{v^2}{2}\right)\right]=q-\rho g v\sin\theta \qquad 2.74$$

Substituting equations 2.40 and 2.55 into equation 2.74 and rearranging gives:

$$\rho\frac{dh}{dt}-\frac{dP}{dt}=q+\frac{f_w\rho v^3}{2D} \qquad 2.75$$

However, the energy equation can be expressed alternatively in terms of the fluid entropy. When the equation 2.48 is multiplied by ρT and becomes:

$$\rho\frac{dh}{dt}-\frac{dP}{dt}=\rho T\frac{ds}{dt} \qquad 2.76$$

Substituting equations 2.76 into equation 2.75 and rearranging gives:

$$\rho T\frac{ds}{dt}=q+\frac{f_w\rho v^3}{2D} \qquad 2.77$$

Equation 2.77 is the energy conservation equation in terms of fluid entropy for one-dimensional flow.

From the above, it may be observed that the final expression of the conservation equations is in terms of 'direct' (i.e. velocity, pressure and entropy/enthalpy) rather than 'conservative' variables (i.e. density, momentum, and total energy). Expressing the conservation equations in the direct variable form is essential in order to compute correctly the propagation speed and the intensity of discontinuities such as shock waves and contact surfaces that can occur in inviscid flows (LeVeque, 2002).

2.4.5 Thermodynamic analysis

The following subsection presents the main equations and correlations employed for determining the two-phase mixture density, thermodynamic function and the heat transferred to the fluid in the pipeline system.

2.4.5.1 Equation of State (EOS)

For the case of compressible flow, a relation in addition to the conservation equations for mass, momentum and energy needs to be provided to ensure that the problem is well-posed, mathematically. This relation is the Equation of State (EOS) which relates thermodynamic properties and is divided into two categories. These are the specialised EOSs, like GERG EOS (GERG, 2004) and general EOSs, like Van der Waals cubic EOS. The performances of different EOS vary for different properties, components and conditions of the fluid (Li et al., 2011).

Many types of EOS have been reviewed concerning thermodynamic property calculations of CO_2 mixtures, but the evaluation results of the EOS performance have not pointed to one particular EOS. The general cubic EOS still show advantages over more complicated or specialised EOS in the calculation of Vapour Liquid Equilibria (VLE), while for volume calculations they cannot compete with equations such as Lee-Kesler (LK) and Statistical Associating Fluid Theory (SAFT) (Li et al., 2011). Based on the study by Li et al. (2011), seven general cubic EOSs were evaluated using many of the experimental data concerning the VLE and the density of CO_2

mixtures including CH_4, N_2, O_2, H_2S, SO_2 and Ar. The EOSs evaluated were Peng-Robinson (PR) (Peng and Robinson, 1976), Redlich-Kwong (RK) (Redlich and Kwong, 1949), Soave-Redlich-Kwong (SRK) (Soave, 1972), Patel-Teja (PT) (Patel and Teja, 1982), 3P1T (Yu et al., 1987), PR-Peneloux (Paul et al., 1989), SRK-Peneloux (Peneloux and Rauzy, 1982), and the improved SRK (Ji and Lempe, 1997). The binary interaction parameters, k_{ij}, were calibrated with respect to the VLE data available. In general, with calibrated k_{ij}, the cubic EOS gave an Absolute Average Deviation (AAD) within 5 % for VLE calculations, and 6 % for calculations of the density, except for the CO_2/SO_2 mixture. Vrabec et al. (2009) proposed to use the PR EOS combined with a model based on Henry’s law constants for the ternary mixture $CO_2/N_2/O_2$ at low temperatures (218-251 K). Their results show that the PR EOS describes both binary and ternary experimental data well, except at high pressures close to the critical region. Wilhelmsen et al. (2012) reported that the SRK and PR give are reasonable prediction for the density and the specific heat capacity in the vapour region whereas deviations above 10 % should be expected in the liquid and supercritical regions for the density of pure CO_2.

Furthermore, it is no doubt that more accurate models such as specialised EOSs are always preferable. More parameters will have to be included to improve the accuracy of this EOS. The GERG EOS for example is principally different from the other EOS because its formulation is based on a multi-fluid approximation, which is explicit in the reduced Helmholtz energy depending on the density, the temperature and the composition. The accuracy of the GERG EOS claims to be very high and the normal range of validity covers temperatures between 90 K and 450 K and pressures less than 35 MPa. This covers a large part of the T/P range for CCS applications, except regions with large temperatures or large pressures. The reported uncertainty of the EOS regarding gas phase density and the speed of sound is less than 0.1 % from 250 K/270 K to 450 K and pressures up to 35 MPa. In the liquid phase of many binary and multicomponent mixtures, the uncertainty of the equation regarding the density is less than 0.1-0.5 %.

Mazzoccoli et al. (2012) reported the study on predicting densities of CO_2 and CO_2-mixtures containing N_2 and CH_4 using different EOS. Based on the authors' study, the GERG-2008 model showed the lowest deviations, however they were not negligible, in particular in the phase equilibrium. Wilhelmsen et al. (2012) concluded that GERG-2004 was the most accurate EOS for all the investigated mixtures (CO_2-CH_4, CO_2-N_2, CO_2-O_2, N_2-O_2 and CO_2-N_2-O_2) except those containing CO_2-O_2 in the two-phase area, where it displayed an AAD of ~20 %. However, the runtime speed of the GERG-2004 showed the most time demanding as compared to others EOS.

Given that the specialised EOS is a multi-parameter equation, it is prohibitively computationally inefficient due to its complicated structures and hence impractical to implement correctly for numerical simulations. The complex structure of the specialised EOS makes the calculation of properties computationally demanding. Because of this situation, general cubic EOS is usually preferred due to the simplest structure and capable of giving reasonable results for the properties of pure CO_2 and CO_2 mixtures.

As a result, the Peng-Robinson (PR) EOS (Peng and Robinson, 1976) is employed in the present study. The details of this equation as previously derived can be found in section 2.1.6.

2.4.5.2 Two-phase mixture density

In the case of liquid and gas mixture its density can be calculated using the PR EOS pseudo-mixture density. This is given by:

$$\rho = \frac{\rho_l \rho_g}{\rho_g (1-x) + \rho_l x} \qquad 2.78$$

where:

$$\rho_g = \frac{PM_g}{Z_g RT} \qquad 2.79$$

$$\rho_l = \frac{PM_l}{Z_l RT} \qquad 2.80$$

Here, x and Z are the fluid quality and compressibility factor, respectively. The subscripts g and l represent the gas and the liquid phase of the fluid.

2.4.5.3 Single and two-phase determination of the thermodynamic function φ

The isochoric thermodynamic function, φ given by equations 2.51 and 2.52 for single-phase fluids is given by Picard and Bishnoi (1987):

$$\varphi = \left(\frac{\partial P}{\partial s}\right)_{\rho} = \frac{\rho \xi T a^2}{C_p} \qquad 2.81$$

where ξ is the isobaric coefficient of volumetric expansion $= \frac{1}{V}\left(\frac{\partial V}{\partial T}\right)_p$. In the case of two-phase flows, φ is calculated numerically in the following manner. Given that:

$$\varphi = \left(\frac{\partial P}{\partial s}\right)_{\rho} \overset{def}{=} \left(\frac{\partial P}{\partial s}\right)_V \qquad 2.82$$

Using one of Maxwell's relations (Walas, 1985):

$$\left(\frac{\partial P}{\partial s}\right)_{\rho} = -\left(\frac{\partial T}{\partial V}\right)_s \qquad 2.83$$

Since the specific volume, $V = \frac{1}{\rho}$:

$$\frac{dV}{d\rho} = -\frac{1}{\rho^2} \qquad 2.84$$

Equation 2.82 becomes:

$$\left(\frac{\partial P}{\partial s}\right)_{\rho} = \rho^2 \left(\frac{\partial T}{\partial \rho}\right)_s \qquad 2.85$$

Hence, from equation 2.82:

$$\varphi = \rho^2 \left(\frac{\partial T}{\partial \rho} \right)_s = \rho^2 \left(\frac{\Delta T}{\Delta \rho} \right)_s \qquad 2.86$$

For two-phase flows, φ can be evaluated numerically by using isentropic flash calculation at a given temperature and pressure as proposed in Mahgerefteh et al. (1997).

2.4.5.4 Fluid/wall heat transfer

In the case of flow in pipelines, the pipeline wall constitutes the immediate surroundings of the fluid. However, except in the case of a perfectly insulated pipeline, the overall external heat transferred to the fluid is influenced by wall and ambient properties/conditions. Newton's cooling law (Picard and Bishnoi, 1987, Chen, 1979, Mahgerefteh et al., 1999) is commonly employed for determining the heat transferred to a fluid flowing in a pipe. It is given by:

$$q = \frac{4}{D_{in}} U_h \left(T_{amb} - T \right) \qquad 2.87$$

where U_h, D_{in} and T_{amb} are the overall heat transfer coefficient, the pipeline inner diameter and ambient temperature, respectively. In the present study, the U_h is taken to be 5 W/m^{2}K.

2.4.6 Hydrodynamic analysis

From the conservation equations derived in the sections 2.4.1-2.4.3, the hydrodynamic parameters are calculated by employing the described equations in the next subsection.

2.4.6.1 Calculation of Fanning friction factor

The Fanning friction factor, f_w is required for calculating the contribution of frictional force to the momentum equation (equation 2.57). It is a function of the flow Reynolds' number. The determination of this friction factor is depended on the surface of the pipe wall and the flow mode of the fluid (Lipovka and Lipovka, 2014).

Ouyang and Aziz (1996) conducted a study, over a wide range of flow conditions $(2000 \le \mathrm{Re} \le 1\times10^8; 10^{-6} \le \frac{\varepsilon}{D_{in}} \le 0.1)$ on the performance of 11 major explicit correlations for predicting friction factor. The predictions of these correlations were compared with the highly accurate Colebrook correlation (Colebrook, 1939). Although the Colebrook correlation is accepted as the most accurate in terms of predictions, it however has the disadvantage of expressing the friction factor in an implicit form with the resultant equation requiring expensive iterations to solve (Ouyang and Aziz, 1996). Many explicit approximations of the Colebrook equation are available (Lipovka and Lipovka, 2014). These approximations vary in their degree of accuracy, depending upon the complexity of their functional forms that generally estimate friction factors with higher accuracy.

From the study conducted by Ouyang and Aziz (1996), the authors recommended the use of the Chen (1979), Serghides (1984) and the Zigrang and Sylvester (1982) correlations. These three were observed to show a maximum absolute deviation of less than 1 % from the Colebrook correlation.

Based on the results reported by Ouyang and Aziz (1996), the Chen correlation is employed in the present study for the calculation of the Fanning friction factor for transition and turbulent flows in rough pipes as shown below:

$$\frac{1}{\sqrt{f_w}} = -2\lg\left[\frac{\varepsilon}{3.7065 D_{in}} - \frac{5.0452}{\mathrm{Re}}\lg\left(\frac{1}{2.8257}\left(\frac{\varepsilon}{D_{in}}\right)^{1.1098} + \frac{5.8506}{\mathrm{Re}^{0.8981}}\right)\right] \qquad 2.88$$

where ε, D_{in} and Re are the pipe roughness, internal diameter of the pipe and Reynold's number, respectively.

For turbulent flow in smooth pipelines, Rohsenow et al. (1998) recommend the correlation proposed by Techo et al. (1965). The authors assert that the equation gives predictions within ± 2 % of extensive experimental measurements. It is given by:

$$\frac{1}{\sqrt{f_w}} = 1.7372\ln\frac{\mathrm{Re}}{1.964\ln\mathrm{Re} - 3.8215} \qquad 2.89$$

In the laminar region, the evaluation of the Fanning friction factor is independent of the pipe roughness. Thus in general, the Fanning friction factor for laminar fully developed flow is given by Bratland (2009):

$$f_w = \frac{16}{\mathrm{Re}} \tag{2.90}$$

2.4.6.2 Single and two-phase speed of sound determination

For single-phase real fluids, the speed of sound through the fluid can be expressed analytically as (Picard and Bishnoi, 1987):

$$a^2 = \frac{\gamma}{k\rho} \tag{2.91}$$

By definition, γ and k can be expressed respectively as (Walas, 1987):

$$\gamma = \frac{C_P}{C_V} \tag{2.92}$$

$$k = -\rho\left(\frac{\partial V}{\partial P}\right)_T \tag{2.93}$$

where C_p and C_v are the specific heats at constant pressure and volume respectively, and V is the specific volume of the fluid.

From equation 2.93, k can be obtained analytically by differentiating the PR EOS. For two-phase flows, the analytical determination of γ and C_p becomes complex (Mahgerefteh et al., 1999). Hence the speed of sound is evaluated numerically at a given temperature and pressure as:

$$a^2 = \left(\frac{\Delta P}{\rho(T,P) - \rho\left(T^*, P - \Delta P\right)}\right)_s \tag{2.94}$$

where the subscript, s and ΔP denote a constant entropy condition and infinitesimal change in pressure ($\Delta P = 1x10^{-6}$ atm), respectively. T^* represents the corresponding fluid temperature obtained by performing a $(P\text{-}\Delta P)/s$ flash.

2.4.7 Numerical methods for the solution of transient fluid flow model

A variety of high-resolution numerical methods have been developed over the past several decades that resolve discontinuities and rapidly changing flows sharply and yet produce at least second-order accuracy in smooth flows. Understanding of the different numerical methods available and appropriate implementation of a scheme for the resolution of a particular problem requires not only a thorough grasp of the physical nature of the flow being considered, but also a good foundation in the mathematical theory of hyperbolic conservation laws.

The resulting system of equations in sections 2.4.1-2.4.3 was shown to be quasilinear and hyperbolic in nature. As these equations contain terms that are unknown or non-linear functions of their dependent and independent variables, they can only be solved numerically (Mahgerefteh et al., 1999). Their complete solution also requires the application of appropriate boundary conditions at the inlet and at the end of the pipeline. These boundary conditions enable closure of the governing equations with their solutions establishing the fluid dynamic and thermo-physical properties in time and space along the pipeline. Three numerical techniques are commonly employed for resolving hyperbolic partial differential equations which are Finite Difference Methods (FDM), Finite Volume Methods (FVM) and Method of Characteristics (MOC).

The FDM is a general mathematical technique that is widely applied to Partial Differential Equations (PDEs). It involves discretising the spatial domain into a series of nodes forming a grid. Finite approximations are then substituted for the derivatives appearing in the PDEs taking values at the nodal points resulting in a system of algebraic equations. Similarly, the FVM breaks the system up into a set of discrete cells. The integral of the PDEs over each cell is approximated to produce a system of algebraic relations. However, numerical diffusion associated with these methods makes them unsuitable for modelling the transient flow following pipeline failure (Mahgerefteh et al., 2009).

The MOC is a mathematical technique that is particularly suited to the solution of hyperbolic PDEs with two independent variables such as distance and time. The MOC resolves the system of PDEs into a system of ordinary differential equations (compatibility equations) through a particular co-ordinate change. These co-ordinates represent curves (characteristic lines) in the space-time plane along which the compatibility equations hold. The method is particularly suitable for systems containing complex boundary conditions, as each boundary condition may be applied individually to each characteristic curve moving into the computational domain (Zucrow and Hoffman, 1975).

In this following section, the formulation and implementation of the MOC used to solve the conservation equations governing single/two-phase homogeneous flow in pipeline is presented.

2.4.7.1 Method of Characteristics (MOC)

The method of characteristics (MOC) is the natural numerical method for quasi-linear hyperbolic systems with two independent variables (e.g. distance and time) (Thorley and Tiley, 1987). It is based on the principle of the propagation of characteristic waves and is therefore well suited to handling fast transient flow where each disturbance is captured along the propagating Mach lines which are used in the formulation of the final form of the finite difference equations (Zucrow and Hoffman, 1975).

In this method, the system of conservation equations as described in sections (2.4.1-2.4.3) is assumed as quasilinear and hyperbolic. A PDE is said to be quasilinear if all derivatives of the dependent function are linear, while their corresponding coefficients may contain nonlinear terms. The conservation equations represented by equations 2.40, 2.57 and 2.74 are clearly linear in the partial derivative terms. Furthermore, terms those are coefficients of the partial derivatives, such as the ρ or a are nonlinear functions of P, s and v. The governing equations are therefore quasilinear in structure.

In the one-dimensional case, the governing equations 2.40, 2.57 and 2.74 can be written in the general form as:

$$A\frac{\partial U}{\partial t}+B\frac{\partial U}{\partial x}=C \tag{2.95}$$

where, A, U, B and C are given by:

$$U=\begin{pmatrix} P \\ s \\ v \end{pmatrix} \tag{2.96}$$

$$A=\begin{pmatrix} 1 & -\varphi & 0 \\ 0 & 0 & \rho \\ 0 & \rho\mathrm{T} & 0 \end{pmatrix} \tag{2.97}$$

$$B=\begin{pmatrix} v & \text{-}\varphi v & \rho a^2 \\ 1 & 0 & \rho v \\ 0 & \rho T v & 0 \end{pmatrix} \tag{2.98}$$

$$C=\begin{pmatrix} 0 \\ \beta_x-\rho g\sin\theta \\ Q_h-v\beta_x \end{pmatrix} \tag{2.99}$$

A system of PDE as given by equation 2.95 is said to be hyperbolic if the eigenvalues satisfying equation 2.100 given below are real and distinct (Prasad and Ravindran, 1985):

$$\left|B-\lambda A\right|=0 \tag{2.100}$$

Thus, for the conservation equations, the above equation may be expressed as:

$$\left|B-\lambda A\right|=\begin{vmatrix} v-\lambda & \text{-}\varphi v+\lambda\varphi & \rho a^2 \\ 1 & 0 & \rho v-\rho\lambda \\ 0 & \rho T v-\lambda\rho T & 0 \end{vmatrix}=0 \tag{2.101}$$

Hence:

$$(v-\lambda)\big(0-(\rho v-\rho\lambda)(\rho T v-\rho\lambda T)\big)+(\varphi v+\lambda\varphi)(0)+\rho a^2\left(\rho T v-\lambda\rho T\right)=0 \tag{2.102}$$

Simplifying equation 2.102 gives:

$$(v-\lambda)\left(-\rho^2T\right)(v-\lambda)^2+\rho^2a^2T(v-\lambda)=0 \qquad 2.103$$

Factorising and dividing equation 2.103 by $-\rho^2T$ gives:

$$(v-\lambda)\left((v-\lambda)^2-a^2\right)=0 \qquad 2.104$$

Solving equation 2.104 to obtain the roots of λ gives:

$$\lambda_1=v \qquad 2.105$$

$$\lambda_2=v+a \qquad 2.106$$

$$\lambda_3=v-a \qquad 2.107$$

It can be seen that the eigenvalues, λ_i in equations 2.105-2.107 are real and distinct. Thus, the system of conservation equations with partial derivatives in terms of *P*, *s* and *v* are hyperbolic. This implies that the behaviour and properties of the physical system described by these equations will be dominated by wave-like phenomena (Prasad and Ravindran, 1985). Indeed the speed of propagation of these waves, known as Mach lines, are given by the eigenvalues ($v+a$) and ($v-a$), which correspond to the right running and left running characteristic (Mach) lines respectively. The path line characteristic is given by λ_1. These characteristics can handle any type of discontinuity in fluid flow such as a shock wave (Prasad and Ravindran, 1985).

To adequately resolve a system of PDE in terms of three dependent variables (e.g. *P*, *s* and *v*), three characteristic lines (i.e. the path line (C_0), the positive (C_+) and negative (C_-) Mach lines) need to be defined. These in essence govern the speed at which expansion and compression waves propagate from the low and high-pressure ends of the pipeline respectively (positive and negative Mach lines), while the path line dictates the rate of flow through any given point along the pipeline. Their corresponding compatibility equations may be solved by standard, single step finite-difference methods for ordinary differential equations. Figure 2.10 is a schematic representation of the characteristic lines at a grid point along the space, *x* and time *t* independent coordinates.

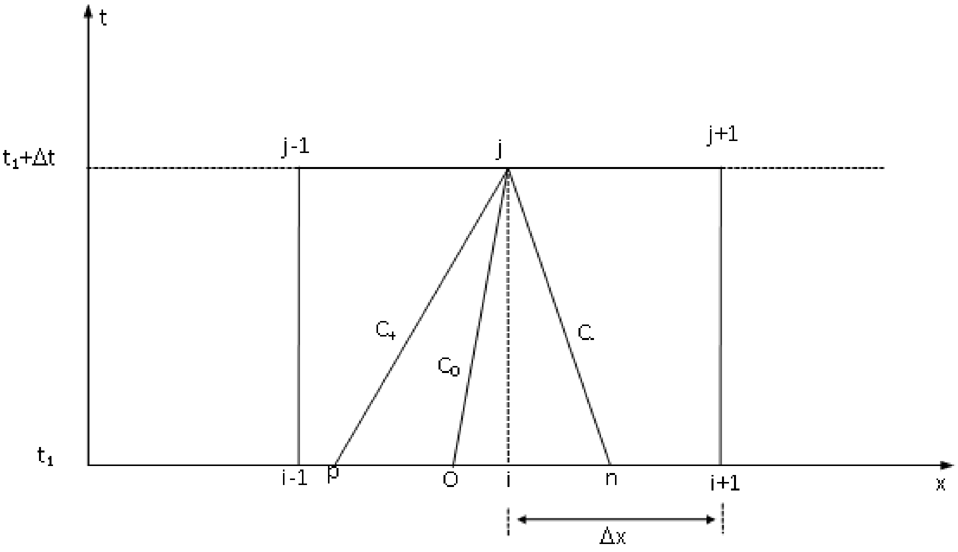

Figure 2.10: A schematic representation of Path line (C_0) and Mach lines (C_+, C_-) characteristics at a grid point along the time, *t* and space, *x* axis.

There are two main grid discretisation methods for the MOC. These are the Characteristic Grid method (CG) which is also known as natural method of characteristics (Wylie et al., 1971) or the Wave Tracing method (Chen, 1993), and the Inverse Marching method which is also known as the Rectangular Grid method or the Method of Specified Time Intervals (Flatt, 1986).

In the CG method, the position of the new solution point is not specified a priori, but is determined from the intersection of left and right running characteristics with origins located at known solution points or initial data. Hence a free floating grid is developed in the *x*-*t* plane as shown in figure 2.11.

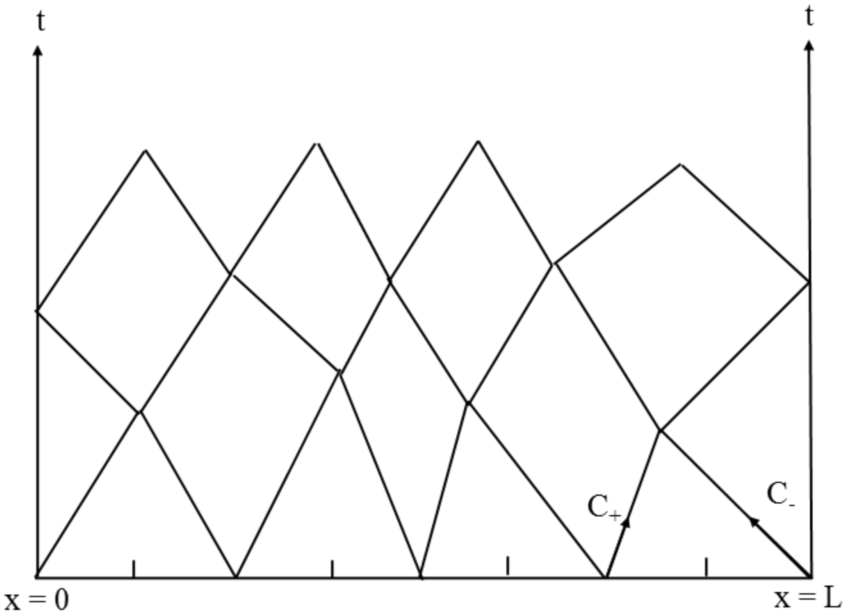

Figure 2.11: The Characteristic grid (Wylie et al., 1971).

This MOC is particularly accurate since the solution progresses naturally along the characteristic lines. However, when more than two characteristic lines are present, i.e. when an energy equation is solved in addition to the mass and momentum conservation equations, a path line (C_0) is present in addition to the two Mach lines (C_+ and C_-) and this introduces some interpolation to locate the path line intersection between known initial points.

Another technique of MOC that can be used for numerical discretisation of the Euler equations is the Inverse Marching method or the mesh method of characteristics called the Method of Specified Time Intervals as shown in figure 2.12. In this method, the location of the solution points in the space-time grid is specified a priori and the characteristic curves are extended backwards in time to intersect a time line on which the initial-data points are known from a previous solution. This method is capable of providing results where needed, however it can suffer from inaccuracy introduced by interpolations at each time step, and the greater the interpolation the larger the error.

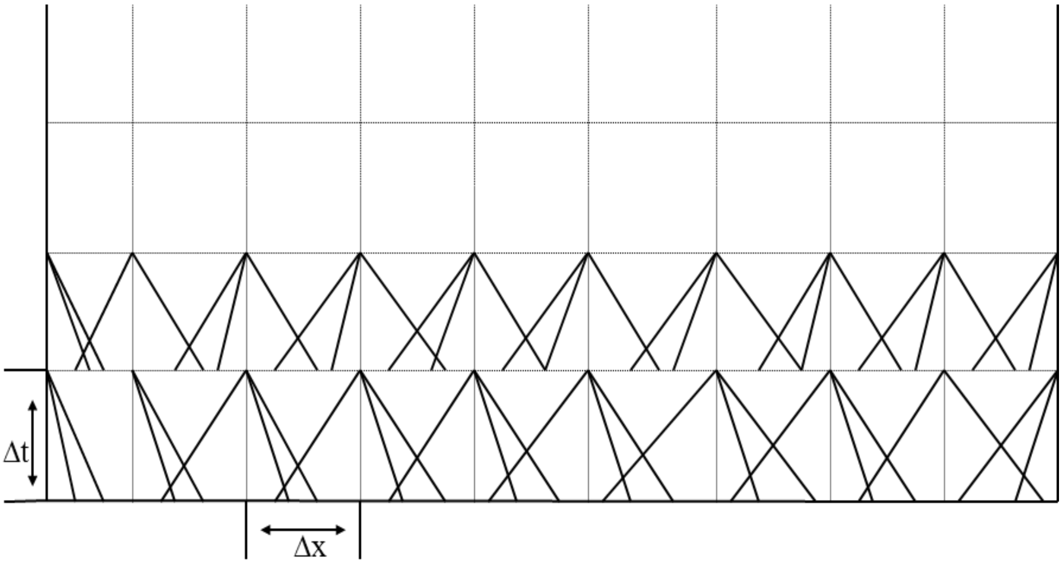

Figure 2.12: The method of Specified Time Intervals (Wylie et al., 1971).

The MOC has many advantages compared with other numerical methods of solution. Discontinuities in the initial value may propagate along the characteristics, making it easy to handle. Large time steps are possible in the natural method, since they are not restricted by a stability criterion. The boundary conditions are also properly posed. The MOC is relatively accurate, but requires the understanding how it operates and to choose a suitable time step. The method can be readily adapted to solve for three dependent variables required for the analysis of non-isothermal transient fluid flow. Discontinuous initial data do not lead to solution with overshoot and details are not smeared in the CG method. Exact solution is possible in the constant coefficient case with the two dependent variables regardless of eventual discontinuities in the initial data, in the case of the natural method.

From the several techniques that have been discussed, the MOC is chosen as the best numerical scheme for the solution of the Euler equations on the basis that it has been proven to be an accurate tool in the solution of hyperbolic equations. While the CG method may be more accurate it does not allow for the introduction of boundary conditions at predefined times. In contrast, the MST method allows control of the time at which input variables are given at boundaries. For this reason, this method is employed in this study and the detailed discussion is presented in the following section.

2.4.7.2 Numerical formulation

The solution of Partial Differential Equations (PDEs) using the MOC comprises two steps:

- Conversion of the PDEs into a system of Ordinary Differential Equations (ODEs) called the compatibility equations.
- Solution of the compatibility equations using an Euler predictor-corrector method.

2.4.7.2.1 Conversion of PDEs to ODEs

According to Zucrow and Hoffman (1975), introducing $\frac{1}{\lambda}$ to represent the slope of the characteristic lines, the conservation equations may be replaced by three compatibility equations, which are valid along the respective characteristic curves. The details of this conversion can be found in Zucrow and Hoffman (1975).

The following is the summary of the main results showing the final form of the compatibility equations and the characteristics along which they hold.

The three compatibility equations associated with the conservation of mass, momentum and energy are:

$$d_o s = \left(\frac{\psi}{\rho T} \right) d_o t \qquad 2.108$$

along the Path line characteristic (C_o):

$$\frac{d_0 t}{d_0 x} = \frac{1}{v} \qquad 2.109$$

$$d_+ P + \rho a d_+ v = \left(a\alpha + \frac{\varphi\psi}{\rho T} \right) d_t t \qquad 2.110$$

along the positive Mach line characteristic (C_+):

$$\frac{d_+ t}{d_+ x} = \frac{1}{v+a} \qquad 2.111$$

$$\rho a d\_v - d\_P = \left(a\alpha - \frac{\varphi\psi}{\rho T} \right) d\_t \qquad 2.112$$

along the negative Mach line characteristic (C_-):

$$\frac{d\_t}{d\_x} = \frac{1}{v-a} \qquad 2.113$$

The C_+ and C_- Mach lines characteristics govern the speed of propagation of the expansion and compression waves while the Path line C_o governs the rate of flow through any given point along the pipeline.

2.4.7.2.2 Solution of the compatibility equations

As described above, the solution of the compatibility equations requires the tracing of characteristic lines in a discretised *x-t* plane as shown in figure 2.10. These compatibility equations are solved based on the Method of Specified Time Intervals (MST) adopting the Euler predictor-corrector technique. It is assumed that the fluid properties are already known at grid points $i-1$, i and $i+1$ at the initial time t_1 (see figure 2.10). The initial conditions at the foot of each characteristic curve (*p*, *o* and *n*) are evaluated by linear interpolation. The compatibility equations are solved by a finite difference method to obtain the flow variables *P*, *s* and *v* at the intersection point *j* at the next time step, $t_1 + \Delta t_1$.

The time step employed is pre-specified, and is in turn calculated subject to the Courant-Friedrichs-Lewy (CFL) criterion. This criterion is a requirement for the stability of the numerical scheme employed for the system under consideration. It is given by:

$$\Delta t \leq \frac{\Delta x}{\left| v + a \right|_{\max}} \qquad 2.114$$

Here, the symbols have the same meaning as those provided in the previous section, with the *Δ* symbol indicating an infinitesimal increment.

2.4.7.2.3 Finite difference solution of compatibility equations

In order to solve these relations as discussed in section 2.4.7.2.1, an Euler predictor-corrector finite difference technique is used to numerically solve the Path (equation 2.108) and characteristic Mach lines equations (equations 2.110 and 2.112). The method consists of an explicit predictor step, which is used as an estimate of the fluid properties at the solution point. The corrector step then uses this as an initial estimate for an implicit approximation of the time step.

2.4.7.2.3.1 First order approximation: predictor step

In the predictor step, the compatibility equations (equations 2.108, 2.110 and 2.112) are expressed in finite difference form as:

Path line compatibility:

$$s_j - s_o = \left[\frac{\psi_o}{\rho_o T_o}\right]\Delta t \qquad 2.115$$

Positive Mach line compatibility:

$$(\rho a)_p (v_j - v_p) + (P_j - P_p) = \left(a\alpha + \frac{\varphi\psi}{\rho T}\right)_p (t_j - t_p) \qquad 2.116$$

Negative Mach line compatibility:

$$(\rho a)_n (v_j - v_n) - (P_j - P_n) = \left(a\alpha - \frac{\varphi\psi}{\rho T}\right)_n (t_j - t_n) \qquad 2.117$$

The subscripts assigned to the various properties in equations 2.115 to 2.117 denote the location in space and time, as shown in figure 2.10. The symbols depicting the flow variables have the same meaning as those described in the previous section (section 2.4.7.1). x_p, x_o and x_n are calculated from a first order finite difference form of the equations 2.109, 2.111 and 2.113. The fluid properties are then linearly interpolated from those at the grid points $i-1, i$ and $i+1$.

2.4.7.2.3.2 Second order approximation: corrector step

In order to improve the accuracy of the first order solution, a second order approximation to the compatibility equations is employed. The finite difference form of the compatibility equations can be expressed as:

Path line compatibility:

$$\frac{1}{2}\left(s_j - s_o\right) = \frac{1}{2}\left(\frac{\varphi_o \psi_o}{\rho_o T_o} + \frac{\varphi_j \psi_j}{\rho_j T_j}\right)\left(t_j - t_o\right) \qquad 2.118$$

Positive Mach line compatibility:

$$\frac{1}{2}\left((\rho a)_p + (\rho a)_j\right)\left(v_j - v_p\right) + \left(P_j - P_p\right) = \frac{1}{2}\left(\left(a\alpha + \frac{\varphi\psi}{\rho T}\right)_p + \left(a\alpha + \frac{\varphi\psi}{\rho T}\right)_j\right)\left(t_j - t_p\right) \qquad 2.119$$

Negative Mach line compatibility:

$$\frac{1}{2}\left((\rho a)_n + (\rho a)_j\right)\left(v_j - v_n\right) - \left(P_j - P_n\right) = \frac{1}{2}\left(\left(a\alpha - \frac{\varphi\psi}{\rho T}\right)_n + \left(a\alpha - \frac{\varphi\psi}{\rho T}\right)_j\right)\left(t_j - t_n\right) \qquad 2.120$$

In a similar manner as that employed in the predictor step, the positions x_p, x_o and x_n are calculated from a second order finite difference form of equations 2.109, 2.111 and 2.113. The fluid properties at these points are then found by linear interpolation, as in the first order step. This calculation is repeated until a certain tolerance ($ca. 10^{-5}$) is satisfied for the three independent flow variables, *i.e.*, *P*, *s* and *v*.

2.5 Application of the transient fluid flow model

In the following, a review of the main studies involving the applications of various transient flow models based on the fundamental equations presented in section 2.4 simulating the dynamic behaviour of high pressurised gas mixtures in pipelines is presented.

2.5.1 OLGA

OLGA is a two-fluid model which solves the conservation equations for mass, momentum and energy for the gas, liquid droplet and liquid film phases at discrete time and distance intervals. The numerical procedure utilises the finite difference method such that the pipeline is divided into a number of segments and a solution is sought at the centre of each segment. The first version of OLGA was developed for the hydrocarbon industry by Statoil in 1983 to simulate slow transients associated with terrain-induced slugging, pipeline start-up, shut-in and variable production rates. Its physical model was initially based on small diameter data for low-pressure air/water flow. Initially, OLGA could successfully simulate bubble/slug flow regime but it was incapable of modelling stratified/annular flow regime. Bendiksen et al. (1991) addressed this problem as well as extending the model to deal with hydrocarbon mixtures.

In OLGA, separate conservation equations are applied for gas, liquid bulk and liquid droplets, which may be coupled through interfacial mass transfer. Two momentum equations are used which are, the combined equation for the gas and possible liquid droplets and also the equation for the liquid film. Heat transfer through the pipe walls is accounted for by a user specified heat transfer coefficient. Different frictional factors are used for the various flow regimes. The pertinent conservation equations are solved using an implicit finite difference numerical scheme which gives rise to numerical diffusion of sharp slug fronts and tails thus failing to predict correct slug sizes. This problem is then addressed in a later version (Nordsveen and Haerdig, 1997) by introducing a Lagrangian type front tracking scheme.

Due to inherent limitations in the numerical methods and two phase models in OLGA (Chen, 1993), proper phase behaviour is not incorporated. No information is available publicly on OLGA’s computational run time. However, considering the fact that the simulation is numerically based on separate conservation equations for the various fluid phases, its computational run time is expected to be exceptionally high when simulating the transient flow in long pipelines containing multi-component hydrocarbon mixtures.

OLGA was validated under transient conditions by Shoup et al. (1998). The simulation results generated were then compared with field data obtained by Deepstar for slow and rapid blowdown of a 5.28 km, 102 mm inner diameter onshore gas condensate pipeline at 4.8 MPa discharging through 12.7 mm (slow blowdown) and 25.4 mm (rapid blowdown) choke openings. The precise mixture composition used was not given. In order to simulate blowdown it was assumed that release occurs through a valve situated at the end of the pipeline. Figures 2.13 and 2.14 respectively show the variation of pressure with time during slow and rapid blowdown. The figures show that reasonable agreement is obtained during slow blowdown, but the model performs relatively poorly when simulating rapid blowdown.

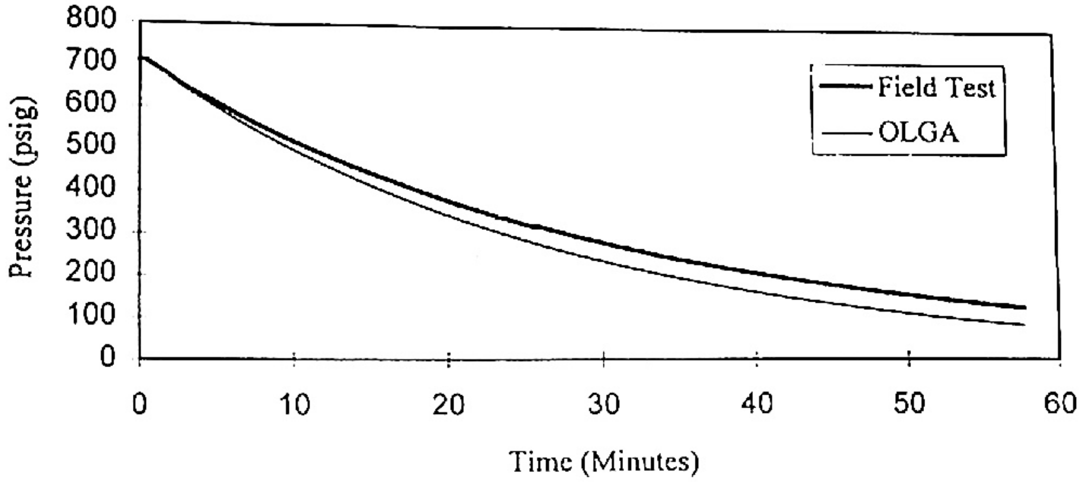

Figure 2.13: Comparison of the field test data with the OLGA simulation result during slow blowdown scenario (Shoup et al., 1998).

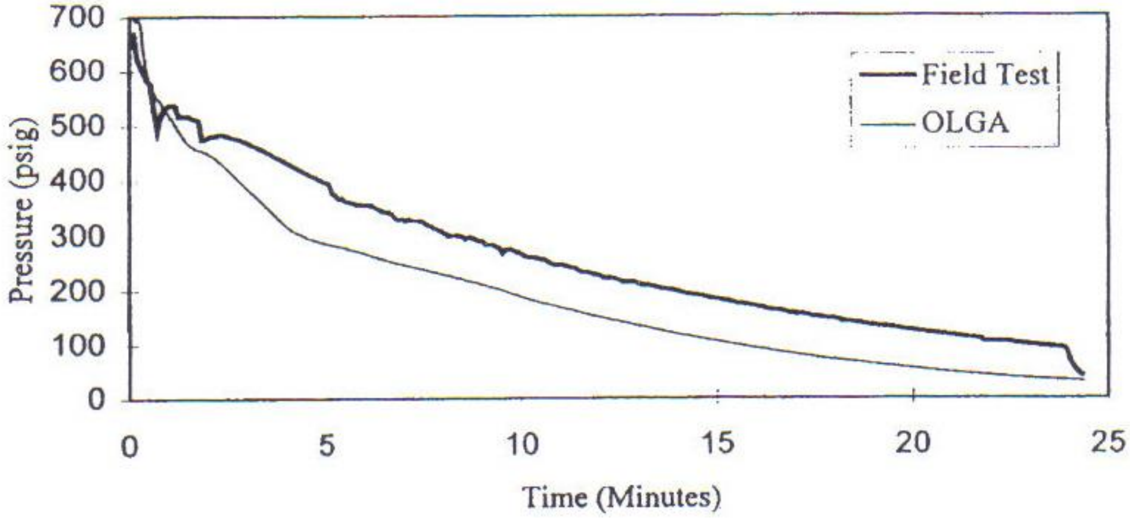

Figure 2.14: Comparison of the field test data with the OLGA simulation result during rapid blowdown scenario (Shoup et al., 1998).

More recently, OLGA was validated against experimental decompression data by Botros et al. (2007). The decompression tests were conducted at the Gas Dynamic Test Facility (GDTF) in Didsbury, Canada. The tests were performed using a 0.172 km long, 49.5 mm inner diameter instrumented shock-tube rig containing inventories ranging from pure nitrogen to typical rich gas mixtures. The decompression of the pipeline was initiated upon failure of a rupture disc. Figure 2.15 shows the variation of pressure with time for the case of rapid blowdown, at an initial pressure and temperature of 105.8 bara and -25.6 ^{o}C respectively at distances of 23.1 m (P14), 47.1 m (P19) and 71.1 m (P24) from the rupture point.

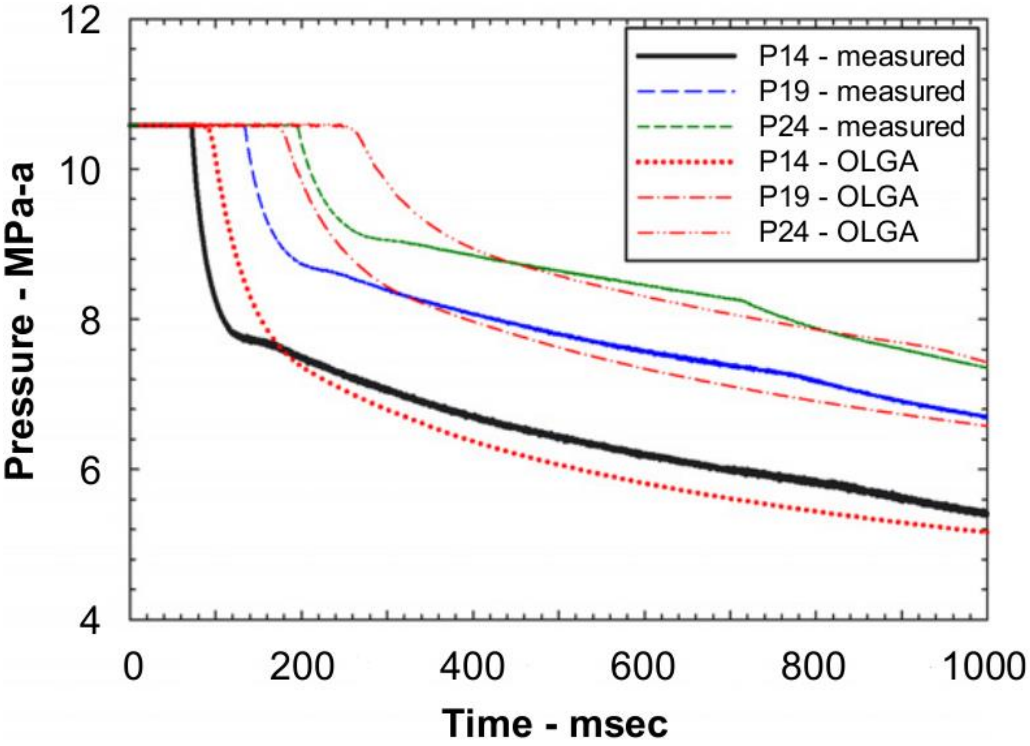

Figure 2.15: Comparison between OLGA and experimental data for case 2 at P14, P19 and P24 (Botros et al., 2007).

The pipeline contained an inventory indicative of a rich gas mixture containing *ca.* 95.6 % methane. As was observed by Botros et al. (2007), the delay in the initial pressure drop predicted by OLGA as compared to the measured data implies that the speed of the front of the decompression wave is under predicted. It is also clear that the predicted pressure drop is greater than that observed in the experimental measurements. These observations are in accord with the under-prediction of the outflow pressure in figure 2.14.

2.5.2 University College London (UCL) model

University College London (UCL) model is a robust computational fluid dynamic simulator for predicting the transient flow conditions in the pipeline system containing high pressurised hydrocarbons. Briefly, the flow modelling involves the numerical solution of the mass, energy, and momentum conservation equations assuming one-dimensional flow using a suitable technique such as the MOC (Zucrow and Hoffman, 1975). This involves the discretisation of the pipeline into a sufficiently large number of space and time elements and determining the transient fluid properties such as pressure, temperature, density, and the fluid phase at the intersection of characteristic lines using interpolation, successive iteration, and flash calculations. Liquid and vapour phases are assumed to be at thermal and mechanical equilibrium. Heat transfer and frictional effects are determined using established flow- and phase-dependent correlations for hydrocarbon mixtures. This model also accounts for inclined pipelines and punctures orientation, handles single or multi-component mixtures, supercritical pure components, and multiple segment pipelines as well as simulates forward and reverse flows of the fluid (Mahgerefteh et al., 1997).

Mahgerefteh et al. (1999) extended the UCL model (Mahgerefteh et al., 1997) to account for real fluid behaviour using the Peng-Robinson Equation of State (PR EOS) (Peng and Robinson, 1976). Two-phase fluid flow is accounted for using the Homogeneous Equilibrium Mixture model (HEM) (Chen et al., 1995a, b) where the constituent phases are assumed to be at thermal and mechanical equilibrium. In addition, curved characteristics were employed, replacing the characteristic lines with parabolas. The latter was claimed to overcome the errors introduced as a result of using linear characteristics, which assumes linear variation of the flow parameters between the grid points.

The long computational runtimes associated with the simulation of long pipelines were partly addressed by using a Compound Nested Grid System (CNGS) in which successively coarser discretisation grids were used away from the rupture plane. Mahgerefteh et al.'s (1999) pipeline flow model was validated against intact end pressure data recorded for the rupture of the Piper Alpha to MCP-01 subsea line (Cullen, 1990) as well as two sets of test results (P40 and P42) obtained from the Isle of Grain depressurisation tests (Richardson and Saville, 1996). Figure 2.16 shows the variation of pressure with time at the intact end of pipeline following the Full Bore Rupture (FBR) of the Piper Alpha to MCP-01 sub-sea line.

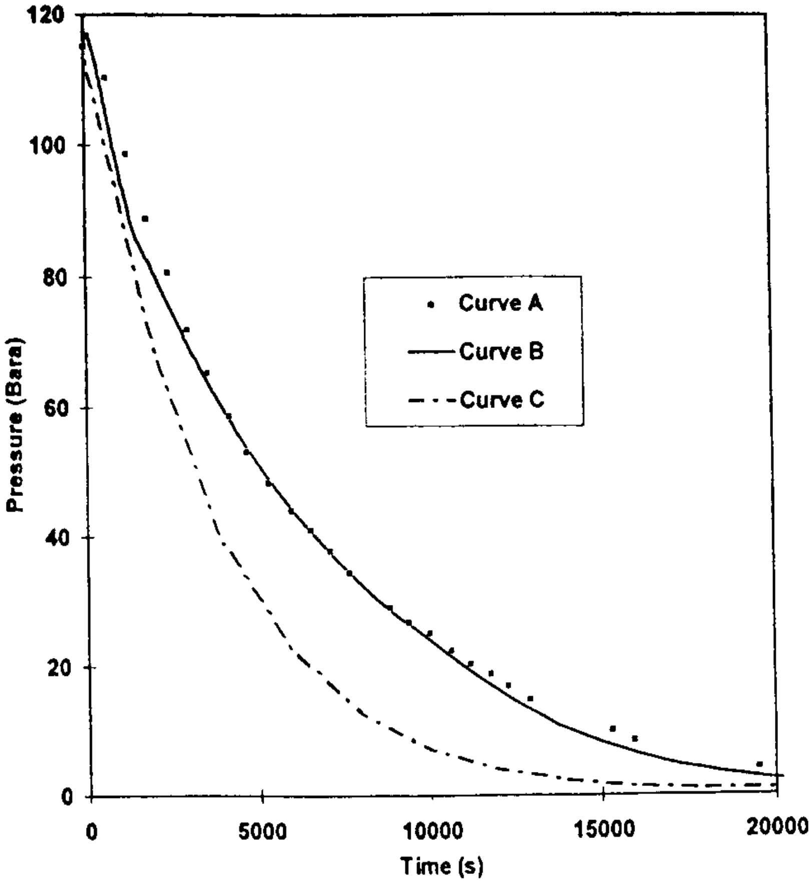

Figure 2.16: Intact end pressure vs. time profiles for the Piper Alpha to MCP pipeline (Mahgerefteh et al., 1999).
Curve A: Field Data
Curve B: CNGS-MOC, CPU runtime = 6 days
Curve C: CNGS-MOC ideal gas, CPU runtime = 1.5 min

Curves A and B are respectively the measured and predictions data using the Compound Nested Grid System Method of Characteristics (CNGS-MOC) while curve C is the corresponding data (CNGS-ideal) generated based on the ideal gas assumption. As it may be observed accounting for real fluid behaviour results in improved agreement with field data. However this is at the cost of a significant increase in the computational runtime (*ca.* 1.5 minutes for ideal gas compared with 6 days based on real fluid behaviour).

In order to assess the impact on computational runtime and simulation accuracy, three different combinations of the formulation of the conservation equations were employed. These included pressure, *P*, enthalpy, *H* and velocity, *U* (*PHU*); pressure, entropy, *S* and velocity (*PSU*); as well as the pressure, density, *D* and velocity (*PDU*) with the latter formulation used by Mahgerefteh et al. (1997). The effect of adopting quadratic interpolation along the space co-ordinate, as opposed to linear interpolation was also investigated.

The *PDU*, *PHU* and *PSU* based conservation equations were used by Oke et al. (2003) to simulate the Isle of Grain rupture P40 test. Briefly, the tests involved depressurization of an instrumented 100 m long and 0.154 m inside diameter pipe containing commercial LPG (95 % propane and 5 % n-butane) at pressure and temperature of 21.6 bar and 17.8 ^{o}C, respectively. Figure 2.17 shows the measured variation of the discharge pressure with time compared to the simulated results. Oke et al. (2003) concluded that the PHU model performed best in terms of accuracy, respectively followed by the PSU and PDU based models. The PHU model also resulted in the least CPU runtime. The computational runtimes required corresponded to 12, 13 and 86 mins for the PHU, PSU and PDU based models respectively on an IBM Pentium IV 2.4 MHz PC. Although the use of quadratic as opposed to linear interpolation marginally improved the model predictions, it also resulted in longer simulation runtime. As may be observed, in all cases, the UCL model produces relatively good predictions of the test data.

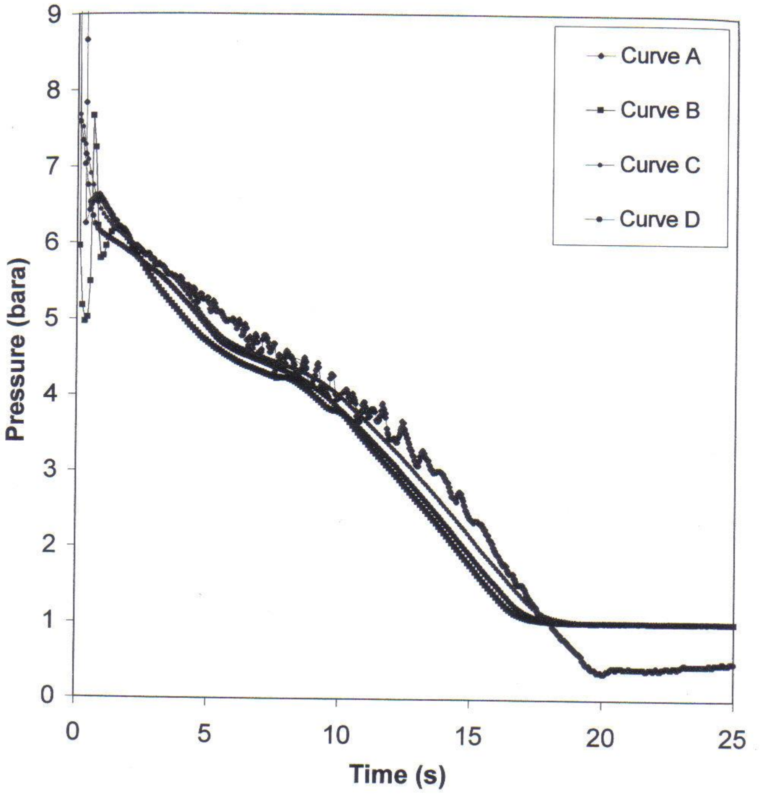

Figure 2.17: FBR pressure vs. time profiles at the open end for test P40 (LPG) showing the effect of primitive variables on simulated results (Oke et al., 2003).
Curve A: Open end measurement
Curve B: Open end simulation results using the PDU model
Curve C: Open end simulation results using the PHU model
Curve D: Open end simulation results using the PSU model

Mahgerefteh and Atti (2006) developed an interpolation technique for Oke's (2003) HEM model to reduce the computational runtime. The conservation equations were formulated using the pressure, enthalpy and velocity (PHU) (Oke et al., 2003) and solved in conjunction with pressure-enthalpy flash calculations. The model was validated by comparison against the results of the Isle of Grain rupture tests as well as the closed end data relating to the MCP-01 riser rupture during the Piper Alpha disaster. Figure 2.18 shows the variation of fluid pressure at the rupture plane for the P40 Isle of Grain test.

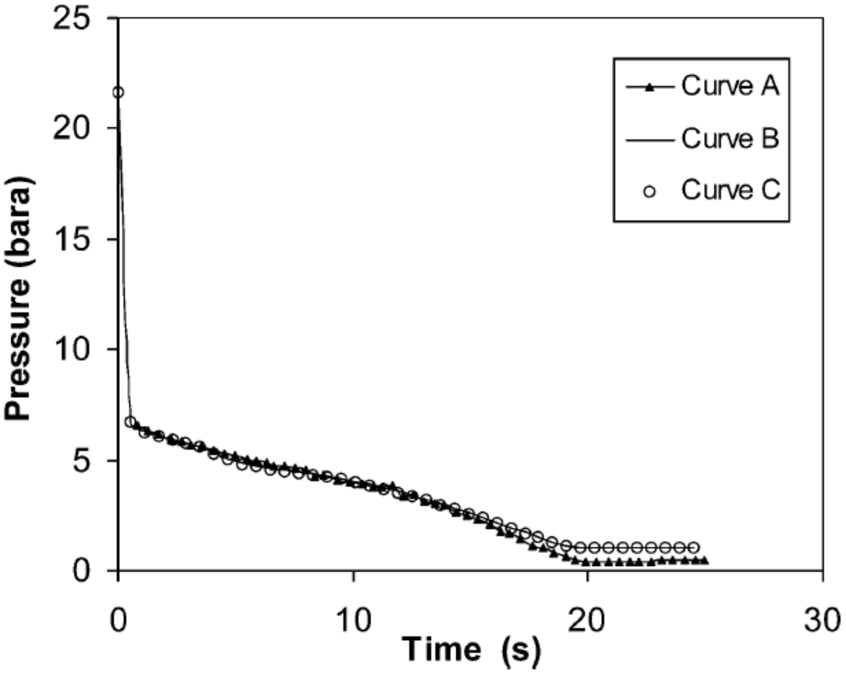

Figure 2.18: Pressure vs. time profiles at open end for test P40 (LPG) (Mahgerefteh et al., 2007).
Curve A: Measurement (Chen et al., 1995a, b)
Curve B: Simulation data without the interpolation scheme: CPU runtime = 12 min
Curve C: Simulation data employing the interpolation scheme: CPU runtime =3.5 min

The measured data is represented by curve A. Curves B and C on the other hand respectively represent the simulation results with and without the interpolation scheme. As it may be observed from figure 2.18 the simulated data (curves B and C) are identical and in good accord with the test data. The use of the interpolation scheme (curve B) results in a 70-80 % reduction in the computational runtime for the cases presented.

2.5.3 SLURP

The mathematical basis of SLURP is the same as that originally developed by Morrow (1982) with the further extension of the thermodynamic property model to account for a wide range of fluids with a consistent degree of accuracy (Cleaver et al., 2003). According to the authors, physical property predictions in SLURP are determined from curves fitted using the PR EOS (Peng and Robinson, 1976) and the COSTALD method for the prediction of liquid densities (Thomson et al., 1982).

Cleaver et al. (2003) validated SLURP by comparing the predicted inventories and mass flow rates with outflow measurements taken from the Isle of Grain LPG experiments (Tam and Higgins, 1990) and the predicted outflow data calculated using the general two-phase pipeline model PROFES (HyproTech, 2003). The Isle of Grain tests used in the validation were full bore rupture (tests T61 and T65) and blowdown (tests T63 and T66) through a circular and triangular orifice respectively. The inventory used in the tests comprised primarily of LPG (*ca.* 95 mole % propane and 5 mole % butane). A discharge coefficient of 0.8 as suggested by Richardson and Saville (1993) was used to simulate test T63 (Cleaver et al., 2003). No information was given by Cleaver et al. (2003) about the comparison between SLURP and test T66 experimental results. Table 2.10 gives a summary of the Isle of Grain test conditions used in the validation.

Table 2.10: Subset of tests from the Isle of Grain experiments used in the validation of SLURP (Cleaver et al., 2003).

Test	Initial conditions		Orifice diameter (mm)	Orifice shape
	Pressure (bara)	Temperature (^oC)		
T61	21.2	Unknown	51	Circular
T63	22.5	18.4	35	Circular
T65	11.6	13.8	51	Circular
T66	21.8	13.3	35	Triangular

Figures 2.19 to 2.21 present the variations of total pipeline inventory with time for tests T61, T63 and T65 respectively. As can be seen in the figures, SLURP performs poorly during the latter stages of depressurisation (figures 2.19 and 2.20 respectively). Cleaver et al. (2003) attributed this to the finite length of the pipeline, as the assumption of an infinitely propagating two-phase region is no longer valid. For the test T65 (figure 2.21) there are significant discrepancies between the test and simulated data. Cleaver et al. (2003) suggest that this is due to the delay in the fluid flashing to two-phase upon pipeline failure.

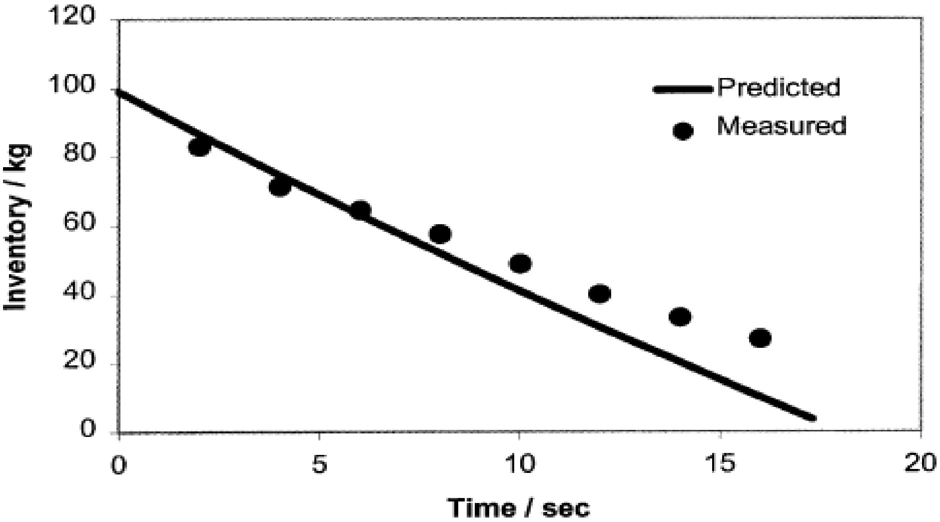

Figure 2.19: Comparison between SLURP model and measured variation of pipeline inventory with time for test T61 (Cleaver et al., 2003).

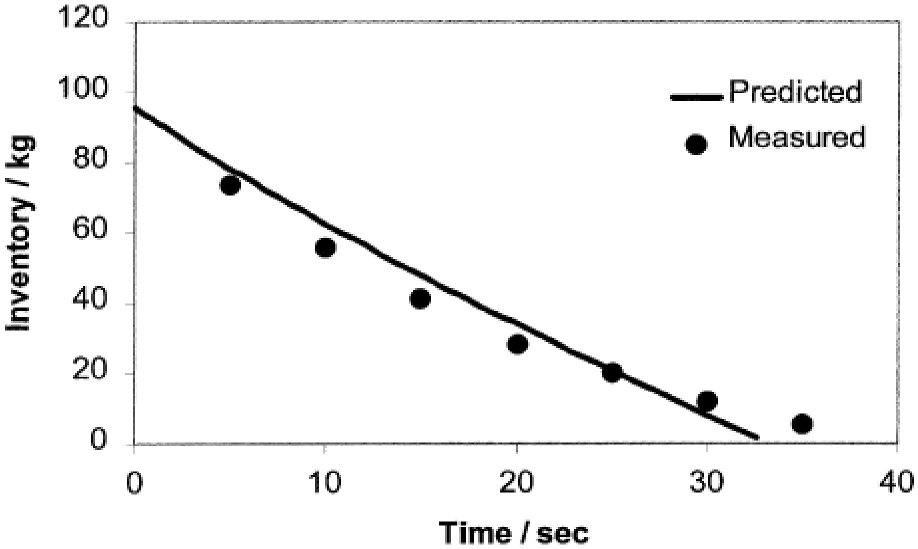

Figure 2.20: Comparison between SLURP model and measured variation of pipeline inventory with time for test T63 (Cleaver et al., 2003).

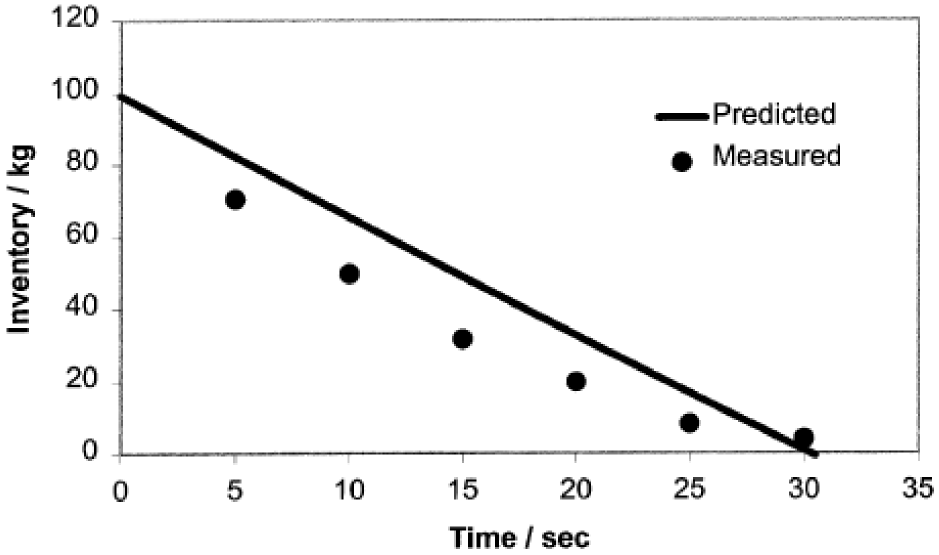

Figure 2.21: Comparison between SLURP model and measured variation of pipeline inventory with time for test T65 (Cleaver et al., 2003).

Cumber (2007) extended SLURP (SLURP_FAUSKE) by reverting to the homogeneous equilibrium flow assumption (SLURP_HEM) by assuming no phase slip and accounting for fluid/wall heat transfer (SLURP_HEM_HT). To study the impact of these extensions to SLURP, a number of propane outflow scenarios were modelled and the results compared against PROFES predictions. Table 2.11 shows the failure scenarios examined.

Table 2.11: Failure scenarios used in the comparison of predicted outflow calculated using SLURP and PROFES for a pipeline at an initial temperature of 15 ^{o}C containing carrying an inventory of 100 % propane (Cumber, 2007).

Case	Initial pressure (barg)	Pipe diameter (mm)
P1	45	250
P2	70	250
P3	20	250

Figure 2.22 shows the comparison of the variation of mass flow rate with time for case P1. As it may be observed, the SLURP models predict a higher flow rate than that given by PROFES with the original SLURP model (SLURP_FAUSKE) giving closest agreement. The figure also shows that the inclusion of heat transfer effects (SLURP_HEM_HT) has little impact on the predicted outflow. Cumber (2007) stated that this was consistent with the findings of Webber et al. (1999) where including wall

heat transfer tended to improve predictions of temperature and pressure profiles but not the discharge rate as compared to measured data.

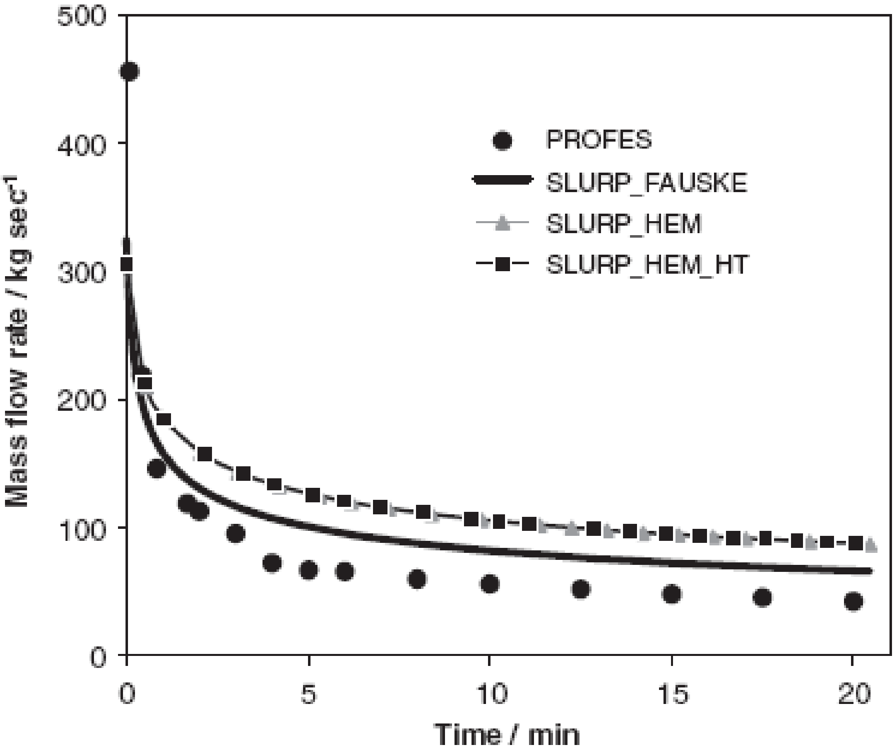

Figure 2.22: Comparison of predicted release rate for a propane pipeline at an initial pressure of 46 bara and 15 ^{o}C (Cumber, 2007).

2.5.4 Terenzi

Terenzi (2006) presented Machnet (Machnet_Real) developed to investigate the impact of real gas behaviour on the interaction between pipeline decompression and ductile fracture propagation. Homogeneous equilibrium is assumed between gas and liquid. Thermodynamic properties, such as the void fraction, are determined by linear interpolation using a look up table with the density and specific internal energy as independent variables. Fluid/wall heat transfer is calculated by solving the Fourier equation in cylindrical geometry between the external environment and the fluid. The Colebrook-White correlation (Keenan and Neumann, 1943) is used to account for frictional effects along the pipeline. The resulting governing system of equations is resolved using Roe (1981) approximate Riemann solver in an explicit Finite Volume Godunov-type scheme.

Terenzi (2006) also developed a model for the decompression of a pipeline transporting an ideal gas (Machnet_Ideal) by assuming zero heat transfer and frictionless flow to derive a similarity solution for the pressure at the exit plane and the speed of the rarefaction wave.

Machnet_Ideal and Machnet_Real's predictions were tested by comparison with the results of tests conducted at the Foothills Pipelines Northern Alberta Burst Test Facility (NABT) (Picard and Bishnoi, 1987). These tests involved the release of natural gas (*ca.* 85 % methane) from pipelines with respective pipeline internal diameters, pressures and temperatures in the ranges of 1219 to 1422 mm, 7.5 to 8.7 MPa and -18 to +18 ^{o}C.

Figure 2.23 shows the variation of the ratio of pressure to initial pressure and void fraction with expansion wave velocity.

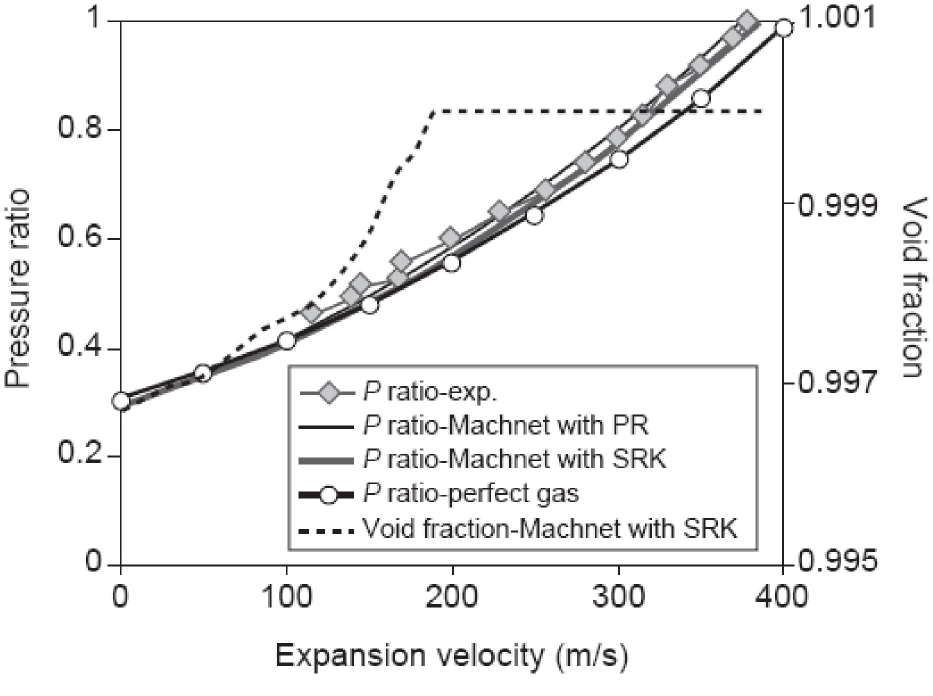

Figure 2.23: Measured and calculated decompression wave speed results of NABT Test 5 (Picard and Bishnoi, 1987).

The simulated results obtained from Machnet_Ideal and Machnet_Real utilising the PR and Soave-Redlich-Kwong (SRK) Equations of State were compared with experimental data. As may be observed, Machnet_Real coupled with either the PR or

SRK shows similar behaviour, while Machnet_Ideal over-predicts the wave speed throughout the decompression process. Additionally, the fluid void fraction falls slightly from unity when the pressure ratio reaches *ca.* 0.55. At this point Machnet_Real predictions using the PR and SRK EOS begin to diverge from the experimental data.

Based on the above data it is clear that the fluid flow model is capable of simulating the decompression wave initiated upon pipeline failure. However, the authors did not present a similar comparison relating to the release characteristics. As such, the efficacy of the model with regards to the prediction of outflow cannot be verified.

2.5.5 Popescu

Popescu (2009) developed a model for analysing the high-pressure release from a pipeline during ductile fracture propagation. The model separates the pipeline into two sections which are ahead of the crack tip (i.e. remaining enclosed inventory within the pipeline) and behind the moving crack. For the portion of the pipeline ahead of the crack tip, one-dimensional conservation equations for mass, momentum and energy are applied. The model accounts for friction through the inclusion of a viscous stress term and couples the conservation equations with the ideal gas EOS. Behind the crack the flow is assumed to be negligible in the axial direction and that all flow is through the crack tip opening. In this region the continuity equation is integrated over the release plane and is combined with the ideal gas choked flow equation (Greenshields et al., 2000).

The model for the flow ahead of the crack tip was validated using the experimental results from two decompression tests. The first test was performed using a 11.5 m pipeline containing methane. The second test used a 34.5 m pipeline containing hydrogen. Both pipelines were instrumented with pressure sensors at 1 and 3 m from the middle of the pipeline. No details about the failure type, ambient conditions, feed temperature or pipeline characteristics were given by Popescu (2009). Figures 2.24 and 2.25 show the comparisons of the predicted and experimental pressure transients for test 1 (11.5 m) and test 2 (34.5 m) respectively. The figures show that the model gives good agreement with experimental data following pipeline failure. However, the speed at which the front of the decompression wave arrives at the probe locations is slightly over-predicted. This is indicated by the faster pressure drop from the initial value. Although good agreement is obtained in the pressure profiles presented, the assumption of ideal gas behaviour means that the model is not applicable to non-ideal or two-phase mixtures. Further, this assumption leads to an incorrect prediction of the speed of sound which is essential for the tracking of the expansion wave. In addition, the performance of the internal flow model is uncertain with respect to long pipelines, where it is likely that heat transfer and friction may be significant.

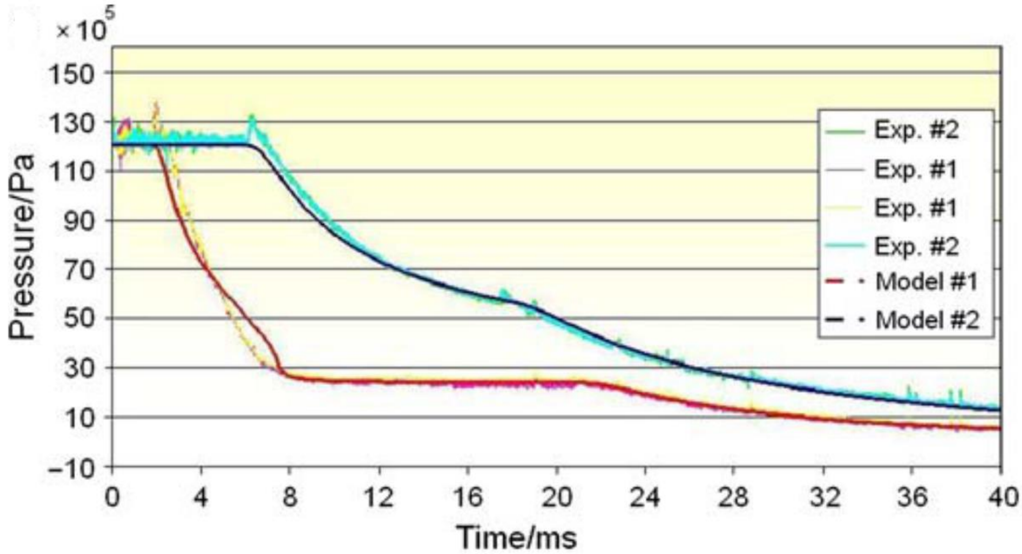

Figure 2.24: Comparison of the variation of pressure with time between predicted and experimental for a 11.5 m pipeline containing methane (Popescu, 2009).

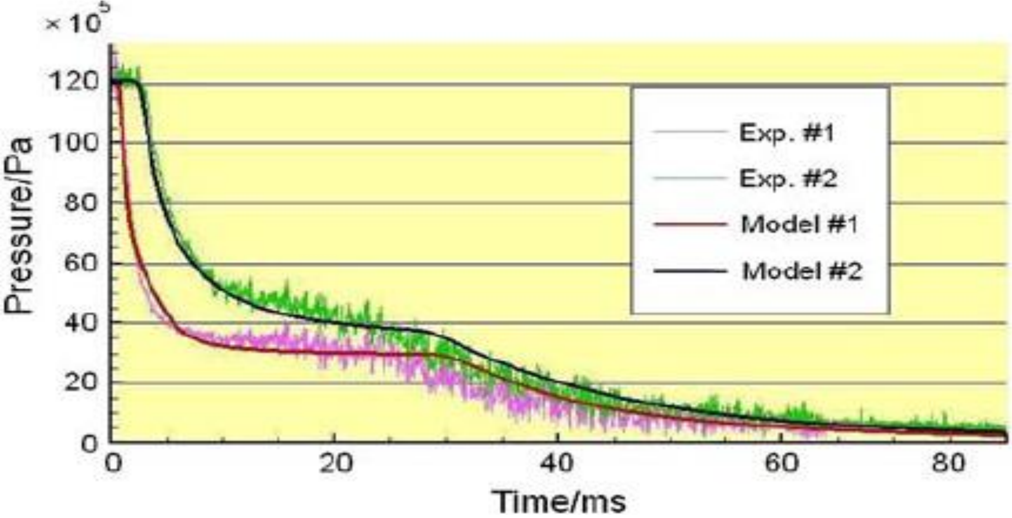

Figure 2.25: Comparison of the variation of pressure with time between predicted and experimental for a 34.5 m pipeline containing hydrogen (Popescu, 2009).

2.6 Concluding remarks

In this section, the mass, momentum and energy conservation equations for the transient fluid flow in a pipeline were presented. These were expressed in terms of the dependent variables pressure, enthalpy/entropy and velocity. The governing system of conservation equations were shown to be quasi-hyperbolic in character. The conservation equations coupled with a Cubic Equation of State representing the foundation of the transient fluid flow model. The various hydrodynamic and thermodynamic relations for predicting the pertinent fluid properties such as the fluid speed of sound, the thermodynamic function and the Fanning friction factor were presented. The formulation and implementation of the Method of Characteristics to solve the conservation equations governing single/two-phase flow in pipelines was also described.

Particular attention is paid to the Method of Characteristics as a solution methodology given its popularity due to its accuracy and robustness. Based on the above reviewed models, OLGA tended to under-predict the pressure profile, occasionally by significant margins. For the models SLURP, Terenzi and Popescu, insufficient data were reported by the researchers to properly assess their suitability for modelling the transient flow of the high pressurised fluid. For these reasons, the present work will extend the UCL model, based on the above formulations and review for the study of transient flow in pressurized pipelines.

In the following chapter 4, special attention will be paid to the design of the associated pipeline infrastructure in order to avoid large flow fluctuations at the delivery point of CO_2 at the sequestration site. In this chapter 4, the development of a transient flow model by employing the UCL model which is in turn used as part of the control strategy for avoiding such phenomena will be studied.

CHAPTER 3:

STUDY OF MULTISTAGE COMPRESSION OF CO_2 WITH IMPURITIES FOR CCS

3.0 Introduction

This chapter deals with multistage compression of impure CO_2 streams for CCS applications. In particular, it covers the description of the types of industrial compression technologies employed and the types of impurities present in the post-combustion, pre-combustion and oxy-fuel streams captured from power plants and industrial processes such as N_2, Ar, O_2, SO_2, H_2O, H_2S, H_2 and *etc*. This is followed by the description of the thermodynamic model developed in this work to determine the total power consumption for multistage compression and intercooler of pure and impure captured CO_2 streams. Using the compression model developed, optimal multistage compression schemes are determined depending on the outlet pressure from the separation unit of the captured streams. The calculated power requirements for compression and intercooler as well as intercooling heat duty for various compression schemes for particular CO_2 mixtures depending on the capture technologies employed are compared and discussed.

3.1 Technical background

Compression of captured CO_2 is the last part of the capture process before transportation using a pipeline to a geological storage site. The process involves the use of mature technologies and techniques that are used in the natural gas industry but with some modifications to suit the properties of CO_2 (Wong, 2006). CO_2 compression differs from most gas compression due to its high molecular weight, highly compressible behaviour and encountering its critical point (Witkowski et al., 2013) where even a small change in temperature or pressure, yields a large change in density (Oakey et al., 2010). The main reasons for integrating CO_2 compression in CCS are to convert the fluid from the gas phase to the dense phase and also to reach the technically and economically optimum pressure for pipeline transportation (Gusca and Blumberga, 2011). However, the compression process requires optimisation due to its high costs and energy penalty (Notebook, 2011, Pei et al., 2014).

Romeo et al. (2009) have reported about 25 % of the total capital requirements of the CCS is due to compression equipment costs. Energy requirements for compressing one tonne of CO_2 are about 100-133 kWh (Pei et al., 2014). According to Moore et al. (2011), the traditional pulverised coal power plant and typical Integrated Gasification Combine Cycle (IGCC) plant present *ca.* 27-37 and 13-17 % of the energy penalty of CCS respectively and the compression part has a significant contribution to this percentage. The CO_2 compression alone reduces the efficiency of a power plant by as much as 8-12 % from the overall process. In a pulverised coal-fired power plant with an amine capture based system, the power required for CO_2 compression is approximately 6-12 % of the total plant rating (Witkowski et al., 2013). These values highlight the necessity for detailed analyses of CO_2 compression in the CCS system in order to minimize both, energetic requirements of the compression and additional capital requirement for the capture system.

In order to efficiently transport large amounts of CO_2, it must be transformed into a form with high density, meaning that transport in a dense phase or at supercritical conditions may be considered as shown in figure 3.1.

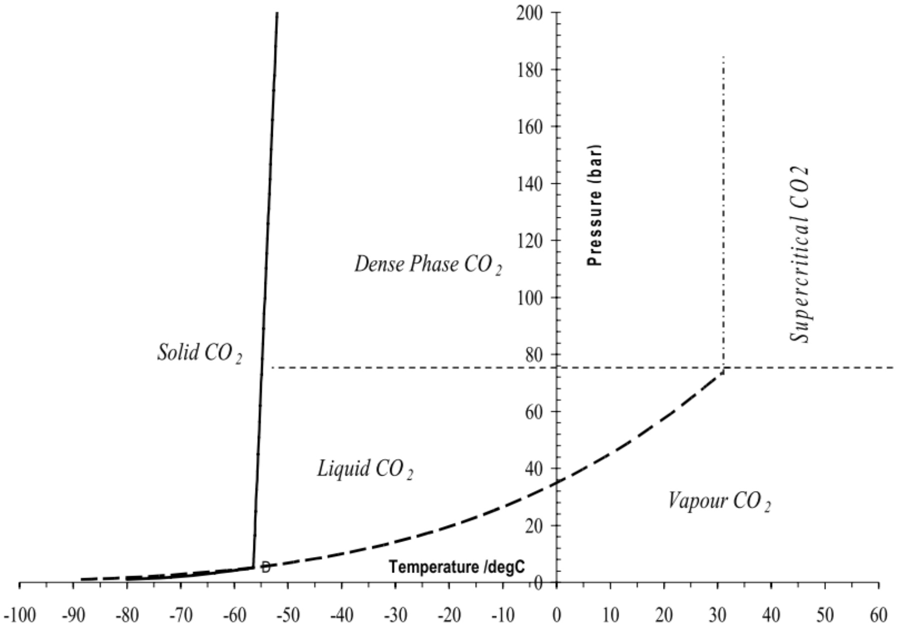

Figure 3.1: Phase diagram for pure CO_2 (Seevam et al., 2008).

A high density is favourable when transporting CO_2, as it is easier to move a dense fluid rather than a gas (Wong, 2006). In the dense phase, the specific volume of CO_2 is more than 500 times smaller compared with values at the gas phase (Romeo et al., 2009). In pipeline systems, CO_2 is transported at high pressure above the critical pressure, most likely in the range of 80-150 bar. The CO_2 must be compressed to a pressure high enough to overcome the frictional and static pressure drops. Typically, the frictional loss can range from 4 to 50 kPa per km, depending on the pipe diameter, mass flow rate and the pipe roughness factor. Furthermore, the CO_2 should be delivered at a pressure higher than the critical pressure to avoid two-phase flow and liquid slugs in the pipeline as well as to prevent liquids in the injection compressor (Aspelund and Jordal, 2007, Romeo et al., 2009). Hence, in order to maintain the CO_2 in the dense phase for the whole pipeline, the inlet pressure of the pipe must be at high enough pressure above the critical point or booster stations must be installed every 100 to 150 km to compensate for the pressure losses (Wong, 2006).

Many researchers have made important studies in the CCS field, but most of them focus on the CO_2 capture process with compression and transportation receiving relatively less attention. In particular, Witkowski and Majkut (2012) and Witkowski et al. (2013) have quantified the power demands for various industrial CO_2 compression systems, including conventional 8-stage integrally geared centrifugal compression, advanced supersonic shockwave compression and multistage compression combined with subcritical or supercritical liquefaction and pumping. The authors found that total compression power was not only determined by the compressor efficiency, but is heavily dependent on thermodynamic processes. These findings provide relevant data and act as a benchmark since they exemplify how various industrial compression strategies can be integrated in the CCS system for near pure CO_2 streams.

Furthermore, several studies have examined the opportunities for integration of compression in CCS and the power generation process. Pei et al. (2014) investigated coupling CO_2 compression with the organic Rankine cycle to re-utilise the heat of compression in power plant operation, showing that the energy requirements can be reduced by *ca.* 17 and 30 % for conventional and shockwave compression, respectively. Also, Romeo et al. (2009) have shown that utilising heat from the inter-cooling process in the pre-heating section of steam cycle can give *ca.* 40 % savings in compression power. Duan et al. (2013) proposed integrating CO_2 compression with liquefaction using an ammonia absorption refrigeration system powered by the exhaust heat from steam turbines with a coal-fired power plant that proved to greatly reduce the power consumed in CO_2 compression. Aspelund and Jordal (2007) have analysed various options for conditioning of CO_2 streams, suggesting using expansion of a fraction of compressed CO_2 as a refrigerant in a condenser column for removing volatile components. While the above studies quantified power requirements for industrial compression of CO_2, their practical application is, however, limited due to the underlying assumption of negligibly small amounts of impurities in CO_2 stream.

The present study evaluates the impact of impurities on power requirements for compression technologies previously recommended for pure CO_2.

3.2 CO_2 stream impurities

In practice, the CO_2 streams in CCS will contain some impurities with range and level, mostly depending on the capture technology. Unlike the CO_2 streams produced in post-combustion and pre-combustion captures, the purity of the separated untreated oxy-fuel CO_2 stream is generally much lower, reaching about 75-90 % v/v. The compositions of CO_2 streams captured in oxy-fuel, pre-combustion and post-combustion captures from coal-burning power plant has recently been reviewed by Porter et al. (2015). Tables 3.1 and 3.2 lists the impurities present in captured CO_2 streams and gives the typical concentrations of the various components.

As can be seen from the data in table 3.1, post-combustion capture (99.66 % v/v of CO_2) has high purity of the CO_2 stream along with oxy-fuel distillation process (99.30 % v/v of CO_2), followed by pre-combustion (98.07 % v/v of CO_2), then the oxy-fuel double flash process (96.70 % v/v of CO_2) and raw oxy-fuel (85 % v/v of CO_2) mixtures. During the oxidation process, NO which is primarily presented as a large proportion in the NO_x composition has converted to NO_2 in the presence of oxygen after a certain residence time (Normann et al., 2013). Early findings by Witkowski and Majkut (2012) on CO_2 compression for the post-combustion mixture did not evaluate the effect of impurities which kept the level of impure components very low. However, due to the high amount of impurities present in the pre-combustion and oxy-fuel streams that generally will affect the energy required for the level of CO_2 compression, the effect of these impure components cannot simply be neglected (IEAGHG, 2011, Kownatzki and Kather, 2011).

Table 3.1: Compositions of CO_2 mixtures captured from oxy-fuel, pre- and post-combustion technologies (Porter et al., 2015).

	Oxy-fuel			Pre-combustion[d]	Post-combustion[d]
	Raw/dehumidified[a]	Double flashing[b]	Distillation[c]		
CO_2 (% v/v)	**85.0**	**96.70**	**99.30**	**98.07**	**99.66**
O_2 (% v/v)	4.70	1.20	0.40	-	0.0035
N_2 (% v/v)	5.80	1.60	0.20	0.02	0.29
Ar (% v/v)	4.47	0.40	0.10	0.018	0.021
NO_x(ppmv)	100	150	33	-	38.8
SO_2 (ppmv)	50	36	37	25	67.1
SO_3(ppmv)	20	-	-	-	-
H_2O(ppmv)	100	-	-	150	100
CO (ppmv)	50	-	-	1300	10
H_2S (ppmv)	-	-	-	1700	-
H_2 (ppmv)	-	-	-	15000	-
CH_4(ppmv)	-	-	-	110	-

Table 3.2: The range of oxy-fuel CO_2 impurities from pulverised coal (Porter et al., 2015).

	Raw/dehumidified			Double flashing			Distillation		
	a	e	b	f	c	b	a	b	g
CO_2(% v/v)	85.0	77.19	74.8	95.84	96.30	96.7	99.94	99.3	>99.95
O_2(% v/v)	4.70	3.210	6.00	1.050	1.10	1.20	0.01	0.40	<30 ppm
N_2(% v/v)	5.80	15.49	16.6	2.030	2.00	1.60	0.01	0.20	Trace
Ar(% v/v)	4.47	4.030	2.30	0.610	0.60	0.40	0.01	0.10	Trace
NO_x(ppmv)	100	-	709	130	0	150	100	33	<5
SO_2(ppmv)	50	800	702	4500	0	36	50	37	
SO_3(ppmv)	20	-	-	-	-	-	20	-	<0.1
H_2O (ppmv)	100	0	1000	0	0	0	100	0	<20
CO (ppmv)	50	-	-	-	-	-	50	-	<10

[a] (Kather and Kownatzki, 2011), [b] (Pipitone and Bolland, 2009), [c] (White et al., 2009), [d] (Porter et al., 2015), [e] (Wilkinson et al., 2001), [f] (Dillon et al., 2005) and [g] (Spero, 2014). *Includes sour compression step prior to removal of inerts.

3.2.1 Oxy-fuel combustion capture

Oxy-fuel combustion is becoming a popular option for CO_2 capture due to some specific advantages. This technology is gaining maturity and can be retrofitted to the existing fleet of modern pulverised coal-fired power plants. In this unit, the fuel is burned in a mixture of purified oxygen and recycled flue gas from the boiler containing mainly CO_2 and water vapour (Kownatzki and Kather, 2011).

During oxy-fuel capture, the CO_2 stream is purified in a sequence of different steps at increasing pressure levels. In particular, water scrubbing in a direct contact cooler can be used at ambient pressure to condense water vapour and remove traces of ash, whereby the removal of some reactive and soluble gases such as SO_3 and HCl can be achieved at pressures of around 15 bar (White et al., 2009). At this stage, the CO_2 stream has purity from *ca.* 70 to 75-85 % v/v (see table 3.2). Also, the 'sour compression' process proposed by Air Products allows for the removal of SO_x and NO_x impurities. To further reduce the amount of non-condensable components (such as O_2, N_2 and Ar) and achieve CO_2 purity of over 95 % v/v, flash-evaporation and distillation are applied at pressures of around 30 bar (Dillon et al., 2005, White et al., 2009, Besong et al., 2013). As such, compression is partially integrated in oxy-fuel CO_2 purification, and higher purity CO_2 streams can be achieved for transporting and storage requirements.

3.2.2 Pre-combustion capture

In pre-combustion systems, the removal of CO_2 occurs before combustion takes place. The main concept in this system is coal gasification followed by a water gas shift reaction and absorption of CO_2 (Erlach et al., 2011). CO_2 can be removed for storage purposes and the resultant H_2 could be used in fuel cells or in gas turbines to generate electricity. The process is operated when O_2 from the air is separated using an Air Separation Unit (ASU) before reaction with steam and coal as a fuel in a gasifier or thermal partial oxidation reactor at 1550 ^oC and 40 bar to produce syngas such as CO and H_2. The products are extracted in the Selexol-based Acid-Gas Recovery (AGR) unit to separate H_2 from other gases, mainly CO_2 using a physical or chemical absorption process at temperature *ca.* 30 ^oC. The clean gas from H_2S absorber enters the CO_2 absorber to produce CO_2-rich fluid stream at *ca.* 25 ^oC, 30-35 bar before pipeline transportation (Lu et al., 2012).

3.2.3 Post-combustion capture

In post-combustion capture processes, CO_2 is separated from flue gas originating from air-fired combustion. Traditionally, amine-based absorption systems operating at close to ambient conditions (*ca.* 1.5 bar and *ca.* 40 ^oC (IEAGHG, 2011)) are used to capture the CO_2 from the flue gas, which typically contains only 5-15 % v/v CO_2, with the remaining major components being O_2, N_2, Ar, H_2O, CO, NO_X and SO_2 (table 3.1). Using amine-based solvents CO_2 can be purified to above 99 % v/v. Due to its relatively high purity, the impact of impurities on thermodynamic properties of post-combustion CO_2 streams is often neglected (Witkowski et al., 2013).

3.2.4 Impact of impurities on CO_2 physical properties

The presence of impurities in CO_2 streams reduces the effective capacity of CO_2 transportation pipelines and storage reservoirs, making the transportation and storage of industrial-grade CO_2 less efficient than for pure CO_2. Additionally, the presence of impurities in CO_2 can shift the boundaries in the CO_2 phase diagram to higher pressures, meaning that higher operating pressures are needed to keep the CO_2 in the dense phase. On the other hand, removing impurities from the CO_2 stream increases the capture and purification costs (Holloway and Akai, 2006). Clearly, in order to minimise the costs of CCS, the costs associated with compression/transportation and injection of impure CO_2 must be optimised in conjunction with the costs of CO_2 stream purification.

Of particular importance for compression is that impurities alter the physical properties and vapour-liquid phase equilibria of CO_2 mixtures (Goos et al., 2011, Ziabakhsh-Ganji and Kooi, 2012) as shown in figure 3.2.

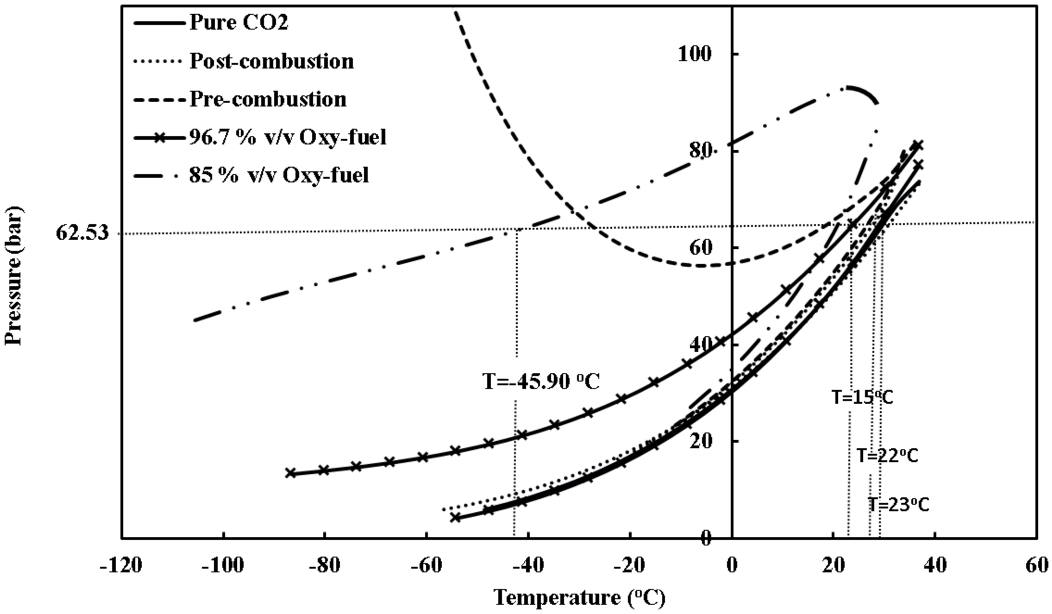

Figure 3.2: Boundaries of VLE region in pressure-temperature phase diagram for pure CO_2, pre-combustion, post-combustion and oxy-fuel streams (85 and 96.70 % v/v CO_2) calculated using PR EoS.

As is shown in figure 3.2, the small amount of impurities in CO_2 mixtures produced in post-combustion and pre-combustion capture has very little impact on the bubble-point and dew-point curves, which remain close to the saturation curve of pure CO_2. However, in the case of the raw dehumidified oxy-fuel mixture, which carry a relatively large amount of impurities (15 % v/v), the bubble point and dew point pressures are remarkably different to the vapour pressure of pure CO_2. As such, unlike the post-combustion and pre-combustion mixtures, the raw oxy-fuel streams can be expected to have physical properties remarkably different from those of pure CO_2. In addition, from figure 3.2, the liquid vapour phase equilibria and especially the cricondenbar pressure (i.e. the pressure above which no gas phase can be found in the fluid) are remarkably different for the three oxy-fuel streams from table 3.1.

Figure 3.2 shows that the range of vapour liquid equilibrium (VLE) data for the mixtures differs from that for pure CO_2. In particular, the saturation pressures for oxy-fuel and pre-combustion mixtures differ significantly from the saturation pressure for pure CO_2 and post-combustion mixture. As can be seen from figure 3.2, the saturation curves for pure CO_2 and post-combustion CO_2 mixture are nearly identical, as can be explained by high purity of post-combustion stream and, hence, have a negligible impact of impurities on the fluid properties. In the case of the pre-combustion and oxy-fuel mixtures, the purity of the CO_2 stream decreases, and hence the larger becomes the deviation from the saturation data of pure CO_2.

The data in figure 3.2 show that the presence of impurities has more significant impact on the bubble point rather than the dew point line. It can be observed that with the increase in the amount of impurities in the CO_2 mixture, in particular non-condensable gases, such as N_2, O_2, Ar and H_2, the bubble point line is shifted towards higher pressures, while the bubble point line temperature is reduced. The effect is mostly pronounced for the oxy-fuel mixture, which carries the largest amount of impurities (table 3.1). On the other hand, the impact of impurities in the pre-combustion and post-combustion mixtures on the bubble point line is relatively small and becomes significant only for the oxy-fuel mixture.

Figure 3.3 illustrates the effect of compression pressure on the gas-phase and supercritical fluid density for pure CO_2 and the CO_2 mixtures at the temperature of 38 ^oC, which corresponds to the typical temperature of CO_2 before compression.

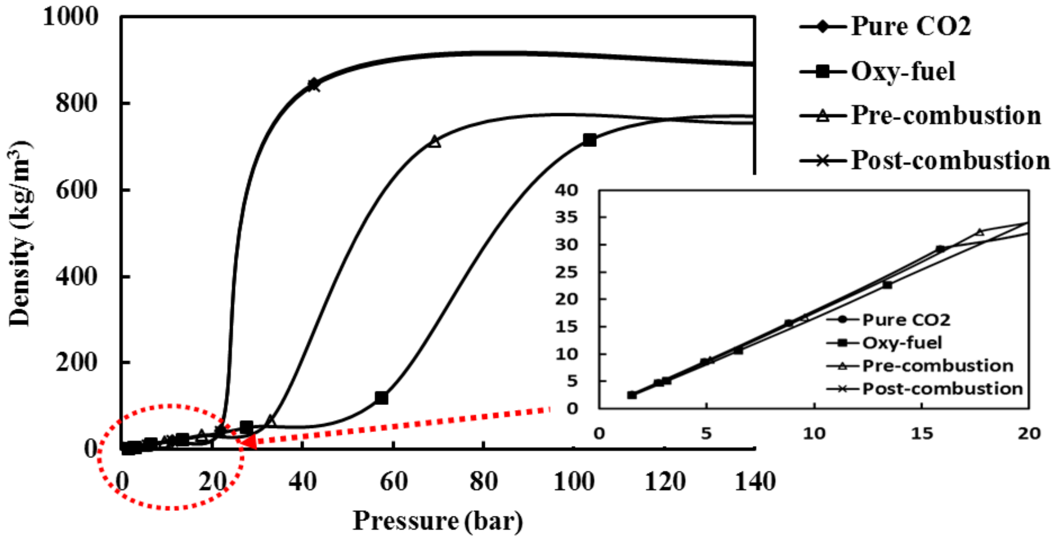

Figure 3.3: The effect of pressure on the density of pure CO_2 and oxy-fuel, pre-combustion and post-combustion CO_2 mixtures. $T_o = 38\ ^oC$.

As can be seen from figure 3.3, at pressures in the range from 1.51 bar to *ca.* 20 bar, the density of mixtures from all different capture technologies is about the same. At pressures above 20 bar, the density increases with pressure and differs considerably between each capture technology. The density of pure CO_2 and mixture of post-combustion rose dramatically with the increase of pressure due to the least fraction of impurities present in the streams. These densities are higher than those of pre-combustion and oxy-fuel CO_2 mixtures, which would result in higher power consumption for compression and liquefaction for subsequent pipeline transportation (Sass et al., 2009).

Figure 3.4 illustrates the effect of pressure on compressibility factor, *Z*, of pure CO_2 and CO_2 mixtures from oxy-fuel, pre-combustion and post-combustion at the temperature of 38 °C.

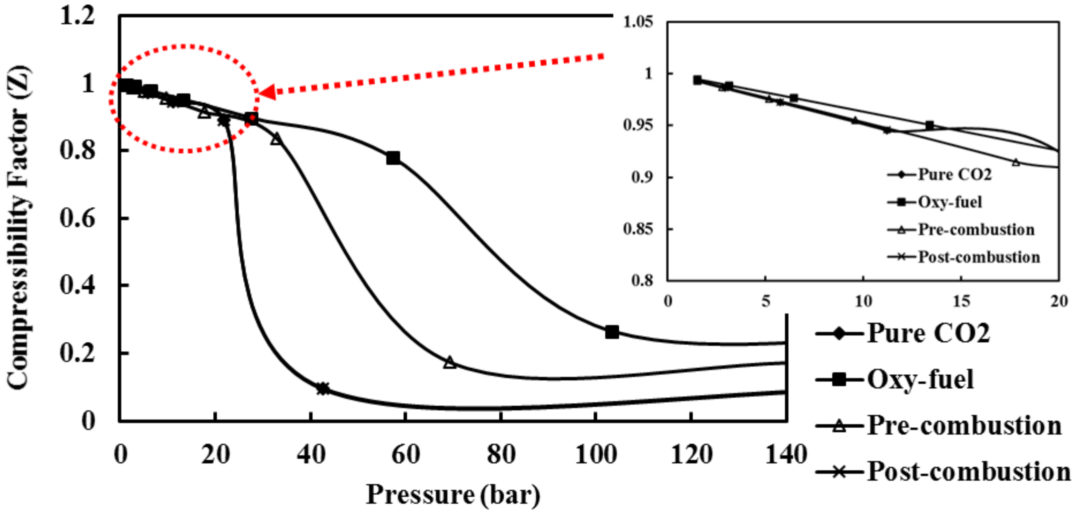

Figure 3.4: Effect of compression pressure on the compressibility factor of pure CO_2 and CO_2 mixtures captured from oxy-fuel, pre-combustion and post-combustion technology. T_o = 38 °C

It can be seen that at pressures in the range from 1.51 to *ca.* 20 bar the compressibility factor linearly decreases with increasing pressure and is almost independent on the CO_2 purity. At pressures above 20 bar the compressibility factor for all mixtures rapidly decreases with pressure. Since the presence of impurities reduces the molecular weight of the CO_2 mixtures, the pipeline transportation of these mixtures at a fixed mass flow rate will be characterised by larger pressure drops, to overcome which higher inlet pressures will be required for less pure CO_2, meaning an increase in the compression power (Moshfeghian et al., 2008, Tabkhi et al., 2008).

Recently, Aspelund and Jordal (2007), de Visser et al. (2008) and Goos et al. (2011) have shown that the energy required for CO_2 stream compression for pipeline transportation increases proportionally with the concentration of the gaseous impurities in CO_2 mixtures. These findings thus lend support and provide guidelines for optimization of compression, transportation and storage processes. However, the implications of this effect both on the selection of an appropriate compression strategy for realistic CO_2 streams and associated energy penalty costs have not received much attention.

3.3 Industrial compression technologies

In CCS, compression of a CO_2 stream coming from capture/purification facilities for pipeline transportation and geological storage can be practically achieved using various different types of industrial compressor, which include conventional multistage integrally geared compressors, advanced supersonic shockwave compressors, and compression and pumping with a subcritical or supercritical liquefaction/refrigeration system. In order to achieve optimal pressure for pipeline transportation, a number of stages of compression are required.

Thus, compression generally occurs in a number of stages integrated with inter-stage cooling equipment. Applying coolers after the compression stages will reduce the power needs for gas compression and therefore the compressor size and total capital requirement of the system (Romeo et al., 2009, Wong, 2006). The main parameters affecting the compression power and cooling requirement necessities in the CCS system are compressor efficiency, pressure ratio and CO_2 inlet pressure. The selection and design of more efficient and economical compression technology are dependent on the conditioning process which determines the thermodynamic state of the CO_2 entering the system.

Table 3.3 summarises the compression technologies adopted in the present study. These selected technologies have been applied to meet the compression service requirements depending on inlet and outlet pressures and volumetric flow rate of the streams (Witkowski and Majkut, 2012). The following gives detailed descriptions of the compression processes for these options.

Table 3.3: Multistage compression technology option.

Option	Compression technology
A	Conventional multistage integrally geared centrifugal compressors
B	Advanced supersonic shockwave compression
C	Multistage compression combined with subcritical liquefaction and pumping
D	Multistage compression combined with supercritical liquefaction and pumping

3.3.1 Option A: Conventional multistage integrally geared centrifugal compressors

Conventional multistage integrally geared centrifugal compressors, Option A, is the preferred choice for CO_2 compression in the power plant industry (Holloway and Akai, 2006). This typical compressor has a limited individual pressure ratio in the range of 1.7-2:1 (Pei et al., 2014). For such pressure ratios, eight stages of the integral geared compressor are required to achieve an overall pressure ratio of 100:1. In this option, a group of cylinders is arranged in series with coolers which are provided between stages in order to reduce the temperature of the compressed gas which minimises its volume resulting in lower compression work. Due to the significant reduction in CO_2 volume during the compression process, the setup requires a large impeller for the first stage and a very small impeller for the last stage (Witkowski and Majkut, 2012). Normally, centrifugal compressors are the common choice for the compression of large amounts of CO_2. The compressors will have an efficiency of 75-85 % (Holloway and Akai, 2006). The first two stages must be designed to withstand the corrosion that is expected due to acidic water. Ideally, the inlet temperature of each compressor should be the same as it was at the initial condition to achieve the perfect cooling or isothermal compression.

Selection, sizing and operation of inter-stage coolers are also important considerations. Intermediate cooling can be done by seawater, freshwater or ambient air heat exchangers. The rejected intercooling heat may potentially be used to regenerate the amine solution in the regeneration column of post-combustion capture applications or to pre-heat the feed-water in the boiler (Witkowski and Majkut, 2012).

In practice, the inlet temperature in each stage is maintained between 35 and 38 ^{o}C, and 110 bar is the minimum discharge pressure to ensure the mixtures are above their critical pressure (Notebook, 2011). Eight or ten-stage designs are particularly sensitive to the two-phase region due to the margin between the two-phase condition, and the compressor stage discharge pressure is in or around the critical point and is somewhat unpredictable depending on the impurities present (Babcock, 2009).

Due to the compression in every stage being nearly adiabatic, there is an incremental increase of outlet temperature in CO_2 compression. Thus, the energy consumption of the system is increased. Implementation of the inter-stage cooling can make the process approach isothermality, which can decrease the power consumption of the compressor (Duan et al., 2013). Existing CO_2 compressors are expensive due to the overall pressure ratio being high and require stainless steel construction to accommodate CO_2 containing water (Witkowski et al., 2013). This compression system can be optimized for each stage due to lower volume and higher pressure at each progressive stage. It is possible to go to different speeds in each stage, so that very high rpm values about 50,000 rpm can be achieved.

Figure 3.5 shows the schematic diagram of an option A with inter-stage cooling by recycling the cooling water.

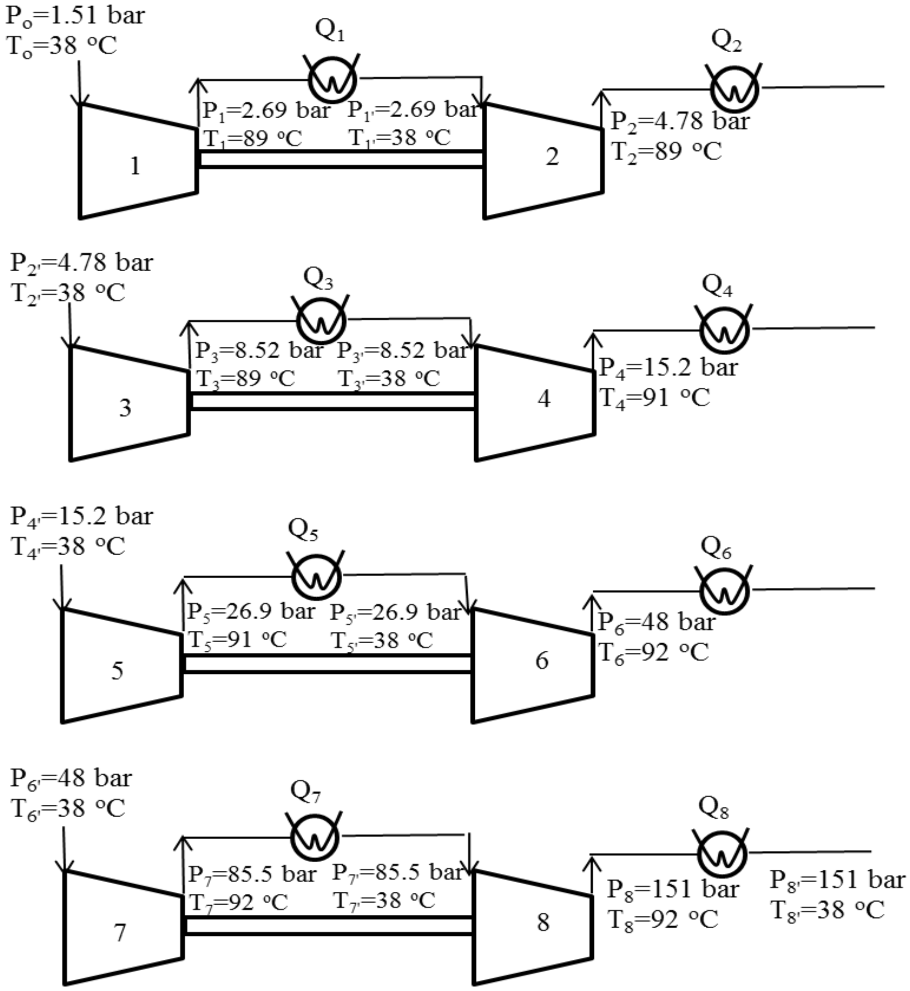

Figure 3.5: Schematic diagram of the compression option A for pure CO_2 stream (adapted from Witkowski and Majkut (2012)).

In the present study, *ca.* 75 % of efficiency is assumed for each compression stage. The CO_2 stream is brought to its final pressure through compression sections intercooled to 38 °C from the compression discharge temperature of *ca.* 90 °C. Based on the study by Witkowski and Majkut (2012), *ca.* 21 % of power savings could be achieved using option A as compared to an in-line centrifugal compression system. In the case of pre-combustion and oxy-fuel mixtures, only four stages of compression system are applied to compress the streams from 15 bar inlet pressure to 151 bar final pressures. The inlet pressure for each stream is chosen depending on the separation technology employed for the system (Besong et al., 2013).

3.3.2 Option B: Advanced Supersonic Shockwave Compression

Option B, Advanced Supersonic Shockwave Compression is uniquely suited for compression of large volumes of CO_2, offering higher compression efficiency of more than 80 % (Kidd and Miller, 2012). This compression option uses high pressure ratios *ca.* 10-12:1 per stage and has a more compact design and lower capital cost as compared to traditional centrifugal compression (option A). It is expected that using one or two stages of supersonic compression, that a compressor energy system will do the same work as option A (Kidd and Miller, 2011). A rotating disk in this compressor will operate at high peripheral speeds, producing air velocities above the speed of sound and creating shock waves that efficiently compress the CO_2. However, because of the high compression ratio applied, even using better performance of the compressor strategy, the power consumption is still tremendous (Duan et al., 2013). This option is a viable alternative to refrigeration, liquefaction and liquid pumping, while avoiding the cost and complexities of the refrigeration plant (Kidd and Miller, 2012). As an additional benefit, it provides the high discharge temperature of *ca.* 279 ^{o}C, which can be made useful, e.g. pre-heat the boiler feed-water or re-generate amine solutions in post-combustion capture applications (Witkowski and Majkut, 2012).

Figure 3.6 shows the schematic illustration of the option B used in this study.

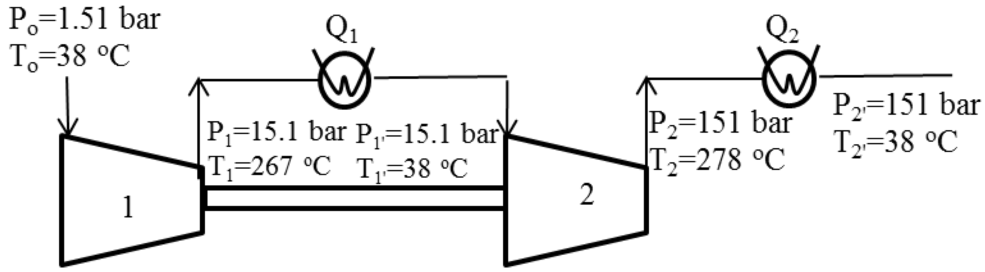

Figure 3.6: Schematic illustration of the industrial compression option B for pure CO_2 stream (adapted from Witkowski and Majkut (2012)).

The compression process of CO_2 begins at an initial pressure of 1.51 bar and continues in the first section at the low pressure (LP) compressor to a pressure of 15.1 bar. The gas is then cooled to 38 ^{o}C and is further compressed in the last section of a high pressure (HP) compressor to a pressure of 151 bar in supercritical condition.

However, in the case of pre-combustion and oxy-fuel mixtures with 15 bar inlet pressure, they are compressed in a single LP compression system to the final pressure.

3.3.3 Option C: Multistage compression combined with subcritical liquefaction and pumping

In this option C, the pump is used at an intermediate pressure rather than a compressor to bring the dense phase to final conditions suitable for pipeline transportation. The underlying premise of the liquefaction approach is that liquid pumps require significantly less power to raise pressure and are considerably less expensive than gas compressors (Duan et al., 2013). Depending on the cooling water temperature, using pumps to build up the fluid pressure from 65 to 150 bar allows a saving of *ca.* 10-15 % of the power spent in conventional gas-phase compression (Holloway and Akai, 2006). The analysis by Witkowski and Majkut (2012) showed that compared with the conventional multistage compression process (option A), option C allowed reduction in the compression power requirement by *ca.* 20.4 %.

Figure 3.7 shows the schematic diagram of the multistage compression integrated with the pumping system.

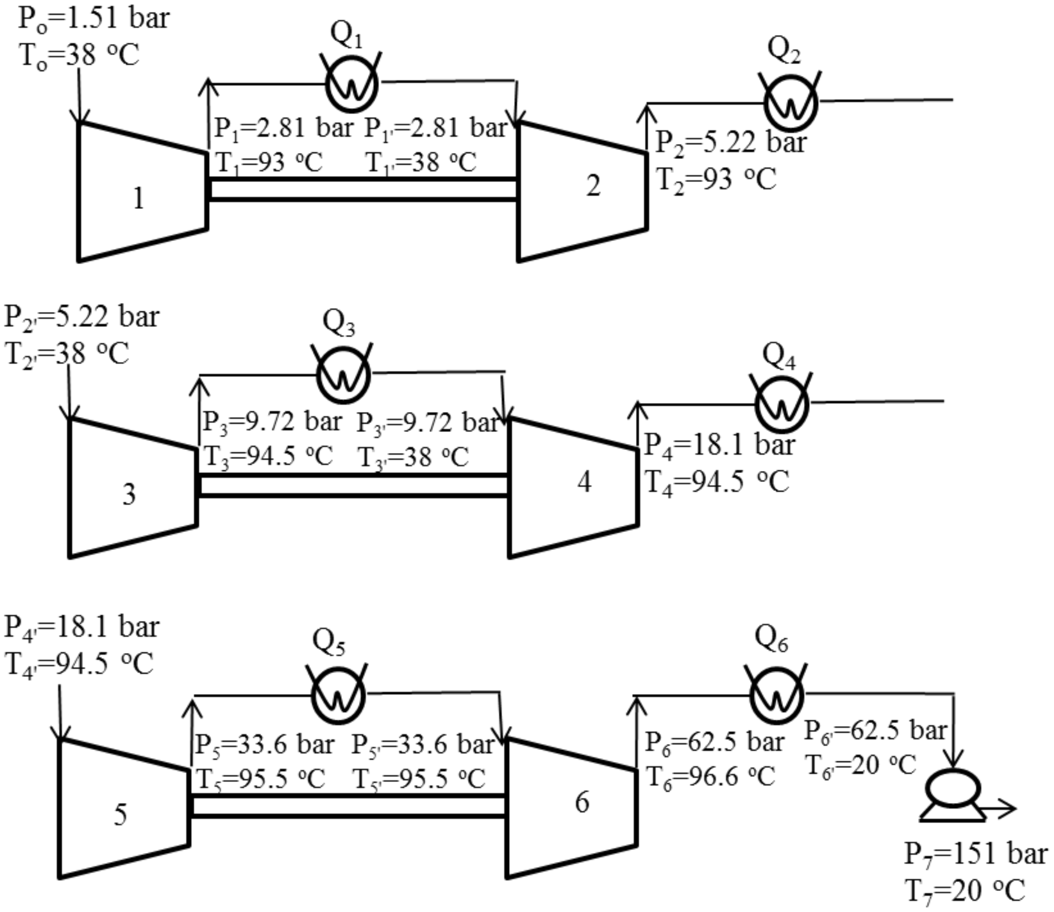

Figure 3.7: Schematic diagram of the compression option C for pure CO_2 (adapted from Witkowski and Majkut (2012)).

CO_2 is converted into liquid at lower pressure using a method of combining the multi-stage compression and lower temperature cooling. Then, the liquefied CO_2 is compressed into a specified pressure using a pump. In this study, six stages of compression are used to bring the pure CO_2 gas to a subcritical pressure of 62.54 bar, while for pre-combustion and oxy-fuel mixtures, three stages of compression are employed.

Liquefaction of CO_2 at subcritical pressure can maximise the contributions of the low-energy intensive pump (Pei et al., 2014). However, requiring a large amount of refrigeration energy for liquefaction purposes is the main drawback in this compression strategy (Duan et al., 2013, Witkowski et al., 2013).

3.3.4 Option D: Multistage compression combined with supercritical liquefaction and pumping

In this compression option, liquefaction of the CO_2 stream is done at pressures slightly above the critical pressure, assuring the minimisation of the energy consumption of the compression system (Witkowski and Majkut, 2012, Pei et al., 2014). Based on the study by Witkowski and Majkut (2012), *ca.* 14.6 % of power reduction for compression of pure CO_2 is reported when using a multistage compression combined with supercritical liquefaction and subsequent pumping, as compared to the conventional multistage compression option (option A). In this option D as depicted in figure 3.8, CO_2 is brought to just above its critical pressure through seven compression sections intercooled to 38 ^{o}C by water at ambient conditions.

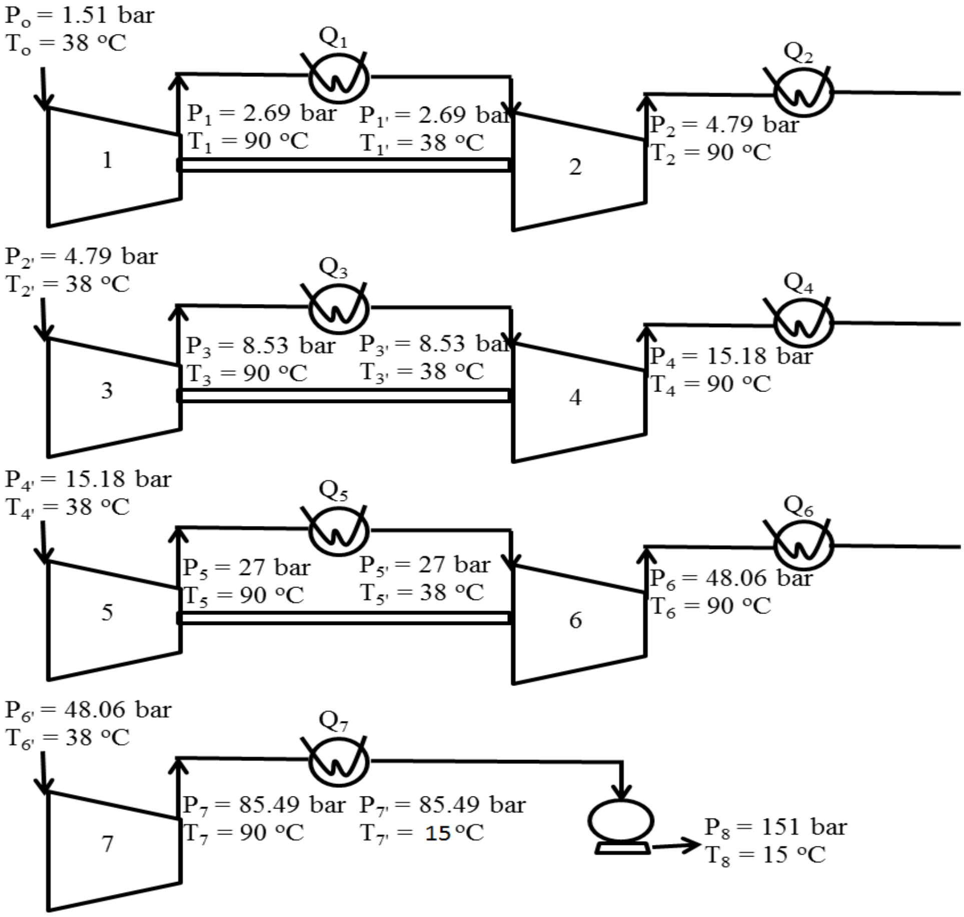

Figure 3.8: Schematic diagram of the compression option D for pure CO_2 (adapted from Witkowski and Majkut (2012)).

Subsequent cooling results in the liquefaction of the CO_2 at the compressor outlet pressure of 85.49 bar, after which a pump is used to bring the dense fluid to the final pressure.

3.4 Methodology: Thermodynamic analysis

In the present study, a thermodynamic analysis method is developed and applied to determine the thermodynamic state of the CO_2 stream and to quantify the compression power consumption for each step of a multistage compression process. The model accounts for isentropic efficiencies of compression/pumping stages and thermal efficiencies of heat exchange in isobaric intercoolers.

In particular, the total power required in the *N*-stage compression/pumping is calculated as:

$$W_{comp} = \sum_{i=1}^{N} \frac{G}{\eta_{comp,i}} \int_{P_i^{in}}^{P_i^{out}} \left(\frac{dp}{\rho} \right)_s \qquad 3.1$$

where, G and ρ are the mass flow rate and the density of CO_2 stream, respectively, while p_i^{in}, p_i^{out} and $\eta_{comp,i}$ are respectively the inlet and outlet pressures and isentropic efficiency of the $i-th$ compression stage. The subscript s denotes isentropic compression.

Using the first law of thermodynamics, $dh = Tds + \frac{dp}{\rho}$ and assuming isentropic compression, equation 3.1 may be written as:

$$W_{comp} = G \sum_{i=1}^{N} \frac{1}{\eta_{comp,i}} \left(h_i^{out} - h_i^{in} \right) \qquad 3.2$$

where h_i^{in} and h_i^{out} are enthalpies of the stream at the suction (*in*) and discharge (*out*) of the $i-th$ compression stage.

The total cooling duty associated with removing the heat of compression and possibly liquefying the CO_2 stream is given by Duan et al. (2013):

$$Q_{cool} = G\sum_{i=2}^{N}\left(h_{i-1}^{out} - h_{i}^{in}\right) \qquad 3.3$$

In the present study, the compression power and cooling duty are calculated as specific values per tonne of CO2 captured, as commonly considered when estimating 'costs of CO2 avoided' (McCoy and Rubin, 2008). The corresponding specific compression power and cooling duty are defined as:

$$w_{comp} = \frac{W_{comp}}{G_{CO_2}} = \frac{1}{\varphi_{CO_2}}\frac{M_m}{M_{CO_2}}\sum_{i=1}^{N}\frac{1}{\eta_{comp,i}}\left(h_{i}^{out} - h_{i}^{in}\right) \qquad 3.4$$

$$q_{cool} = \frac{Q_{cool}}{G_{CO_2}} = \frac{1}{\varphi_{CO_2}}\frac{M_m}{M_{CO_2}}\sum_{i=2}^{N}\left(h_{i-1}^{out} - h_{i}^{in}\right) \qquad 3.5$$

where G_{CO_2} and φ_{CO_2} are respectively the mass flow rate and mole fraction of CO2 component in a mixture, while M_m and M_{CO_2} are molecular weights of the mixture and CO2, respectively.

While in previous studies, the power demand for inter-stage cooling was generally assumed to be small with the demand for liquefaction characterised in terms of the cooling duty (Witkowski et al., 2013, Posch and Haider, 2012), the present analysis uses a simple and effective thermodynamic model based on Carnot refrigeration cycle for estimation of the power demand for cooling/liquefaction of the CO2 stream. In this model, the CO2 cooling power demand is associated with the work spent in an ideal compression refrigeration cycle when moving the heat from a coolant evaporation temperature, T_{ev} to a condensation temperature, T_{cond} (Jobson, 2014):

$$w_{cool} = \frac{q_{cool}}{\eta_{cool}}\left(\frac{T_{cond} - T_{ev}}{T_{ev}}\right) \qquad 3.6$$

where η_{cool} is the efficiency of refrigeration process. In the present study, the coolant evaporation temperature, T_{ev} is set to be 5 ^{o}C less than the CO2 stream cooling temperature, while the condensation temperature, T_{cond}, is assumed to be 38 ^{o}C. This model, advantageously, does not involve specification of the type of refrigerant, hence enabling the comparison of the cooling and liquefaction power consumption for various multistage compression strategies.

Using equations 3.1 to 3.5 require knowledge of the fluid thermodynamic properties of CO_2 mixtures, namely enthalpies, which can be calculated using dedicated models as described in the next section. The integral in equation 3.1 defines the compression work done on the fluid which is valid irrespective of the CO_2 mixture phase state, and hence can be applied to evaluate compression work for the gas and pumping works for the liquid. This integral is evaluated numerically using a 15-point Gauss-Kronrod quadrature rule in QUADPACK library (Piessens, 1983).

3.5 Properties of CO_2 mixtures with impurities

In order to evaluate the enthalpies in equations 3.2-3.5, Peng-Robinson Equation of State (PR EOS) (Peng and Robinson, 1976) is used in the present study as one of the most computationally efficient equations for the modelling of the vapour-liquid behaviour of CO_2 and its mixtures with various components (Seevam et al., 2008, Zhao and Li, 2014, Li and Yan, 2009). In particular, the fluid density, ρ, is calculated from the PR EOS:

$$P = \frac{RT\rho}{1-\rho b_c} - \frac{a_c \alpha \rho^2}{1+2b_c\rho - \rho^2 (b_c)^2} \qquad 3.7$$

where P and T are respectively the pressure and temperature, while a_c, α and b_c are the model parameters which are defined as:

$$a_c = 0.45724 \frac{R^2 T_c^2}{P_c^2} \qquad 3.8$$

$$b_c = 0.07780 \frac{RT_c}{P_c} \qquad 3.9$$

$$\alpha = \left(1+\kappa\left(\frac{T}{T_c}\right)^{0.5}\right)^2 \qquad 3.10$$

$$\kappa = 0.37464 + 1.5422\omega - 0.26922\omega^2 \qquad 3.11$$

Here P_c and T_c are respectively the fluid critical pressure and temperature, and ω is the fluid acentric factor.

In the case of a mixture, a_c, α and b_c are respectively evaluated using the appropriate linear mixing rules and combining rules (Sandler, 2007, Wei and Sadus, 2000, Zhao and Li, 2014):

$$a_c\alpha = \sum_{i=1}^{N}\sum_{j=1}^{N} y_i y_j \left(1-\delta_{ij}\right)\sqrt{\left(a_c\alpha\right)_i\left(a_c\alpha\right)_j} \qquad 3.12$$

$$b_c = \sum_{i=1}^{N} y_i b_{ci} \qquad 3.13$$

where $\left(a_c\alpha\right)_i$, $\left(a_c\alpha\right)_j$ and b_{ci} are the PR EOS parameters for the $i-th$ and $j-th$ components, while δ_{ij} is the parameter characterising interaction between components i and j in the mixture. The δ_{ij} is estimated using correlations proposed by Nishiumi and Arai (1988) and Valderrama and Reyes (1983) for binary mixtures involving hydrocarbons, inert gas, polar components and hydrogen. Table 3.4 lists the binary interaction parameter δ_{ij} calculated for the CO_2 and various impurities relevant to the study.

Table 3.4: Values of the interaction parameter, δ_{ij} for the various binary mixtures (Valderrama and Reyes, 1983, Nishiumi and Arai, 1988).

	CO_2	N_2	H_2	O_2	CO	H_2S	SO_2	H_2O	CH_4	Ar
CO_2	0	-0.02	0.34	0	0	0.11	0	0	0.11	0
N_2	-0.02	0	0.05	0	0	0.15	0	0	0.04	0
H_2	0.34	0.05	0	0	0.07	0.14	0.33	0.28	-0.02	-0.05
O_2	0	0	0	0	0	0	0	0	0	0
CO	0	0	0.07	0	0	0	0	0	0	0
H_2S	0.11	0.15	0.14	0	0	0	0	0	0.08	0
SO_2	0	0	0.33	0	0	0	0	0	0	0
H_2O	0	0	0.28	0	0	0	0	0	0.51	0
CH_4	0.11	0.04	-0.02	0	0	0.08	0	0.51	0	0
Ar	0	0	-0.05	0	0	0	0	0	0	0

In particular, to calculate the fluid enthalpy, *h* and temperature at a given pressure and entropy, *s*, pressure-entropy flash calculations are performed by solving simultaneously the following two equations (Sandler, 2007):

$$h = h^{IG} + RT(Z-1) + \frac{T\left(\frac{d(a_c\alpha)}{dT}\right) - a_c\alpha}{2\sqrt{2b_c}} \ln\left[\frac{ZRT + \left(1+\sqrt{2}\right)Pb_c}{ZRT + \left(1-\sqrt{2}\right)Pb_c}\right] \quad 3.14$$

$$s = s^{IG} + R\ln\left(Z - \frac{pb_c}{RT}\right) + \frac{1}{2\sqrt{2b_c}}\frac{da_c}{dt}\ln\left[\frac{ZRT + \left(1+\sqrt{2}\right)Pb_c}{ZRT + \left(1-\sqrt{2}\right)Pb_c}\right] \quad 3.15$$

where h^{IG} and s^{IG} are respectively the fluid enthalpy and entropy in the ideal gas state. While $z = \frac{p}{RT}$ is the fluid compressibility. The derivative $\frac{d(a_c\alpha)}{dT}$ is defined as:

$$\frac{d(a_c\alpha)}{dT} = -0.45724\frac{R^2T_c^2}{P_c}\kappa\sqrt{\frac{\alpha}{TT_c}}. \quad 3.16$$

In the present study, the above properties (equations 3.14 and 3.15) are calculated using PR EOS implemented in REFPROP v.9.1 (Lemmon and Huber, 2010).

3.6 Results and Discussions: Multistage compression of CO_2 streams containing impurities

As mentioned earlier in section 3.1, the general objective of the study is to evaluate the previously recommended compression options by Witkowski and Majkut (2012) for the case of pre-combustion and oxy-fuel streams. As the cost of compression much depends on the power consumption, the primary objective is to compare the power demands for compression of pure CO_2 with pre-combustion and oxy-fuel CO_2 streams. To make such a comparison, the thermodynamic analysis method as described in sections 3.4 and 3.5 is used where the power demand for compression is calculated using the rigorous equations accounting for real fluid behaviour of CO_2 and its mixtures with impurities.

During multistage compression different fluid phases (gas or liquid) at certain stages of compression are encountered. Impurities can affect the vapour liquid equilibrium of CO_2. As such, another objective of this study is to examine how the difference in vapour-liquid phase equilibria of pure CO_2 with pre-combustion and oxy-fuel mixtures would impact the multistage compression. Here the feasibility of adapting the compression options recommended for pure CO_2 to impure CO_2 streams captured in pre-combustion and oxy-fuel combustion processes is assessed. The study is performed for a given number and pressure ratios of the compression stages. In particular, given that pure CO_2 (analogous to post-combustion capture and oxy-fuel distillation streams) and impure pre-combustion and oxy-fuel streams enter the final compression at different pressure levels (1.51 bar for pure CO_2 and *ca.* 15-30 bar in case of pre-combustion and oxy-fuel streams), the pure CO_2 compression strategy is adapted only for the last few stages of compression, starting from one compression stage where the pressure is close to the pre-combustion and oxy-fuel pressure levels. Suitable temperature conditions for the multi-stage compression of pre-combustion and oxy-fuel streams are then identified and compared to those for pure CO_2.

This section is focused on the thermodynamic analysis of the impact of impurities in the CO_2 streams originating from pre-combustion and oxy-fuel capture technologies (table 3.1) on the power consumed in multistage compression options described in section 3.3.

Firstly, the operating conditions of the pure CO_2, pre-combustion and the oxy-fuel streams and thermodynamic paths for the compression options are set to match the fluid phase requirements for the processes of compression, liquefaction and pumping. The operating parameters are set depending on the real application in the process industry. This is followed by the application of the equations in sections 3.4 and 3.5 to calculate the power requirements for compression and intercooler as well as intercooling duty of pure and impure CO_2 streams.

In the present study, in order to determine the power requirements in various compression strategies, the basic parameters of compression processes are set the same for all the compression options based on recommendations from the previous study performed by Witkowski and Majkut (2012) for pure CO_2. In particular, the study assumes compression of the CO_2 stream to a dense phase fluid at 151 bar pressure, as required for pipeline transportation and geological storage. Furthermore, the CO_2 mass flow rate is set to 156.4 kg/s, while the intermediate cooling temperature is set to 38 ^oC. Following the study by Witkowski and Majkut (2012), the compressor isentropic efficiency is set to 0.75 for multistage centrifugal compressor (option A), 0.85 for the shock wave compression (option B) and 0.8 for the compression combined with pumping (options C and D), while the cooling system efficiency is set to 0.6 (Jobson, 2014). The pressure and temperature at the inlet of the compressor depend on the parameters of the stream coming from separation/purification facilities. Thus, for pure CO_2 (approximating post-combustion or oxy-fuel distillation level of CO_2 purity), following Witkowski and Majkut (2012) and Witkowski et al. (2013), the pressure and temperature at the inlet of the compressor are set to 1.51 bar and 38 ^oC, while in the case of the pre-combustion mixture, the inlet properties are set to 15 bar, 38 ^oC depending on the purification technology applied.

The dehumidified raw oxy-fuel CO_2 stream has a purity of around 75-85 % v/v and is produced at *ca.* 15 bar pressure, while further purification to *ca.* 96.70 % v/v CO_2 can be performed with combined compression and flash-distillation separation at pressures ranging from *ca.* 15 to 30 bar and temperatures ranging from -24 to -55 °C. Although the change in CO_2 purity level from 85 to 96.70 % v/v will affect the properties of the CO_2 stream, this would only affect relatively a small portion of the gas-phase compression from ambient pressure to *ca.* 30 bar, without any significant impact on the rest of the compression to 151 bar pressure level. Therefore, in the present study, 15 bar is considered as the starting pressure from which pre-combustion (98.07 % v/v) and oxy-fuel CO_2 streams of 85 and 96.70 % v/v purity are compressed for pipeline transport and subsequent sequestration.

The rest of this section describes the adaptation of the various compression options to the pure and impure CO_2 streams. To illustrate these changes to the compression schemes, pressure-enthalpy diagrams in figures 3.9 to 3.12 are plotted showing the comparison of compression paths for options A-D from table 3.3 for pure CO_2 and CO_2 streams from pre-combustion and oxy-fuel capture technologies, respectively. Phase envelopes of both pure CO_2 and CO_2 streams with different amounts of impure components are calculated with the Reference Fluid Thermodynamic and Transport Properties database program REFPROP (Lemmon and Huber, 2010) by employing PR EoS for calculation of CO_2 streams properties.

3.6.1 Multistage compression of an impure CO_2 stream

Figure 3.9 illustrates the application of the compression option A to the pure CO_2 and impure CO_2 mixtures. The pathways 0 to 8' show the repeated compression and cooling down of the pure CO_2 stream performed at 1.51 bar, 38 ^oC initial conditions to 151 bar, 38 ^oC suitable for pipeline transportation (figure 3.9(a)).

With the compression in every stage being nearly adiabatic, this results in an increment of outlet temperature in CO_2 compression. Implementation of the inter-stage cooling can make the process approach isothermality, which can decrease the power consumption of the compressor. The inlet and outlet pressure conditions as well as pressure ratio are the most influential parameters in determining the number of compressor stages. In order to compress the pure CO_2 stream, the pressure ratio is applied at *ca.* 1.78 which results in the eight stages of compressor being used for this compression option. Processes 0-1, 1'-2, 2'-3, 3'-4, 4'-5, 5'-6, 6'-7 and 7'-8 are the adiabatic compression in compressors, and processes 1-1', 2-2', 3-3', 4-4', 5-5', 6-6', 7-7' and 8-8' are the inter-stage cooling system used to reduce the outlet temperature approximately between 90-95 ^oC from each compressor stage to 38 ^oC. At the first stage of the compressor, CO_2 gas from inlet 0 is compressed into state 1 before it flows through the cooler at point 1-1'. Then it flows through stage two at state 2 to increase the pressure. The process is repeated until the phase of CO_2 is changed to supercritical conditions at high pressure, above the critical pressure of approximately 151 bar. However, in the case of the pre-combustion and oxy-fuel mixtures, the compression and cooling down processes (pathways 0-4') as shown in figures 3.9(b)-(d) are somewhat different amongst each stream. The presence of impurities affects the enthalpy and the pattern of the pathways, especially at magnitude 3-3' indicating the phase changes from gas to supercritical conditions. In this case, the compression process for pre-combustion and oxy-fuel mixtures are started at *ca.* 15 bar with only four stages of compression applied.

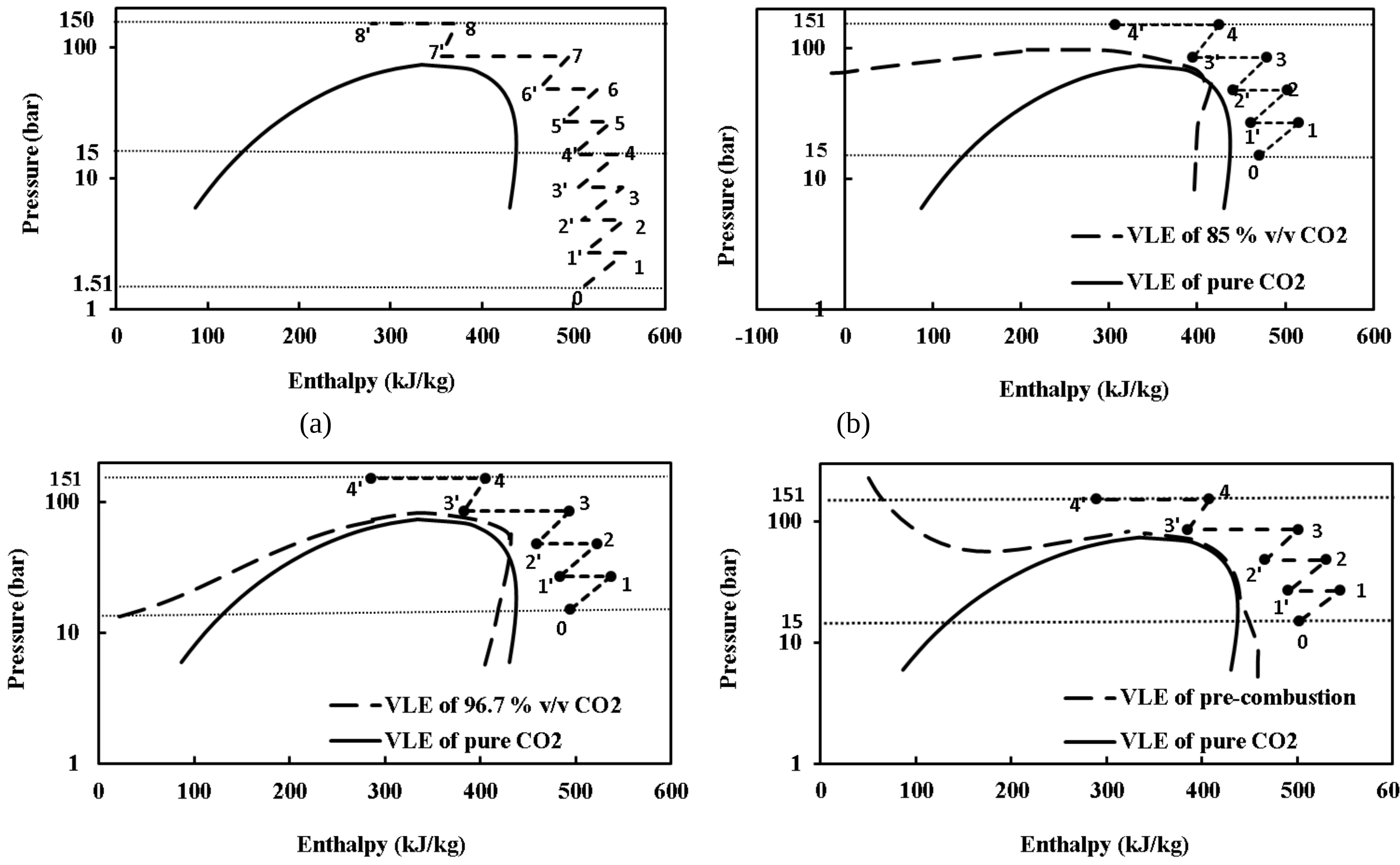

(a)

(b)

(c)

(d)

Figure 3.9: Phase envelope boundaries and thermodynamic paths for compression of pure CO_2 (a), 85 % v/v CO_2 purity (b), 96.70 % v/v CO_2 purity (c) from oxy-fuel captures and pre-combustion mixture (d) using compression option A (dashed lines).

The effect of impure components in the pre-combustion and oxy-fuel streams (figures 3.9(b)-(d)) lead to a change in the phase envelope boundary (solid line) with the lifted bubble and dew point lines (dash line) located at higher pressure and also reducing the supercritical region by influencing the tolerance limit of the transportation pressure.

Figure 3.10 illustrates the thermodynamic compression paths for option B, achieved using the advanced supersonic shockwave compression with a pressure ratio of 10 per stage. In the case of pure CO_2, the 2-stage compressor which involves Low Pressure (LP) and High Pressure (HP) stages is used to increase the pressure from 1.51 to 151 bar at discharge (figure 3.10(a)), while for the pre-combustion and oxy-fuel mixtures, the inlet pressures are 15 bar and hence only single stage compression is used as shown in figures 3.10(b)-(d).

Applying only the LP stage of compression option B to compress the pre-combustion and oxy-fuel mixtures is practically feasible in CCS applications which significantly reduce the total capital costs of the overall process (Baldwin and Williams, 2009). The intercooling system is applied to reduce the temperature after the compression from *ca.* 279 ^{o}C back down to 38 ^{o}C.

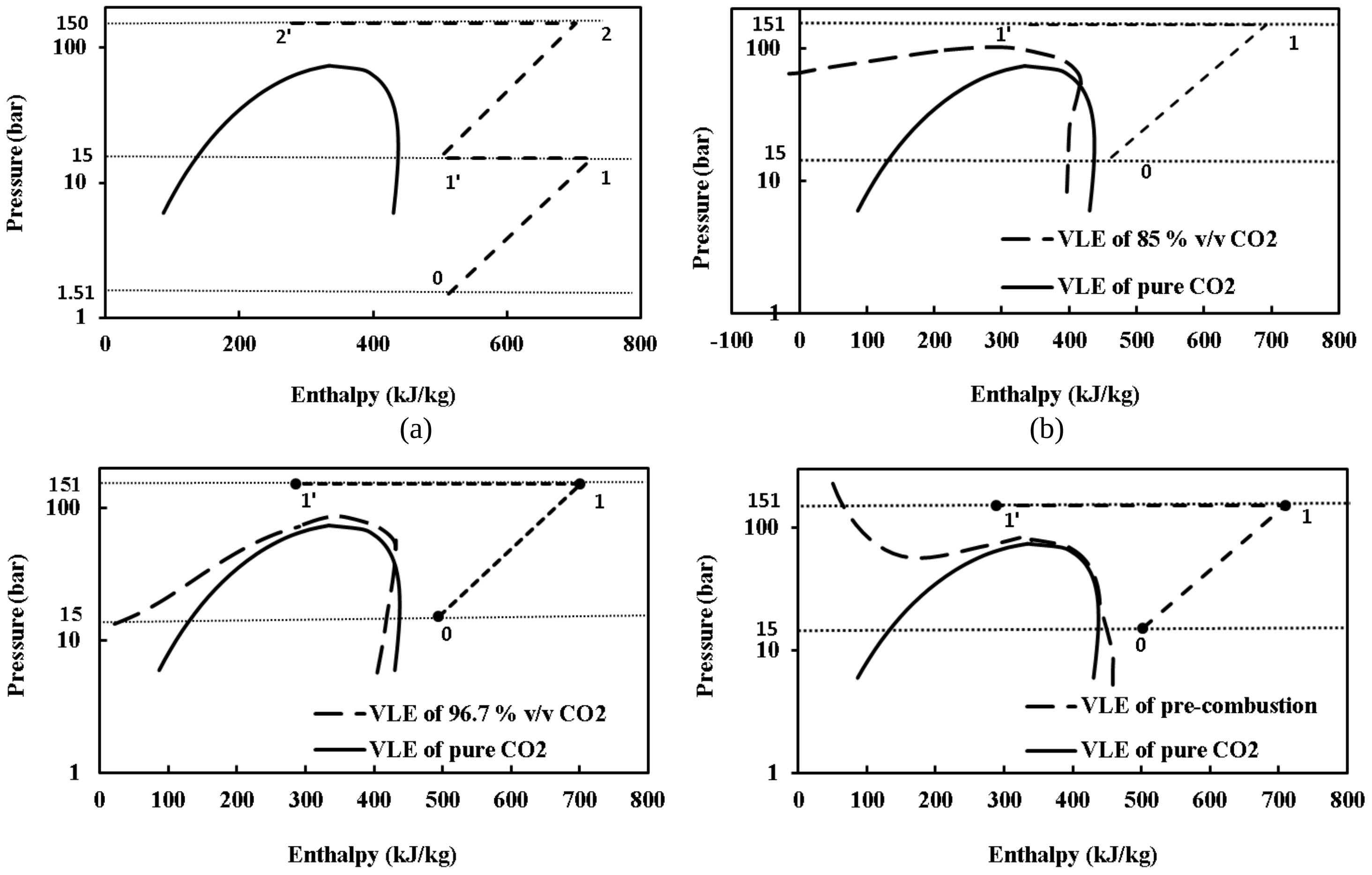

(a) (b)

(c) (d)

Figure 3.10: Phase envelope boundaries and thermodynamic paths for compression of pure CO_2 (a), 85 % v/v CO_2 purity (b), 96.70 % v/v CO_2 purity (c) from oxy-fuel captures and pre-combustion mixture (d) using compression option B (dashed lines).

In figure 3.11, the thermodynamic compression paths are shown in compression option C, which combines multistage compression with pumping following the liquefaction of CO_2 at subcritical pressures. In this option, the 6-stage and 3-stage compression processes are respectively adapted for pure CO_2 and the impure CO_2 streams to compress the fluid before liquefaction and pumping to the final pressure of 151 bar with the pressure ratio of *ca.* 1.86 applied. The final temperature for pure CO_2 at the outlet pumping station is *ca.* 23 ^{o}C while for impure CO_2 streams, the final temperatures are decreased with increasing impurities from 20 ^{o}C for pre-combustion carrying 98.07 % v/v purity, followed by 15 and -67 ^{o}C for 96.70 and 85 % v/v purity of CO_2, respectively.

As mentioned in section 3.3.3, the advantage of option C comes from the fact that using pumps is cheaper than operating compressors. However, in order to use this advantage, the liquefaction should be achieved at intermediate pressures below the discharge pressure of the compressor (151 bar) without a significant rise in the process cost. Thus, Witkowski and Majkut (2012) and Holloway and Akai (2006) have recommended liquefaction at a pressure around 62.53 bar, which corresponds to the bubble point temperature of 23 ^{o}C for pure CO_2. In the case of oxy-fuel and pre-combustion streams with a purity of 96.70 and 98.07 % v/v, the bubble point temperatures and pressures are respectively at *ca.* 15 ^{o}C, 62.53 bar and 20 ^{o}C, 62.53 bar.

In comparison, the oxy-fuel mixture with 85 % v/v of pure CO_2 has the bubble point temperature of *ca.* -67 ^{o}C which is much lower than the other CO_2 streams. As such, liquefaction of this CO_2 stream at 62.53 bar using room-temperature utility streams is not practically feasible and would require using refrigeration systems.

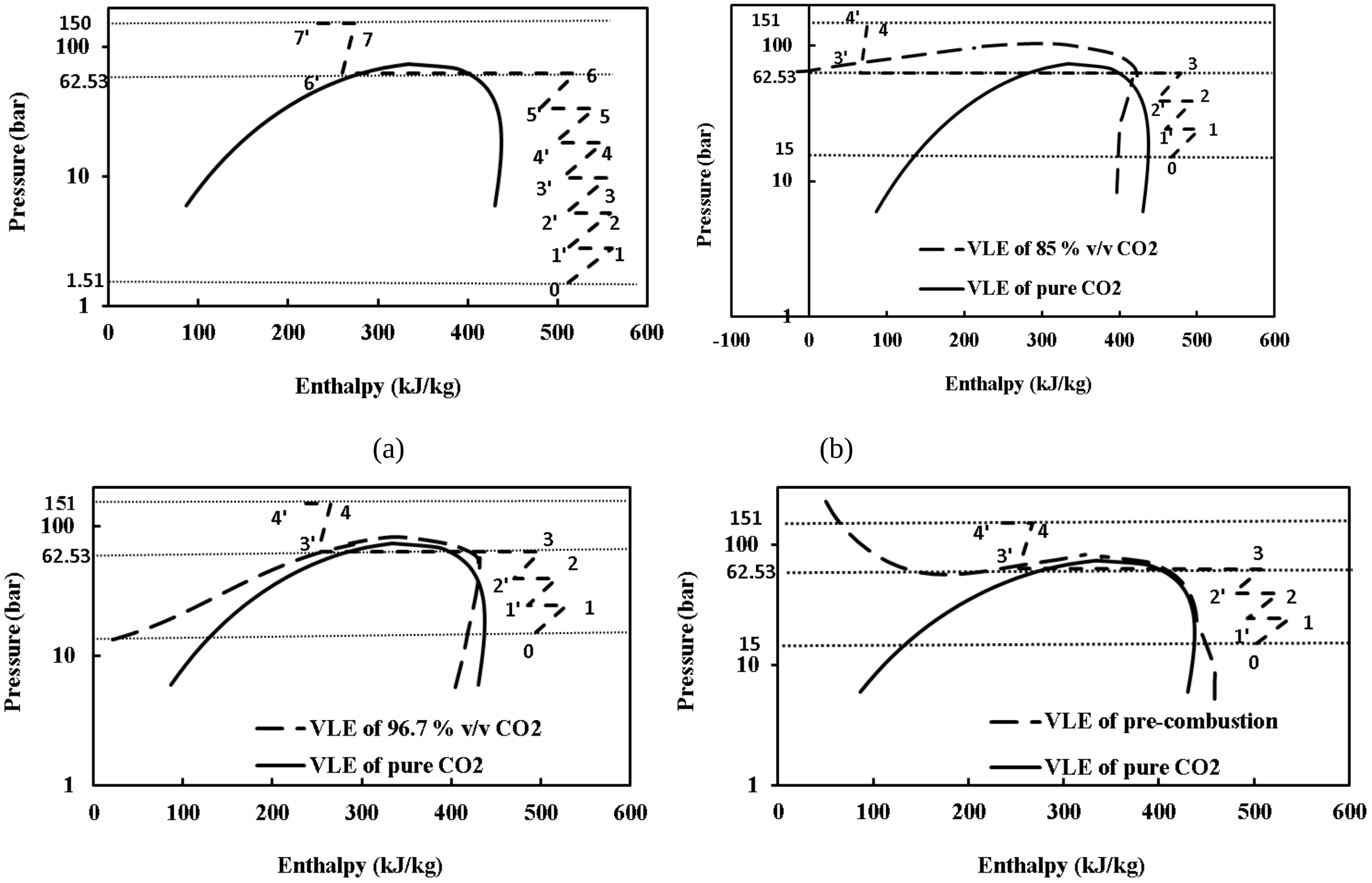

(a) (b)

(c) (d)

Figure 3.11: Phase envelope boundaries and thermodynamic paths for compression of pure CO_2 (a), 85 % v/v CO_2 purity (b), 96.70 % v/v CO_2 purity (c) from oxy-fuel capture and pre-combustion mixtures (d) using compression option C (dashed lines).

The presence of impurities significantly affects the properties compared to pure CO_2 with changes in the critical pressure and temperature of the stream. In such cases, the liquefaction would require using cryogenic coolants, increasing the cost of the whole process.

Figure 3.12 shows the thermodynamic paths in the case of compression option D, where 7-stage of compression are combined with supercritical liquefaction and pumping to compress the pure CO_2. In the case of the oxy-fuel mixture with 85 % v/v CO_2 purity (figure 3.12(b)), four stages of compression are used, while for 96.70 and 98.07 % v/v purity, three stages of compression are respectively adapted before pumping for supercritical liquefaction to discharge conditions as shown in figures 3.12(c) and (d). The supercritical liquefaction pressures are chosen to be just above the maximum saturation pressure of the streams, i.e. 85.49 bar for pure CO_2, 96.70 and 98.07 % v/v purity of CO_2 streams and 115 bar for the 85 % v/v purity from oxy-fuel mixture. The corresponding 'liquefaction' temperatures are *ca.* 15 ^oC for pure CO_2 and *ca.* 10 ^oC for 96.70 and 98.07 % v/v purity of the CO_2 streams, respectively, while *ca.* 5 ^oC for the oxy-fuel mixture with 85 % v/v purity. As can be seen in figure 3.12(a), the pressure of pure CO_2 is increased slightly above the critical pressure (73.77 bar) using seven stages of compression with pressure ratio of *ca.* 1.78 applied before liquefaction using water as a cooling medium. Meanwhile, 3-stage compression is adapted for both 96.70 and 98.07 % v/v CO_2 purity. In comparison, the oxy-fuel mixture with 85 % v/v purity is compressed to the supercritical liquefaction pressure of 115 bar through four compression stages followed by liquefaction and pumping to 151 bar for pipeline transportation.

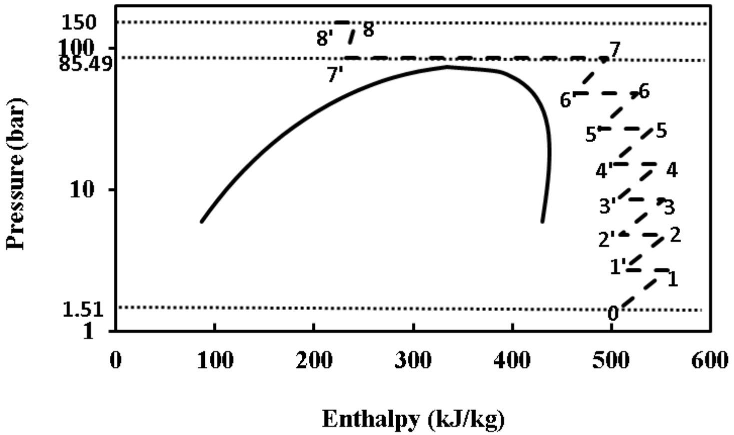
150
100
85.49
10
1.51
1
Pressure (bar)
Enthalpy (kJ/kg)
0
100
200
300
400
500
600
8'
8
7'
7
6
6
5'
5
4'
4
3'
3
2'
2
1'
1
0

(a)

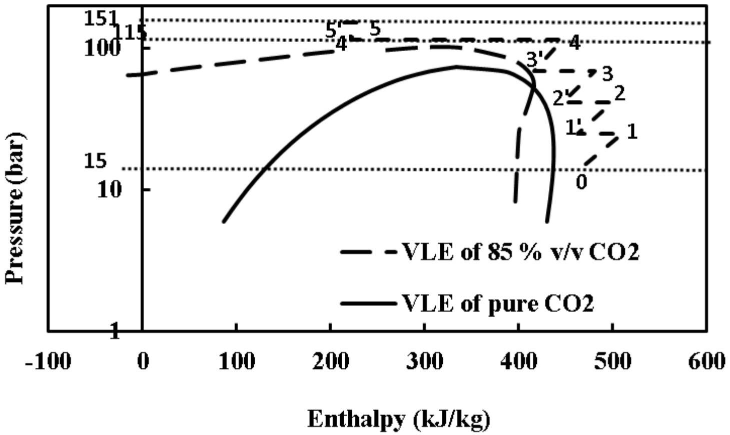
151
115
100
15
10
1
Pressure (bar)
Enthalpy (kJ/kg)
-100
0
100
200
300
400
500
600
5'
5
4'
4
3'
3
2'
2
1'
1
0
VLE of 85 % v/v CO2
VLE of pure CO2

(b)

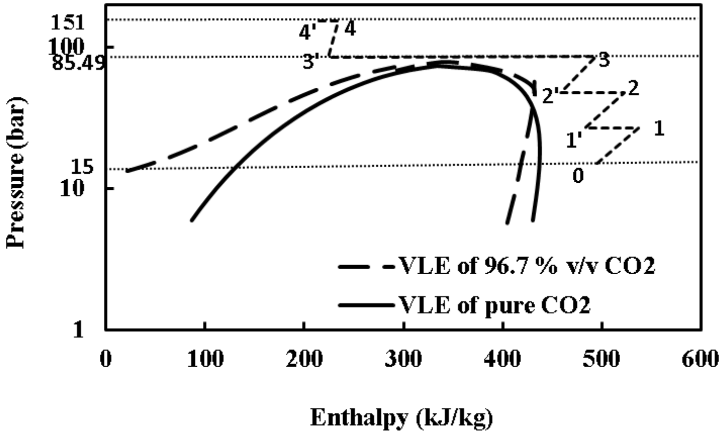
151
100
85.49
15
10
1
Pressure (bar)
Enthalpy (kJ/kg)
0
100
200
300
400
500
600
4'
4
3'
3
2'
2
1'
1
0
VLE of 96.7 % v/v CO2
VLE of pure CO2

(c)

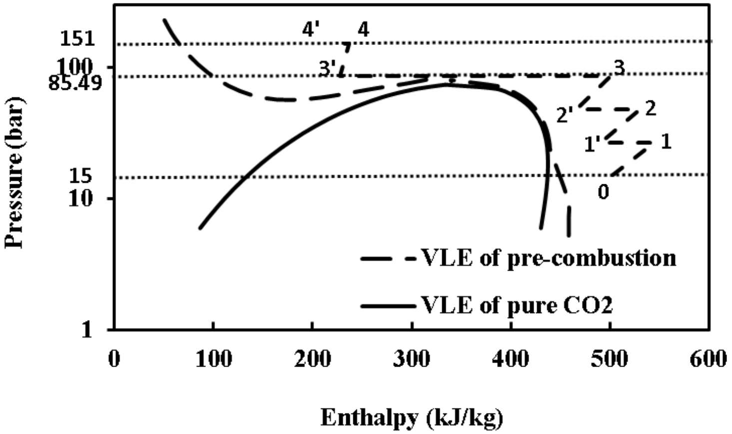
151
100
85.49
15
10
1
Pressure (bar)
Enthalpy (kJ/kg)
0
100
200
300
400
500
600
4'
4
3'
3
2'
2
1'
1
0
VLE of pre-combustion
VLE of pure CO2

(d)

Figure 3.12: Phase envelope boundaries and thermodynamic paths for compression of pure CO_2 (a), 85 % v/v CO_2 purity (b), 96.70 % v/v CO_2 purity (c) from oxy-fuel capture and pre-combustion mixtures (d) using compression option D (dashed lines).

3.6.2 Multistage compression power demands

Table 3.5 summarises the results of the calculation of the total power of compression and intercooling as well as cooling duty for 156.4 kg/s of pure CO_2 and impure CO_2 streams. The presented results are calculated using the equations in sections 3.4 and 3.5 for the multistage compression options A, B, C and D as listed in table 3.3. To enable comparison for streams originating at different initial pressures (1.51 bar for pure CO_2 and 15 bar in case of pre-combustion and oxy-fuel mixtures), the analysis is performed starting from 15 bar and 38 ^{o}C.

Table 3.5: Compression power, cooling duty and cooling power in multistage compression/intercooling of various CO_2 streams (table 3.1), evaluated for different compression options.

	CO_2	Compression technology options			
	(% v/v)	A	B	C	D
Compression power (kWh/tonne$_{CO2}$)					
Oxy-fuel:					
Raw dehumidified	85.00	51	64	36	40
Double flashing	96.70	42	55	32.5	35
Pre-combustion	98.07	41	54	32.5	34.5
Pure CO_2	100	39	53	32	34
Cooling duty (kWh/tonne$_{CO2}$)					
Oxy-fuel:					
Raw dehumidified	85.00	88.78	105	145	112
Double flashing	96.70	90.5	106	102	98
Pre-combustion	98.07	90.5	106	102	98
Pure CO_2	100	90.9	107	97	97
Cooling power (kWh/tonne$_{CO2}$)					
Oxy-fuel:					
Raw dehumidified	85.00	2.42	2.86	114.5	25.9
Double flashing	96.70	2.47	2.89	16.8	19.2
Pre-combustion	98.07	2.47	2.89	13.6	19.2
Pure CO_2	100	2.47	2.89	11.1	15.9

In figures 3.13(a), (b), (c) and (d), the data from table 3.5 are plotted, showing respectively the compression power, cooling duty, cooling power and total power consumption of compression power and cooling power of compression options A, B, C and D for pure CO_2 and impure CO_2 streams captured from different capture technologies employed.

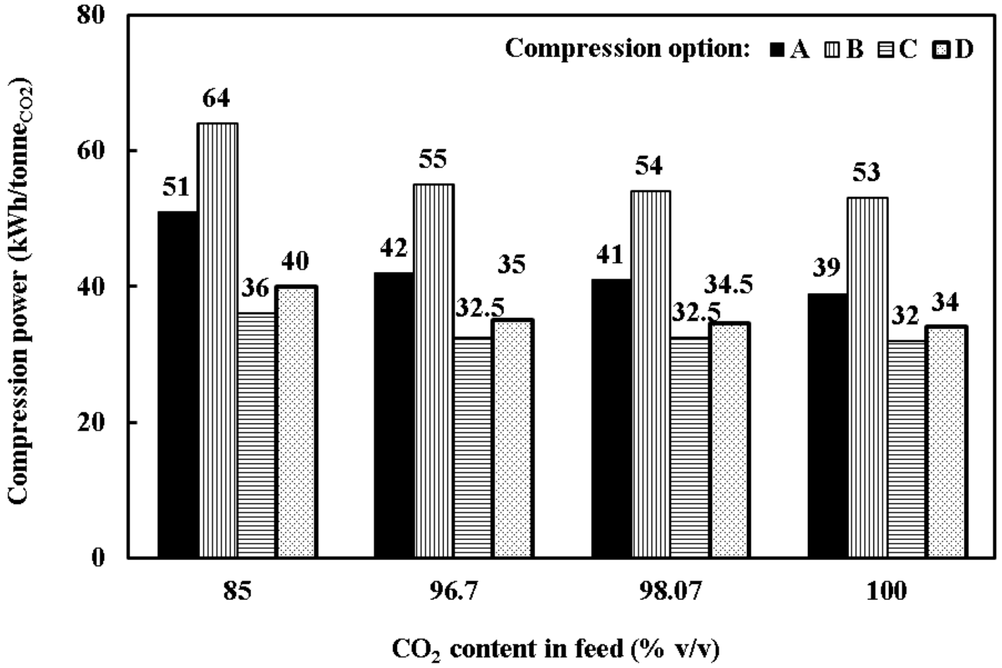

(a)

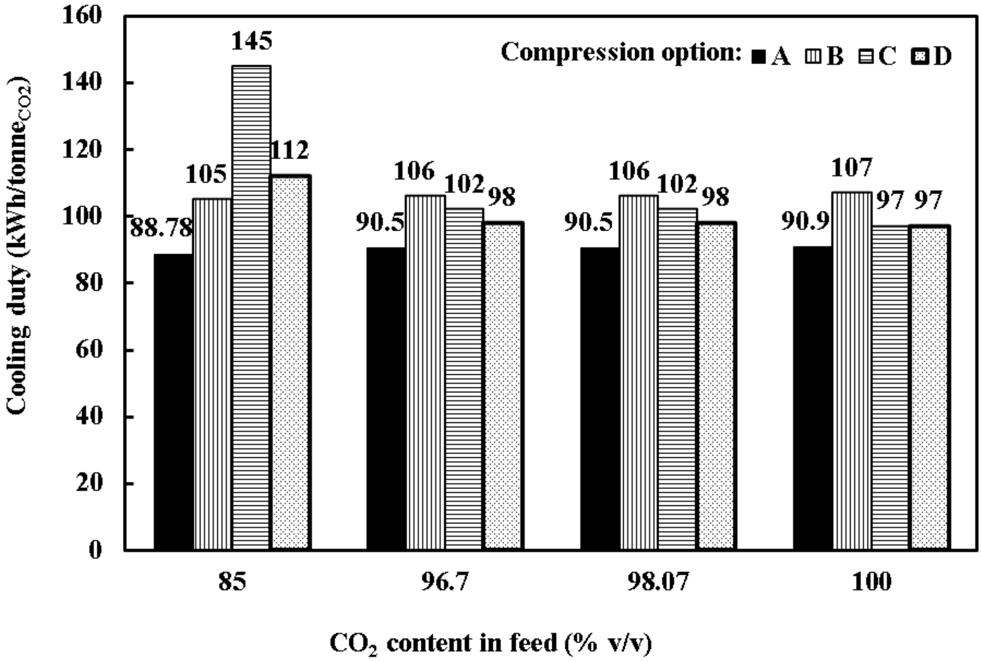

(b)

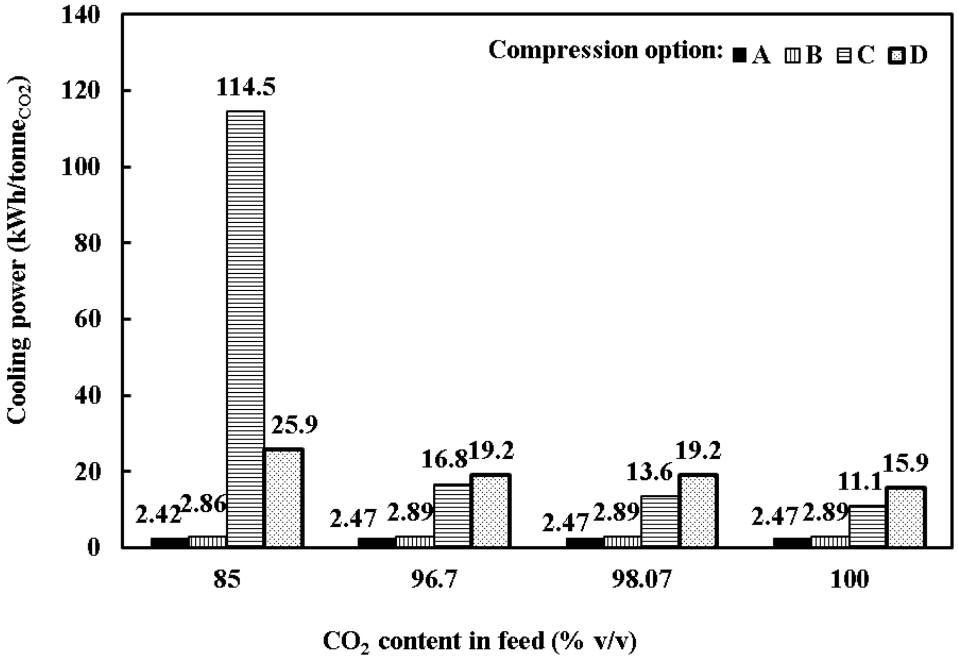

(c)

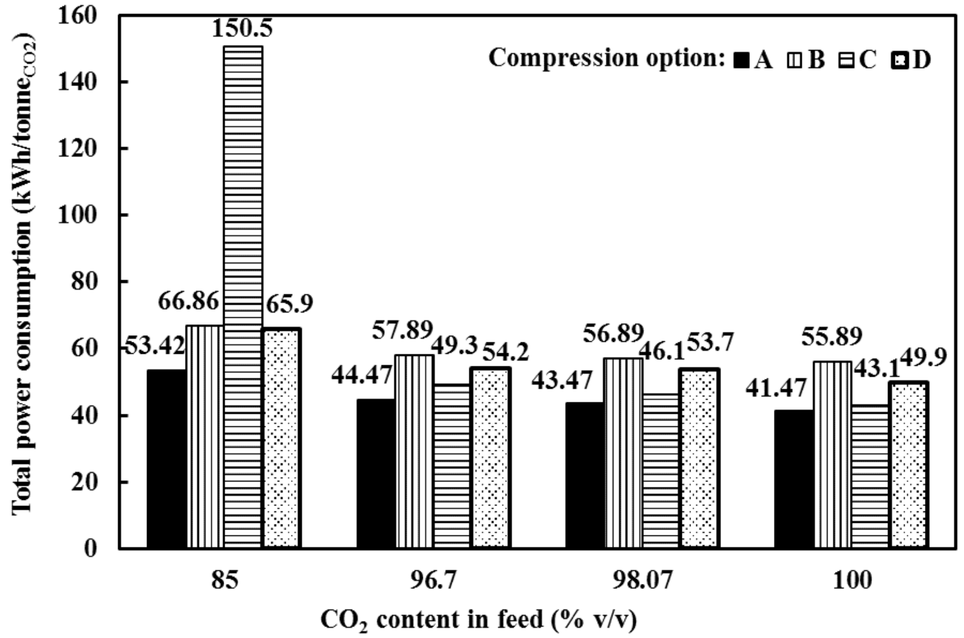

(d)

Figure 3.13: Compression power (a), cooling duty (b), cooling power (c) and (d) total power consumption (compression power and cooling power) of multistage compression options A, B, C and D (table 3.3) for pure CO_2 and the impure CO_2 mixtures (table 3.1).

As can be seen from the results illustrated in figures 3.13(a), (b) and (d), the presence of impurities in the CO_2 stream affects both the compression power demand and cooling duty for multistage compression systems. The energy requirements in the range of *ca.* 32-53 kWh/tonne$_{CO2}$ for the compression options adapted in this study for pure CO_2 stream at 15 bar initial pressures are in agreement with the previous studies by Walspurger and Dijk (2012), IEAGHG (2011) and Witkowski et al. (2013). The power demand for compression of pure CO_2 using supersonic compressors (option B) is estimated to be *ca.* 35 % higher than that for the centrifugal compression (option A). On the other hand using liquefaction and pumping (options C and D) reduces the compression power demands by *ca.* 18 and 13 % when compared to multistage centrifugal compressors (option A).

Also, the results in figure 3.13(a) show nearly equal power demands for compression of the double-flash 96.7 % v/v purity oxy-fuel and the 98.07 % v/v purity pre-combustion streams. This can be attributed to the fact that the pre-combustion CO_2 stream contains 1.5 % v/v of hydrogen (table 3.1), which is relatively small compared to 3.2 % v/v of volatiles (N_2, O_2 and Ar) found in oxy-fuel double-flash stream, but has stronger effect on the physical properties of the fluid, particularly the density and, hence, the compression power.

Remarkably, the results in figures 3.13(a) and (b) indicate that multistage compression is characterised by a large cooling duty. In particular, when using compression options A-D to compress CO_2 streams carrying less than *ca.* 5 % v/v of impurities, the inter-stage cooling duty is predicted to be *ca.* 2-3 times bigger than the compression power. This primarily can be attributed to non-ideal behaviour of the CO_2 fluid and significant decrease in the fluid enthalpy with pressure, impacting the compression power and cooling duty in equations 3.4 and 3.5.

In the case of raw dehumidified oxy-fuel stream of 85 % v/v purity, the cooling duty becomes particularly large, reaching *ca.* 145 kWh/tonne$_{CO2}$, which can be attributed to relatively low temperature (-62 ^{o}C) considered for liquefaction of the 85 % v/v purity oxy-fuel CO_2 stream. Possible strategies for removing such large amounts of heat from the CO_2 compression may include optimising the heat integration between the CO_2 compression and other processes in the CCS plant.

The relatively large cooling duty in comparison with the compression power can be primarily attributed to the fact that at pressures above *ca.* 15 bar the enthalpy of gas-phase CO_2 depends not only on temperature but becomes a strong function of pressure. As a result, the enthalpy increase in isentropic compression becomes less than the enthalpy decrease in the subsequent cooling to the original temperature. The latter can be illustrated by e.g. figure 3.10(a), where the enthalpy changes in the compression (1'-2) and cooling (2-2') processes can be compared directly. It is important to note that actual power demand for operating the cooling system is not equivalent to the cooling duty and may be significantly reduced by integrating the cooling system operation with other processes in the CCS capture and CO_2 emission plant.

Figure 3.13(c) shows the estimates of power consumptions for operation of the cooling system as part of multistage compression process. From comparison of the data in figures 3.13(a) and (c), it can be seen that the cooling system is expected to consume less than *ca.* 5 % of power spend on compression in options A and B, while using compression options C (compression combined with subcritical liquefaction and pumping) and D (compression combined with supercritical liquefaction and pumping) results in significant increase in the cooling system power demands, which reach *ca.* 218 % and 42 % of the compression power when applied to oxy-fuel dehumidified CO_2 streams respectively.

Figure 3.13(d) shows the variation of the calculated total power demands consisting of compression power and cooling power for the different compressors against the CO_2 purity. As can be seen in the figure 3.13(d), option B, advanced supersonic shockwave compression for pre-combustion and oxy-fuel streams (85 % v/v and 96.7 % v/v CO_2 purity), indicates a requirement of *ca.* 25-31 % additional total power demand as compared to option A. Also, the results of option C show that the power requirement can be reduced by *ca.* 6-11 % as compared to the compression option A. However, applying compression option C for oxy-fuel mixture, carrying 85 % v/v purity requires by *ca.* 150.5 kWh/tonne$_{CO2}$ (181 %) more power than that for compression option A. From this result, the compression with subcritical liquefaction using utility streams (option C) is not feasible for 85 % v/v purity of CO_2, because of the requirement of cryogenic refrigerant systems which are more costly to operate than conventional compression (option A). The compression combined with supercritical liquefaction (option D) has almost the same power consumption as option A.

While the minimum acceptable levels of impurities are dictated by specific transportation and storage conditions, the cost of CO_2 purification should be traded off against the costs of compression, transportation and storage of impure CO_2 stream. The results in figures 3.13(a), (c) and (d) provide estimates for the power demand in compression per tonne of CO_2 avoided, which is relevant for analysis of the relative costs of mitigation of CO_2 emissions (McCoy and Rubin, 2008).

Additionally, the relative changes in the compression power demand and cooling duties associated with the presence of impurities in CO_2 streams, are calculated as:

$$\delta w_{comp} = \frac{w_{comp} - w_{comp}^{CO_2}}{w_{comp}^{CO_2}} \times 100\% \qquad 3.17$$

$$\delta q_{cool} = \frac{q_{cool} - q_{cool}^{CO_2}}{q_{cool}^{CO_2}} \times 100\% \qquad 3.18$$

where w_{comp} and q_{cool} are respectively the specific compression power and cooling duty of impure CO_2 streams, while $w_{comp}^{CO_2}$ and $q_{cool}^{CO_2}$ are those corresponding to the pure CO_2.

Figures 3.14(a) and (b) show respectively the relative changes δw_{comp} and δq_{cool}, calculated using equations 3.17 and 3.18 based on the data presented in table 3.5 for the CO_2 streams of various purities. As can be seen from figure 3.14(a), the compression power generally increases with the decrease in CO_2 purity. This can be explained by the fact that compression power (see equation 3.1) is inversely proportional to the fluid density which progressively decreases with the increase in the amount of the impurities. In the case of oxy-fuel stream carrying 85 % v/v purity, the multistage compression (figure 3.14(a)) demands *ca.* 12-30 % more power than compression of pure CO_2.

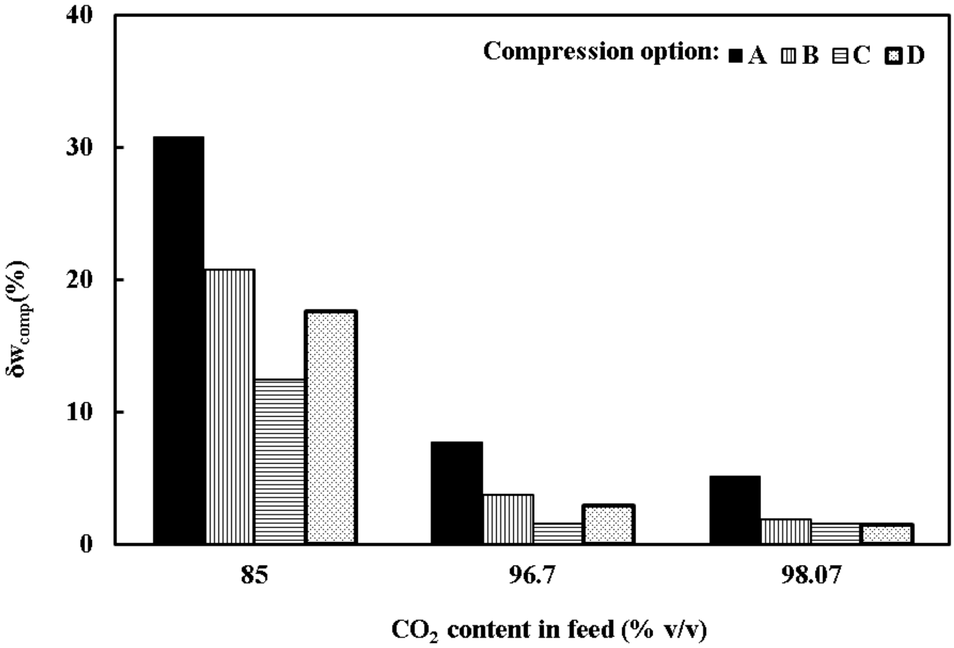

(a)

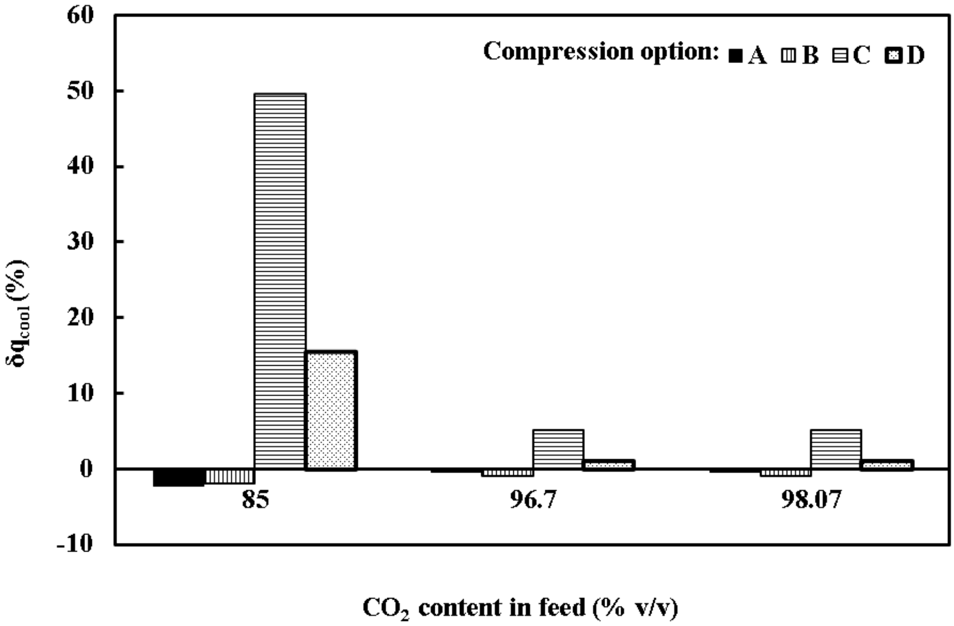

(b)

Figure 3.14: The relative relation in the compression power (a) and inter-stage cooling duty (b) caused by the presence of impurities in the CO2 streams (options A-D).

Remarkably, the impact of CO_2 stream purity on the intercooling duty (figure 3.14(b)) is non-monotonic. In particular, when using compression options A, B and D, the impact of impurities on the cooling duty becomes notable only for the oxy-fuel CO_2 stream of 85 % purity, where the cooling is reduced by less than *ca.* 2 % for options A and B and increased by more than *ca.* 15 % for option D when compared to pure CO_2. In the case of the compression option C, the cooling duty is slightly increased (by *ca.* 5 %) for pre-combustion and oxy-fuel double-flash streams, and becomes by *ca.* 50 % larger than for the pure CO_2 when applied to oxy-fuel dehumidified CO_2 stream. The latter increase in the cooling duty can be attributed to the decrease in the bubble point temperature of the CO_2 mixture with the impurities as discussed earlier and as can be seen from the data in table 3.1.

3.7 Conclusions

In this chapter, a brief introduction of the compression system employed in CCS, concentrating specifically on those works examining the opportunities for integration of the compression in CCS and the power generation process was presented. The types of industrial compression technologies and the impurities present in the captured CO_2 streams were also discussed. This chapter further presented the development and application of a detailed thermodynamic model to compute and compare power requirements for various multistage compression strategies for CO_2 streams. The CO_2 streams considered included those captured from oxy-fuel and pre-combustion coal-fired power plants. Several industrial compression options as previously recommended for high-purity CO_2 streams captured in a post-combustion plant (Witkowski et al., 2013) were considered. The four compression options examined included gas-phase compression using conventional multistage integrally geared centrifugal compressors, supersonic shockwave compressors and multistage compressors combined with subcritical as well as supercritical liquefaction and pumping. In order to estimate the power demand for inter-stage cooling and liquefaction, a thermodynamic model based on Carnot refrigeration cycle was applied. Given the relatively high pressures of CO_2 streams captured in oxy-fuel and pre-combustion processes, the analysis was performed for the high-pressure compression phase starting at 15 bar.

The results of a thermodynamic analysis performed for determining the power requirements for the compression of CO_2 streams for pipeline transportation and subsequent geological sequestration were presented. It was found that for oxy-fuel and pre-combustion CO_2 streams of purity higher than *ca.* 96 % v/v, the compression power for the four compression strategies examined was not significantly affected by the presence of impurities. In case of the oxy-fuel stream with 85 % v/v CO_2 purity, the compression power requirement for the four compression schemes considered was found to increase by *ca.* 12-30 % more than that for the compression of pure CO_2. Given that the power demand for compression increases with the amount of CO_2 stream impurities which removal would raise the capture costs, there is a potential trade-off between the costs of compression and purification. By combining the present methodology with a cost-benefit analysis model for the compression and purification, an optimal CO_2 stream purity for a given CCS plant may be determined.

The power demand for operating the inter-stage coolers is estimated to be relatively small in comparison with the compression power demand (less than *ca.* 5 %) when using the centrifugal and shock-wave compressors. However, when using compression combined with subcritical and supercritical liquefaction and pumping, the cooling system operation can take up about 50 % of the compression power when applied to the oxy-fuel double-flash and pre-combustion CO_2 streams. In the case of oxy-fuel dehumidified CO_2 mixture, the cooling power is predicted to be nearly 1.5 times higher than the compression power demand when applying to compression combined with subcritical liquefaction and about 65 % of the compression power for the compression combined with supercritical liquefaction and pumping.

The relatively high estimated power demand for the operation of the compressor cooling system can be attributed to large cooling duties for the liquefaction of impure CO_2 streams. In particular, the cooling duty was shown to increase by up to 50 % when compressing oxy-fuel CO_2 with 85% v/v purity as compared to that for pure CO_2. Remarkably, for CO_2 streams of higher than 96 % v/v purity, compression combined with subcritical liquefaction and pumping can result in as much as *ca.* 15 % increase in efficiency as compared to conventional centrifugal compression. The liquefaction can be achieved at subcritical pressures around 62.53 bar using conventional water cooling systems at temperatures in the range 10-20 ^oC. At the same time, the study shows that operating such a system becomes less feasible for lower grade CO_2 streams due to incomplete liquefaction of the CO_2 stream. In particular, given the low bubble-point temperatures of oxy-fuel streams of *ca.* 85 % CO_2 purity, liquefaction at 62.53 bar would require using coolant temperatures as low as -62 ^oC which would not be economically viable. This temperature may be increased by applying CO_2 liquefaction at higher pressures, however, to determine the optimal conditions for the liquefaction, the trade-off between the costs for operating compressors and cooling/pumping system should be carefully considered.

In practice, a whole-system approach should be applied to optimise the compression and purification system design and balance the costs associated with operation of specific equipment, such as compressors and refrigeration units.

CHAPTER 4:

TRANSIENT FLOW MODELLING IN CO_2 PIPELINES DURING LINE PACKING AND LINE DRAFTING

4.0 Introduction

During the pipeline transportation of CO_2 in CCS operations, it is important to ensure reliable and stable CO_2 flow conditions at the injection point into the geological storage site in order to ensure its efficient use and safe operation. However, flexible operation (such as that encountered in the case of a fossil fuel power plant (section 4.1)) leads to a variable feed CO_2 flow rate at the capture point and consequently causing disturbances to the flow conditions in the transportation pipeline and ultimately at the delivery point. In addition, given that the most economical mode of pipeline transportation of CO_2 is in the dense 'liquid' phase, unwanted two-phase flow may occur in the event that the line pressure or temperature fall below the CO_2 saturation conditions. This may result in cavitation or water-hammer effect with associated mechanical vibration and pipe erosion and ultimately the real risk of pipe failure (Liljemark et al., 2011).

As such, a properly designed and operated pipeline system is required in order to maintain and allow the control of the CO_2 flow rate, pressure and temperature in order to avoid the above risks. 'Pipe line packing' is one of the most effective approaches (Aghajani et al., 2017) with the pipeline acting as a battery to hedge against intermittency. The term 'line packing' is generally used to describe the pipeline's buffering capacity where the pressure is varied to 'pack' more or less CO_2 in the pipe, which in essence, becomes a storage vessel. In pipeline terminology, increasing the inventory (and hence the pressure) is called 'line packing', while decreasing it for example during outflow or a drop in the feed flow rate is called 'line drafting'. The use of a pipeline as line packing is an appropriate control strategy to ensure that the fluctuation of the flow in the pipeline system may be minimised. For example, in natural gas pipelines transmission, when the gas supply is interrupted, the line pack in the pipeline starts drafting which continues to deliver gas to the downstream end.

In order to investigate the efficacy of line packing during line drafting method, an appropriate mathematical model predicting transient fluid behaviour in the pipeline system is required.

In the study by Chebouba (2015), the decision-making tool on the gas line pack management of the “GZ1 Hassi R’mell-Arzew” gas pipeline was investigated by applying NSGA-II mode FRONTIER solver in order to minimise the total power consumption in the compression stations as well as to maximise gas line pack. From the author’s study, a decision aid tool to make an appropriate decision for operators can be provided to determine the discharge pressures and number of compressors to be put in service. Aghajani et al. (2017) presented the results of the impact of pipeline design and operation on the line packing capability by employing a statistical analytical tool such as Artificial Neural Network (ANN) (Hagan et al., 1997). This modelling software was shown to be a useful tool for evaluation of the available input parameters to increase the capacity of the pipeline as line packing.

Currently, there are no reported detailed studies on assessing the hydraulic transient analysis of line packing for CO_2 pipelines. Given the markedly different fluid phase behaviour of CO_2 as compared to gaseous hydrocarbons such as natural gas, an appropriate flow simulation tool is required to enable the transient analysis during line packing and line drafting in CO_2 transmission pipelines as part of their integration in the CCS chain.

This chapter focuses on the development and testing of a numerical CFD model developed for such purpose. The model is based on the numerical solution of the conservation equations using the Method of Characteristics. It incorporates PR EOS to deal with CO_2 and its various mixtures. Following its verification, the numerical model is employed to conduct a systematic study on the impact of operational flexibility involving a temporal reduction in the upstream CO_2 feed flow rate on the transient flow behaviour in the pipe over a period of 8 hours; typical for a fossil fuel power plant during overnight operation. A particular focus of attention is determining the optimum pipeline design and operating line packing conditions required in order to maximise the delay in the transition from dense phase flow to the highly undesirable two-phase flow following the ramping down of the CO_2 feed flow rate. The investigations are conducted for both pure CO_2 and its various realistic mixtures representative of the most common types of CO_2 capture technologies.

As a means of its verification, in the case of transportation of CO_2 in its dense phase, (considered to be the most economical mode of its transportation), the numerical model’s predictions are compared against those based on a simple analytical model for incompressible flows.

4.1 Factors that influence the operating flexibility of power plants as part of CCS

In order to achieve a carbon-neutral power supply for the future global energy system, a significant increase in the proportion of renewable energy in the power supply mix is required. To achieve this goal, the proportion of electricity generation from renewable energy is expected to increase from 20 % in 2010 to 36 % in 2020, 44 % in 2030 and 52 % in 2050 (Capros et al., 2013). Hydro generation is the largest contributor to renewable electricity in Europe but its potential is for the most part already utilised.

This means that a significant part of the development of renewable electricity in the future will be based on variable generation such as wind and solar photovoltaic. However these energy supplies, like electricity demand, have a variable nature that is not perfectly predictable. Consequently, short- and long-term variability and uncertainty in the electricity load-generation balancing is likely to increase in the future. To cope with this increasing variability and uncertainty, the electricity system will need to have sufficient flexibility to maintain the demand versus generation balancing at all times (Hussy et al., 2014).

Flexibility is the ability of an electricity system to maintain continuous service in the face of rapid and large fluctuations in supply or demand. Increasing amounts of reserve power from firm sources of supply are needed as the total capacity of such variable generators increases (Haines and Davison, 2009). Therefore, fossil-fired power plants have to continue to play a significant role in ensuring the electric supply balance demand. The majority of initial studies on CCS plant design and economics have assumed that power plants installed with CCS will be ‘baseload’ plants, which are very likely to be operated whenever they are available. Since many renewable resources are intermittent, these fossil-fired power plants will, however, be expected to be more responsive plants that will not always be used when they are available to cope with this scenario (Chalmers et al., 2012).

As long as the share of variable Renewable Energy Sources (RES) in a power system is low, the system can operate as usual. However, when RES is deployed on a large scale, a new challenge emerges. This is precisely the situation that Europe is facing today. When the wind stops blowing or the sun stops shining, gas-, coal-, and oil-fired plants are employed to supply the needed electricity and to maintain the operational requirements of the electrical grids. Sudden and massive requests for power, so-called power ramps, create new requirements for conventional generators in the fossil-fired power plant (Eurelectric, 2011).

The other factors that influence the operating flexibility of power plants are due to the variable electricity demand. The value of electricity sales can also vary significantly between jurisdictions and over time. For example, prices tend to be lower during the night as demand is lower (Chalmers et al., 2009). Two possible scenarios which follow variable electricity market demand trends are illustrated in figure 4.1 depending on the type of the plant itself.

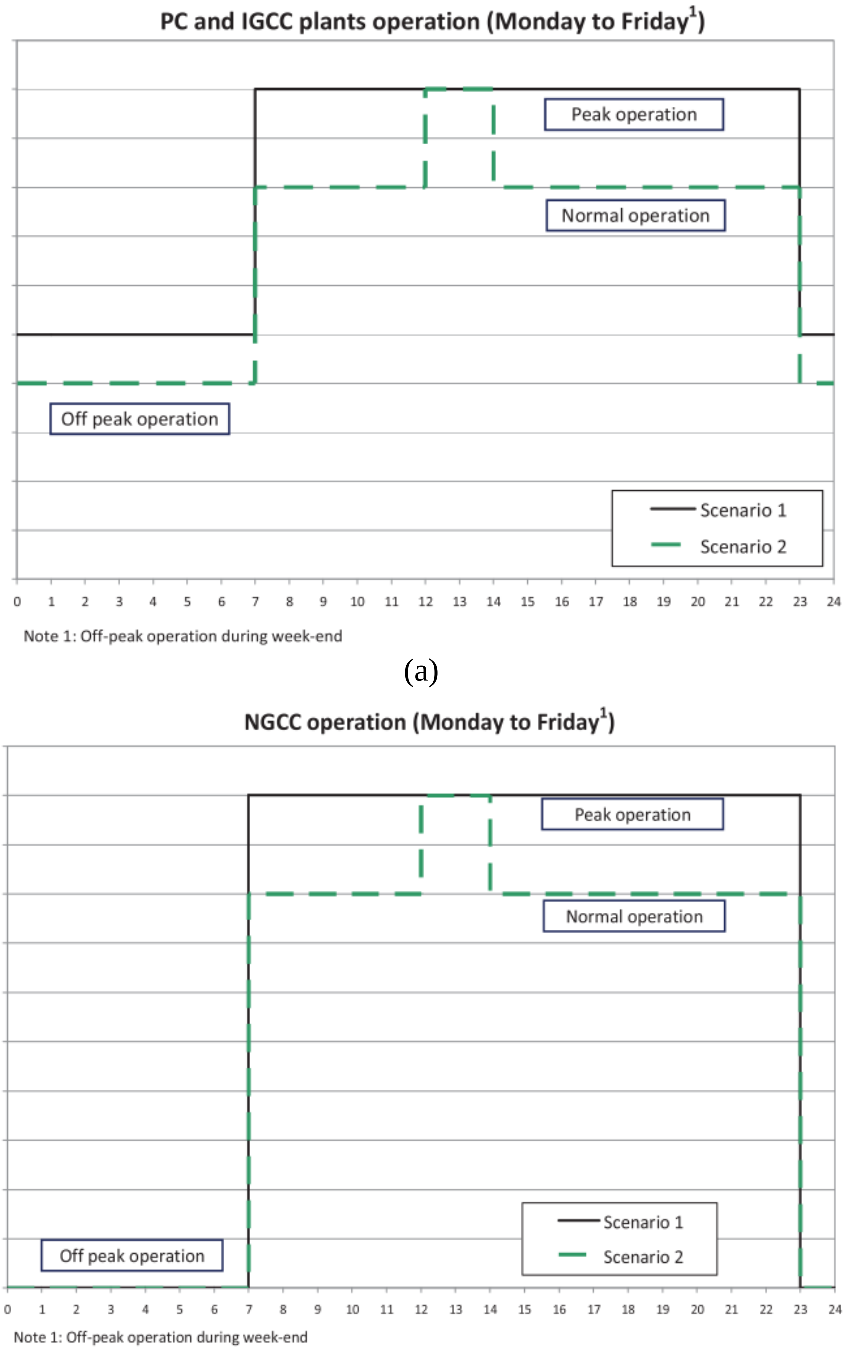

(b)

Figure 4.1: Pulverised Coal (PC) and Integrated Gasification Combined Cycle (IGCC) (a) and Natural Gas Combine Cycle (NGCC) (b) plants operating load following electricity demand trends (Domenichini et al., 2013).

These include weekly (scenario 1) and daily (scenario 2) for different types of power plants. In scenario 1, the PC, IGCC and NGCC plants are operated for 16 hours during peak operation, while in the scenario 2; *ca.* 2 hours of electricity is demanded during peak operation followed by 14 hours of normal operating conditions for all the power plants employed as shown in figures 4.1(a) and (b).

In the case of off-peak operation during night time and weekends, PC and IGCC plants are operated for 8 hours (figure 4.1(a)), whilst in the NGCC plant, the low demand of electricity is utilised during this operation (figure 4-1(b)) (Domenichini et al., 2013).

Employing the conventional fossil-fired power plants however will release both CO_2 and atmospheric pollutants such as NO_x, SO_2 and particulate matters, which would not be emitted by renewable energy sources (Eurelectric, 2011). While this is widely recognised, the impact of part-loading during off-peak operation on the efficiency of conventional thermal power plants is often neglected.

Even the most efficient fossil-fired power plant, Combined Cycle Gas Turbine (CCGT)) will see efficiency drop significantly below its ‘normal’ efficiency when it is not used at its rated full power. Such plants usually operate at an efficiency level of about 55 % dropping to as low as 35 % when its load is reduced to 50 % or less of the rated power output.

Part-loading of coal-fired plants and nuclear plants reduces efficiency by about (maximum) 10 % (Eurelectric, 2011). The lower the efficiency, the smaller the power produced for a given fuel input. However, the drop in efficiency increases the quantities of CO_2 and atmospheric pollutants produced per unit of electricity generated. In other words, power plants emit more pollutants per kWh of electricity produced than if operated at full capacity (Eurelectric, 2011).

For these reasons, careful consideration should be given to retrofit the existing or new fossil power plants with the Carbon Capture and Sequestration (CCS). In all CCS schemes, CO_2 is collected from a large point source before it is treated and compressed for transport for safe geological sequestration (Chalmers et al., 2011).

4.1.1 Constant flow of CO_2 to transport and storage

Most thermal power plants are designed for base load operation with a relatively small number of starts and stops per year. The boundary conditions for thermal power plants are thereby changing towards an increasing need for cyclic loads and operation involving frequent starts and stops. In addition, the amount of CO_2 produced by a thermal power plant depends upon the electricity demand and its variation with time. Demand can vary during the day as well as seasonally over the course of a year. According to Jensen et al. (2016a), CO_2 emissions are based on the load of the unit, which can be fairly constant for 8-12 hours with only minimal change. At other times, the load can change either higher or lower, at the rate of 1-2 % a minute. The 1 to 2 % rate change can sometimes continue in the same direction for as long as 30-45 minutes. Because the changes are completely at the whim of the market, the operators are not able to predict the load on an hour to hour basis. A CO_2 capture plant associated with an electricity-generating station will be forced to adapt to this type of variation in both quantity of CO_2 produced and in the flue gas composition with time.

The requirement of the power plants to follow a variable electricity market demand trend leads to an uneven captured CO_2 flow rate and a consequent fluctuation of the operating conditions in the pipeline and sequestration site. In addition, in practice, it is important to understand the impact of variable CO_2 loading on the flow behaviour in the associated pipeline system. Based on the study by Liljemark et al. (2011) on the effect of a load change in the pipeline it was found to result in the slow formation of two-phase flow in the pipe. According to the study by Klinkby et al. (2011) during shut-down process, the pressure and temperature dropped below the critical point and phase changed from dense phase to gas and liquid were occurred in the upper part of the well and in the pipeline. Using very low loads of less than 20 % of the full load will cause problems with keeping the supercritical conditions along the pipeline and in the well due to a combination of lower pressure and cooling.

As a consequence, a properly designed preventive measure is required to maintain a constant CO_2 flow rate in the pipeline system, thus avoiding pressure fluctuations and consequent possible changes of the CO_2 physical state. Such a measure is the focus of the present study, discussed in the next section.

4.1.1.1 Pipeline packing

A CO_2 pipeline system can be controlled so that the supply and demand of CO_2 can be regulated. The introduction of strategically placed temporary storage into pipeline system can help to attenuate variation. There are different types of temporary storage including pipeline packing, where the storage can be achieved by increasing the gas pressure and loading more gas into a pipeline. In response to the upset operation conditions, use of a pipeline line pack across the consolidated network of pipelines and storage facilities can be used like a battery to hedge against intermittency. A line pack depends on the pressure levels in the pipeline, and it constantly changes as pressure is varied. Typically, pipelines build up line pack during periods of decreased demand and draw it down during periods of increased demand (Rigos et al., 2011).

To illustrate a line packing scenario, a simple pipeline system with a compressor station and a mainline valve at the end of the pipeline is shown in figure 4.2. The pipeline has been operating in steady state condition for a long time as indicated by the solid line in figure 4.2.

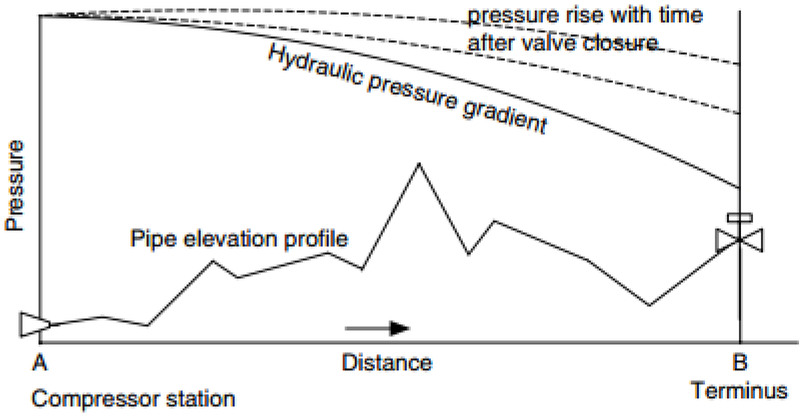

Figure 4.2: Pipeline packing (Menon, 2005).

During line packing, the flow of fluid out of the pipeline is stopped by closing (or throttling) a downstream valve whilst still allowing fluid to flow into the pipeline upstream. As a result, the fluid contained in the pipeline is compressed (packed) and the pressure of the contained fluid within the pipeline increases as shown by the dashed lines in figure 4.2. This will result in an increase in line pack in the downstream section of the pipe, which will progress toward the upstream end. The transient pressure waves moving upstream will eventually reach the discharge of the compressor, causing the discharge pressure to rise. If the increased pressure attains the Maximum Allowable Operating Pressure (MAOP) of the pipeline, the downstream valve will open.

A line pack is highly dependent on pipeline specifics. In the case of a natural gas system, depending on the length of the supply chain, it takes many hours or even days for natural gas to complete the journey from the wellhead to the city-gate in order to replenish the line-pack. Communication between the Independent System Operator (ISO) and the pipeline about mass flow variability could enable a pipeline to increase a line pack before an interruption in flow event. Even better, routine operating procedures should be developed to ensure pipeline readiness to supply fluid in response to an abrupt reduction in the flow rate. A pipeline and the suppliers behind it must be compensated for the additional fuel used to replenish the line pack in order to offset under-performance when the mass flow is lower than expected (Rigos et al., 2011).

Aghajani et al. (2017) investigated the impact of pipeline design and operation on the line packing capability of a dense phase CO_2 pipeline network. The results produced are illustrated in figure 4.3 showing the effect of varying pipeline length, mass flow rate and inlet as well as outlet pressure on line packing time for a fixed inner diameter of the pipeline transporting pure dense phase CO_2.

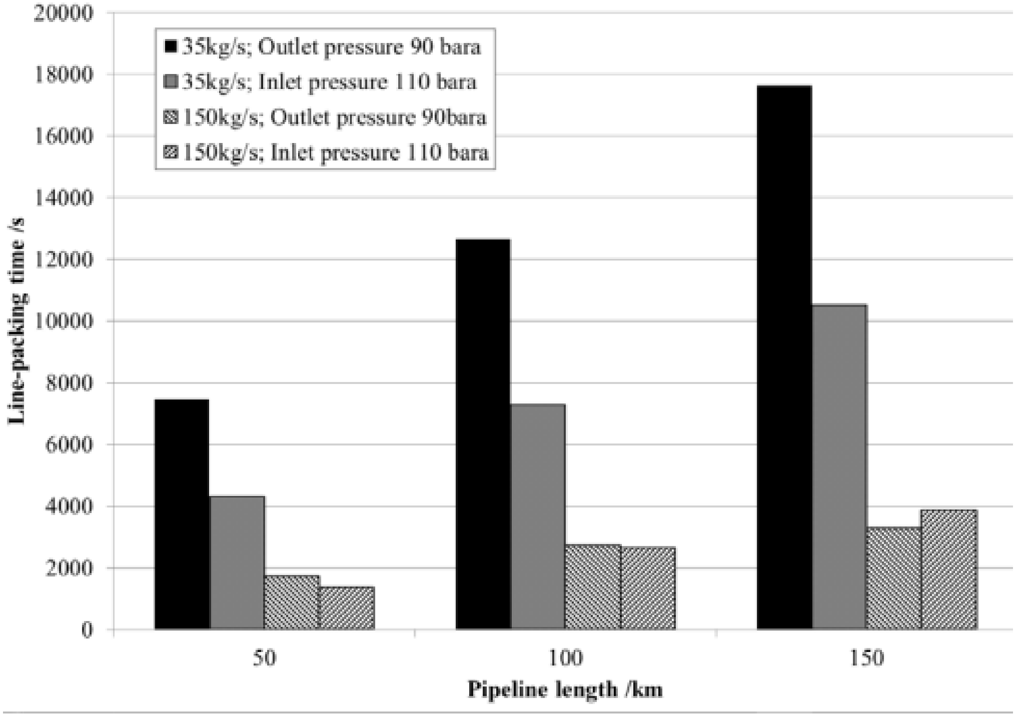

Figure 4.3: Effect of changes in flow rate and inlet and outlet pressure management on the line-packing time for a 457 mm outer diameter, 11 mm wall thickness pipeline containing pure dense phase CO_2 (Aghajani et al., 2017).

According to the data presented, the biggest effect of changing the pressure at the inlet and outlet was observed at lower flow rates. At the lower flow rates, changing the outlet pressure condition increases the line packing time by approximately 70 % for all pipeline lengths. From the results, the authors claimed that if a combined strategy of managing the outlet pressure and lowering the flow rate is possible, then the line packing times can be increased by factors of up to five times depending on pipeline length.

4.1.1.2 Pipeline drafting

Much of the short-term (i.e. daily and hourly) gas demand variation is accommodated by drawing from aboveground liquefied gas storage vessels or by an intentionally varying pipeline operation by increasing and decreasing pressure so as to use the pipeline for temporary storage. The practice, termed “line packing” or “packing,” increases the volume stored while “drafting” or “de-packing” reduces the volume (Jensen et al., 2016a). When the gas supply is interrupted, the line pack in the pipeline starts reducing which continues to deliver gas to the downstream end. During this scenario, the pressures continue to fall along the pipeline for a certain period of time (Menon, 2005).

Currently there is no methodology for assessing the line drafting characteristics of dense phase CO_2 pipelines.

The following presents the development of a numerical transient pipe flow model for simulating line packing and line drafting in pressurised CO_2 pipelines. This then followed by its application to realistic case studies to test its efficacy as a tool for investigating line packing as a means for smoothing out flow transients following a disturbance in the upstream pipe flow conditions and the subsequent impact on the fluid phase during line drafting.

4.2 Numerical pipe flow model

4.2.1 Governing equations

In this study, the multiphase transient pipe flow is approximated by the Homogeneous Equilibrium Mixture (HEM) model where the constituent phases are assumed to remain at thermal and mechanical equilibrium during decompression. The corresponding conservation equations expressed in terms of pressure, P, specific entropy, s and flow velocity, v as dependent variables are given by:

$$\frac{dP}{dt}-\varphi\frac{ds}{dt}+\rho a^2\frac{\partial v}{\partial x}=0 \qquad 4.1$$

$$\rho\frac{\partial v}{\partial t}+\rho v\frac{\partial v}{\partial x}=-\frac{\partial P}{\partial x}-\frac{f_w\rho}{2D}v|v|-\rho g\sin\theta \qquad 4.2$$

$$\rho T\frac{ds}{dt}=q_h+\frac{f_w\rho v^3}{2D} \qquad 4.3$$

where θ, g, ρ, T, a and D are respectively the pipeline elevation, gravitational constant, density, temperature, speed of sound and pipe inner diameter, a function of time, t and space, x while φ is given by the thermodynamic function, $\left(\frac{\partial P}{\partial s}\right)_\rho$ and f_w is the Fanning friction factor calculated using Chen's correlation as described in sections 2.4.5.2 and 2.4.6, respectively. q_h is the heat flux at the pipe wall and is defined via the heat transfer equation as described in section 2.4.5.4.

4.2.2 Boundary conditions

The conservation equations presented in the equations 4.1-4.3 are closed by the boundary conditions as presented in the following section.

4.2.2.1 Variable flow rate at the pipeline inlet

In this study, to account for the variation of the flow rate at the pipe inlet, the local conservation equations are first modified following Thompson (1987) and Thompson (1990), which read:

$$\frac{\partial\rho}{\partial t}+\frac{1}{a^2}\left[\ell_2+\frac{1}{2}\left(\ell_3+\ell_1\right)\right]=0 \qquad 4.4$$

$$\frac{\partial P}{\partial t}+\frac{1}{2}\left(\ell_3+\ell_1\right)=0 \qquad 4.5$$

$$\frac{\partial v}{\partial t}+\frac{1}{2\rho a}\left(\ell_3-\ell_1\right)=0 \qquad 4.6$$

where ℓ_1, ℓ_2 and ℓ_3 are the so-called wave amplitudes defined as follows.

Following Thompson (1987), in the case of subsonic inflow, ℓ_1 is given by:

$$\ell_1=\lambda_1\left(\frac{\partial P}{\partial x}-\rho a\frac{\partial v}{\partial x}\right) \qquad 4.7$$

and the above can be approximated applying finite difference method:

$$\ell_1=\left(v_i-a_i\right)\frac{1}{\Delta x}\left[P_{i+1}-P_i-\rho_i a_i\left(v_{i+1}-v_i\right)\right] \qquad 4.8$$

With regards to ℓ_2, isentropic flow conditions are further assumed, and as a result, ℓ_2 vanishes (Thompson, 1990).

$$\ell_2=0 \qquad 4.9$$

For the definition of ℓ_3, the corresponding formulation is more mathematically involved. Equations 4.4 and 4.6 can be recast into the following form:

$$v\frac{\partial \rho}{\partial t}=-\frac{v}{a^2}\left[\ell_2+\frac{1}{2}\left(\ell_3+\ell_1\right)\right] \qquad 4.10$$

$$\rho\frac{\partial v}{\partial t}=-\frac{\rho}{2\rho a}\left(\ell_3-\ell_1\right) \qquad 4.11$$

Addition of the resulting equations gives:

$$v\frac{\partial \rho}{\partial t}+\rho\frac{\partial v}{\partial t}=-\frac{v}{a^2}\left[\ell_2+\frac{1}{2}(\ell_3+\ell_1)\right]-\frac{1}{2a}\left(\ell_3-\ell_1\right) \qquad 4.12$$

Note the RHS of equation 4.12 is simply the expanded form of the rate of change in the flow rate, $\frac{\partial \rho v}{\partial t}$. Knowing ℓ_1 and ℓ_2 (see equations 4.8 and 4.9), ℓ_3 can now be expressed in terms of $\frac{\partial \rho v}{\partial t}$, such that:

$$\ell_3 = \frac{\left(-2v_i\ell_2 - 2Aa_i^2 - \ell_1(v_i - a_i)\right)}{v_i + a_i} \qquad 4.13$$

where:

$$A = \frac{\partial}{\partial t}(\rho v) \qquad 4.14$$

Herein, *A* is specified based on specific requirements by operational flexibility (see section 4.1).

In the present study, the calculation of mass flux, ρv over the time during the ramping down process is introduced by the following hyperbolic tangent function:

$$\rho v = -\alpha \tanh(x) + \beta \qquad 4.15$$

where the coefficients of α , β and *x* respectively represent the reduction trends of the mass flux during ramping down, while the relationship of α and β can be fitted in the form of $\alpha + \beta = (\rho v)_o$. Here $(\rho v)_o$ represents the mass flux at the initial conditions.

In order to determine the specific requirements of the ramping down during flexible operation following the reduction of the mass flux to 50 % of its initial value, the extension of the equation 4.15 as a function of time can be expressed as:

$$\rho v = \begin{cases} (\rho v)_o \ \text{ if } 0 \le \mathrm{t} \le 1000 \\ -\frac{(\rho v)_o}{4}\tanh\left(\frac{t-1000}{100}\right) + \left((\rho v)_o - \frac{(\rho v)_o}{4}\right) \ \text{ if } 1000 < \mathrm{t} \le 1700 \\ 0.5(\rho v)_o \ \text{ if } 1700 < \mathrm{t} \le 28800 \end{cases} \qquad 4.16$$

Here the value of *A* (see equation 4.14) can be determined from the derivation of the relative function of equation 4.16:

$$\frac{\partial}{\partial t}(\rho v)=\begin{cases}0 \text{ if } 0\le t\le 1000\\ -\frac{(\rho v)_o}{4\times 100}\operatorname{sec}h^2\left(\frac{t-1000}{100}\right) \text{ if } 1000< t\le 1700\\ 0 \text{ if } 1700< t\le 28800\end{cases} \tag{4.17}$$

Along with equation 4.17, it is therefore possible to predict the variable mass flux for that particular time. In the case study, the valve closure is set to be started at 1000 s within 700 s. After this period, the value of mass flux is set constant to 50 % of its initial value within 28800 s (8 hours) of operation. It is highlighted that the relationships developed in equations 4.15-4.17 are only applicable to the modelled case studies.

To this end, the local governing equations at the pipe inlet are readily solved. Applying backward Euler method, the corresponding primitive variables flow velocity, *v* and pressure, *P* are given by:

$$v_{j+1}=\frac{\left(-\ell_3(v_j+a_j)-\ell_1(v_j-a_j)\right)\Delta t}{2\rho_j a_j^{\,2}}+u_j \tag{4.18}$$

$$P_{j+1}=\left(\left(\frac{-\ell_3(v_j+a_j)-\ell_1(v_j-a_j)}{2a_j}\right)+\ell_3\right)\Delta t+P_j \tag{4.19}$$

where, j represents the known values at the previous time level and $j+1$ is the unknown values at the current time level. As entropy is assumed constant for inflow, other pertinent fluid properties can be calculated by performing the pressure-entropy flash calculations, using Peng-Robinson Equation of State (PR EOS), previously presented in section 2.1.6.

4.2.2.2 Outlet boundary condition

At the outlet of the pipeline, simple zero-order extrapolation method is applied, where all variables are equated to the corresponding values at the last numerical cell centre in the computational domain.

4.2.3 Numerical method

Using MOC (see section 2.4.7.1), the conservation equations 4.1 to 4.3 may be replaced with three compatibility equations along their corresponding characteristic lines by:

$$d_o s = \left(\frac{\psi}{\rho T} \right) d_o t \qquad 4.20$$

along the Path line characteristic (C_o):

$$\frac{d_0 t}{d_0 x} = \frac{1}{v} \qquad 4.21$$

$$d_+ P + \rho a d_+ v = \left(a\alpha + \frac{\varphi\psi}{\rho T} \right) d_t t \qquad 4.22$$

along the positive Mach line characteristic (C_+):

$$\frac{d_+ t}{d_+ x} = \frac{1}{v + a} \qquad 4.23$$

$$\rho a d\_v - d\_P = \left(a\alpha - \frac{\varphi\psi}{\rho T} \right) d\_t \qquad 4.24$$

along the negative Mach line characteristic ($C\_$):

$$\frac{d\_t}{d\_x} = \frac{1}{v - a} \qquad 4.25$$

The values of P, s, ρ, v and a, as a function of time and distance along the pipeline are obtained by the inverse marching method of characteristics as described in chapter

2. This involves dividing the pipeline into a large number of distance (*Δx*) and time elements (*Δt*) and expressing the compatibility equations in finite difference form paying due regard to the Courant stability criterion (equation 2.114) regarding the maximum allowable distance and time elements. These finite difference equations are in turn solved at the intersection of the linear characteristics lines with the spatial axis using iteration and interpolation in conjunction with *P-s* (pressure-entropy) flash calculations.

4.3 Analytical model

As explained earlier (see section 4.3), despite its rigour, the numerical transient pipe flow model described above is computationally demanding. In practice, this restricts its use for routine applications. In an attempt to address this shortcoming, and for its verification, the following describes the development of a simple analytical pipe flow model based on the assumption of incompressible and isothermal flow where all the fluid in the pipe travels at the same velocity. This is a reasonable approach given that as mentioned previously, the most economical method for transportation of CO_2 is in the dense phase (Chaczykowski and Osiadacz, 2012, Witkowski and Majkut, 2012) where the liquid like fluid will have a small compressibility. The above is then followed by testing of the analytical model's applicability based on the comparison of its predictions against those obtained from the numerical pipe flow model.

The resulting momentum conservation for incompressible isothermal flow reads (Apsley, 2013):

$$\rho \frac{dv}{dt} = -\frac{\Delta P}{L} - \frac{f_w \rho}{2D} v|v| - \rho g \sin\theta \qquad 4.26$$

where *v*, *L* and *D* are respectively the velocity, pipeline length and inner diameter of the pipe, while *ΔP* is the pressure drop across the length of the pipe. The latter is obtained from the predictions from the numerical flow model presented in section 4.3.

To solve the above equation 4.26, the differential-algebraic solver library DASSL (Brenan et al., 1996) is employed. The thermodynamic properties of CO_2 are determined using the Peng-Robinson Equation of State (section 2.1.6).

4.4 Results and discussion

In this section, the simulation results are divided into three parts. In the first part, simulations of the unsteady impure CO_2 flow in response to a change in the upstream CO_2 feed flow rate (e.g. from the power plant) are performed to investigate the impact of load fluctuation on the transported fluid in the pipe. Also included in the same section is a case study investigating the influence of the line packing on maintaining the near-steady flow condition for pure dense phase CO_2 during flexible operation. The tests are performed include employing both the simple analytical and the computationally demanding numerical pipeline flow model for verification purposes.

In the second part, the optimum pipeline design and operation parameters including pipeline dimensions, inlet temperature as well as inlet mass flow rate for the line packing method are determined. Finally, the efficacy of the optimised variables for the design stage of line packing is tested for the CO_2 streams containing various types of stream impurities.

4.4.1 Effect of operational flexibility on pipeline flow

In order to study the effect of operational flexibility on the pipe flow in the context of CCS, a case study is carried out applying pipeline flow models developed above. Table 4.2 shows the pipeline dimensions, and the prevailing conditions for the case study.

Table 4.2: Simulation input data for the case study.

Parameter	Value
Initial pressure (bar)	150
Initial temperature (K)	311.15
Ambient temperature (K)	278.15
Ambient pressure (bar)	1.01
Pipeline length (km)	50
Pipeline thickness (mm)	10
Pipeline outer diameter (mm)	457
Fanning friction factor	0.002
Pipe roughness (mm)	0.0457
Number of grids	2000
Pipe orientation to the horizontal plane (°)	0
Feed flow rate (kg/s)	100
Heat transfer coefficient (W/m^{2}K)	5
Material of construction	Stainless steel
CFL factor	0.9
Feed CO_2 composition (% v/v):	
• Pure CO_2	100
• Pre-combustion	98.07
• Oxy-fuel:	
Double flashing	96.7
Raw/dehumidified	85

The test case relates to a 50 km length, 457 mm outer diameter and 10 mm wall thickness horizontal steel pipeline transporting CO_2 and its various mixtures corresponding to pre-combustion and oxy-fuel capture technologies. The feed compositions in the CO_2 streams employed are presented in table 3.1. Given the relatively small proportion of impurities, post-combustion CO_2 stream (see table 3.1), is not considered in the study. The feed flow rate is assumed to be 100 kg/s at 150 bar and 311.15 K. Under these conditions, the CO_2 streams are in the supercritical state. The pipe roughness assumed to be 0.0457 mm corresponding to mild steel (McCoy and Rubin, 2008). The simulation is performed using a computational grid of 2000 equally-spaced numerical cells with a CFL factor of 0.9.

In order to simulate a flow disturbance for example, as a result of a change in loading or due to a gradual feed valve closure, at 1000 s the pipe feed flow rate is assumed to decrease to 50 % of its initial value over a period of 700 s in a non-linear manner following the function given by equation 4.17 (section 4.3.2.1).

Figures 4.4 and 4.5 respectively show the corresponding simulated fluid velocity, pressure, temperature and density variations with time at the pipeline inlet and outlet over 16650 s of simulation time. All data were generated using the transient numerical pipe flow model. The vertical dashed, dotted and solid lines for all the mixtures as shown in figure 4.4(a) mark the start (1000 s) and the completion (1700 s) of the feed flow ramp down.

As it may be observed in figure 4.4(a), for all CO_2 concentrations considered, the commencement of valve closure at 1000 s is marked by a rapid and almost of instantenous drop in the flow velocity to constant values throughout the rest of the simulation time.

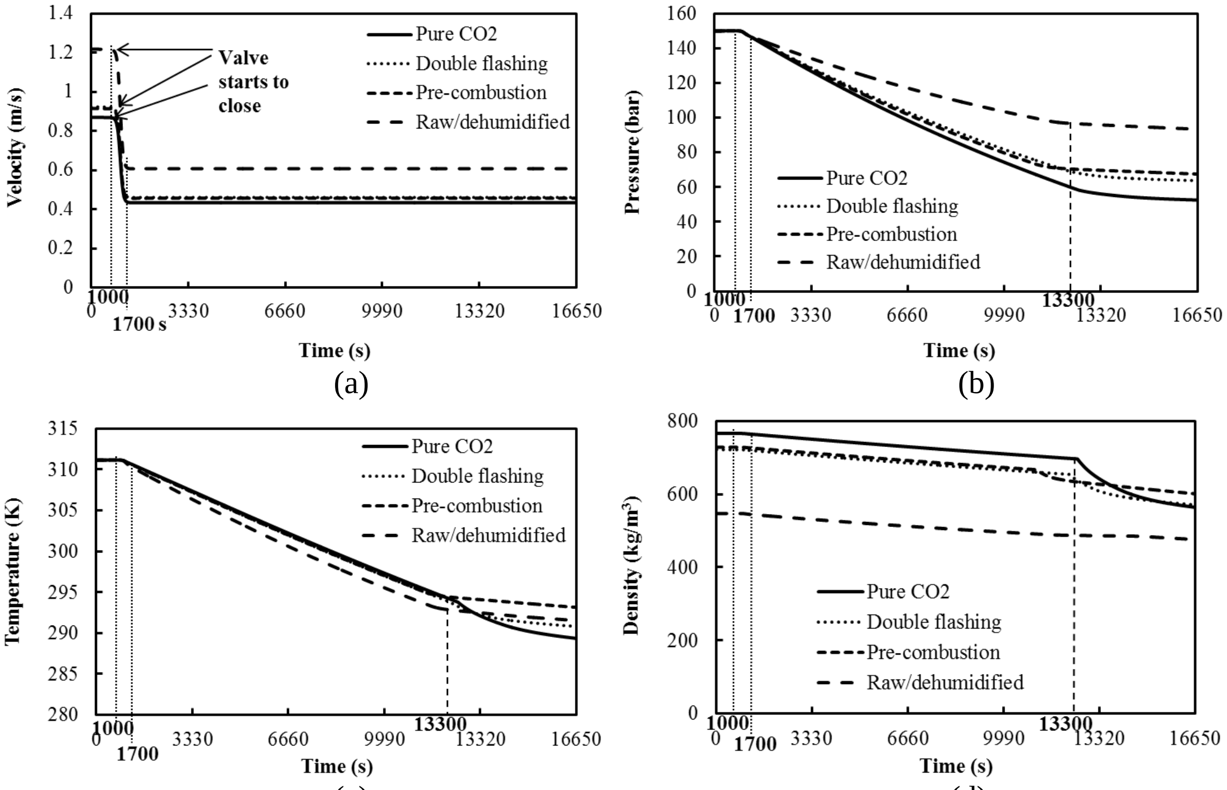

(a) (b)

(c) (d)

Figure 4.4: The transient variations in velocity (a), pressure (b), temperature (c) and density (d) for pure CO_2 and CO_2 with impurities at pipeline inlet following the linear ramping down of feed flow rate. The vertical dotted lines indicate mark the start (1000 s) and the completion (1700 s) of the feed flow ramp down at a rate of 100 kg/s down to 50 % of the initial value. Inlet pressure = 150 bar, inlet temperature = 311.15 K, mass flow rate = 100 kg/s, pipe length = 50 km and inner pipe diameter = 437 mm (see also table 4.2).

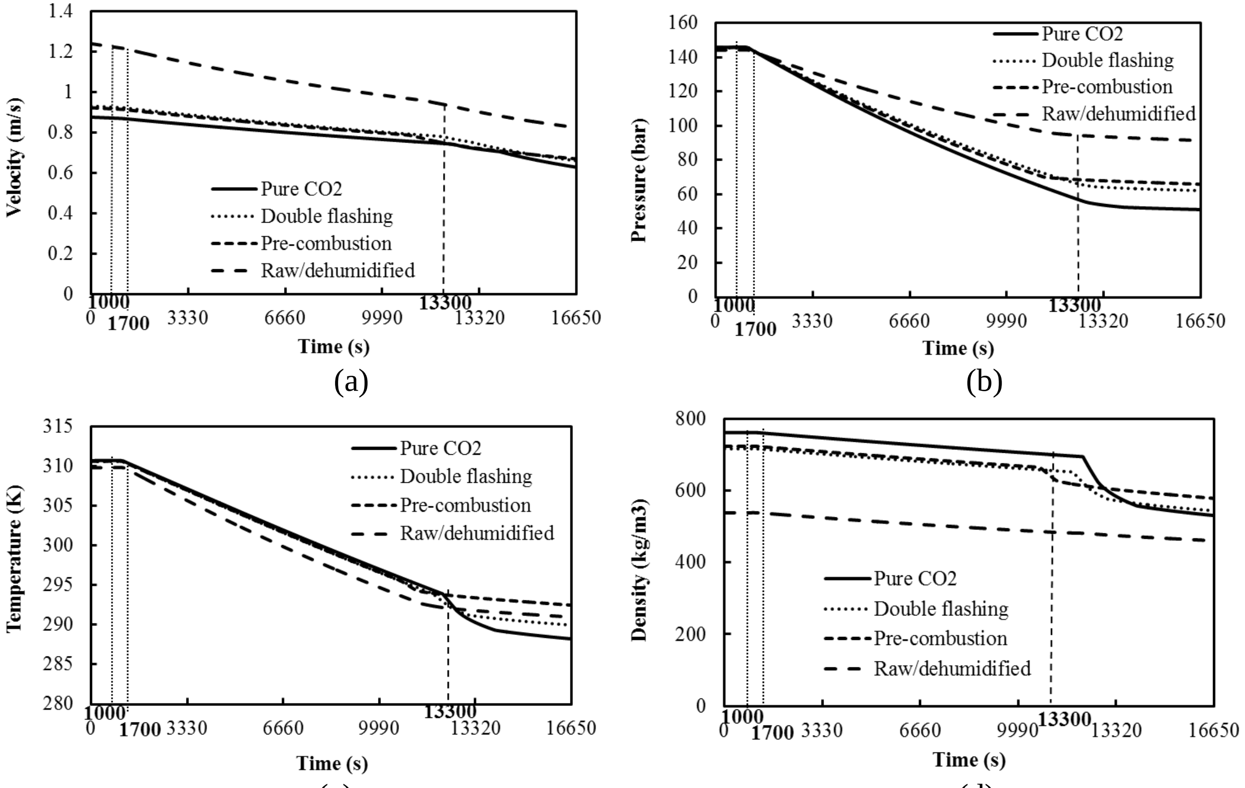

(a) (b)

(c) (d)

Figure 4.5: The transient variations in velocity (a), pressure (b), temperature (c) and density (d) for pure CO_2 and CO_2 with impurities at pipeline outlet following the linear ramping down of feed flow rate. The vertical dotted lines indicate mark the start (1000 s) and the completion (1700 s) of the feed flow ramp down at a rate of 100 kg/s down to 50 % of the initial value. Inlet pressure = 150 bar, inlet temperature = 311.15 K, mass flow rate = 100 kg/s, pipe length = 50 km and inner diameter = 437 mm (see also table 4.2).

As compared to the fluid velocity, the fluid pressure (figure 4.4(b)) and temperature (figure 4.4(c)) also show a drop in their magnitudes at 1000 s, but this is followed by a much lower rate of decrease remaining relatively constant in the first 13300 s. This is followed by a second inflection in the slope as indicated by the vertical dashed lines, marking the transition from the supercritical to the two-phase state (see latter in figure 4.7). The observed drop in the fluid temperature throughout is due to its depressurisation induced expansion cooling.

In contrast, the commencement of valve closure is not marked by a noticeable discontinuity in the fluid density (figure 4.4(d)), where a much lower rate of drop as compared to the fluid pressure, velocity and temperature is observed.

Turning to the effect of CO_2 stream impurities on the flow transients resulting from the partial inlet valve closure as shown in figures 4.4 and 4.5, it is clear that all the flow parameters are affected by the presence of impurities, with the impact increasing with the percentage of the impurity. The raw-dehumidified oxy-fuel mixture with 85 % v/v CO_2 shows the highest reduction in flow parameters compared to other streams. In the case of pre-combustion (98.07 % v/v CO_2) and double flashing oxy-fuel mixture (96.7 % v/v CO_2), the flow parameters are almost the same as with pure CO_2.

Returning to the data in figure 4.5 showing the corresponding transient variations in the flow parameters at the pipe outlet following the disturbance in the feed flow rate. As it may be observed, in contrast to the behaviour at the pipeline inlet (figure 4.4), the commencement of the closure of the inlet valve is not marked by the nearly instantaneous rapid drop in the flow velocity (figure 4.5(a)) at the pipe outlet. Apart from this, and with exception of marginal drops in their values, all the trends observed, including those for the various CO_2 impurity streams, are very similar to those at the pipe inlet. The vertical dashed lines mark the transition from the supercritical to the two-phase state.

To aid clarity, figure 4.6 shows the superimposed plots of the transient variations of the flow parameters at the pipe inlet and outlet plotted for the pure CO_2 chosen as an example.

As it may be observed, in the case of the fluid temperature, pressure and density, the deviation between the inlet and outlet values occurs at approximately 13300 s following the start of valve closure.

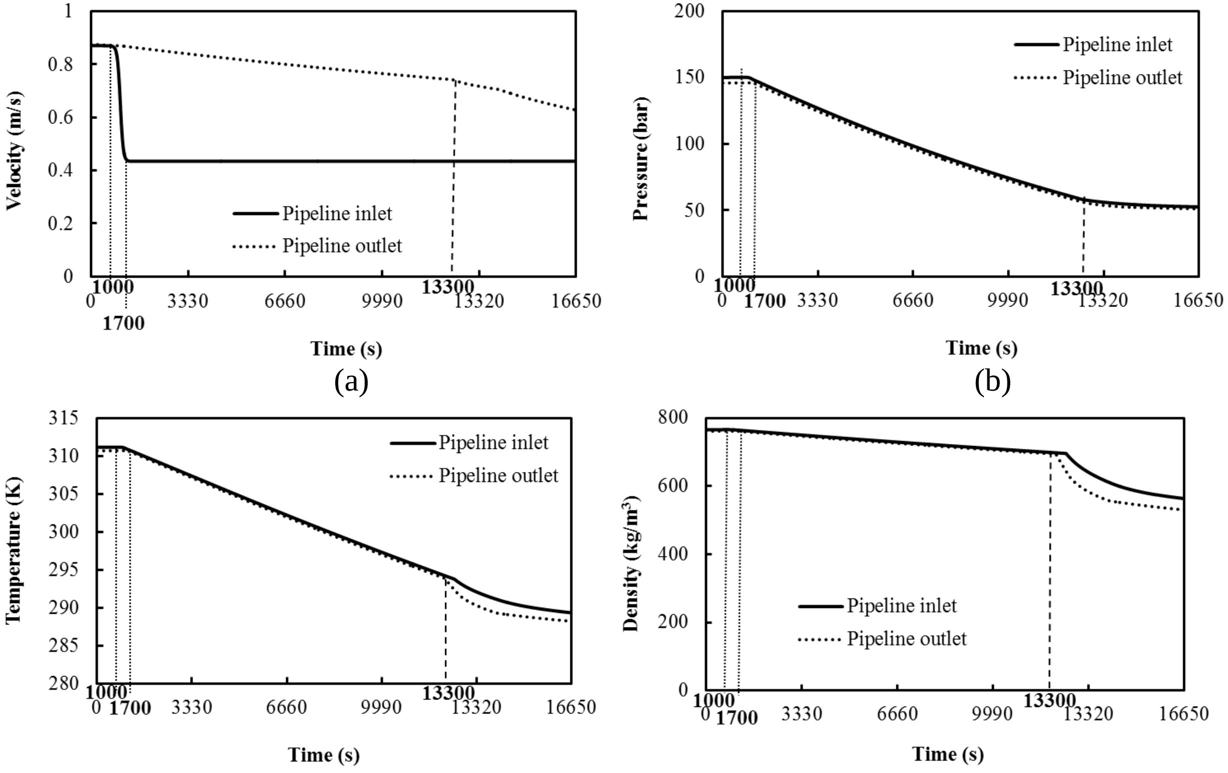

(a) (b)

(c) (d)

Figure 4.6: The transient variations in velocity (a), pressure (b), temperature (c) and density (d) for pure CO_2 at pipeline inlet and outlet following the linear ramping down of feed flow rate. The vertical dotted lines indicate mark the start (1000 s) and the completion (1700 s) of the feed flow ramp down at a rate of 100 kg/s down to 50 % of the initial value. Inlet pressure = 150 bar, inlet temperature = 311.15 K, inlet mass flow = 100 kg/s, pipe length = 50 km and inner diameter = 437 mm (see also table 4.2).

As mentioned above, the second inflections observed in the slopes of the curves indicated in figures 4.4-4.6 occuring after *ca.*13300 s correspond to the change in the fluid phase from supercritical to the two-phase state. To illustrate this further, figure 4.7 shows the fluid phase diagrams presented in the form of dew point and bubble point curves for pure CO_2 and the three CO_2 mixtures under consideration. This data was generated using the REFPROP (Lemmon and Huber, 2010) physical properties model incorporating the PR EOS.

Also included in each plot are the corresponding pressure and temperature trajectories at the pipe inlet and outlet during valve closure as extracted from figures 4.4(b-c) and 4.5(b-c). As it may be observed, for the most part, the fluid within the pipeline remains in the supercritical state. Given the very high speed of sound in the supercritical state (*ca.* 1000 m/s; (Han et al., 2010)), this explains the marginal diffrence in the fluid properties at the pipe inlet and outlet at any given time during the feed ramping down (see figure 4.7).

The intersection of the pressure/temperature trajectories with the bubble point curves marks the transition from the supercritical to the two-phase state. This is in turn manifested in the second inflections in the rate of change in the fluid properties as shown in figures 4.4 to 4.6 occuring at 13300 s where the deviations between the fluid parameters becomes more pronounced due to the lower speed of sound (*ca.* 350 m/s; Han et al., 2010) in the two-phase mixtures.

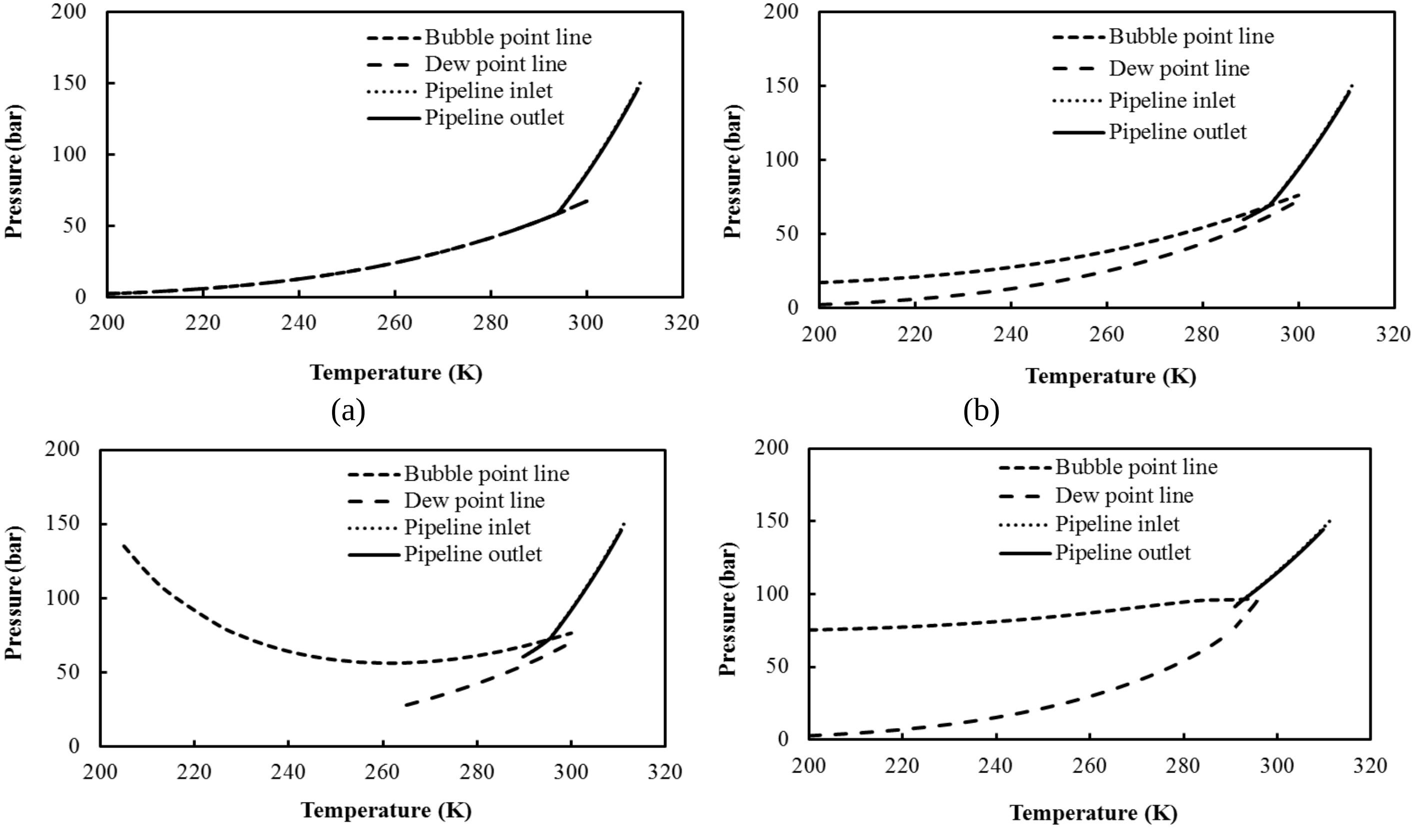

(a) (b) (c) (d)

Figure 4.7: Pipe inlet and outlet pressure-temperature trajectories in relation to the dew and bubble point curves following the non-linear ramping down of feed flow rate for pure CO_2 (a), double flashing (b), pre-combustion (c) and raw/dehumidified (d) compositions.

Table 4.3 lists the temperatures and pressures at which the transition from the supercritical to the two-phase region occurs for the pure CO_2 and its various mixtures. As it may be observed the pressure at which the transition to the two-phase state occurs increases with the decrease in the purity of the CO_2 stream.

Table 4.3: The supercritical to two-phase transition pressures and temperatures as a function of CO_2 purity (see table 3.1 for mixture compositions).

	% v/v CO_2	Transition pressure (bar)	Transition temperature (K)
Pure CO_2	100.0	58	293.8
Pre-combustion	98.07	73.1	295.5
Oxy-fuel:			
Double flashing	96.7	69.2	293.9
Raw/dehumidified	85.00	94.7	292.1

In practice the above means that as the proportion of impurities incerases in the CO_2 stream, higher operating line pressures are required in order to avoid the risk of the undesired two-phase flow occuring during feed ramping down process. In the case of the raw/dehumidified CO_2 mixture for example, the line pressure must not fall below 94.7 bar and exceed 292.1 K at any time to ensure operation in the dense phase.

In order to compensate for such upset condition as well as to maintain the operating pressure above the critical point, utilising the pipeline as line packing will be considered in section 4.5.2.

4.4.1.1 Performance of the analytical model

As the chosen conditions of the CO_2 stream during valve closure following flexible operation is ‘nearly incompressible’ (the fluid stays in the dense phase supercritical state during the most part), the predictions from the simplified analytical incompressible flow model describe in section 4.4 is compared against those obtained from the computationally demanding numerical pipeline model. The transmission pipeline is assumed to be 50 km long, outer diameter of 400 mm and 20 mm wall thickness transporting pure CO_2 at feed temperature and pressure of 293.15 K and 95 bar respectively. The remaining pertinent flow, ambient and computational parameters are set the same as those given in table 4.2.

Figure 4.8 shows a comparison of the predicted fluid velocity profiles as a function of time at both ends of the test pipe predicted from both models. Expectedly, the analytical model is presented only by a curve given that it is based on incompressible flow assumption. On the other hand, in the case of pipeline flow model, two distinctive velocity profiles are predicted; those at the pipeline inlet and outlet.

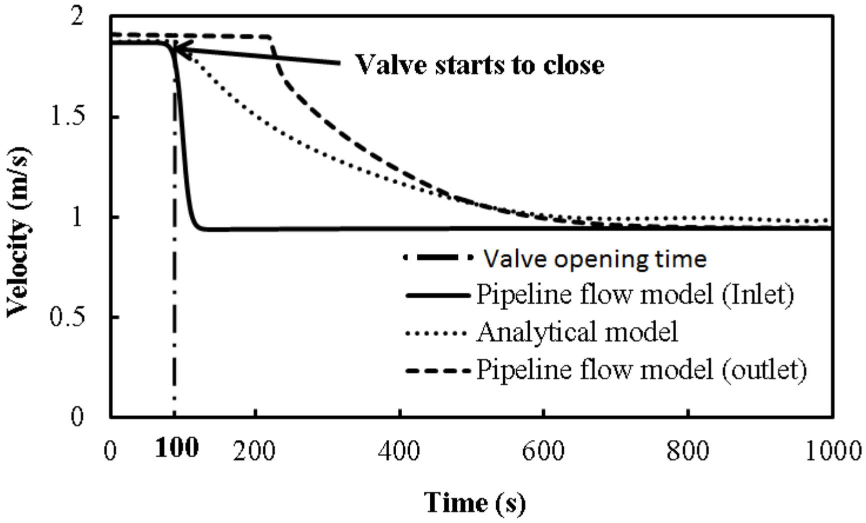

Figure 4.8: Comparison of time variation of the fluid flow velocity based on the numerical (solid and square dot lines) and analytical pipe flow models (rounded dotted line).

It is interesting to note that the fluid velocity transient predicted using the analytical model lies mostly in between the inlet and outlet velocities produced from the numerical pipeline flow model. In particular, the velocity profiles calculated from the numerical model predicts the velocity stabilisation after *ca.*700 s.

4.4.2 Optimal parameter investigation for avoiding two-phase flow during flexible operation

The following presents the results of a series of parametric investigations determining the impact of the various design and operation parameters on the time taken for the transition from supercritical to the undesired two-phase flow at the delivery point following the ramping down of the supercritical CO_2 feed flow rate. The above mimics' the flexible operation of a coal power plant, for example during night-time power ramp down. Such information is highly useful in practice from an operational point of view.

The parameters investigated include pipeline diameter, length, inlet temperature and mass flow rate. The simulations are performed using the numerical model, based on ramping down of the feed flow rate after 1000 s of steady flow operation by 50 % over 700 s following the ramping down function given by equation 4.17. Unless otherwise stated all the conditions tested are the same as those given in table 4.2.

4.4.2.1 Effect of pipeline dimension

Three pipeline lengths of 50 km, 100 km and 150 km corresponding to the pipe inner diameters and wall thicknesses presented in table 4.4 are investigated.

Table 4.4: Pipeline dimensions.

Inner diameter (mm)	Wall thickness (mm)
437	10
486	11
535	12
584	13
874	20

The pipe thicknesses presented in table 4.4 are the minimum safe design values calculated using equation 4.27 (McCoy and Rubin, 2008) based on the maximum operating pressure of 150 bar.

$$Thickness = \frac{P_{MOP}D_o}{2SEF} \quad 4.27$$

where P_{MOP}, D_o, S, E and F are the maximum operating pressure of the pipeline, the outer pipe diameter, the specified minimum yield stress for the pipe material, the longitudinal joint factor and the design factor, respectively. In order to determine the thickness of the pipe, the longitudinal joint factor is set to 1.0, the design factor is 0.72 and the minimum yield stress is 4830 bar for mild steel (McCoy and Rubin, 2008).

Figure 4.9 shows the simulated variation of line drafting time (defined as the time lapsed to reach the two-phase flow) at the pipe end for various pipeline lengths and inner diameters following the commencement of feed ramp down to 50 % of its initial value for pure CO_2.

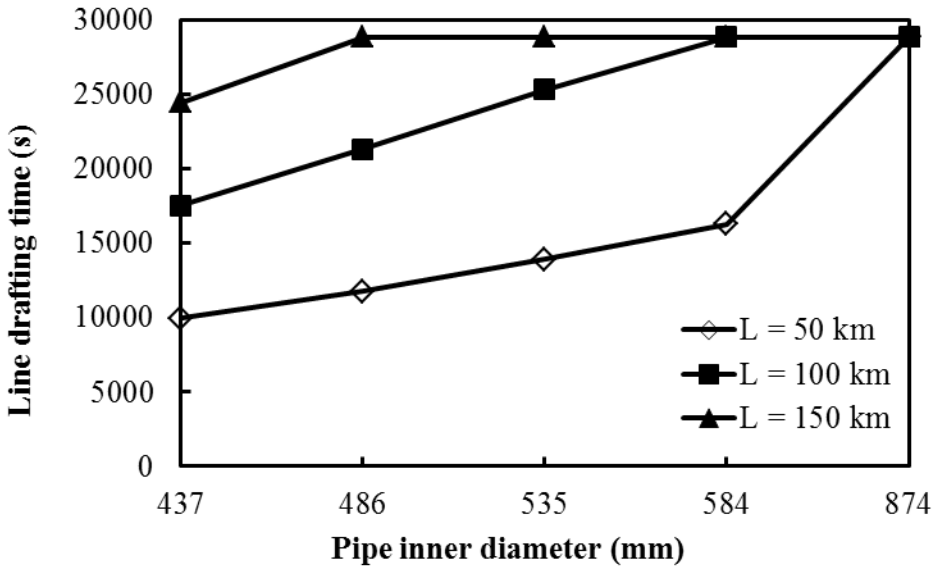

Figure 4.9: Effect of pipeline dimensions on the line drafting time for pure CO_2 following feed ramp down. Parameters: inlet pressure = 150 bar, inlet temperature = 311.15 K, ambient temperature = 278.15 K, inlet mass flow = 100 kg/s and pipe thickness (see table 4.4).

As can be seen in figure 4.9, the line drafting time is significantly affected by the length and the inner diameter of the pipeline. For the same pipeline length, the line drafting time (the time lapsed to reach the two-phase flow) increases with an increase in the pipe inner diameter, with the effect decreasing with increase in the pipeline length. For the maximum pipeline length of 150 km, in the ranges tested, the increase in the pipe inner diameter beyond 486 mm has no impact on the line drafting time.

On the other hand, for the same pipe inner diameter, the line drafting time generally increases with the pipe length. In the case of the 150 km pipeline however, no further increase in the line drafting time may be observed beyond a pipe internal diameter of 486 mm.

The precise mechanism-giving rise to the above observed trends is difficult to discern. The most likely explanation is that these arise because of counteracting interaction of pipeline length and diameter. The reduction in the pressure drop with increase in pipe diameter results in a delay in the transition to two-phase flow and hence an increase in the line drafting time. On the other hand, an increase in the pipeline length results in an increase in the pressure drop resulting in an increase in the line drafting time. According to the data in figure 4.9, the shortest length of the pipe (50 km) with the largest inner diameter (874 mm) just satisfies the single phase flow condition for 8 hours (28800 s) of operation; typical duration for the ramping down of a power plant during night-time operation. For this reason, preserving the practical context, the proceeding investigations are performed based on these pipeline dimensions.

4.4.2.2 Effect of feed stream inlet temperature

To elucidate the effect of feed stream inlet temperature on the line drafting time, the inlet temperature in the 50 km pipeline with 874 mm inner diameter is assumed to vary from 283.15 to 311.15 K. The corresponding data for pure CO_2 are shown in figure 4.10.

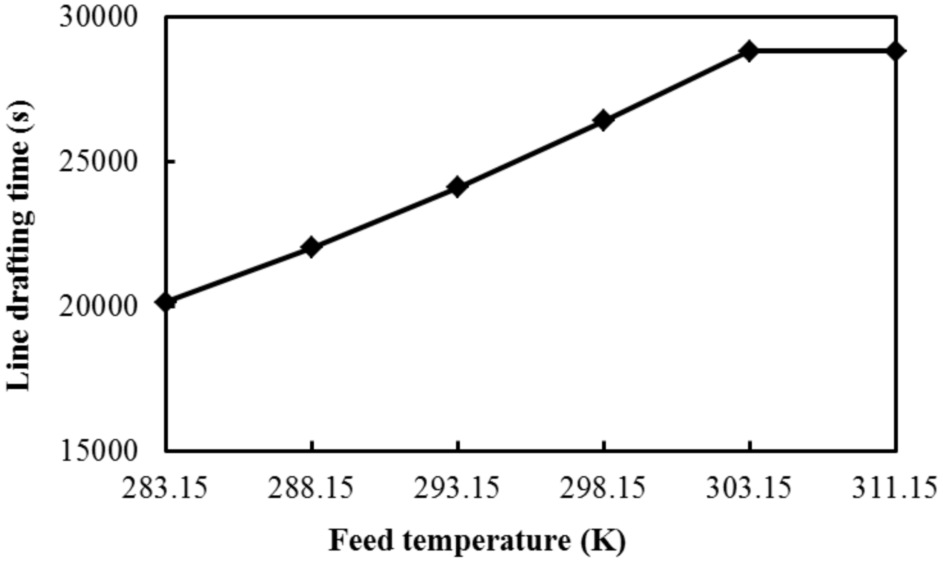

Figure 4.10: Effect of feed temperature on the line drafting time for pure CO_2. Parameters: inlet pressure = 150 bar, ambient temperature = 278.15 K, inlet mass flow = 100 kg/s, pipeline length = 50 km and pipeline inner diameter = 874 mm.

As it may be observed from figure 4.10, the line drafting time increases almost in a linear manner with increasing feed temperature up to 303.15 K, beyond which no further increase in the line drafting time is obtained. The increase in the feed temperature results in two counteracting factors affecting the line drafting time:

i) reduction in the viscosity of dense phase CO_2 (Moshfeghian, 2009), leading to a reduction in the pressure drop and hence an increase in the line drafting time.

ii) the lowering of the pressure at which two-phase flow occurs thus resulting in a decrease in the line drafting time.

Based on the data presented in figure 4.10, it is reasonable to postulate that the effect of the reduction in viscosity is the dominant factor up to the feed temperature of 311.15 K. Beyond this temperature, this effect is counteracted by the earlier transition to two-phase flow with the net effect of only a marginal increase in the line drafting time. In keeping with a practical perspective, given that a high feed temperature poses the risk of damage to the pipeline external coating (Chaczykowski et al., 2012), an inlet temperature of 303.15 K is chosen for the proceeding investigation.

4.4.2.3 Effect of feed mass flow rate

Figure 4.11 shows the variation of line drafting time against initial CO_2 feed mass flow rate in the range of 100 to 150 kg/s for 874 mm inner diameter, 50 km long pipe. As it may be observed, the increase on the mass flow rate and hence the increase in the pressure drop results in a drop in the line drafting time from a maximum value of 28800 s (100 kg/s feed) to 23707 s (150 kg/s feed).

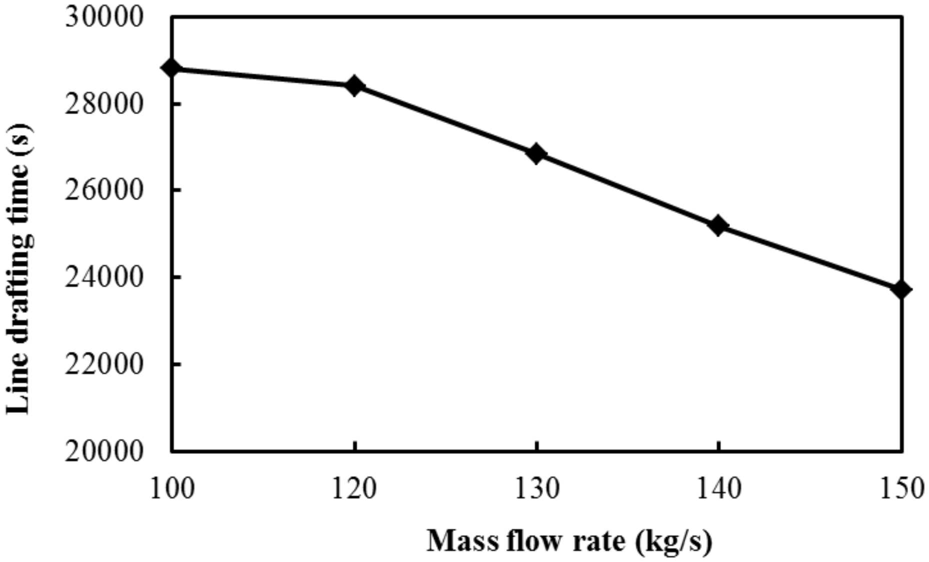

Figure 4.11: Effect of initial feed mass flow rate on the line drafting time of pure CO_2. Parameters: inlet pressure = 150 bar, inlet temperature = 303.15 K, ambient temperature = 278.15 K, pipeline length = 50 km, pipeline inner diameter = 874 mm.

Also an initial feed flow rate of 100 kg/s can maintain the dense phase in the pipe for 8 hours following the feed ramp down.

4.4.3 Application of the optimised line packing parameters

The following presents the results of a case study demonstrating the efficacy of the flow model presented above (see section 4.3) as a design and operational control tool for avoiding two-phase flow for CO_2 pipelines following feed ramping and line drafting. Figures 4.12 and 4.13 respectively show the variation of pressure and temperature as a function of time at the pipeline inlet and outlet for a 50 km, 874 mm inner diameter pipeline containing CO_2 and its various mixtures based on the various capture technologies. The data are presented over 8 hours duration (28800 s) representing the overnight flexible operation of a power plant. The feed flow rate is assumed to be gradually ramped down from maximum of 100 kg/s to 50 kg/s over 700 s following the control function given by equation 4.17. All the remaining relevant parameters are given in the figure caption and table 4.4.

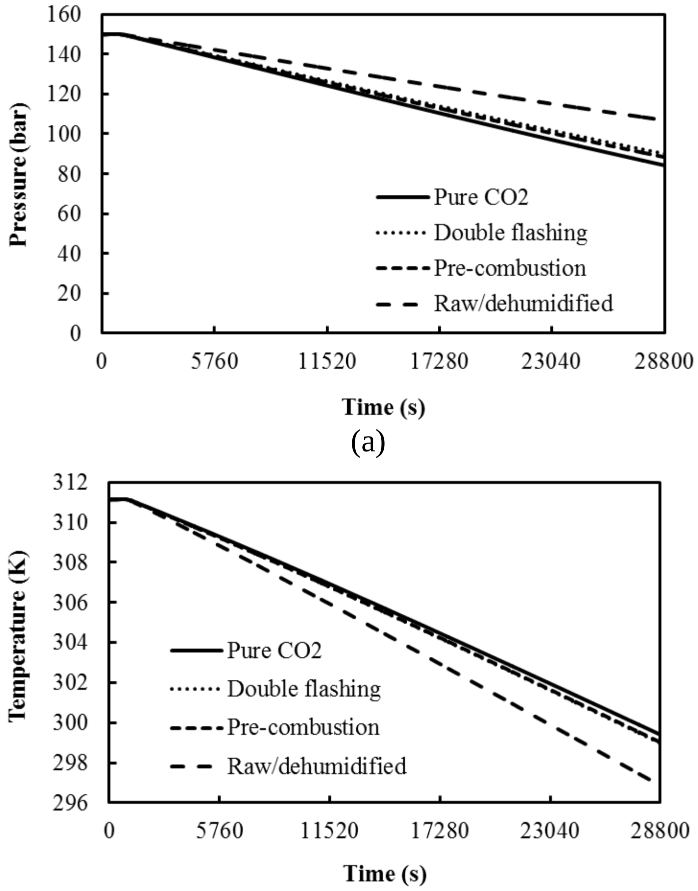

(a)

(b)

Figure 4.12: Change in pressure (a) and temperature (b) of pure CO_2 and CO_2 with impurities at pipeline inlet during flexible operation. Parameters: inlet pressure = 150 bar, mass flow rate = 100 kg/s, inlet temperature = 303.15 K, ambient temperature = 278.15 K, pipeline length = 50 km and pipeline inner diameter = 874 mm.

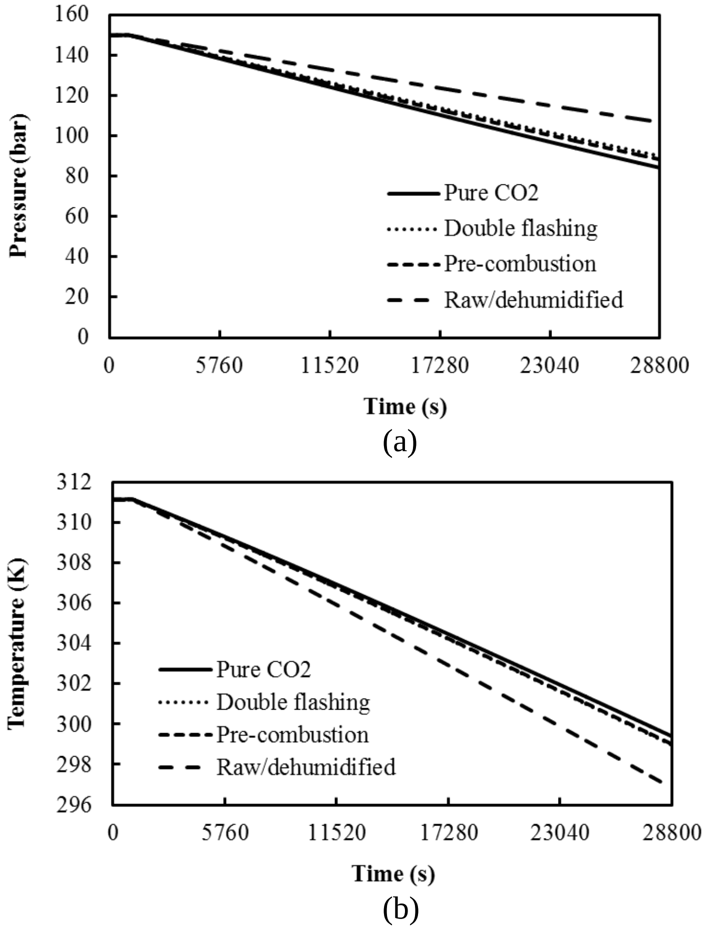

Figure 4.13: Change in pressure (a) and temperature (b) of pure CO_2 and CO_2 with impurities at pipeline outlet during flexible operation. Parameters: inlet pressure = 150 bar, mass flow rate = 100 kg/s, inlet temperature = 303.15 K, ambient temperature = 278.15 K, pipeline length = 50 km and pipeline inner diameter = 874 mm.

Figure 4.14 shows the variation of the pressure and temperature trajectories as extracted from the data in figures 4.12 and 4.13 for the pure CO_2 and its three mixtures superimposed on the corresponding vapour liquid equilibrium diagrams. As it is clear, none of the pressure/temperature trajectories cross the two-phase envelope. This means that for the design and operational conditions chosen, the CO_2 stream and its mixtures will remain in the supercritical dense phase during the overnight power ramping down process.

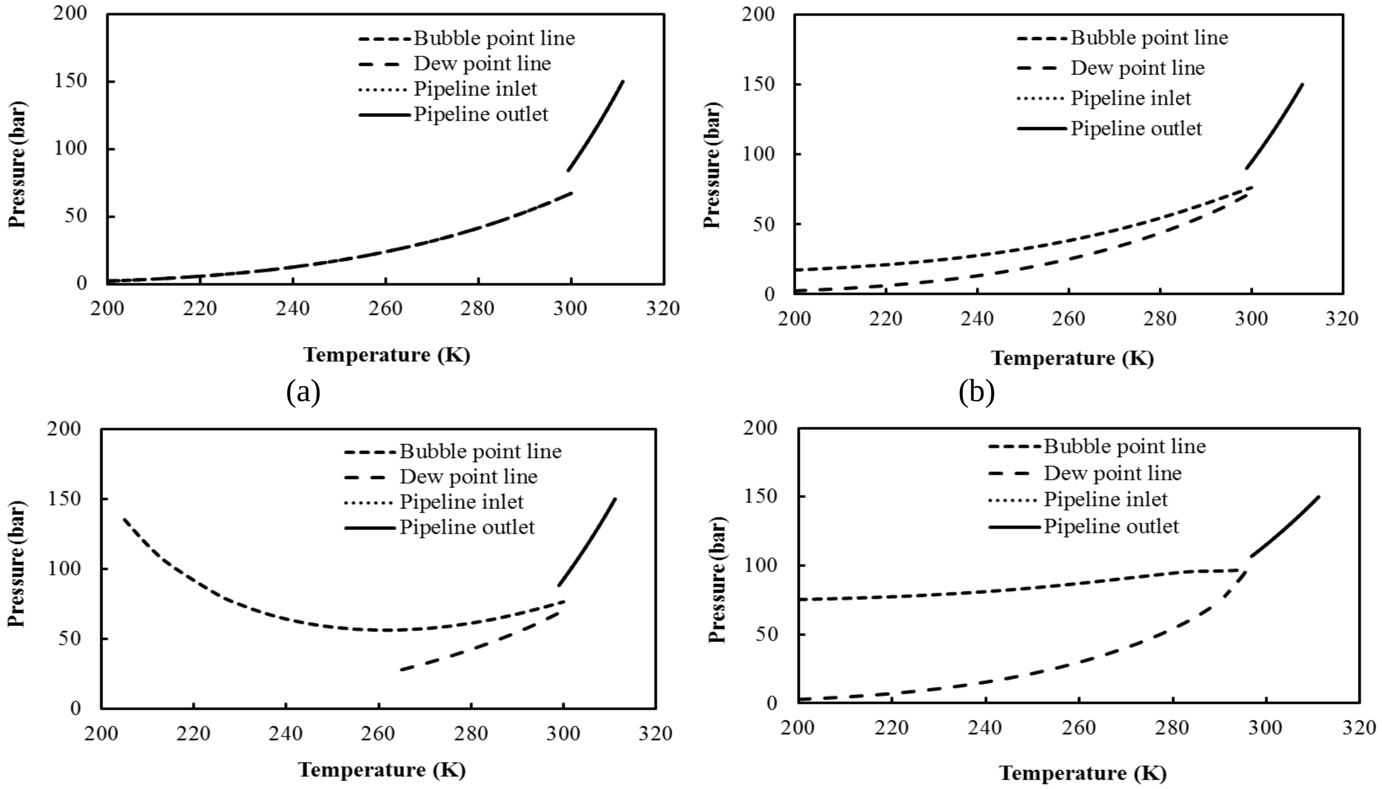

(a) (b)

(c) (d)

Figure 4.14: Pressure-temperature diagram of pure CO_2 (a), double flashing (b), pre-combustion (c) and raw/dehumidified (d) showing the fluid flows in supercritical condition during flexible operation. Parameters: inlet pressure = 150 bar, mass flow rate = 100 kg/s, inlet temperature = 303.15 K, ambient temperature = 278.15 K, pipeline length = 50 km, pipeline inner diameter = 874 mm.

CHAPTER 5:

CONCLUSIONS AND RECOMMENDATIONS FOR FUTURE WORK

5.1 Conclusions

This thesis described the development and testing of rigorous mathematical models for

i) determining the power consumption for multistage compression with intercooling for transporting high pressure CO_2 and the optimum configurations for such systems

ii) simulating the transient flow in high pressure CO_2 pipelines with line packing and line drafting during flexible operation

The following is a summary of the main findings.

In chapter 2, the basic thermodynamic and energy balance relations for calculating the power requirement of multistage compression and cooling duty were discussed. These presented equations coupled with a cubic equation of state representing the foundation of the multistage compression model. The thermodynamic relations for predicting the pertinent fluid properties such as the fluid enthalpy, entropy and discharge temperature were also presented.

The application of the general equations for modelling multistage compressor and intercooler for the CO_2 pipeline transportation was reviewed. Most of the reviewed studies have focused on design and optimisation of compression systems capable of handling the operating constraints for near pure CO_2 streams as well as examining the opportunities for integration of the compression in CCS and the power generation process. Practically, the CO_2 streams in CCS will contain some impurities, whose nature and concentrations depend on the emission source and capture technology applied. In this thesis, the effect of CO_2 impurities from various capture technologies on the power requirement of several industrial compression schemes as those previously recommended for near pure CO_2 streams captured in a post-combustion plant were investigated.

In the second part of chapter 2, the mass, momentum and energy conservation equations for developing the numerical transient fluid flow model in a pipeline were presented. These were expressed in terms of the dependent variables pressure, enthalpy/entropy and velocity. The governing system of conservation equations were shown to be quasi-hyperbolic in character. The various hydrodynamic and thermodynamic expressions for predicting important parameters including the speed of sound, fluid viscosity as well as fluid flow and phase dependent friction coefficient were presented. Based on the detailed review of the reported transient fluid flow models, the UCL model was found to be the most robust, performing best in terms of accuracy and was according used as the starting point for further fundamental development in this work. The Method of Characteristics was chosen to solve the conservation equations, as it is well suited to handling the dynamic flow in the pipeline system. The formulation and implementation of the Method of Characteristics based on the Method of Specified Time intervals was also described. The governing conservation equations were converted into compatibility and characteristic equations. These were then discretised using the Euler predictor-corrector technique.

In chapter 3, a brief introduction of the compression systems employed in CCS, concentrating specifically on those works examining the opportunities for integration of the compression in CCS and the power generation process was presented. The types of industrial compression technologies and the impurities present in the captured CO_2 streams were also discussed. This chapter further presented the development and application of a detailed thermodynamic model to compute and compare power requirements for multistage compression strategies and inter-coolers as well as cooling duty for CO_2 streams. The CO_2 streams considered included those captured from oxy-fuel and pre-combustion coal-fired power plants. The four compression options examined included gas-phase compression using conventional multistage integrally geared centrifugal compressors, supersonic shockwave compressors and multistage compressors combined with subcritical as well as supercritical liquefaction and pumping. In order to estimate the power demand for inter-stage cooling and liquefaction, a thermodynamic model based on the Carnot refrigeration cycle was applied. Given the relatively high pressures of CO_2 streams captured in oxy-fuel and pre-combustion processes, the analysis was performed for the high-pressure compression phase starting at 15 bar.

The results of a thermodynamic analysis performed for determining the power requirements for the compression of CO_2 streams for pipeline transportation and subsequent geological sequestration were presented. It was found that for oxy-fuel and pre-combustion CO_2 streams of purity higher than *ca.* 96 % v/v, the compression power for the four compression strategies examined was not significantly affected by the presence of impurities. In the case of the oxy-fuel stream with 85 % v/v CO_2 purity, the compression power requirement for the four compression schemes considered was found to increase by *ca.* 12-30 % more than that for the compression of pure CO_2. Given that the power demand for compression increases with the amount of CO_2 stream impurities the removal of which would raise the capture costs, there is a potential trade-off between the costs of compression and purification. By combining the present methodology with a cost-benefit analysis model for the compression and purification, an optimal CO_2 stream purity for a given CCS plant may be determined.

The power demand for operating the inter-stage coolers was estimated to be relatively small in comparison with the compression power demand (less than *ca.* 5 %) when using the centrifugal and shock-wave compressors. However, when using compression combined with subcritical and supercritical liquefaction and pumping, the cooling system operation can take up about 50 % of the compression power when applied to the oxy-fuel double-flash and pre-combustion CO_2 streams. In the case of oxy-fuel raw/dehumidified CO_2 mixture, the cooling power was predicted to be nearly 1.5 times higher than the compression power demand when applying to compression combined with subcritical liquefaction and about 65 % of the compression power for the compression combined with supercritical liquefaction and pumping.

The relatively high estimated power demand for the operation of the compressor cooling system can be attributed to large cooling duties for the liquefaction of impure CO_2 streams. In particular, the cooling duty was shown to increase by up to 50 % when compressing oxy-fuel CO_2 with 85 % v/v purity as compared to that for pure CO_2. Remarkably, for CO_2 streams of higher than 96 % v/v purity, compression combined with subcritical liquefaction and pumping can result in as much as *ca.* 15 % increase in efficiency as compared to conventional centrifugal compression. The liquefaction can be achieved at subcritical pressures around 62.53 bar using conventional water cooling systems at temperatures in the range 10-20 ^oC. At the same time, the study showed that operating such a system becomes less feasible for lower grade CO_2 streams due to incomplete liquefaction of the CO_2 stream. In particular, given the low bubble-point temperatures of oxy-fuel streams of *ca.* 85 % CO_2 purity, liquefaction at 62.53 bar would require using coolant temperatures as low as -62 ^oC which would not be economically viable. This temperature may be increased by applying CO_2 liquefaction at higher pressures, however, to determine the optimal conditions for the liquefaction, the trade-off between the costs for operating compressors and cooling/pumping system should be carefully considered. In practice, a whole-system approach should be applied to optimise the compression and purification system design and balance the costs associated with the operation of specific equipment, such as compressors and refrigeration units.

In chapter 4, a brief introduction of the concept of flexible operation typically encountered in the case of fossil fuel power plants was presented. Methods for improving the flexibility of industrial or utility processes with CCS and the control strategies to deal with this scenario were also discussed. Chapter 4 further presented the development and testing of a numerical CFD model simulating unsteady state fluid flow behaviour in high-pressure CO_2 transportation pipelines employed as part of the CCS chain. This work was undertaken given that in practice, the flow rate of CO_2 produced from the emission source and subsequently transported in the pipeline will often change due to operational constraints. Given that the most economical method for pipeline transportation of CO_2 is in the dense liquid phase, the reduction in the CO_2 flow may result in the formation of the highly undesirable two-phase flow during line drafting.

Following the presentation of its development, the transient flow model's predictions were compared against those based on a far less computationally demanding analytical model. The latter was based on the assumption that the transported dense phase CO_2 is incompressible and remains so throughout the flow process. A reasonable degree of agreement was demonstrated between the two models.

Following its verification, the transient numerical model was employed to conduct a series of realistic parametric studies investigating the transient flow behaviour following a simulated flexible operation involving a gradual 'prescribed' reduction in the feed flow rate. The investigations involved changes in the pipeline internal diameter, overall length, feed flow rate and temperature and investigating their impacts on the resulting pressure and temperature at the pipeline inlet and outlet over a period of 8 hours; the latter being the typical duration for a power plant during night-time operation. In keeping with a practical perspective, pure CO_2 as well as its three mixtures typical of those for the various commercial capture technologies were included in the above investigations.

The critically important time lapsed to reach the two-phase flow (termed as 'the line drafting time') following a feed ramp down was obtained by superimposing the simulated pipe inlet and outlet pressure and temperature trajectories on the corresponding fluid phase envelops.

Based on the results obtained, the following conclusions may be made for the specific case studies examined:

i) Impact of pipeline length and internal diameter

Increasing the pipeline length from 50 to 150 km for the same pipe inner diameter (437 mm) resulted in an increase in the line drafting time given that the upstream flow disturbance took longer to propagate to the downstream pipe end. However, as the pipelines length increased to 150 km, the increase in the pipe inner diameter beyond 486 mm was found to have no further impact on the line drafting time. The most likely explanation for this is the counteracting impacts of increase in pipe diameter (reduced pressure drop hence an increase in the line drafting time) and the pipe length (increased pressure drop hence a decrease in the line drafting time).

ii) Impact of feed temperature

It was found that the line drafting time increases following an increase in the inlet feed temperature of transported CO_2 stream up to 303.15 K. This is believed to be due to the reduction in the viscosity of dense phase CO_2, leading to a reduction in the pressure drop and hence an increase in the line drafting time. Beyond the operating inlet feed temperature of 311.15 K, the line drafting time only marginally increased. This is believed to be due to the lowering of the pressure at which two-phase flow occurs.

iii) Impact of the CO_2 stream concentration

The simulation studies revealed that the fluid flow properties were significantly affected by the CO_2 stream composition. In the case of the raw/dehumidified oxy-fuel stream with 85 % v/v CO_2 purity, with the passage of time during the ramping down process, the pressures at pipeline inlet and outlet were found to be considerably higher than for the remaining streams due to the higher critical pressure and larger pressure variation along the saturation curve of the mixture. In addition, the largest temperature and pressure drop corresponded to raw/dehumidified stream, given its lower density and thus the higher flow velocity as compared to the other CO_2 streams. In the case of pre-combustion and double flashing, given the relatively low impurity concentration, the flow parameters were found to be nearly identical to those for pure CO_2 .

Based on the pipeline design and operation optimisation study conducted, it was shown that two-phase flow could be avoided during the 8 hours ramping down process for pure CO_2 and all its stream mixtures investigated.

Finally, the simulation results presented in this work demonstrated that a pipeline packing capacity may be used as a preventive measure to avoid the undesirable two-phase flow during flexible operation and hence compensate against large fluctuations in the upstream flow conditions. The appropriate choice of the pipeline overall dimensions and upstream flow conditions play critical roles in delaying the transition to two-phase. The numerical simulation presented in this work is intended to enable this.

Having said this, whilst using pipeline packing may be used as a short-term storage option, which may allow operational issues elsewhere in the network to be addressed, it will not provide a solution to a major planned or unplanned outage at the capture or injection site. In such situations, the use of more effective techniques such as large capacity intermediate CO_2 storage should be considered.

5.2 Recommendations for future work

At present, the compression model for pure CO_2 and impure CO_2 streams presented in this work is limited to determining the power consumption of compression and inter-stage cooler as well as the cooling duty of intercooling system. Its application to perform an economic analysis that leads to the minimum capital and operating costs of the industrial compression technology options available would be desirable.

Further investigations related to the compression process should be carried out for each impure component in the CO_2 gas mixtures to investigate the effect of impurities on the physical properties of the fluid and hence the compression power.

The pipeline fluid flow model should be extended to deal with transient fluid flow scenarios in pipeline networks covering start-up, shut-down and compressor trip to investigate the efficacy of pipeline network as line packing.

In the present study, the main focus has been on the use of the pipeline itself to hedge against fluctuations in the upstream flow conditions. Given the limited practical scope of the above strategy in particular when dealing with large flow fluctuations, the extension of this work to other preventive measures such as fabricated intermediate

CO_2 storage vessels or underground CO_2 storage along the length of the pipeline should be undertaken. This exercise should however be conducted in line with the corresponding safety, capital and operating cost implications.

The effect of variable and intermittent flows of CO_2 on wellbore integrity and storage reservoirs in saline formations, depleted oil and gas fields is not well understood, presenting an obvious important extension of this work.

References

AGHAJANI, H., RACE, J. M., WETENHALL, B., SANCHEZ FERNANDEZ, E., LUCQUIAUD, M. & CHALMERS, H. 2017. On the Potential for Interim Storage in Dense Phase CO_2 Pipelines. *International Journal of Greenhouse Gas Control*, 66, 1-28.

APSLEY, D. 2013. Unsteady flow in pipes. Available: http://personalpages.manchester.ac.uk/staff/david.d.apsley/lectures/hydraulics2/t5.pdf [Accessed 6th November 2017].

ASPELUND, A. & JORDAL, K. 2007. Gas conditioning-The interface between CO_2 capture and transport. *International Journal of Greenhouse Gas Control*, 1, 343-354.

AUSTBØ, B. 2015. *Use of optimization in evaluation and design of liquefaction processes for natural gas*. Norwegian University of Science and Technology. Available:https://brage.bibsys.no/xmlui/bitstream/handle/11250/280210/NTNU_Bjorn_Austbo_PhD_avhandling_ny.pdf?sequence=1&isAllowed=y [Accessed 20th June 2016].

BABCOCK, D. 2009. Low-cost, high efficiency CO_2 compressors. *Carbon Capture Journal*, Sept/Oct 2009, 1-4. Available: http://www.carboncapturejournal.com/news/the-past-present-and-future-of-co2-compression/3203.aspx?Category=featured [Accessed 20th December 2014].

BALDWIN, P. & WILLIAMS, J. 2009. *Capturing CO_2-Gas compression vs. liquefaction* [Online]. Available: http://www.powermag.com/capturing-co2-gas-compression-vs-liquefaction/ [Accessed 28th October 2015 2015].

BENDIKSEN, K. H., MAINES, D., MOE, R. & NULAND, S. 1991. The dynamic two-fluid model OLGA: theory and applications. *Society of Petroleum Engineers Journal*, 6, 171-180.

BESONG, M. T., MAROTO-VALER, M. M. & FINN, A. J. 2013. Study of design parameters affecting the performance of CO_2 purification units in oxy-fuel combustion. *International Journal of Greenhouse Gas Control*, 12, 441-449.

BRATLAND, O. 2009. *Pipe Flow 1: Single-phase flow assurance*. Available: http://www.drbratland.com/ [Accessed 28th October 2015].

BRENAN, K. E., CAMPBELL, S. L. & PETZOLD, L. R. 1996. Classics in applied mathematics, *Numerical Solution of Initial-Value Problems in Differential-Algebraic Equation*, Siam.

CAPROS, P., DE VITA, A., TASIOS, N., PAPADOPOULOS, D., SISKOS, P., APOSTOLAKI, E., ZAMPARA, M., PAROUSSOS, L., FRAGIADAKIS, K. & KOUVARITAKIS, N. 2013. EU energy, transport and GHG emissions trends to 2050, Reference scenario 2013. European Commission.

CENGEL, Y. A. & BOLES, M. A. 2011. *Thermodynamics: An engineering approach, seventh edition,* Mc Graw Hill.

CHACZYKOWSKI, M. & OSIADACZ, A. J. 2012. Dynamic simulation of pipelines containing dense phase/supercritical CO_2-rich mixtures for carbon capture and storage. *International Journal of Greenhouse Gas Control,* 9**,** 446-456.

CHALMERS, H. & GIBBINS, J. 2007. Initial evaluation of the impact of post-combustion capture of carbon dioxide on supercritical pulverised coal power plant part load performance. *Fuel,* 86**,** 2109-2123.

CHALMERS, H., GIBBINS, J. & LEACH, M. 2012. Valuing power plant flexibility with CCS: the case of post-combustion capture retrofits. *Mitigation and Adaptation Strategies for Global Change,* 17**,** 621-649.

CHALMERS, H., LEACH, M. & GIBBINS, J. 2011. Built-in flexibility at retrofitted power plants: What is it worth and can we afford to ignore it? *Energy Procedia,* 4**,** 2596-2603.

CHALMERS, H., LUCQUIAUD, M., GIBBINS, J. & LEACH, M. 2009. Flexible operation of coal fired power plants with post combustion capture of carbon dioxide. *Journal of Environmental Engineering,* 135**,** 449-458.

CHEBOUBA, A. 2015. Multi objective optimization of line pack management of gas pipeline system. *Journal of Physics: Conference Series,* 574**,** 1-4.

CHEN, J.-R. 1993. *Modelling of transient flow in pipeline blowdown problems.* Ph.D thesis, Imperial College London.

CHEN, N. H. 1979. An explicit equation for friction factor in pipe. *Industrial & Engineering Chemistry Fundamental,* 18**,** 296-297.

CHEN, Q., KANG, C., XIA, Q. & KIRSCHEN, D. S. 2012. Optimal Flexible Operation of a CO_2 Capture Power plant in a combined energy and carbon emission market. *IEEE Transactions on Power Systems,* 27**,** 1602-1609.

CLEAVER, R. P., CUMBER, P. S. & HALFORD, A. 2003. Modelling outflow from a ruptured pipeline transporting compressed volatile liquids. *Journal of Loss Prevention in the Process Industries,* 16**,** 533-543.

COLEBROOK, C. F. 1939. Turbulent Flow in Pipes with Particular reference to the Transition Region between the Smooth and Rough Pipe Laws. *Institution of Civil Engineering Journal,* 11**,** 133-156.

CUMBER, P. S. 2007. Outflow from fractured pipelines transporting supercritical ethylene. *Journal of Loss Prevention in the Process Industries,* 20**,** 26-37.

DE NEVERS, N. & DAY, A. 1983. Packing and Drafting in Natural Gas Pipelines. *Journal of Petroleum Technology*, 35, 1-4.

DE VISSER, E., HENDRIKS, C., BARRIO, M., MØLNVIK, M. J., DE KOEIJER, G., LILJEMARK, S. & LE GALLO, Y. 2008. Dynamis CO_2 quality recommendations. *International Journal of Greenhouse Gas Control,* 2**,** 478-484.

DILLON, D. J., PANESAR, R. S., WALL, R. A., ALLAM, R. J., WHITE, V., GIBBINS, J. & HAINES, M. R. 2005. Oxy-combustion processes for CO_2 capture from advanced supercritical PF and NGCC power plant. *Research Gate***,** 1-10.

DOMENICHINI, R., MANCUSO, L., FERRARI, N. & DAVISON, J. 2013. Operating Flexibility of Power Plants with Carbon Capture and Storage (CCS). *Energy Procedia,* 37**,** 2727-2737.

DUAN, L., CHEN, X. & YANG, Y. 2013. Study on a novel process for CO_2 compression and liquefaction integrated with the refrigeration process. *International Journal of Energy Research,* 37**,** 1453-1464.

DUSCHEK, W., KLEINRAHM, R. & WAGNER, W. 1990. Measurement and correlation of the (pressure, density, temperature) relation of carbon dioxide I. The homogeneous gas and liquid regions in the temperature range from 217 K to 340 K at pressures up to 9 MPa. *Journal of Chemical and Thermodynamics,* 22**,** 827-840.

ERLACH, B., SCHMIDT, M. & TSATSARONIS, G. 2011. Comparison of carbon capture IGCC with pre-combustion decarbonisation and with chemical-looping combustion. *Energy,* 36**,** 3804-3815.

EURELECTRIC 2011. Power statistics & trends 2011 synopsis. VGB POWERTECH special issue: vgb contribution on availability/unavailability of power plants. Available: http://orael.ru/inside/experience/statistics/Power_Statistics_and_Trends_Synospsis-2011.pdf [Accessed 28th October 2015].

FLATT, R. 1986. Unsteady compressible flow in long pipelines following a rupture. *International Journal for Numerical Methods in Fluids,* 6**,** 83-100.

GOOS, E., RIEDEL, U., ZHAO, L. & BLUM, L. 2011. Phase diagrams of CO2 and CO_2-N_2 gas mixtures and their application in compression processes. *Energy Procedia,* 4**,** 3778-3785.

GREENSHIELDS, C. J., VENIZELOS, G. P. & IVANKOVIC, A. 2000. A fluid-structure model for fast brittle fracture in plastic pipes. *Journal of Fluids and Structures,* 14**,** 221-234.

GUSCA, J. & BLUMBERGA, D. 2011. Simplified dynamic life cycle assessment model of CO_2 compression, transportation and injection phase within carbon capture and storage. *Energy Procedia,* 4**,** 2526–2532.

HAGAN, M. T., DEMUTH, H. B., BEALE, M. H. & JESÚS, O. D. 1997. *Neural Network Design 2nd Edition*. Available: http://hagan.okstate.edu/NNDesign.pdf [Accessed 28th October 2015].

HAINES, M. R. & DAVISON, J. E. 2009. Designing carbon capture power plants to assist in meeting peak power demand. *Energy Procedia,* 1**,** 1457-1464.

HAN, D.-H., SUN, M. & BATZLE, M. 2010. CO_2 velocity measurement and models for temperatures. *Geophysics,* 75**,** E123-E129.

HOLLOWAY, S. & AKAI, M. 2006. Carbon Dioxide Transport, Injection and Geological Storage. *2006 IPCC Guidelines for National Greenhouse Gas Inventories.* Available:http://www.ipcc-nggip.iges.or.jp/public/2006gl/pdf/2_Volume2/V2_5_Ch5_CCS.pdf [Accessed 3rd March 2016].

HUSSY, C., KLAASSEN, E., KOORNNEEF, J. & WIGAND, F. 2014. International comparison of fossil power efficiency and CO_2 intensity-update 2014 final report. Sustainable energy for everyone. Available: https://www.ecofys.com/files/files/ecofys-2014-international-comparison-fossil-power-efficiency.pdf [Accessed 28th October 2015].

HYPROTECH 2003. ProFES - Reference Guide. Houston: Aspentech. Available: https://courses.cs.ut.ee/MTAT.03.243/2015_spring/uploads/Main/PUM.pdf [Accessed 28th October 2015].

IEAGHG 2011. Technical specifications: Impact of CO_2 Impurity on CO_2 Compression, Liquefaction and Transportation (IEA/Con/13/213).

IEAGHG 2012. Operating flexibility of power plants with CCS. International Energy Agency (IEA). Available: http://ieaghg.org/docs/General_Docs/Reports/2012-06%20Reduced.pdf [Accessed 29th October 2015].

JENSEN, M. D., SCHLASNER, S. M., SORENSEN, J. A. & HAMLING, J. A. 2016. Operational flexibilty of CO_2 transport and storage. *In:* IEAGHG (ed.). Energy & Environmental Research Center. Available: http://ieaghg.org/docs/General_Docs/Reports/2016-04.pdf [Accessed 28th March 2017].

JI, W. R. & LEMPE, D. A. 1997. Density improvement of the SRK equation of state. *Fluid Phase Equilibria,* 130**,** 49-63.

JOBSON, M. 2014. Distillation: Fundamentals and Principles. Energy Considerations in Distillation. Academic Press, Elsevier.

KATHER, A. & KOWNATZKI, S. 2011. Assessment of the different parameters affecting the CO_2 purity from coal fired oxyfuel process. *International Journal of Greenhouse Gas Control,* 5, 204-209.

KEENAN, J. H. & NEUMANN, E. P. 1943. Measurement of friction in a pipe for subsonic and supersonic flow of air. NACA Wartime Reports. Available: http://www.dtic.mil/dtic/tr/fulltext/u2/b806006.pdf [Accessed 20th November 2016].

KIDD, H. A. & MILLER, H. F. 2011. World’s First Supersonic CO_2 Compression Test Facility. Available: http://204.168.70.44/insights/Spring11/insights_Spring11_RamgenTest.pdf. [Accessed 28th October 2015].

KIDD, H. A. & MILLER, H. F. 2012. Compression solutions for CO_2 applications-Traditional centrifugal and supersonic technology. Available: http://en.youscribe.com/catalogue/educational-resources/education/quizzes-and-revision/compression-solutions-for-co2-applications-traditional-1413713. [Accessed 28th October 2015].

KLINKBY, L., NIELSEN, C. M., KROGH, E., SMITH, I. E., PALM, B. & BERNSTONE, C. 2011. Simulating rapidly fluctuating CO_2 flow into the Vedsted CO_2 pipeline, injection well and reservoir. *Energy Procedia,* 4**,** 4291-4298.

KOWNATZKI, S. & KATHER, A. 2011. CO_2 Purity in Coal Fired Oxyfuel Processes. *2nd Oxyfuel Combustion Conference.* Queensland, Australia

LEMMON, E. W. & HUBER, M. L. 2010. *NIST Standard Reference Database 23* [Online]. Available: http://www.nist.gov/srd/nist23.cfm [Accessed 29 October 2015].

LEVEQUE, R. J. 2002. *Finite Volume Methods for Hyperbolic Problems,* Cambridge texts in applied mathematics, Cambridge University Press.

LI, H., JAKOBSEN, J. P., WILHELMSEN, Ø. & YAN, J. 2011. PVTxy properties of CO_2 mixtures relevant for CO_2 capture, transport and storage: Review of available experimental data and theoretical models. *Applied Energy,* 88**,** 3567-3579.

LI, H. & YAN, J. 2009. Evaluating cubic equations of state for calculation of vapor–liquid equilibrium of CO_2 and CO_2-mixtures for CO_2 capture and storage processes. *Applied Energy,* 86**,** 826-836.

LILJEMARK, S., ARVIDSSON, K., MC CANN, M. T. P., TUMMESCHEIT, H. & VELUT, S. 2011. Dynamic simulation of a carbon dioxide transfer pipeline for analysis of normal operation and failure modes. *Energy Procedia,* 4**,** 3040-3047.

LIPOVKA, A. Y. & LIPOVKA, Y. L. 2014. Determining hydraulic friction factor for pipeline systems. *Journal of Siberian Federal University. Engineering & Technologies,* 1**,** 62-82.

LU, K., ZHOU, J., ZHOU, L., CHEN, X. S., CHAN, S. H. & SUN, Q. 2012. Pre-combustion CO_2 capture by transition metal ions embedded in phthalocyanine sheets. *The Journal of Chemical Physics,* 136**,** 234703.

LUDTKE, K., H. 2004. *Process centrifugal compressors: Basic, Function, Operation, Design, Application* Springer-Verlag Berlin Heidelberg 2004.

MAHGEREFTEH, H. & ATTI, O. 2006. Modeling low-temperature-induced failure of pressurized pipelines. *AIChE Journal,* 52**,** 1248-1256.

MAHGEREFTEH, H., RYKOV, Y. & DENTON, G. 2009. Courant, Friedrichs and Lewy (CFL) impact on numerical convergence of highly transient flows. *Chemical Engineering Science,* 64**,** 4969-4975.

MAHGEREFTEH, H., SAHA, P. & ECONOMOU, I. G. 1997. A Study of the Dynamic Response of Emergency Shutdown Valves Following Full Bore Rupture of Gas Pipelines. *Process Safety and Environmental Protection,* 75**,** 201-209.

MAHGEREFTEH, H., SAHA, P. & ECONOMOU, I. G. 1999. Fast Numerical Simulation for Full Bore Rupture of Pressurized Pipelines. *AiCHE Journal,* 45**,** 1191-1201.

MARTYNOV, S. B., DAUD, N. K., MAHGEREFTEH, H., BROWN, S. & PORTER, R. T. J. 2016. Impact of stream impurities on compressor power requirements for CO_2 pipeline transportation. *International Journal of Greenhouse Gas Control,* 54**,** 652-661.

MAZZOCCOLI, M., BOSIO, B. & ARATO, E. 2012. Analysis and Comparison of Equations-of-State with p-ρ-T Experimental Data for CO_2 and CO_2-Mixture Pipeline Transport. *Energy Procedia,* 23**,** 274-283.

MCCOY, S. & RUBIN, E. 2008. An engineering-economic model of pipeline transport of CO2 with application to carbon capture and storage. *International Journal of Greenhouse Gas Control*, 2**,** 219-229.

MCMULLEN, J. 2016. *The Importance of Production Allocation in Oil & Gas* [Online]. Schneider Electric. Available: http://software.schneider-electric.com/products/simsci/design/pro-ii/ [Accessed 4th July 2017].

MECHLERI, E., LAWAL, A., STAFFELL, I. & DOWELL, N. M. 2016. Evaluation of process control strategies for normal, flexible and upset operation conditions of CO_2 post combustion capture processes. IEAGHG. Available: http://ieaghg.org/docs/General_Docs/Reports/2016-07.pdf [Accessed 28th October 2015].

MENON, E. S. 2005. *Gas pipeline hydraulics,* CRC Press, Taylor & Francis.

METZ, B., DAVIDSON, O., CONINCK, H. D. & MEYER, M. L. L. 2005. IPCC Special Report on Carbon Dioxide Capture and Storage. Intergovernmental Panel on Climate Change. Available: https://www.ipcc.ch/pdf/special-reports/srccs/srccs_wholereport.pdf [Accessed 28th October 2015].

MODEKURTI, S., ESLICK, J., OMELL, B., BHATTACHARYYA, D., MILLER, D. C. & ZITNEY, S. E. 2017. Design, dynamic modeling, and control of a multistage CO_2 compression system. *International Journal of Greenhouse Gas Control*, 62**,** 31-45.

MOORE, J. J., LERCHE, A., DELGADO, H., ALLISON, T. & PACHECO, J. Development of Advanced Centrifugal Compressors and Pumps for Carbon Capture and Sequestration Applications. Proceedings of the Fortieth Turbomachinery Symposium, September 12-15, 2011 2011 Houston, Texas. 107-120.

MOSHFEGHIAN, M. 2009. *Variation of properties in the dense phase region; Part 1 Pure Compounds* [Online]. PetroSkills'. Available: http://www.jmcampbell.com/tip-of-the-month/2009/12/variation-of-properties-in-the-dense-phase-region-part-1-pure-compounds/ [Accessed 22 March 2017].

MOSHFEGHIAN, M., LILLY, L. L. & BOTHAMLEY, M. 2008. Feed-gas molecular weight affects centrifugal compressor efficiency. *Compressor & Turbines Optimization & Troubleshooting Conference.* Aberdeen. [Online]. Available: https://www.scribd.com/document/187312736/Feed-Gas-Molecular-Weight-Affects-Centrifugal-Compressor-Efficiency [Accessed: 28th October 2015].

NEWCOMER, A. & APT, J. 2007. Storing syngas lowerss the carbon price for profitable coal gasification. *Environmental Science Technology*, 41**,** 7974-7979.

NISHIUMI, H. & ARAI, T. 1988. Generalization of the binary interaction parameter of the Peng-Robinson Equation of State by component family. *Fluid Phase Equilibria,* 42**,** 43-62.

NORDSVEEN, M. & HAERDIG, A. 1997. Simulation of severe slugging during depressurisation of an oil/gas pipeline. *Modelling, Identification and Control,* 18**,** 61-73.

NORMANN, F., JANSSON, E., PETERSSON, T. & ANDERSSON, K. 2013. Nitrogen and sulphur chemistry in pressurised flue gas systems: A comparison of modelling and experiments. *International Journal of Greenhouse Gas Control,* 12**,** 26-34.

NOTEBOOK, E. S. 2011. CO_2 compression for capture and injection in today's environmental world [Online]. Available: http://www.dresser-rand.com/news-insights/engineers-notebook-co2-compression-for-capture-and-injection-in-todays-environmental-world/ [Accessed 29 November 2015].

OAKEY, J., KARA, F., PATCHIGOLLA, K. & STIFF, S. 2010. The effects of impurities for capture technologies on CO_2 compression and transport. Final Report ed. Centre for Energy and Resource Technology: Cranfield University. [Online]. Available: http://www.bcura.org/Final%20Projects/b93_final_report.pdf [Accessed 28 October 2015].

OKE, A., MAHGEREFTEH, H., ECONOMOU, I. & RYKOV, Y. 2003. A transient outflow model for pipeline puncture. *Chemical Engineering Science,* 58**,** 4591-4604.

OUYANG, L.-B. & AZIZ, K. Development of new wall friction factor and interfacial friction factor correlations for gas-liquid stratified flow in wells and pipelines. SPE Western Regional Meeting, 22-24 May 1996. Society of Petroleum Engineers, 11.

PATEL, N. C. & TEJA, A. S. 1982. A new cubic equation of state for fluids and fluid mixtures. *Chemical Engineering Science,* 37**,** 463-473.

PAUL, M. M., NAHEIRI, T. & OH, E. M. 1989. A density correction for the Peng-Robinson equation of state. *Fluid Phase Equilibria,* 47**,** 77-87.

PEI, P., BARSE, K., GIL, A. J. & NASAH, J. 2014. Waste heat recovery in CO_2 compression. *International Journal of Greenhouse Gas Control,* 30**,** 86-96.

PENELOUX, A. & RAUZY, E. 1982. A consistent correction for Redlich-Kwong-Soave volumes. *Fluid Phase Equilibria,* 8**,** 7-23.

PENG, D.-Y. & ROBINSON, D. B. 1976. A New Two-Constant Equation of State. *Industrial & Engineering Chemistry Fundamentals,* 15**,** 59-64.

PICARD, D. J. & BISHNOI, P. R. 1987. Calculation of the thermodynamic sound velocity in two-phase multicomponent fluids. *International Journal of Multiphase Flow*, 13**,** 293-308.

PIESSENS, R. 1983. *Quadpack: a subroutine package for automatic integration*, Berlin ; New York : Springer-Verlag, 1983.

PIPITONE, G. & BOLLAND, O. 2009. Power generation with CO_2 capture: Technology for CO_2 purification. *International Journal of Greenhouse Gas Control,* 3**,** 528-534.

POPESCU, M. 2009. Modeling of fluid dynamics interacting with ductile fraction propagation in high pressure pipeline. *Acta Mechanica Sinica*, 25**,** 311-318.

PORTER, R. T. J., FAIRWEATHER, M., POURKASHANIAN, M. & WOOLLEY, R. M. 2015. The range and level of impurities in CO_2 streams from different carbon capture sources. *International Journal of Greenhouse Gas Control*, 36**,** 161-174.

POSCH, S. & HAIDER, M. 2012. Optimization of CO_2 compression and purification units (CO_2CPU) for CCS power plants. *Fuel*, 101**,** 254-263.

PRASAD, P. & RAVINDRAN, R. 1985. *Partial differential equations*, Wiley Eastern Limited, New Delhi.

PRICE, J. F. 2006. Lagrangian and Eulerian representations of fluid flow: kinematics and the equations of motion. Woods Hole Oceanographic Institution [Online]. Available: http://www.whoi.edu/science/PO/people/jprice/class/ELreps.pdf [Accessed 28th October 2015].

REDLICH, O. & KWONG, J. N. S. 1949. On the thermodynamics of solutions. V. an equation of state. Fugacities of gaseous solutions. *Chemical Reviews,* 44**,** 233-244.

RICHARDSON, S. M. & SAVILLE, G. 1993. Blowdown of vessels and pipelines. *ICheme Symposium***,** 195-209.

RICHTMYER, R. D. 1960. Taylor instability in shock acceleration of compressible fluids. *Communications on Pure and Applied Mathematics*, XIII**,** 297-319.

RIGOS, D. A., SHAPIRO, B. L. & LEVITAN, R. L. 2011. Leaning on line pack. *Public Utilities Fortnightly,* 149**,** 18-26.

ROE, P. L. 1981. Approximate Riemann Solvers, Parameter and Difference Schemes. *Journal of Computational Physics,* 43**,** 357-372.

ROHSENOW, W. M., HARTNETT, J. P. & CHO, Y. I. 1998. Handbook of heat transfer. New York: McGraw-Hill.

ROMEO, L. M., BOLEA, I., LARA, Y. & ESCOSA, J. M. 2009. Optimization of intercooling compression in CO_2 capture systems. *Applied Thermal Engineering,* 29**,** 1744-1751.

SANDLER, S. I. 2007. *Chemical and Engineering Thermodynamics*, John Wiley & Sons Australia, Limited, 2007.

SASS, B. M., FARZAN, H., PRABHAKAR, R., GERST, J., SMINCHAK, J., BHARGAVA, M., NESTLEROTH, B. & FIGUEROA, J. 2009. Considerations for treating impurities in oxy-combustion flue gas prior to sequestration. *Energy Procedia,* 1**,** 535-542.

SEEVAM, P. N., RACE, J. M., DOWNIE, M. J. & HOPKINS, P. Transporting the Next Generation of CO_2 for Carbon, Capture and Storage: The Impact of Impurities on Supercritical CO_2 Pipelines. 7th International Pipeline Conference, Sept 29th-Oct 3rd, 2008 2008 Calgary, Alberta, Canada. 1-13.

SERGHIDES, T. K. 1984. Estimate friction factor accurately. *Chemical Engineering (New York),* 91**,** 63-64.

SIDEK, N. A. C. 2013. *An introduction to the computational fluid dynamics*, Penerbit UTM Press. Universiti Teknologi Malaysia.

SOAVE, G. 1972. Equilibrium constants from a modified Redlich-Kwong equation of state. *Chemical Engineering Science,* 27**,** 1197-1203.

SPERO, C. 2014. Callide Oxyfuel Project - Lessons Learned. Global CCS Institute [Online]. Available: https://www.globalccsinstitute.com/publications/callide-oxyfuel-project-lessons-learned [Accessed 28th October 2015].

SUWAN, K. & ANDERSON, A. 1992. Method of lines applied to hyperbolic fluid transient equations. *International Journal for Numerical Methods in Engineering,* 33**,** 1501-1511.

TABKHI, F., AZZAROPANTEL, C., PIBOULEAU, L. & DOMENECH, S. 2008. A mathematical framework for modelling and evaluating natural gas pipeline networks under hydrogen injection. *International Journal of Hydrogen Energy,* 33**,** 6222-6231.

TAM, V. H. Y. & HIGGINS, R. B. 1990. Simple transient release rate models for releases of pressurised liquid petroleum gas from pipelines. *Journal of Hazardous Materials,* 25**,** 193-203.

TECHO, R., TICKNER, R. R. & JAMES, R. E. 1965. An accurate equation for the computation of the friction factor for smooth pipes from the Reynolds number. *Journal of Applied Mechanics,* 32**,** 443.

TERENZI, A. 2006. Influence of Real-Fluid Properties in Modeling Decompression Wave Interacting with Ductile Fracture Propagation. *Oil & Gas Science and Technology,* 60**,** 711-719.

THOMPSON, K. W. 1987. Time dependent boundary conditions for hyperbolic systems. *Journal of Computation Physics,* 68**,** 1-24.

THOMPSON, K. W. 1990. Time-dependent boundary conditions for hyperbolic systems, II. *Journal of Computation Physics,* 89**,** 1-23.

THOMSON, G. H., BROBST, K. R. & HANKINSON, R. W. 1982. An improved correlation fordensities of compressed liquids and liquid mixtures. *The American Institute of Chemical Engineers,* 28**,** 671-676.

THORLEY, A. R. D. & TILEY, C. H. 1987. Unsteady and transient flow of compressible fluids in pipelines-some experimental studies. *International Journal of Heat and Fluid Flow,* 8**,** 3-15.

TWU, C. H., BLUCK, D., CUNNINGHAM, J. R. & COON, J. E. 1991. A cubic equation of state with a new alpha function and a new mixing rule. *Fluid Phase Equilibria,* 69**,** 33-50.

TWU, C. H., COON, J. E. & CUNNINGHAM, J. R. 1995. A new generalised alpha function for a cubic equation of state. Part 1. Peng-Robinson equation. *Fluid Phase Equilibria,* 105**,** 49-59.

VALDERRAMA, J. & REYES, L. R. 1983. Vapor-liquid equilibrium of hydrogen-conatinign mixtures. *Fluid Phase Equilibria,* 13**,** 195-202.

VAN DEEN, J. K. & REINTSEMA, S. R. 1983. Modelling of high-pressure gas transmission lines. *Applied Mathematical Modelling,* 7**,** 268-273.

VRABEC, J., KEDIA, G. K., BUCHHAUSER, U., MEYER-PITTROFF, R. & HASSE, H. 2009. Thermodynamic models for vapor–liquid equilibria of nitrogen+oxygen+carbon dioxide at low temperatures. *Cryogenics,* 49**,** 72-79.

WACKER, C. & KISOR, K. 2012. Integrally Geared Centrifugal Compressors for High-Pressure CO_2. *Carbon Management Technology Conference.* Orlando, Florida, USA.

WALAS, S. M. 1987. *Phase equilibrium in Chemical Engineering,* Boston, Butterworth Publisher.

WALSPURGER, S. & DIJK, H. A. J. V. 2012. EDGAR CO2 purity type and quantities of impurities related to CO2 point source and capture technology: a Literature study. ECN.

WEBBER, D. M., FANNELOP, T. K. & WITLOX, H. W. M. 1999. Source terms from two-phase flow in long pipelines following an accidental breach. *International Conference and Workshop on Modeling the Consequences of Accidental Releases of Hazardous Materials* [Online]. Available: https://www.dnvgl.com/Images/Source-terms-or-two-phase-flow-in-long-pipelines-following-and-accidental-breach_tcm8-12635.pdf [Accessed 28th October 2015].

WEI, Y. S. & SADUS, R. J. 2000. Equations of State for the Calculation of fluid phase equilibria. *AiCHE Journal*, 46**,** 169-196.

WHITE, V., ALLAM, R. & MILLER, E. 2009. Purification of Oxyfuel-Derived CO_2 for Sequestration or EOR [Online]. Available: http://www.netl.doe.gov/File%20Library/Research/Coal/ewr/co2/5309-Air-Products-oxy-combustion-GHGT-8-paper.pdf [Accessed 28th October 2015].

WILHELMSEN, Ø., SKAUGEN, G., JØRSTAD, O. & LI, H. 2012. Evaluation of SPUNG* and Other Equations of State for Use in Carbon Capture and Storage Modelling. *Energy Procedia*, 23**,** 236-245.

WILKINSON, M. B., BODEN, J. C., PANESAR, R. S. & ALLAM, R. J. 2001. CO_2 Capture via Oxyfuel Firing- Optimisation of a Retrofit Design concept for a refinery power station boiler. *First National Conference on Carbon Sequestration*. Washington DC.

WITKOWSKI, A. & MAJKUT, M. 2012. The impact of CO_2 compression systems on the compressor power required for a pulverized coal-fired power plant in post-combustion carbon dioxide sequestration. *The Archieve of Mechanical Engineering*, LIX**,** 59, 343-360.

WITKOWSKI, A., RUSIN, A., MAJKUT, M., RULIK, S. & STOLECKA, K. 2013. Comprehensive analysis of pipeline transportation systems for CO_2 sequestration. Thermodynamics and safety problems. *Energy Conversion and Management*, 76**,** 665-673.

WONG, S. 2006. CO_2 Compression and Transportation to Storage Reservoir. Asia-Pacific Economic Cooperation [Online]. Available: http://science.uwaterloo.ca/~mauriced/earth691duss/CO2_Materials_From_ARC_APEC_Beijing_2006/CarSeq_Module4.pdf. [Accessed 28th October 2015].

WOOLLEY, R. M., FAIRWEATHER, M., WAREING, C. J., PROUST, C., HEBRARD, J., JAMOIS, D., NARASIMHAMURTHY, V. D., STORVIK, I. E., SKJOLD, T., FALLE, S. A. E. G., BROWN, S., MAHGEREFTEH, H., MARTYNOV, S., GANT, S. E., TSANGARIS, D. M., ECONOMOU, I. G., BOULOUGOURIS, G. C. & DIAMANTONIS, N. I. 2014. An integrated, multi-scale modelling approach for the simulation of multiphase dispersion from accidental CO_2

pipeline releases in realistic terrain. *International Journal of Greenhouse Gas Control,* 27**,** 221-238.

WU, Y., HAMILTON, J. F. & SHENGHONG, W. 1982. Optimization of Shell-and-Tube Intercooler in Multistage Compressor system. *International Compressor Engineering Conference.*

WYLIE, E. B., STONER, M. A. & STREETER, V. L. 1971. Network system transient calculations by implicit method. *Society of Petroleum Engineers of AIME,* 11**,** 356-362.

YOO, B.-Y., CHOI, D.-K., KIM, H.-J., MOON, Y.-S., NA, H.-S. & LEE, S.-G. 2013. Development of CO_2 terminal and CO_2 carrier for future commercialized CCS market. *International Journal of Greenhouse Gas Control,* 12**,** 323-332.

YU, J.-M., BENJAMIN, C. Y. L. & IWAI, Y. 1987. Simutaneous calculations of VLE and saturated liquid and vapor volumes by means of a 3P1T cubic EoS. *Fluid Phase Equilibria,* 37**,** 207-222.

ZHAO, Q. & LI, Y.-X. 2014. The influence of impurities on the transportation safety of an anthropogenic CO_2 pipeline. *Process Safety and Environmental Protection,* 92**,** 80–92.

ZIABAKHSH-GANJI, Z. & KOOI, H. 2012. An Equation of State for thermodynamic equilibrium of gas mixtures and brines to allow simulation of the effects of impurities in subsurface CO_2 storage. *International Journal of Greenhouse Gas Control,* 11**,** S21-S34.

ZIGRANG, D. J. & SYLVESTER, N. D. 1982. An explicit approximations to the solution of Colebrook's friction factor equation. *AiCHE Journal,* 28**,** 514-515.

ZUCROW, M. J. & HOFFMAN, J. D. 1975. *Gas Dynamics,* School of Mechanical Engineering Purdue University, John Wiley & Sons.

Appendix A: Multistage compression (Fortran Plato IDE)

```
Program Compression
! Calculation of compression work for 8 stages adiabatic or polytropic process with &
! intermediate liquefaction

Use Properties
Use Prop_vap
Use Prop_liq
Implicit double precision (a-h, o-z)
Real ( kind = SELECTED_REAL_KIND(R=40) ), external :: dW_Sconst
Real ( kind = SELECTED_REAL_KIND(R=40) ), external :: dW_Sconst_liq
Real t_bub
Double precision mw_liq
Parameter (ncmax = 20)       ! max number of components in mixture
Dimension z(ncmax), Xv(ncmax), Xl(ncmax)
Parameter (n_stages = 8)
Double precision :: P1_= 0.15       ! initial pressure, MPa
Double precision :: Pratio_=1.78    ! compression ratio
Double precision :: eta_= 0.8        ! compressor efficiency
Double precision :: T1_= 38          ! gas temperature at the compressor inlet, oC
Double precision :: T_cool = 38 + 273.15 ! liquefaction temperature, K
Double precision :: G = 156.4        ! mass flow rate, kg/s
Double precision :: den_wat = 1000 ! kg/m3 ! water density
Double precision :: spe_ = 4.181   ! kJ/kgoC specific heat water
Double precision :: del_T = 5        ! oC
Character*255 herr,herr2
Common /propCO2/ z, mw_liq
Call refprop

! Calculate the bubble point and dew point lines
! Bubble point line
imax = 20
T = 250.
dT = (310. - t)/imax
open(unit=30,file='bubble_dew_point.csv',status='replace')

 do i = 1, imax
 kph = 1   ! input z is liquid composition
 call SATT (T,z,kph,p,rhol,rhov,Xl,Xv,ierr,herr)
 rhov_ = rhov*mw_liq  ! kg/m3
 rhol_ = rhol*mw_liq
 p_bub = p*1.d3
 s_v = s_vap(rhov_,T)
 s_l = s_liq(rhol_,T)
 h_v = e_vap(rhov_,T)+(p/(rhov_))*1.d3
 h_l = e_liq(rhol_,T)+(p/(rhol_))*1.d3
```

```
! Dew point

! kph = 2   ! input z is vapor composition
! call SATT (T,z,kph,p,rhol,rhov,Xl,Xv,ierr2,herr2)
! p_dew = p*1.d3
! rhov_ = rhov*mw_liq  ! kg/m3
! rhol_ = rhol*mw_liq
! h_v = e_vap(rhov_,T)+(p/rhov_)*1.d3
! h_l = e_liq(rhol_,T)+(p/rhol_)*1.d3
! s_v = s_vap(rhov_,T)
! s_l = s_liq(rhol_,T)

T = T + dT
read*

!write(30,130) i,T,p_bub/1.d5,p_dew/1.d5, ierr, ierr2
write(30,130)i,T,p_bub/1.d5,rhol,rhov,h_l,h_v,s_l,s_v

end do
130 format(1X,I6,8(',',E10.4))
read*

! Calculation of multistage compression
print*," Isentropic compression with inter-stage cooling and liquefaction"
p_cr = 7.83d6      ! MPa
p2 = P1_*1.d6;    ! MPa
p_top = P1_*1.d6*Pratio_**n_stages
w_sum = 0;
w1_sum = 0;
q_sum = 0;
ww_sum = 0;
kph = 1   ! for the bubble point calculations
T_bub = T_cool - 10.
 i = 0
 print*, "  i      T1      T2      T3      p1      p2      W      Q"
 open(unit=40,file='comp.csv',status='replace')

 do while (i.lt.n_stages .and. p2.lt.p_top )
 i = i+1
 if (T_bub.lt.T_cool) then
 ! gas compression
 p1 = p2
 p2 = p1*Pratio_
 T1 = 273.15 + T1_  ! K
 d1 = den_vap(p1,T1)
 s_o =  s_vap(d1,T1)
 h1 = h_vapS(p1,s_o)
```

```
 Z_o   = p1/d1/(8314./mw_liq)/T1
 w1 = Z_o*8314./mw_liq*T1*DLOG(p2/p1)
 ! adiabatic compression work w_adiab = h2-h1

CALL qk15 ( dW_Sconst, p1, p2, w, abserr, resabs, resasc )

 w  = w *G/eta_*1.d-3;
 w_sum = w_sum + w;
 w1  = w1 *G/eta_*1.d-3;
 w1_sum = w1_sum + w1;

 ! non-adiabatic compression work:  w = w_adiab/eta
 ! hence h2'-h1 = (h2'-h1)/eta
 ! update the enthalpy h2 to h2'

 h2 = h_vapS(p2,s_o)
 h2 = h1 + (h2-h1)/eta_

! the compressor discharge temperature T2:
call PH_flash(p2,h2,T2,d2)

else
! liquid compression (pumping) to final pressure
p1 = p2
p2 = p_top
T1 = T_cool
d1 = den_liq(p1,T1)
s_o =  s_liq(d1,T1)
h1 = h_liqS(p1,s_o)
Z_o   = p1/d1/(8314./mw_liq)/T1
w1 = Z_o*8314./mw_liq*T1 * DLOG(p2/p1)
! adiabatic compression work w_adiab = h2-h1

CALL qk15 ( dW_Sconst_liq, p1, p2, w, abserr, resabs, resasc )
w  = w *G/eta_*1.d-3;
w_sum = w_sum + w;
w1  = w1 *G/eta_*1.d-3;
w1_sum = w1_sum + w1;

! non-adiabatic compression work:  w = w_adiab/eta
! hence h2'-h1 = (h2'-h1)/eta
! update the enthalpy h2 to h2'

 h2 = h_liqS(p2,s_o)
 h2 = h1 + (h2-h1)/eta_liq

 ! the compressor discharge temperature T2:
```

```
    call PH_flash(p2,h2,T2,d2)

   endif

  ! cooling/ liquefaction process
  call SATP (p2/1.d3,z,kph,T_bub,rhol,rhov,Xl,Xv,ierr,herr)
  if (T_bub.ge.T_cool) then

  ! gas cooling & liquefaction
  T3 = T_cool
  d3 = den_liq(p2,T3)
  s3 =  s_liq(d3,T3)
  h3 = h_liqS(p2,s3)
  ! h3 = h_liquidS (T3,s3)
  Q = G*(h2-h3)*1.d-3;
  q_sum = q_sum + Q;

  else

! gas cooling to T1
if (i.lt.n_stages) then
T3 = 273.15 + T1_ ! K
 d3 = den_vap(p2,T3)
 s3 =  s_vap(d3,T3)
 h3 = h_vapS(p2,s3)
 Q = G*(h2-h3)*1.d-3;
 q_sum = q_sum + Q;
 ww = Q*0.03*(p2-p1)/(1000*eta_HE*eta_pump*den_wat*spe_*del_T);
 ww_sum = ww_sum + ww
 else
 T3 = 273.15+T1_!T_cool !   - final cooling to T_cool
 d3 = den_vap(p2,T3)
 s3 =  s_vap(d3,T3)
 h3 = h_vapS(p2,s3)
 Q = G*(h2-h3)*1.d-3;
 q_sum = q_sum + Q;
 ww = Q*0.03*(p2-p1)/(1000*eta_HE*eta_pump*den_wat*spe_*del_T);
 ww_sum = ww_sum + ww

 endif
 endif
 write(40,140)i,Z_o,mw_liq,T1,T2,T3,p1,p2,w,w1,Q,ww,h1,h2,h3,d1,d2,d3
 enddo

140 format(1X,I6,17(',',E15.4))
print*
print*, " W_sum =",w_sum
```

```
print*, " Q_sum =",Q_sum
read*
contains
End Program Compression

================================================================
Double Precision Function f_Fanning(Re, EPSoverD)
================================================================
Implicit none
Double Precision :: Re, EPSoverD
! Fanning friction factor evaluated using the Colebrook and White equation:
f_Fanning = 0.0625/(DLOG10(EPSoverD/3.7 + 5.74/Re**0.9))**2.
End Function f_Fanning

================================================================
Double Precision Function dW_Tconst(p)
================================================================
Use Properties
Use Prop_vap
Double Precision :: p,T
Real(kind = SELECTED_REAL_KIND(R=40)) :: dW_Tconst
T = T_o
dW_Tconst = 1./den_vap(p,T)
End Function dW_Tconst

================================================================
Function dW_Sconst(p)
================================================================
Use Properties
Use Prop_vap
Double Precision :: p,T
Real(kind = SELECTED_REAL_KIND(R = 40)) :: dW_Sconst
dW_Sconst = 1./den_vapS(p,s_o)
End Function dW_Sconst

================================================================
Double Precision Function dW_Sconst_liq(p)
================================================================
Use Properties
Use Prop_liq
Implicit double precision (a-h,o-z)
Double Precision :: p,T
dW_Sconst_liq = 1./den_liqS(p,s_o)
End Function dW_Sconst_liq
```

```
==============================================================
Double Precision Function Fun_1(x)
==============================================================
Use Properties
Use Prop_vap
Implicit none
Double Precision :: x
Fun_1 = 1
End Function Fun_1
```

Appendix B: Line Packing

Numerical pipe flow model
Subroutine at pipeline inlet

```
SUBROUTINE FIRST_POINT(IT,IX,DX,DT,T2,U2,A2T,P2,R2,H2,HTC2,
&  TWAL2,ICHECK,IPS,FirstPointType)

IMPLICIT REAL*8 (A-H,O-Z)
PARAMETER (EPS = 1.D-5, EPS1 = 9.0D-5,NCOMPONENTS = 71,NPIPE=11)
PARAMETER (NPHYS=10,NCMAX=71, PI=3.141592654D0, PUNIT=101325.D0,
&   RGAS=8.31439D0, ACGRAV=9.8066352D0, RGATM=82.057D-6)
DIMENSION DDPIPE(NPIPE),PWTHICK(NPIPE),AAPIPE(NPIPE),
&   DDPOUT(NPIPE),AAPIPVOL(NPIPE),AAPMASENG(NPIPE),
&   AAPMASENGCON(NPIPE),EEXTHTC(NPIPE),RRADIN(NPIPE),
&   RRADOUT(NPIPE),UUINIT(NPIPE),UUX2(NPIPE)
REAL*8 LPIPE, P2_
REAL*8, EXTERNAL::FCN
INTEGER::N,ips
REAL*8::XG(1),FVEC,WA,PDIFF,PSET,RSET,T2,T_2,PMICH,TMICH
REAL*8:: TC,PC,ACEN,PP,ER
DOUBLE PRECISION FF,C1,C2,C3,C4,C5,C6,C7,C8,C9,C10,C11,C12
DOUBLE PRECISION MASSFLUX,MASSFLOWRATE
DOUBLE PRECISION TZBC1, TZBC2, TFUN1, TFUN2, TBRENT, PSAT, TSAT,
&   RSAT
DOUBLE PRECISION K_,AC,BC,ALPHA,P_2
LOGICAL SUCCES
INTEGER FirstPointType
COMMON/PIPED/DPIPE, LPIPE, RF
COMMON/ENVRM/ PEXTB, TINFC, HTC
COMMON/CGRID/C1,C2,C3,C4,C5,C6,C7,C8,C9,C10,C11,C12,C13,C14,C15,
&   C16,C17,C18,C19,C20,C21
COMMON/BRENT/TBRENT
COMMON /SATURATED/PSAT,TSAT,RSAT,ASAT,ISATURATE
COMMON/TZBRAC/TZBC1,TZBC2, TFUN1, TFUN2
COMMON/TPROPS/ ENTR,RMICH,AMICH, GAMMA, ES1, ISB
```

```
COMMON/TVISC/VIS
COMMON/COMPOSITION / ZCOMP(NCOMPONENTS),
&ZCOMPORIG(NCOMPONENTS)
COMMON/ TIMING/TFIRST, TMIDPT, TENDPT, TFLASH, IFT1, IMT1, IET1, &
& NMT, NET
COMMON/ PHASECALC/IPHASE
COMMON /CARRYON/ ISWITCH2,SNT,HNT,ZT1,WMT1,CPT1,CVT1
COMMON/INCLINATION/DEGORIENT,IA11,AT1,AT2,ES11,ES22,SN1,SN2
COMMON/ PSPECIAL /PLOW, IENERGY, IPON, APMASENG, &
&APMASENGCON, EXTHTC
COMMON /FROMPIPE1AND2 /INO1,IFIXIT
COMMON/ THERMOTRAJECT/ IENTROPY
COMMON/MULIDIA/DDPIPE,INOSPIPE
COMMON/INTERP/INTERPOLATE
COMMON /PUMPORRESERV/PSOFHD, IKNOWCURVE, ACURVE, BCURVE,
& &PATRSVIN, IRSVOR, ICOMPRES
COMMON /ALTIMES/ TIME, TIMEP, TIMEDURA1, TIMEDURA2,
&TIMEDURA3, UFDIF1
COMMON/SPECIAL/PX2,UX2,PX3,TX3,RX3,AX3,ESX3,VISX3,HX3,XLPIPE2
COMMON/SET/PSET,RSET,RPERM

DPIPE = DDPIPE(INOSPIPE)

TINF = TINFC+273.15D0
IF (IENERGY.EQ.0) THEN
TWDN = TINF
TWUP = TINF
TWSP = TINF
HTDN = HTC
HTUP = HTC
HTSP = HTC
ELSE
TWDN = C21
TWUP = C19
TWSP = C19
HTDN = C18
HTUP = C16
HTSP = C16

IF (IENERGY.EQ.2.OR.IENERGY.EQ.4) HTDN = HTC
IF (IENERGY.EQ.2.OR.IENERGY.EQ.4) HTUP = HTC
IF (IENERGY.EQ.2.OR.IENERGY.EQ.4) HTSP = HTC
ENDIF

IF (INO1.EQ.2.AND.IFIXIT.GT.1) THEN
GCV = -1.D0
ELSE
```

```
GCV = 1.D0
ENDIF
GSTHETA = ACGRAV*DSIN(DEGORIENT*PI/180.D0)*GCV
PEXT = PEXTB * 1.D5
RPERM = RGAS/WMT1
X = IX*DX
ODX = 1.D0 / DX
EPS2 = 5.D-3
EPSN = 5.D-7
IF (IENTROPY.EQ.1) THEN
IMICH = 2
ELSE
IMICH = 1
ENDIF
SPECIN = 0.D0
ICHECK = 0

! IF (FirstPointType == 0 ) Then
! This was added to ensure that we don't have instabilities in the program
! C1 = 0.D0
! End If

! EVALUATE QUANTITIES AT THE INTERMEDIATE POINTS N AND 0

DO 227 ITERM = 1, 100
ISATCHECK = 0
IJUMP = 0
IF (ITERM.EQ.1) THEN
DTDX = DT/DX
B1 = -(C5 - C1) * DTDX
A1 = 1.D0 - B1
A2 = (C6 - C2) * DTDX
B2 = 1.D0 - A2

! CALCULATE FLUID VELOCITY AND SPEED OF SOUND AT THE & &
&INTERMEDIATE POINTS

DENOM = 1.D0 / (A1*B2-A2*B1)
UN = (B2*C1-B1*C2) * DENOM
AN = (A1*C2-A2*C1) * DENOM
U0 = C1/A1

! AND THE POSITIONS OF THESE INTERMEDIATE POINTS

XN = X - DT*(UN - AN)
X0 = X - DT*U0
ELSE
```

```
DTDX = DT/(2.D0*DX)
B1 = -(C5 - C1) * DTDX
A1 = 1.D0 - B1
A2 = (C6 - C2) * DTDX
B2 = 1.D0 - A2
DENOM = 1.D0 / (A1*B2-A2*B1)
C1N = C1+B1*U2-B1*A2T
C2N = C2-A2*U2+A2*A2T
C10N = C1+B1*U2
UN = (B2*C1N-B1*C2N) * DENOM
AN = (A1*C2N-A2*C1N) * DENOM
U0 = C10N/A1
X0 = X - DT*((U0+U2)/2.D0)
XN = X - DT*((UN+U2)/2.D0 - (AN+A2T)/2.D0)
ENDIF

! AND NOW EVALUATE THE REMAINING PROPERTIES AT THE &
!INTERMEDIATE POINTS
IF (DABS(X0-X).GT.DX.AND.X0.GT.X) THEN
DX0 = DX
ELSEIF (X0.LT.X) THEN
DX0 = 0.D0
ELSE
DX0 = X0-X
ENDIF
IF (DABS(XN-X).GT.DX.OR.(XN-X).LT.(0.)) THEN
DXN = DX
ELSE
DXN = XN-X
ENDIF
P0 = C7 + (C9 - C7)*ODX*(DX0)
H0 = C13 + (C15 - C13)*ODX*(DX0)
PN = C7 + (C9 - C7)*ODX*(DXN)
HN = C13 + (C15 - C13)*ODX*(DXN)

! EVALUATE DENSITY AND E = R2(DT/DR)s BY T-P FLASH CALCS AT
!POINTS 0 AND N
SPECIN = H0/RPERM
PMICH = P0 / 1.01325D5

! IF (INTERPOLATE.EQ.1) THEN
! CALL getdata(pmich,sPECIN,rmich,amich,tmich,hmich,es1,VIS,IPS)
! ELSE

CALL PHASES (TMICH,PMICH,IMICH,SPECIN,IPS)
! END IF
T0 = TMICH
```

```
R0 = RMICH
A0 = AMICH
ES0 = ES1
IF (U0.NE.0.D0) THEN

! CALC. THE FRICTION FACTOR AT THIS POINT FOR THE CALCULATION
!OF WALL SHEAR STRESS

RE0 = R0*DABS(U0)*DPIPE/VIS
CALL FRICTIONFCT(RE0,R0,U0,IPS,FF)
B0 = -2.D0 * FF / DPIPE * R0 * U0 * DABS(U0)
B01 = B0
B0 = B0 - R0*GSTHETA
ELSE
B01 = 0.D0
B0 = 0.D0 - R0*GSTHETA
ENDIF

! CALC. FRICTIONAL FORCE EFFECTS AND HEAT TRANSFER EFFECTS

Q0 = 4.D0 * HTSP * (TWSP - T0) / DPIPE
PSI0K = ES0 * (Q0 - U0 * B01) / R0 / T0
IF (IENTROPY.EQ.1) THEN
PSI0 = (Q0 - U0 * B01)/(R0*T0)
ELSE
PSI0 = (Q0 - U0 * B01)
ENDIF
A20 = A0 * A0

SPECIN = HN/RPERM
PMICH = PN / 1.01325D5
IF (INTERPOLATE.EQ.1) THEN
CALL getdata(pmich,sPECIN,rmich,amich,tmich,hmich,es1,VIS,IPS)
ELSE

CALL PHASES (TMICH,PMICH,IMICH,SPECIN,IPS)
END IF
TN = TMICH
RN = RMICH
ESN = ES1
AN = AMICH

! CALC. THE FRICTION FACTOR AT THIS POINT FOR THE CALCULATION
!OF WALL SHEAR STRESS

 IF (UN.NE.0.D0) THEN
 REN = RN*DABS(UN)*DPIPE/VIS
```

```
CALL FRICTIONFCT(REN,RN,UN,IPS,FF)
BN = -2.D0 * FF / DPIPE * RN * UN * DABS(UN)
BN1 = BN
BN = BN - RN*GSTHETA
ELSE
BN1 = 0.D0
BN = 0.D0 - RN*GSTHETA
ENDIF

! CALC. FRICTIONAL FORCE EFFECTS AND HEAT TRANSFER EFFECTS

QN = 4.D0 * HTDN * (TWDN - TN) / DPIPE
PSIN = ESN * (QN - UN * BN1) / RN / TN
ABN = AN * BN
RAN = RN * AN

! INITIAL APPROXIMATIONS

IF (ITERM.EQ.1) THEN
U2 = U0
R2 = R0
H2 = H0
P2 = P0
A2T = A0
PSI02 = PSI0
PSI2 = PSI0K
PSINM = PSIN
RANM = RAN
ABNM = ABN
ELSE
PSINM = (PSIN + PSI2) * 0.5D0
RANM = (RAN + RA2) * 0.5D0
ABNM = (ABN + AB2) * 0.5D0
ENDIF
A20M = (A20 + A2T * A2T) * 0.5D0
PSI0M = (PSI0 + PSI02) * 0.5D0
R0MN = (R0 + R2) * 0.5D0

! CALCULATE AK2

AK2 = (PSINM - ABNM) * DT

! EVALUATE P AND U  AND R

IF (FirstPointType==1) THEN
! BOUNDARY CONDITIONS FOR THE RESERVOIR AND PUMP BOUNDARY
!CONDITIONS
```

```
! THE FOLLOWING IF STATEMENT CONTROLS WHETHER WE HAVE A
!PUMP OR A RESERVOIR, AN !ALTERATION FOR THE RESERVOIR WAS
!MADE AS THE PRESSURE P2 WAS NOT SET TO THE FEED !PRESSURE AS
!SHOULD BE THE CASE FOR THIS BOUNDARY CONDITION

IF (IRSVOR.EQ.2) THEN
IF (ICOMPRES .EQ.0) THEN
P2 = PATRSVIN
SPECIN = C13/RPERM
PMICH = C7 / 1.01325D5
IF (INTERPOLATE.EQ.1) THEN
CALL getdata(pmich,sPECIN,rmich,amich,tmich,hmich,es1,VIS,IPS)
ELSE

CALL PHASES (TMICH,PMICH,IMICH,SPECIN,IPS)
END IF
U2=C1*RMICH/R2

END IF

IF (ICOMPRES .EQ.1) THEN

SPECIN = C13/RPERM
PMICH = C7 / 1.01325D5
IF (INTERPOLATE.EQ.1) THEN
CALL getdata(pmich,sPECIN,rmich,amich,tmich,hmich,es1,VIS,IPS)
ELSE

CALL PHASES (TMICH,PMICH,IMICH,SPECIN,IPS)
END IF

U2 = C1*RMICH/R2

P2 = AK2  + RANM*(U2 - UN) + PN
IF (P2.LT.PEXT) THEN
P2 = PEXT
ENDIF
END IF
!******************************************************************
! The above to add in the option of compressor as flow source which delivers constant
!flow source
 !******************************************************************
ELSE
!**************************************************************************
**************
! The pump calculations were incorrect as ACURVE and BCURVE were in the
!wrong places. Also !ACURVE and BCURVE have to be multiplied by 1D5 since
```

```
!calculations for P2 are done in pascal and !not bar. This multiplication is done when
!the data is read into the code.
!****************************************************************
COEF1 = ACURVE
COEF2 = BCURVE + RANM
COEF3 = PN + AK2 - (RANM*UN + PSOFHD)
COEF4 = COEF2**2- 4.D0*COEF1*COEF3
IF (COEF4.LE.(0.D0)) THEN
U2 = 0.D0
P2 = PSOFHD
ELSE
U2 = ((-COEF2)+DSQRT(COEF4))/(2.*COEF1)
P2 = PSOFHD-U2*BCURVE-(U2**2)*ACURVE
IF (P2 .LT. PEXTB*1.D5) THEN
P2 = PEXTB * 1.D5
ENDIF
ENDIF
END IF
ELSE IF (FirstPointType==0) THEN

! BOUNDARY CONDITIONS FOR THE CLOSED END BOUNDARY
!CONDITIONS
! U2 = 0.D0
! P2 = AK2  + RANM*(U2 - UN) + PN
! if (p2 .lt.pext)then
! p2=pext
! end if
! if (time .le.10)then
! P2 = 150.d5
! SPECIN = C13/RPERM
! PMICH = C7 / 1.01325D5
! IF (INTERPOLATE.EQ.1) THEN
! CALL getdata(pmich,sPECIN,rmich,amich,tmich,hmich,es1,VIS,IPS)
! ELSE
! CALL PHASES (TMICH,PMICH,IMICH,SPECIN,IPS)
! END IF
! U2=C1*RMICH/R2
! IF (IENTROPY .EQ. 1)THEN
! H2 = (PSI0M*DT)+H0
! ELSE
! H2 = (PSI0M*DT+(P2-P0))/R0MN+H0
! END IF
! SPECIN = H2/RPERM
! PMICH = P2 / 1.01325D5
! CALL getdata(pmich,sPECIN,rmich,amich,tmich,hmich,es1,VIS,IPS)
! CALL PHASES (TMICH,PMICH,IMICH,SPECIN,IPS)
! T2 = TMICH
```

```
! ES2 = ES1
! A2T = AMICH
! VIS2 = VIS
! r2 = rmich
! else

SPECIN = C13/RPERM
PMICH = C7 / 1.01325D5

CALL getdata(pmich,sPECIN,rmich,amich,tmich,hmich,es1,VIS,IPS)
R_=766.066202328043005d0
U_=0.261091770851317d0
RU=-((R_*U_)/(4*100))*(1/(cosh((time-1000)/100)))**2

if (time .ge. 1700.d0)then
RU=0.d0
end if

L1 = ((C1-AMICH)/DX)*(C9-C7-RMICH*AMICH*(C5-C1))
L2 = 0.D0
L3 = (1/(C1+AMICH))*(-2*AMICH**2*RU-(C1-AMICH)*L1-2*C1*L2)


P2 = DT*((-L3*(C1+AMICH)/(2*AMICH))-(L1*(C1-AMICH)/(2*AMICH))-
L1)+C7

if (time .le.1700) then
U2 = ((-L5*(C1+AMICH)-L1*(C1-AMICH))*DT)/(2*RMICH*AMICH**2)+C1
else
U2 = ((-L5*(C1+AMICH)-L1*(C1-AMICH))*DT)/(2*RMICH*AMICH**2)
&  +0.130401308496721d0

end if

if (U2 <= 0.d0) then
U2 = 0.d0;
end if

H2 = -1375.204764883919779d0

SPECIN = H2/RPERM
PMICH = P2 / 1.01325D5

CALL getdata(pmich,sPECIN,rmich,amich,tmich,hmich,es1,VIS,IPS)

T2 = TMICH
R2 = RMICH
```

```
ES2 = ES1
A2T = AMICH
VIS2 = VIS
H2_in=hmich

IF (P2.LT.PEXT) THEN
P2 = PEXT
ENDIF

ELSE IF (FirstPointType==2) THEN
! BOUNDARY CONDITIONS FOR THE PIPE CONNECTOR BOUNDARY
!CONDITIONS
IF (ITERM.EQ.1) THEN
R2 = RX3
RA2 = RX3*AX3
T2 = TX3
P2 = PX3
A2T = AX3
ES2 = ESX3
H2 = HX3
END IF
U2 = ((P2-PN)-AK2)/RANM + UN
ELSE IF (FirstPointType==4) THEN
!BOUNDARY CONDITIONS FOR THE FIXED PRESSURE BOUNDARY
!CONDITIONS

P2 = PX3
END IF

HOLD = H2/RPERM
ROLD = R2
POLD = P2
UOLD = U2

SPECIN = H2/RPERM
H2F = SPECIN
PMICH = P2 / 1.01325D5
IF (INTERPOLATE.EQ.1) THEN
CALL getdata(pmich,sPECIN,rmich,amich,tmich,hmich,es1,VIS,IPS)
ELSE
CALL PHASES (TMICH,PMICH,IMICH,SPECIN,IPS)
ENDIF
ES2 = ES1
A2T = AMICH
VIS2 = VIS
! EVALUATE THE CHANGE IN P AND R AT THIS ITERATION
```

```
IF (ITERM.EQ.1) GOTO 567
IF (ITERM.GT.1) THEN
IF (XNOLD.GT.(0.)) THEN
DEVXN = DABS(XN-XNOLD)/DABS(XNOLD)
ELSEIF (XN.GT.(0.)) THEN
DEVXN = DABS(XN-XNOLD)/DABS(XN)
ELSE
DEVXN = 0.D0
ENDIF
IF (X0OLD.GT.(0.)) THEN
DEVX0 = DABS(X0-X0OLD)/DABS(X0OLD)
ELSEIF (X0.GT.(0.)) THEN
DEVX0 = DABS(X0-X0OLD)/DABS(X0)
ELSE
DEVX0 = 0.D0
ENDIF
ENDIF
DEVP = DABS(P2 - POLD)/DABS(POLD)
DEVH = DABS(H2F - HOLD)/DABS(HOLD)
IF (DEVH.LT.EPS.AND.DEVH.LT.EPS) GO TO 500
IF (ITERM.GT.5.AND.DEVH.LT.EPS1.AND.DEVP.LT.EPS1) GOTO 500

IF (DEVXN.GT.(0.D0).AND.DEVX0.GT.(0.D0)) THEN
IF (ITERM.GE.50.AND.DEVXN.LT.EPSN.AND.DEVX0.LT.EPSN) GOTO 500
ENDIF
567    B2 = 0.D0 - R2*GSTHETA
B21 = 0.D0
Q2 = 4.D0 * HTSP * (TWSP - T2) / DPIPE
PSI2 = ES2 * (Q2 - U2 * B21) / R2 / T2
IF (IENTROPY.EQ.1) THEN
PSI02 = (Q2 - U2 * B21)/(R2*T2)
ELSE
PSI02 = (Q2 - U2 * B21)
ENDIF
RA
AB2 = A2T * B2
! this was added to serve as a new set of convergence criteria
XNOLD = XN
X0OLD = X0
227 CONTINUE
WRITE (28,*)
&'  WARNING: NO CONVERGENCE AT POINT IX = ', IX,
&'  AND TSTEP = ',IT
ICHECK = 1
500   CONTINUE

IF (FirstPointType==1) THEN
```

```
!BOUNDARY CONDITIONS FOR THE RESERVOIR AND PUMP BOUNDARY
!CONDITIONS
!THE FOLLOWING HAS BEEN ALTERED SO THAT IF THERE IS ZERO FLOW
!AT THE RESERVOIR THE
!PRESSURE IS NO LONGER ASSUMED TO BE VARIABLE.

IF (IRSVOR.NE.2.AND.(U2.LT.(0.D0))) THEN
TIMEP = TIME
WRITE(32,*) 'PUMP SHUTDOWN/VALVE CLOSURE HAS OCCURRED @ TIME =', TIME
PRINT *,'RESERVOIR VALVE CLOSURE/PUMP SHUTDOWN HAS OCCURRED'
ENDIF
END IF
TWAL1 = C19
IF (U2.NE.0.D0) THEN
RE2 = R2*DABS(U2)*DPIPE/VIS
CALL FRICTIONFCT(RE2,R2,U2,IPS,FF2)
ELSE
FF2 = 0.D0
ENDIF
REY2 = R2*DABS(U2)*DPIPE/VIS
CALL HeatCoef(P2,T2,REY2,R2,U2,FF2,DX,IPS,HTC2,TWAL1,DT,TWAL2,ICOR)
IFT1 = ITERM
RETURN

END
```

Subroutine at pipeline outlet

```
!  This subroutine calculates the pressure (P2) at the end of the pipeline: for a closed
!end pipeline
!  This subroutine is specially used for a pipeline in whose end is closed
!  a mixture of second order interpolation and first order solution methods would be
!employed in this subroutine.

SUBROUTINE END_POINT (IT,DX,DT,T2,U2,A2T,P2,R2,H2,HTC2,TWAL2,
& IPRES,ICHECK,IPS,EndPointType)
IMPLICIT REAL*8 (A-H,O-Z)
PARAMETER (EPS = 5.D-7, EPS1 = 5.D-7,NCOMPONENTS = 71,NPIPE=11)
PARAMETER (NPHYS=10,NCMAX=71, PI=3.141592654D0, PUNIT=101325.D0,
& RGAS=8.31439D0, ACGRAV=9.8066352D0, RGATM=82.057D-6)
REAL*8 LPIPE,xpold,xp,x0old,DEVP,DEVH,DT_P
LOGICAL SUCCES
integer::interpolate
```

```
REAL*8, EXTERNAL::FCN_
INTEGER::N
REAL*8, DIMENSION(1):: XG1, FVEC1, WA(8)
DIMENSION PBOUNDL(NPIPE),TBOUNDL(NPIPE),ABOUNDL(NPIPE),
&UBOUNDL(NPIPE), RBOUNDL(NPIPE), EBOUNDL(NPIPE),
VBOUNDL(NPIPE), HBOUNDL(NPIPE)
DIMENSION XO(NCMAX), YO(NCMAX),XU(NCMAX)
INTEGER EndPointType
DOUBLE PRECISION TZBC1, TZBC2, TFUN1, TFUN2, TBRENT, PSAT, TSAT,
& RSAT, FF
DOUBLE PRECISION K_,AC,BC,ALPHA,P_2
COMMON/PIPED/DPIPE, LPIPE, RF
COMMON/ENVRM/ PEXTB, TINFC, HTC
COMMON/TPROPS/ ENTR, RMICH, AMICH, GAMMA, ES1, ISB
COMMON/BRENT/TBRENT
COMMON/SPECIAL/PX2,UX2,PX3,TX3,RX3,AX3,ESX3,VISX3,HX3,XLPIPE2
COMMON /ORIFICE3/ ORDIAMT, ORHEIGHT, XLPIPE(NPIPE), IORIENT, &
&DIS1, IZ3
COMMON/TVISC/VIS
COMMON /SATURATED/PSAT,TSAT,RSAT,ASAT,ISATURATE
COMMON/CGRID/C1,C2,C3,C4,C5,C6,C7,C8,C9,C10,C11,C12,C13,C14,C15,C16,
&C17,C18,C19,C20,C21
COMMON/TZBRAC/TZBC1,TZBC2, TFUN1, TFUN2
COMMON/COMPOSITION / ZCOMP(NCOMPONENTS),
&ZCOMPORIG(NCOMPONENTS)
COMMON/ PHASECALC/IPHASE
COMMON/INCLINATION/DEGORIENT,IA11,AT1,AT2,ES11,ES22,SN1,SN2
COMMON /CARRYON/ ISWITCH2,SNT,HNT,ZT1,WMT1,CPT1,CVT1
COMMON /CARRYON2/ SNT2,HNT2,WMT2,CPT2,CVT2,ZT2
COMMON/ PSPECIAL /PLOW,IENERGY, IPON,APMASENG,
&APMASENGCON, EXTHTC
COMMON /FROMPIPE1AND2 /INO1,IFIXIT
COMMON/ THERMOTRAJECT/ IENTROPY
COMMON/COMPONENTS / NCOMP, IV(NCMAX)
COMMON/INTERP/INTERPOLATE
COMMON/PIPESMEET/DXB,NBB,ITB,PO,TO,XO,YO,ZOX,ZOY,VOL,VEL,
&DENT,IP,NPA1,NPA2,ORJMAS1,GANGLE,RUX1,RUX2,RUY,RMST1, PJT1, &
&HJT1
COMMON /FEEDCOMP1 /XU
COMMON/RUPTURE/PBOUNDL,TBOUNDL, ABOUNDL, UBOUNDL,
&RBOUNDL,EBOUNDL,VBOUNDL,HBOUNDL
COMMON/PUNCRESULTS/PZ1,PZ2,TZ1,TZ2,VZ1,VZ2,AZ1,AZ2,DZ1,DZ2,
&IPZ1,IPZ2,HTCZ1,NZIP1,TMTIP1(2,5),PLGSTR(5),PTGSTR(5),PRDSTR(5)
COMMON /DISCHARGE /POUT,DISAREA1,IDISCAL,DISAREA2,DENSITL
COMMON/SET_/DT_P,PSIPM_P,ABPM_P,PP_P,RAPM_P,UP_P

TINF = TINFC + 273.15D0
```

```
APIPE = PI*(DPIPE**2)/4.D0
IF (IENERGY.EQ.0) THEN
TWDN = TINF
TWUP = TINF
TWSP = TINF
HTDN = HTC
HTUP = HTC
HTSP = HTC
ELSE
TWDN = C19
TWUP = C20
TWSP = C19
HTDN = C16
HTUP = C17
HTSP = C16
IF (IENERGY.EQ.2.OR.IENERGY.EQ.4) HTDN = HTC
IF (IENERGY.EQ.2.OR.IENERGY.EQ.4) HTUP = HTC
IF (IENERGY.EQ.2.OR.IENERGY.EQ.4) HTSP = HTC
ENDIF
PEXT = PEXTB * 1.D5
IF (INO1.EQ.2.AND.IFIXIT.GT.1) THEN
GCV = -1.D0
ELSE
GCV = 1.D0
ENDIF
GSTHETA = ACGRAV*DSIN(DEGORIENT*PI/180.D0)*GCV
RPERM = RGAS/WMT1
IF (IENTROPY.EQ.1) THEN
IMICH = 2
ELSE
IMICH = 1
ENDIF
SPECIN = 0.0
IPRES = 0
EPS2 = 5.D-7
EPSN = 5.D-7
ICHECK = 0

DT_P = DT

! IF (EndPointType==4) THEN
! This was added to ensure that we don't have instabilities in the program
! C1 = 0.D0
! END IF

XN = XLPIPE(IZ3)
LPIPE = XN
```

```
X = XN
ODX = 1.D0/DX
IF (C7.LE.C8) THEN
CPLST = C7
CPGT = C8
ELSE
CPLST = C8
CPGT = C7
ENDIF
DO 49 ITERM = 1, 100

IF (ITERM.EQ.1) THEN
DTDX = DT/DX
B1 = (C1 - C3) * DTDX
A1 = B1 + 1.D0
A2 = (C2- C4) * DTDX
B2 = A2 + 1.D0
ELSE
DTDX = DT/(2.D0*DX)
B1 = (C1 - C3) * DTDX
A1 = 1.D0 + B1
A2 = (C2-C4) *DTDX
B2 = 1.D0+A2
C1P = C1-B1*U2-B1*A2T
C2P = C2-A2*U2-A2*A2T
C0 = C1-B1*U2
ENDIF

! CALCULATE FLUID VELOCITY AND SPEED OF SOUND AT THE
!INTERMEDIATE POINTS

DENOM = 1.D0 / (A1*B2-A2*B1)
IF (ITERM.EQ.1) THEN
UP_P = (B2*C1-B1*C2) * DENOM
AP = (A1*C2-A2*C1) * DENOM
U0 = C1/A1
X0 = X - DT*U0
XP = X - DT*(UP_P + AP)
ELSE
UP_P = (B2*C1P-B1*C2P) * DENOM
AP = (A1*C2P-A2*C1P) * DENOM
U0 = C0/A1
X0 = X - DT*((U0+U2)/2.D0)
XP = X - DT*((UP_P+U2)/2.D0 + (AP+A2T)/2.D0)
ENDIF

! AND THE POSITIONS OF THE INTERMEDIATE POINTS
```

```
! AND PRESSURE AND DENSITY AT THE INTERMEDIATE POINTS
IF (DABS(X0-X).GT.DX.OR.X0.GT.X) THEN
DX0 = 0.D0
ELSEIF (DABS(X0-X).GT.DX.AND.X0.LT.X) THEN
DX0 = -DX
ELSE
DX0 = X0-X
ENDIF
IF (DABS(XP-X).GT.DX.OR.(XP-X).GT.(0.)) THEN
DXP = -DX
ELSE
DXP = XP-X
ENDIF

! AND PRESSURE AND DENSITY AT THE INTERMEDIATE POINTS

P0 = C8 + (C7 - C8)*ODX*(DX0+DX)
H0 = C14 + (C13 - C14)*ODX*(DX0+DX)
PP_P = C8 + (C7 - C8)*ODX*(DXP+DX)
HP = C14 + (C13 - C14)*ODX*(DXP+DX)

IF (EndPointType == 6 .OR.EndPointType == 7) THEN
! BOUNDARY CONDITIONS FOR THE PUNCTURE AT THE END AND FULL
!BORE RUPTURE
!BOUNDARY CONDITIONS

UN = UBOUNDL(IZ3)
AN = ABOUNDL(IZ3)
PN = PBOUNDL(IZ3)
RN = RBOUNDL(IZ3)
TN = TBOUNDL(IZ3)
HN = HBOUNDL(IZ3)
ESN = EBOUNDL(IZ3)
VISN = VBOUNDL(IZ3)

SPECIN = HN/RPERM
PMICH = PN / 1.01325D5
CALL PHASES (TMICH,PMICH,IMICH,SPECIN,IPS)
TN = TMICH
RN = RMICH
ESN = ES1

!CALC. THE FRICTION FACTOR AT THIS POINT FOR THE CALCULATION
!OF WALL SHEAR STRESS
IF (UN.NE.0.D0) THEN
REN = RN*DABS(UN)*DPIPE/VIS
CALL FRICTIONFCT(REN,RN,UN,IPS,FF)
```

```
BN = -2.D0 * FF / DPIPE * RN * UN * DABS(UN)
BN1 = BN
BN = BN - RN*GSTHETA
ELSE
BN1 = 0.D0
BN = 0.D0 - RN*GSTHETA
ENDIF

! CALC. FRICTIONAL FORCE EFFECTS AND HEAT TRANSFER EFFECTS

QN = 4.D0 * HTDN * (TWDN - TN) / DPIPE
PSIN = ESN * (QN - UN * BN1) / RN / TN
ABN = AN * BN
RAN = RN * AN

Else
PSIN = 0.d0
RAN = 0.d0
ABN = 0.d0
END IF

! AND CALCULATE DENSITY AND E = (DT/DR)S BY T-P FLASH CALCS
! AT THIS POINT A THERMODYNAMIC INCONSISTENCY MIGHT OCCUR
!SINCE THE SPEED OF SOUND IS CALCULATED AS AN INTERPOLATED
!VALUE AND NOT FROM THE GIVEN THERMODYNAMIC MODEL. IT IS
!EXPECTED THAT BY USING A SMALL STEP THIS DEVIATION DOES NOT
!AFFECT RESULTS.

SPECIN = H0/RPERM
PMICH = P0 / 1.01325D5
CALL PHASES (TMICH,PMICH,IMICH,SPECIN,IPS)
T0 = TMICH
R0 = RMICH
A0 = AMICH
ES0 = ES1
IF (U0.NE.0.D0) THEN
! CALC. THE FRICTION FACTOR AT THIS POINT FOR THE CALCULATION
!OF WALL SHEAR STRESS
RE0 = R0*DABS(U0)*DPIPE/VIS
CALL FRICTIONFCT(RE0,R0,U0,IPS,FF)
B0 = -2.D0 * FF / DPIPE * R0 * U0 * DABS(U0)
B01 = B0
B0 = B0 - R0*GSTHETA
ELSE
B01 = 0.D0
B0 = 0.D0 - R0*GSTHETA
ENDIF
```

```
! CALC. FRICTIONAL FORCE EFFECTS AND HEAT TRANSFER EFFECTS
Q0 = 4.D0 * HTSP * (TWSP - T0) / DPIPE
PSI0K = ES0 * (Q0 - U0 * B01) / R0 / T0
IF (IENTROPY.EQ.1) THEN
PSI0 = (Q0 - U0 * B01)/(R0*T0)
ELSE
PSI0 = (Q0 - U0 * B01)
ENDIF
A20 = A0 * A0
RA0 = A0*R0
AB0 = A0*B0
SPECIN = HP/RPERM
PMICH = PP_P / 1.01325D5
CALL PHASES (TMICH,PMICH,IMICH,SPECIN,IPS)
TP = TMICH
RP = RMICH
ESP = ES1
AP = AMICH
! CALC. THE FRICTION FACTOR AT THIS POINT FOR THE CALCULATION
!OF WALL SHEAR STRESS

IF (UP_P.NE.0.D0) THEN
REP = RP*DABS(UP_P)*DPIPE/VIS
CALL FRICTIONFCT(REP,RP,UP_P,IPS,FF)
! CALC. FRICTIONAL FORCE EFFECTS AND HEAT TRANSFER EFFECTS
BP = -2.D0 * FF / DPIPE * RP * UP_P * DABS(UP_P)
BP1 = BP
BP = BP - RP*GSTHETA
ELSE
BP1 = 0.D0
BP = 0.D0 - RP*GSTHETA
ENDIF
QP = 4.D0 * HTUP * (TWUP - TP) / DPIPE
PSIP = ESP * (QP - UP_P * BP1) / RP / TP
RAP = RP * AP
ABP = AP * BP
! INITIAL APPROXIMATIONS

IF (ITERM.EQ.1) THEN
U2 = U0
R2 = R0
A2T = A0
H2 = H0
P2 = P0
PSI02 = PSI0
PSI2 = PSI0K
```

```
RA2 = RA0
PSIPM_P = PSIP
PSINM = PSIN
RAPM_P = RAP
RANM = RAN
ABPM_P = ABP
ABNM = ABN
ELSE
PSIPM_P = (PSIP + PSI2) * 0.5D0
PSINM = (PSIN + PSI2) * 0.5D0
RAPM_P = (RAP + RA2) * 0.5D0
RANM = (RAN + RA2) * 0.5D0
ABPM_P = (ABP + AB2) * 0.5D0
ABNM = (ABN + AB2) * 0.5D0
ENDIF
R0MN = (R0 + R2) * 0.5D0

A20M = (A20 + A2T * A2T) * 0.5D0
PSI0M = (PSI0 + PSI02) * 0.5D0

EndPointType = 4;

IF (EndPointType == 4 ) THEN
!BOUNDARY CONDITIONS FOR THE CLOSED END BOUNDARY
!CONDITIONS
!U0 = 0.d0

POLD = P2
ROLD = R2
UOLD = U2
HOLD = H2/RPERM

U2 = U0
H2 = -1375.132160407311630d0
P2 = ((PSIPM_P + ABPM_P) * DT)+PP_P -RAPM_P*(u2-UP_P)

if (P2 .le.73.8d5)then
pause
end if

IF (P2.LT.PEXT) THEN
P2 = PEXT
ENDIF

SPECIN = H2/RPERM
PMICH = P2 / 1.01325D5
```

```
CALL getdata(pmich,sPECIN,rmich,amich,tmich,hmich,es1,IPS)
R2 = RMICH
T2 = TMICH
ES2 = ES1
A2T = AMICH
VIS2 = VIS
H2_out=hmich

write(101,*)time,P2,R2,U2
write(103,*)T2,H2_out,H2,R2

ELSE IF (EndPointType == 3) THEN
!BOUNDARY CONDITIONS FOR THE FIXED PRESSURE BOUNDARY
!CONDITIONS
ROLD = R2
UOLD = U2
HOLD = H2/RPERM
POLD = P2

P2 = PX3
AK1 = ((PSIPM_P + ABPM_P) * DT)- (P2-PP_P) + RAPM_P*UP_P

! EVALUATE THE CHANGE IN U, P AND R AT THIS ITERATION
U2 = AK1/RAPM_P
IF (IENTROPY.EQ.1) THEN
H2 = ( PSI0M * DT) + H0
ELSE
H2 = ( PSI0M * DT + (P2 - P0))/ R0MN + H0
ENDIF
ELSE IF (EndPointType == 5) THEN
!BOUNDARY CONDITIONS FOR THE CONNECTOR BOUNDARY
!CONDITIONS
IF (ITERM.EQ.1) THEN
R2 = RX3
RA2 = RX3*AX3
T2 = TX3
P2 = PX3
A2T = AX3
ES2 = ESX3
H2 = HX3
END IF
POLD = P2
ROLD = R2
UOLD = U2
HOLD = H2/RPERM

AK1 = ((PSIPM_P + ABPM_P) * DT)- (P2-PP_P) + RAPM_P*UP_P
```

```
! EVALUATE THE CHANGE IN U, P AND R AT THIS ITERATION

U2 = AK1/RAPM_P
ELSE IF (EndPointType == 6 .OR.EndPointType == 7) THEN
!BOUNDARY CONDITIONS FOR THE PUNCTURE AT THE END AND FULL
!BORE RUPTURE

POLD = P2
ROLD = R2
UOLD = U2
HOLD = H2/RPERM

AK1 = (PSIPM_P + ABPM_P) * DT
AK2 = (PSINM - ABNM) * DT

U2 = (AK1 - AK2 + RAPM_P*UP_P + RANM*UN + PP_P - PN)/ (RANM + &
&RAPM_P)
ITES2 = 0
P2 = AK1  - RAPM_P*(U2 - UP_P) + PP_P

IF (P2.LT.PEXT.OR.P2.GT.(3.*CPGT)) THEN
IF (P2.LT.PEXT) THEN
P2 = PEXT
ELSE
P2 = C7
ENDIF
AK1 = ((PSIPM_P + ABPM_P) * DT)- (P2-PP_P) + RAPM_P*UP_P
U2 = AK1/RAPM_P
ENDIF
IF (IENTROPY.EQ.1) THEN
H2 = ( PSI0M * DT) + H0
ELSE
H2 = ( PSI0M * DT + (P2 - P0))/ R0MN + H0
ENDIF
SPECIN = H2/RPERM
H2F = SPECIN
PMICH = P2 / 1.01325D5
CALL getdata(pmich,sPECIN,rmich,amich,tmich,hmich,es1,IPS)
T2 = TMICH
ES2 = ES1
A2T = AMICH
VIS2 = VIS
R2 = RMICH
SU = SNT
HU = HNT
HU = HU + (U2**2)*WMT1/(2.D0*RGAS)
```

```
RMWD = WMT1
PUP1 = P2/PUNIT
PD = PEXT/PUNIT
N9 = NCOMP
CALL ORIFICE(CPT1,CVT1,HU,PD,PUP1,SU,XU,N9,VEL,DENT,
&PO,TO,VOL,YO,XO,ZOX,ZOY,IC,IP)
QDIS = VEL*DISAREA2*DENT
IMK = 2
SPECK = SU

U2 = QDIS/(R2*APIPE)
IF (U2.GT.A2T) THEN
P2 = PO*PUNIT
PMICH = PO
SPECIN = SU
IMK = 2
U2 = VEL

ENDIF
END IF
! EVALUATE THE CHANGE IN U, P AND R AT THIS ITERATION
! The following are standard bounds that have been developed to ensure
! that the solution obtained is admissible
SPECIN = H2/RPERM
H2F = SPECIN
PMICH = P2 / 1.01325D5
799   CALL PHASES (TMICH,PMICH,IMICH,SPECIN,IPS)
T2 = TMICH
ES2 = ES1
A2T = AMICH
VIS2 = VIS
R2 = RMICH
! CHECK CONVERGENCE

IF (ITERM.EQ.1) GOTO 576
DEVP = DABS(P2 - POLD)/DABS(POLD)
DEVH = DABS(H2F - HOLD)/DABS(HOLD)
IF (ITERM.GT.1) THEN
IF (XPOLD.LT.X) THEN
DEVXP = DABS(XP-XPOLD)/DABS(XPOLD)
ELSEIF (XP.LT.X) THEN
DEVXP = DABS(XP-XPOLD)/DABS(XP)
ELSE
DEVXP = 0.D0
ENDIF
IF (X0OLD.LT.X) THEN
DEVX0 = DABS(X0-X0OLD)/DABS(X0OLD)
```

```
ELSEIF (X0.LT.X) THEN
DEVX0 = DABS(X0-X0OLD)/DABS(X0)
ELSE
DEVX0 = 0.D0
ENDIF
ENDIF
IF (DEVP.LT.EPS.AND.DEVH.LT.EPS) GO TO 111
IF (ITERM.GT.5.AND.DEVH.LT.EPS1.AND.DEVP.LT.EPS1) GOTO 111

IF (DEVX0.GT.(0.D0).AND.DEVXP.GT.(0.D0)) THEN
IF (ITERM.GE.50.AND.DEVX0.LT.EPSN.AND.DEVXP.LT.EPSN) GOTO 111
ENDIF
576   B2 = 0.D0
B21 = B2
B2 = B2 - R2*GSTHETA
Q2 = 4.D0 * HTSP * (TWSP - T2) / DPIPE
PSI2 = ES2 * (Q2 - U2 * B21) / R2 / T2
IF (IENTROPY.EQ.1) THEN
PSI02 = (Q2 - U2 * B21)/(R2*T2)
ELSE
PSI02 = (Q2 - U2 * B21)
ENDIF
RA2 = R2 * A2T
AB2 = A2T * B2
! this was added to serve as a new set of convergence criteria
XPOLD = XP
X0OLD = X0
49  CONTINUE
!  WRITE (28,*)
!    & 'WARNING: NO CONVERGENCE IN THE TERMINAL POINT AT TSTEP
!= ',IT
ICHECK = 5
111   CONTINUE
A2 = A2T
TWAL1 = C19
IF (U2.NE.0.D0) THEN
REY2 = R2*DABS(U2)*DPIPE/VIS
CALL FRICTIONFCT(REY2,R2,U2,IPS,FF2)
ELSE
FF2 = 0.D0
ENDIF
REY2 = R2*DABS(U2)*DPIPE/VIS
CALL HeatCoef(P2,T2,REY2,R2,U2,FF2,DX,IPS, HTC2,TWAL1,DT,TWAL2,
&ICOR)
IF (EndPointType == 6 .OR.EndPointType == 7) THEN
! BOUNDARY CONDITIONS FOR THE PUNCTURE AT THE END AND FULL
!BORE RUPTURE
```

```
! BOUNDARY CONDITIONS

ABOUNDL(IZ3) = A2T
UBOUNDL(IZ3) = U2
RBOUNDL(IZ3) = R2
PBOUNDL(IZ3) = P2
TBOUNDL(IZ3) = T2
EBOUNDL(IZ3) = ES2
VBOUNDL(IZ3) = VIS2
HBOUNDL(IZ3) = H2

IF (INTERPOLATE.EQ.1) THEN
CALL getdata(PO,SPECK,rmich,amich,TO,hmich,es1,IPZZ)
ELSE
CALL PHASES (TO,PO,IMK,SPECK,IPZZ)
ENDIF
IF (NZIP1.NE.1) THEN
NZIP1 = 1
PZ1 = PO*PUNIT
TZ1 = TO
AZ1 = AMICH
VZ1 = VEL
DZ1 = RMICH
IPZ1 = IPZZ
IF (PZ1.GT.PEXT) VZ1 = AZ1
ENDIF
IF (IFIXIT.GT.2) THEN
NZIP1 = 0
PZ2 = PO*PUNIT
TZ2 = TO
AZ2 = AMICH
VZ2 = VEL
DZ2 = RMICH
IPZ2 = IPZZ
IF (PZ2.GT.PEXT) VZ2 = AZ2
ENDIF

ELSE IF (EndPointType == 3) THEN
RE2 = R2*DABS(U2)*DPIPE/VIS
RX3 = R2
VISX3 = VIS
TX3 = T2
AX3 = A2
HX3 = H2
ESX3 = ES2
! Input values for common carryon2 which is used as input values into the orifice
!subroutine
```

```
SNT2  = SNT
HNT2 = HNT
CVT2  = CVT1
CPT2  =  CPT1
WMT2 = WMT1
ZT2 = ZT1

END IF

RETURN
END SUBROUTINE
```

Appendix C: Analytical method (Fotran Plato IDE)

```
Program line_packing
Use types
Use Thermodynamics
Implicit double precision (a-h, o-z)
Double precision mw_liq
Character hrf*3, herr*255
Dimension x(20),xl(20),xv(20),xdew(20),ybub(20)
External RES, JAC, DMACH
Integer NEQ, INFO_(15), IDID, LRW, IWORK(22), LIW, IPAR(1)
Real(kind=dp_t):: T, Y(1), YPRIME(1), TOUT, RTOL(1), ATOL(1), RWORK(550),
&RPAR(1)
Real(kind=dp_t):: z_, dv_, dl_, Re
Common/propCO2/x,mw_liq
Common/properties/T_o,A_p,Q_o,R_oo,h_,w_o,P_,P_o,d_t,D_o,P1,P2,tout,ff
Call refprop

Open(unit = 10, file = 'Output1.csv')
Open(unit = 20, file = 'Output2.csv')
Open(unit = 30, file = 'Output3.csv')

! Set up of DASSL solver
t_end = 1000.d0      ! s
NOUT = 1000          ! number of outputs before t_end
d_t = t_end/NOUT
DTOUT = d_t          ! time increment for output
TOUT1 = 1.0D-9       ! 1st time step
NERR = 0
RTOL = 1.0D-5         !  relative tolerance
ATOL = 0.             !  absolute tolerance
NEQ = 1              ! Number of equations
LRW = 550
LIW = 21 + NEQ
```

```
DO 115 I = 1,15
115    INFO_(I) = 0

TOUT = TOUT1
ERO = 0.0D0

! Set up the pipelines
A_p = 0.25d0*pi*(D_p-2.d0*th_p)**2.d0 ! area of pipe

! Initial condition in the pipe
P_o = 150.d5 !Pa
P_0 = P_o/1.d3
T_0 = 293.15d0
call TPFLSH (t_0,p_0,x,D,Dl,Dv,xl,xv,q,e,h,s,cv,cp,w,ierr,herr)
p1=p_0
t1=t_0
h1 = h/R
R1 = d
CALL PDFLSH (p1,r1,X,t,Dl,Dv,xL,XV,q,e,h,s,cv,cp,w,ierr,herr)
p_o = p1
r_o = r1
r_oo=821.439616740959309d0  !r1*mw_liq
T_o = T
H_o = H
s_o = s
write(10,1000) p_o,r_o,t_o,h_o,s_o
1000 format(5(E16.8,' , '))
Q_o = m_o/(r_oo)
P1_ = 150.d5
U1_ = Q_o/A_p
!calculate for the friction factor
! Fanning friction factor evaluated using the Colebrook and White equation:
 RF=3.5d-3
 vis=6.667882247302339d-5!6.79742895985103d-5
 RENS =(r_oo*U1_*(D_p-2.d0*th_p))/vis
 FC01 = DLOG10((1.D0/2.82577D0)*(RF/(D_p-
2.d0*th_p))**1.1098D0+5.8506D0/RENS**0.8981D0)
 FC0 = 1.D0/(-2.D0*DLOG10(DABS((RF/3.7065D0/(D_p-2.d0*th_p))-
&5.0452D0/RENS*FC01)))
 FF = (FC0**2)/4.D0
 P2 = P1_-(ff*u1_*abs(u1_)*r_oo*L_p1*2/(D_p-2*th_p))
 U1(1) = U1_

! Initialisation of DASSL variables:
T = 0.0D0
YPRIME(1) = 0.
```

```
DO 170 IOUT = 2,NOUT
Y(1) = U1(IOUT-1)

call DDASSL(RES,NEQ,T,Y,YPRIME,TOUT,INFO_,RTOL,ATOL,IDID, &
&RWORK,LRW,IWORK,LIW,RPAR,IPAR,JAC)

! Update the system properties:
U1(IOUT) = Y(1)
print*,'tout=',tout,'U1_=',U1(IOUT)
write(20,1100)tout,U1(IOUT)
1100 format(2(E16.8,' , '))

170  TOUT = TOUT + DTOUT
End program line_packing

Subroutine JAC (T, Y, YPRIME, PD, CJ, RPAR, IPAR)
End Subroutine JAC

Subroutine Res(T, Y, YPRIME, DELTA, IRES, RPAR, IPAR)
Use Types
Use Thermodynamics
Implicit double precision (a-h, o-z)
Double precision mw_liq
Real(kind=dp_t):: velocity1,pressure1
Parameter (ncmax=20)
Dimension x(20),Xv(20),Xl(20),xbub(20),xdew(20)
Character*255 herr
Integer  IRES, IPAR(*),IDID
Real(kind=dp_t)::  T, Y(*), YPRIME(*), DELTA(*), RPAR(*),z_
Common/propCO2/x,mw_liq
common/properties/T_o,A_p,Q_o,R_oo,h_,w_o,P_,P_o,d_t,D_o,P1,P2,tout,ff
call refprop

velocity1 = Y(1)
call res2 (tout,deltap)

DELTA(1)=YPRIME(1)*L_P1-
(deltap/r_oo)+(2*ff*L_p1*velocity1*abs(velocity1))/((D_p-2*th_p))

write(30,*)tout,deltap
end subroutine Res

subroutine Res2(tout,deltap)
use thermodynamics
use types
implicit double precision (a-h,o-z)
```

```
double precision mw_liq
dimension x(20),xl(20),xv(20),xdew(20),ybub(20)
character*255 herr,herr2
common/propCO2/x,mw_liq
common/properties/T_o,A_p,Q_o,R_oo,h_,w_o,P_,P_o,d_t,D_o,P1,P2
call Refprop

!deltaz=(-TANH((tout-1100)/200)+1)/2*(208.4324834-57.8)+57.8
!deltap=(-TANH((tout-1100)/200)+1)/2*(1701871.115-471751.7721)+471751.7721
!deltap=0.000609579069534849*tout**6 - 0.104976950870991000000*tout**5 + &
!& 6.58878936743713*tout**4 - 173.73403752339*tout**3 +
1484.47817728482*tout**2 - 6737.77106902003*tout + 337782.926219389

if (tout .ge. 0. .and. tout .le.100)then

deltap= -0.00000530219697092438*tout**6 + 0.00117701278114168*tout**5 - &
& 0.0979122065946285*tout**4 + 3.76763301191386*tout**3 -
66.6452217213809*tout**2 + &
& 423.959992289543*tout + 1677105.98473996

else

deltap=0.00000000000623773287684354*tout**6 -
0.000000214272996150165*tout**5 + &
& 0.000292626445075141*tout**4 -
0.204831650658114*tout**3+80.3706174185315*tout**2- &
& 18473.706438655*tout + 2689977.87126665

  end if

end subroutine res2

subroutine jac_(n,xg,fvec,fjac,ldfjac,iflag)
integer ldfjac
!real(kind=dp_t):: xg(n),fvec(n),fjac(ldfjac,n)
return
end  subroutine

Module Types
Implicit None
! Double precision floating point data are declared as
! REAL(KIND=dp_t), this is akin to the old non-standard
! REAL*8, or DOUBLE PRECISION
! integer, parameter :: dp_t = kind(0.0d0)
integer, parameter, public :: dp_t = selected_real_kind(15,307)
! Single precision floating point data are declared as
! REAL(kind=sp_t), or simply as REAL.
```

```
! integer, parameter :: sp_t = kind(0.0)
integer, parameter, public :: sp_t = selected_real_kind(6, 37)
End Module Types

Module thermodynamics
use Types
real(kind=dp_t),dimension(100000)::U1
real(kind=dp_t)::
p,D,Dl,Dv,xl,xv,q,e,h,S,cv,cp,w,tbub,tdew,Dlbub,Dvdew,ybub,xdew,U_,P_,P2_
real(kind=dp_t), parameter:: pi = 3.14159265358979323846264 3_dp_t
real(kind=dp_t), parameter:: g = 9.80665_dp_t
real(kind=dp_t), parameter:: R = 8.3144621_dp_t
real(kind=dp_t), parameter:: m_o = 156.4d0
real(kind=dp_t), parameter:: L_p1 = 50000.d0 !m
real(kind=dp_t), parameter:: D_p = 0.4d0  ! pipes' diameter
real(kind=dp_t), parameter:: th_p = 0.02d0! pipes' thickness
integer, parameter:: nprint = 1, n=1
real(kind=dp_t), parameter:: tol = 1.d-5
real(kind=dp_t):: xg(1),press2,pressure2
integer:: iflag,icomp,info_a
contains

subroutine Refprop
implicit double precision(a-h,o-z)
double precision mw_liq
integer::info,iflag
integer::u,icomp
parameter (ncmax=20)
dimension x(ncmax),xl(ncmax),xv(ncmax),xdew(ncmax),ybub(ncmax)
character hrf*3, herr*255
character*255 hf(ncmax),hfmix
common/propCO2/x,mw_liq
call SETPATH('C:\Users\Nor\Desktop\Pipe 25-1-2015-FortranCode\Pipe_pump')
  hfmix='hmx.bnc'
  hrf='DEF'

! CO2:
  u=1
  x(1)= 1
  hf(1)='CO2.fld'

! Impurities - Oxyfuel - raw:

! u=10
! hf(2)='NITROGEN.fld';       x(2)= 0.085
! hf(3)='HYDROGEN.fld';     x(3)= 0.
! hf(4)='OXYGEN.fld';          x(4)= 0.06
```

```
! hf(5)='CO.fld';                 x(5)= 0.00005
! hf(6)='H2S.fld';                x(6)= 0.
! hf(7)='SO2.fld';                x(7)= 0.0008
! hf(8)='WATER.fld';              x(8)= 0.0001
! hf(9)='NO2.fld';                x(9)= 0.000609
! hf(10)='ARGON.fld';             x(10)=0.04

! Impurities - Precombustion:

! u=10
! hf(2)='NITROGEN.fld';     x(2)= 0.0002
! hf(3)='HYDROGEN.fld';     x(3)= 0.015
! hf(4)='OXYGEN.fld';       x(4)= 0.
! hf(5)='CO.fld';           x(5)= 0.0013
! hf(6)='H2S.fld';          x(6)= 0.0017
! hf(7)='SO2.fld';          x(7)= 0.0007
! hf(8)='WATER.fld';        x(8)= 0.00015
! hf(9)='METHANE.fld';      x(9)= 0.00011
! hf(10)='ARGON.fld';       x(10)=0.00018

! Impurities - Postcombustion:
! u=10
!hf(2)='NITROGEN.fld';     x(2)= 0.0029
!hf(3)='HYDROGEN.fld';     x(3)= 0.
!hf(4)='OXYGEN.fld';       x(4)= 0.00035
!hf(5)='CO.fld';           x(5)= 0.00001
!hf(6)='H2S.fld';          x(6)= 0.
!hf(7)='SO2.fld';          x(7)= 0.0000671
!hf(8)='WATER.fld';        x(8)= 0.01
!hf(9)='NO2.fld';          x(9)= 0.0000388
!hf(10)='ARGON.fld';       x(10)=0.00021

 do  j = 2, u
      x(1)= x(1) - x(j)
     enddo

call SETUP (u,hf,hfmix,hrf,ierr,herr)
call SETHMX (hfmix,ierr,herr)
!if (ierr.ne.0) write (*,*) herr
!call PREOS (2)
!Molecular weight of the mixture:
 mw_liq = WMOL(x)  ! g/mol
end subroutine Refprop

end module thermodynamics
```